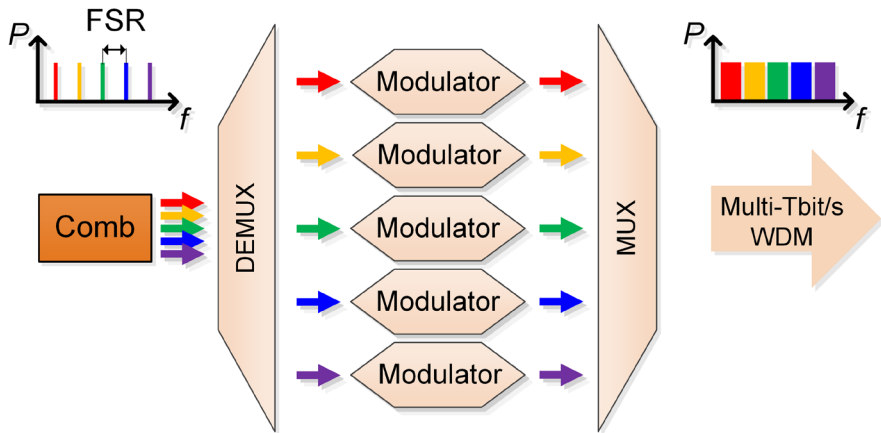


Pablo Marin-Palomo

Chip-scale optical frequency comb sources for terabit communications



Pablo Marin-Palomo

**Chip-scale optical frequency comb sources
for terabit communications**

Karlsruhe Series in Photonics & Communications, Vol. 33
Edited by Profs. C. Koos, W. Freude and S. Randel

Karlsruhe Institute of Technology (KIT)
Institute of Photonics and Quantum Electronics (IPQ)
Germany

Chip-scale optical frequency comb sources for terabit communications

by
Pablo Marin-Palomo

Karlsruher Institut für Technologie
Institut für Photonik und Quantenelektronik

Chip-scale optical frequency comb sources for terabit communications

Zur Erlangung des akademischen Grades eines Doktor-Ingenieurs
von der KIT-Fakultät für Elektrotechnik und Informationstechnik des
Karlsruher Instituts für Technologie (KIT) genehmigte Dissertation

von Pablo Marin-Palomo, M.Sc.

Tag der mündlichen Prüfung: 26. Februar 2021

Hauptreferent: Prof. Dr. Christian Koos

Korreferenten: Prof. Dr. Jens Biegert

Prof. Dr.-Ing. Dr. h.c. Wolfgang Freude

Impressum



Karlsruher Institut für Technologie (KIT)
KIT Scientific Publishing
Straße am Forum 2
D-76131 Karlsruhe

KIT Scientific Publishing is a registered trademark
of Karlsruhe Institute of Technology.
Reprint using the book cover is not allowed.

www.ksp.kit.edu



*This document – excluding parts marked otherwise, the cover, pictures and graphs –
is licensed under a Creative Commons Attribution 4.0 International License
(CC BY 4.0): <https://creativecommons.org/licenses/by/4.0/deed.en>*



*The cover page is licensed under a Creative Commons
Attribution-NonCommercial 4.0 International License (CC BY-ND 4.0):
<https://creativecommons.org/licenses/by-nd/4.0/deed.en>*

Print on Demand 2022 – Gedruckt auf FSC-zertifiziertem Papier

ISSN 1865-1100

ISBN 978-3-7315-1129-8

DOI 10.5445/KSP/1000137870

Table of Contents

Abstract (German)	v
Abstract	ix
Achievements of the present work	xiii
1 Introduction	1
1.1 Need for coherent massively-parallel WDM with chip-scale frequency comb generators	3
1.2 Evolution of optical frequency comb generators and their applications	5
2 Theoretical background	11
2.1 Coherent data transmission setups and signal processing	11
2.1.1 Signal encoding and shaping	13
2.1.2 In-phase/quadrature (IQ) modulator	16
2.1.3 Wavelength-division multiplexing (WDM) and polarization-division multiplexing (PDM)	18
2.1.4 Transmission link	20
2.1.5 Optical receiver front-end and ADC	24
2.1.6 Digital signal processing algorithms	26
2.1.7 Quality metrics for K -ary QAM signals	28
2.2 Optical frequency combs	31
2.3 Frequency comb generation in QD-MLLD	36
2.3.1 Frequency comb properties	37
2.3.2 Phase noise reduction techniques	38
2.4 Frequency comb generation with Kerr-nonlinear microresonators	40
2.4.1 Kerr comb formation: From Turing patterns to solitons	40
2.4.2 Dissipative Kerr solitons in SiN microresonators	45

3	Performance of chip-scale optical frequency comb generators in coherent WDM communications	47
3.1	Introduction	48
3.2	OSNR limitations in a comb-based WDM system.....	50
3.3	OSNR limitations considering frequency combs with flat spectra.....	55
3.4	OSNR limitations considering frequency combs with line-to-line power variations	60
3.5	Summary.....	66
4	DC-driven quantum-dash mode-locked laser diode for Tbit/s WDM transmission	67
4.1	Introduction	68
4.2	Quantum-dash mode-locked laser diodes.....	70
4.3	Phase noise characteristics of QD-MLLD.....	74
4.3.1	Phase-noise and linewidth model.....	75
4.3.2	Short-term linewidth from measured FM-noise spectrum.....	78
4.3.3	Long-term linewidth measurement	80
4.4	Coherent transmission using QD-MLLD	82
4.4.1	Influence of comb-carrier linewidth and OSNR on coherent communications.....	83
4.4.2	Data recovery using feed-forward symbol-wise blind phase search.....	87
4.4.3	42 GBd PDM-QPSK 7.83 Tbit/s data transmission.....	91
4.4.4	38 GBd PDM-16QAM 10.68 Tbit/s data transmission	93
4.5	Summary.....	95
5	Microresonator-based Kerr comb generators for massively parallel coherent optical communications	97
5.1	Introduction	99
5.2	Generation of dissipative Kerr soliton frequency combs in SiN microresonators	102
5.3	Soliton Kerr comb generators for as multi-wavelength carriers for WDM transmission.....	104

5.4	Data transmission using DKS combs both at the transmitter and at the receiver.....	108
5.5	Power conversion efficiency of dissipative Kerr solitons.....	108
5.6	Summary.....	110
6	Summary and Outlook	111
6.1	Summary.....	111
6.2	Outlook.....	112
	Appendices.....	115
A.	Performance of chip-scale optical frequency comb generators in coherent WDM communications: Additional information.....	117
A.1	OSNR penalty when using frequency comb sources at the receiver side.....	117
A.2	Omission of modulated noise.....	119
B.	Microresonator-based solitons for WDM communications (Tx, Rx).....	121
B.1	Methods	122
B.1.1	Fabrication of high- Q Si_3N_4 microresonator.....	122
B.1.2	Soliton comb generation	123
B.1.3	Dissipative Kerr soliton comb tuning and interleaving	125
B.1.4	Data transmission experiments	125
B.1.5	Transmission impairments and data rates	126
B.1.6	Characterization of the OSNR penalty of frequency comb source	128
B.2	Kerr soliton frequency comb generation.....	129
B.3	Data transmission experiments using Kerr-soliton frequency combs in the transmitter	133
B.4	OSNR measurements	137
B.4.1	Theoretical required OSNR for error free transmission with FEC	137
B.4.2	OSNR measurements	139
B.5	Coherent reception using a Kerr-soliton frequency comb LO.....	142
B.6	Energy consumption analysis.....	146

B.6.1	Electrical power consumption of comb generators and ITLA array.....	147
B.6.2	Dispersion and coupling parameters of SiN microresonators	152
B.6.3	OSNR for DKS and ITLA WDM sources	155
C.	Bibliography	161
D.	Glossary.....	179
D.1	List of Abbreviations.....	179
D.2	List of mathematical symbols.....	183
	Acknowledgments	187
	List of Publications	191
	Book Chapter	191
	Journal Publications	191
	Conference Publications	193

Abstract (German)

Seit der Erfindung des ARPANET und dem Aufbau eines weltweiten Kommunikationsnetzwerks in den späten 1980er Jahren nimmt dessen Nutzung unaufhörlich zu. Nach Angaben des IT-Konzerns Cisco steigt der Datenverkehr in allen Netzebenen exponentiell an und verdoppelt sich alle drei Jahre. Besonders deutlich erkennbar ist dieser Anstieg in jüngster Zeit bei Verbindungen, die zwei oder mehr Rechenzentren innerhalb eines Ballungsraumes verbinden und Entfernungen von wenigen bis 100 Kilometern überbrücken. Um Übertragungsengpässe zu vermeiden, sollten diese Verbindungen große Datenraten von einigen Terabit-pro-Sekunde ermöglichen. Für Langstreckennetze über Tausende von Kilometern, bei denen die Kosten für die Glasfaserinfrastruktur dominieren, wird seit den 1990er Jahren das Wellenlängenmultiplexverfahren (engl. wavelength-division multiplexing, WDM) mit hunderten von optischen Kanälen eingesetzt. Der Trend zu kürzeren Verbindungen, die in weitaus größeren Stückzahlen eingesetzt werden, verlagert jedoch den wirtschaftlichen Fokus weg von der Faserinfrastruktur hin zu den zugehörigen Transceivern und deren Größe und Kosten. Während die photonische Integration bereits kostengünstige kohärente Multi-Terabit/s-Transceiver im Chipformat durch eine kompakte Realisation von Modulatoren, Multiplexern, Detektoren und anderen passiven Komponenten ermöglicht, ist die Skalierbarkeit der Kanalzahl sowohl am Sender als auch am Empfänger einer WDM-Verbindung noch immer durch den Mangel an geeigneten optischen Quellen begrenzt.

In diesem Zusammenhang erweisen sich optische Frequenzkammquellen als besonders attraktive Multi-Wellenlängen-Lichtquellen, die sowohl am Sender als auch am Empfänger eine große Anzahl von wohldefinierten Trägern bereitstellen können. Im Gegensatz zu den Trägern unabhängiger Laserquellen sind die Träger eines Frequenzkamms streng frequenzäquidistant und ihre absolute Frequenz ist durch nur zwei Parameter, den Linienabstand, den sogenannten freien spektralen Bereich (engl. free spectral range, FSR), und die Zentralfrequenz, perfekt bestimmt. Damit wird die Notwendigkeit einer individuellen Wellenlängenstabilisierung hinfällig.

Unter den verschiedenen Frequenzkammgenerator-konzepten sind integrierte Kammquellen der Schlüssel zu hoch skalierbaren, preiswerten und kompakten WDM-Transceivern. Durch diese Kammquellen können Dutzende oder sogar Hunderte von schmalbandigen optischen Trägern auf einem Mikrochip energieeffizient realisiert werden.

Das Ziel dieser Arbeit ist es, das Potenzial von integrierten Frequenzkammquellen für kohärente, massiv-parallele WDM-Übertragung zu erforschen und experimentell zu bestätigen. In diesem Zusammenhang wird eine breit angelegte Studie durchgeführt, um den Einfluss der Frequenzkamm-eigenschaften auf die Leistungsfähigkeit der WDM-Verbindungen zu untersuchen und die Anforderungen an den Frequenzkamm zur Maximierung der Übertragungskapazität zu bestimmen. Der Fokus liegt dabei auf der Charakterisierung von zwei vielversprechenden integrierten Kammquellen und deren Einsatz in WDM-Übertragungsexperimenten. Bei der ersten untersuchten Kammquelle handelt es sich um eine sogenannte modengekoppelte Quantenstrich-Laserdiode (engl. quantum-dash mode-locked laser diode, QD-MLLD), die eine kleine Grundfläche mit einem einfachen Gleichstrombetrieb kombiniert und ein flaches, breitbandiges Kamm-Spektrum bietet. Die zweite untersuchte Kammquelle ist ein Kerr-nichtlinearer Siliziumnitrid (SiN)-Mikroresonator, der mit einem Dauerstrichlaser (engl. continuous wave, CW) betrieben. Durch ein Gleichgewicht von Dispersion und Nichtlinearität entsteht eine stabile ultrakurze Pulsfolge, ein sogenannter Solitonenzug, der einem mehrere Telekommunikationsbänder überspannenden Frequenzkamm entspricht. Die Ergebnisse dieser Untersuchungen sind in den internationalen Fachzeitschriften *Nature* und *Optics Express* [J1]-[J3] sowie in Konferenzbeiträgen [C1]-[C3] veröffentlicht worden.

Kapitel 1 gibt einen kurzen Überblick über die Entwicklung von Frequenzkammquellen, von Tischgeräten bis hin zu photonisch integrierten Chips. Insbesondere zeigt dieses Kapitel die Vorteile der Verwendung von integrierten Kammquellen für die massiv-parallele WDM-Übertragung. Das Kapitel endet mit einer Beschreibung der in dieser Arbeit untersuchten Kammquellen.

Kapitel 2 fasst die wichtigsten Eigenschaften und Limitierungen von Frequenzkämmen im Hinblick auf die kohärente Kommunikation zusammen. Darüber hinaus beschreibt das Kapitel die Technologie und den Mechanismus der Frequenzkamm-Erzeugung in einer QD-MLLD und in einem Kerr-nichtlinearen Mikroresonator.

Kapitel 3 untersucht das Potenzial von integrierten Frequenzkämmen als Lichtquellen am Sender und am Empfänger für massiv-parallele WDM-Verbindungen. Die breit angelegte Studie hilft verschiedene Kammgenerator-typen in Bezug auf ihre Leistungsfähigkeit in Übertragungsnetzwerken zu vergleichen. Insbesondere wird unter Berücksichtigung der optischen Leistung und des optischen Träger-Rausch-Verhältnisses (engl. optical carrier-to-noise ratio, OCNR) des Frequenzkamms ein Ausdruck für die maximal mögliche Verbindungsdatenrate, hergeleitet.

Kapitel 4 widmet sich der Demonstration des Potenzials von QD-MLLD als Multi-Wellenlängen-Lichtquellen in massiv-parallelen WDM-Datenübertragungen. Während diese DC-getriebenen Bauelemente kompakt sind und einen flachen und breitbandigen Frequenzkamm liefern, wird durch das starke Phasenrauschen ihrer Kammlinien die Signalqualität und die Leistungsfähigkeit der kohärenten Datenübertragung beeinträchtigt, was ihre Verwendung auf eher einfache Modulationsformate wie z.B. OOK oder QPSK beschränkt. Die in dieser Arbeit beschriebenen Experimente zeigen, dass das starke Phasenrauschen durch eine spezielle digitale Phasen-nachführungstechnik, die auf symbolweiser blinder Phasensuche (engl. blind phase search, BPS) beruht, überwunden werden kann. Dies ermöglicht die Übertragung eines Datenstroms von 11,6 Tbit/s über eine Faserlänge von 75 km durch Verwendung von 16QAM, was der höchsten Datenrate mit QD-MLLD zum Zeitpunkt der Veröffentlichung [J2] entspricht.

Kapitel 5 erforscht das Potenzial von Kerr-nichtlinearen SiN-Mikroresonatoren als Multi-Wellenlängen-Lichtquellen in massiv-parallelen WDM-Datenübertragungen. Durch Antreiben des SiN-Mikroresonators mit einem CW-Laser bei richtig gewählter optischer Leistung und Wellenlänge kann ein einzelner ultrakurzer Puls, ein sogenanntes dissipatives Kerr-Soliton (DKS), im Resonator erzeugt werden. Der resultierende Solitonenzug, der den

Mikroresonator verlässt, entspricht einem breitbandigen Frequenzkamm mit rauscharmen Kammlinien. Unter Verwendung von DKS-Kämmen konnte ein Datenstrom von 55,0 Tbit/s über eine Faserlänge von 75 km übertragen werden, was zum Zeitpunkt der Veröffentlichung [J1] der höchsten Datenrate mit einer integrierten Frequenzkammquelle entspricht.

Kapitel 6 fasst die wichtigsten Ergebnisse dieser Arbeit zusammen und gibt einen Ausblick auf den Einsatz von Frequenzkammquellen im Chip-Format für weitere WDM-Anwendungen.

Abstract

Since the establishment of the ARPANET and the foundation of the internet in the late 1980s, internet usage has been unceasingly increasing. According to the IT conglomerate Cisco, data traffic is increasing exponentially, doubling every three years, across all network levels¹. Recently, this increase became more pronounced for datacenter interconnects, which link two or more data centers across a metropolitan area with typical distances from a few kilometers to 100 km. To overcome transmission bottlenecks, these links should provide multi-terabit per second connectivity. For long-haul networks of hundreds to thousands of kilometers, where the cost of the fiber infrastructure dominates, wavelength-division multiplexing (WDM) transmission using tens or hundreds of channels has been used since the 1990s. However, the trend towards shorter links, which are deployed in much larger quantities, is shifting the market concerns from the fiber infrastructure to the size and cost of the associated transceivers. While high-density photonic integration technology already allows for the realization of low-cost chip-scale multi-terabit/s coherent transceivers by dense integration of modulators, multiplexers, detectors, and other passive components, the scalability of the number of channels both at the transmitter and receiver of a WDM link is still limited by the lack of adequate optical sources.

In this context, optical frequency comb sources emerge as particularly attractive multi-wavelength light sources that can provide large numbers of well-defined carriers both at the transmitter and receiver side. In contrast to the carriers from independent laser sources, the carriers from a frequency comb are strictly equidistant in frequency and their absolute frequency is perfectly determined by only two parameters: the line spacing, or free spectral range (FSR), and the center frequency. This eliminates the need for individual wavelength stabilization.

Amongst different frequency comb generator concepts, chip-scale comb sources are key components for highly scalable WDM transceivers with cheap

¹ Cisco, "Cisco Visual Networking Index: Forecast and Trends, 2017-2022, (White Paper)," 2019.

and compact form factors. These comb sources can provide tens or even hundreds of optical narrow-band lines from a power-efficient micro-chip.

The goal of this thesis is to explore and experimentally prove the potential of chip-scale frequency comb sources for coherent massively-parallel WDM transmission. In this context, a broad study is performed to investigate the influence of frequency comb properties on the performance of the WDM link, and to determine the comb requirements for maximizing the transmission capacity. The focus is then put on characterizing and testing two highly-promising chip-scale comb sources for their use in massively parallel WDM transmission by performing various data transmission experiments. The first comb source investigated is the so-called quantum-dash mode-locked laser diode (QD-MLLD), which combines a small footprint with simple operation by a direct current (DC) and offers a flat broadband comb spectrum. The second comb source investigated is a microresonator-based Kerr comb generator, consisting of a Kerr-nonlinear silicon nitride (SiN) microresonator driven by a continuous-wave (CW) laser. Kerr comb generators can produce a stable ultra-short pulse sequence or a soliton train corresponding to a frequency comb spanning several telecommunication bands. The results of these investigations have been published in the international journals *Nature* and *Optics Express* [J1]-[J3], and in conference contributions [C1]-[C3].

Chapter 1 motivates the need for coherent WDM systems with chip-scale frequency comb devices as multi-wavelength light sources. The chapter gives an overview of how frequency comb technology evolved from macroscopic bench-top-type devices to chip-scale assemblies.

Chapter 2 provides the required theoretical background to understand the system-level experiments described in this thesis and summarizes the main properties and limitations of frequency combs with a focus on coherent communications. The chapter includes a description of the components in a coherent WDM communication system and of the associated signal processing. The chapter further describes the technology and mechanism of frequency comb generation in a QD-MLLD and in a Kerr-nonlinear microresonator.

Chapter 3 investigates the potential of chip-scale frequency comb sources as multi-wavelength light sources at the transmitter and as multi-wavelength local oscillators (LO) at the receiver of massively-parallel WDM links. This broad study helps to compare different comb generator types in terms of their achievable transmission performance. In particular, by considering the optical power and the optical carrier-to-noise ratio (OCNR) of the frequency comb, an expression is obtained for the maximum data rate the link can transmit.

Chapter 4 is dedicated to demonstrate the potential of QD-MLLD as multi-wavelength light sources for coherent WDM data transmission. While these DC-driven devices are compact and provide a flat and broadband frequency comb, the strong phase noise of the comb lines has limited their use to rather simple modulation formats such as OOK or QPSK. The experiments described in this chapter show that the strong phase noise is overcome by a dedicated digital phase-tracking technique that relies on symbol-wise blind phase search. This allows transmitting an 11.55 Tbit/s data stream over a fiber length of 75 km using 16QAM, corresponding to the highest data rate with these devices at the time of the publication.

Chapter 5 explores the potential of microresonator-based Kerr comb generators as multiwavelength light sources for coherent WDM data transmission. By pumping a SiN microresonator with a CW-laser set at the required power and wavelength, a single ultra-short pulse, termed dissipative Kerr soliton (DKS), is generated in the cavity. The resulting soliton train that leaves the microresonator corresponds to a broadband frequency comb with low-noise comb lines. Using DKS combs, a 55 Tbit/s data stream is transmitted over a fiber length of 75 km, corresponding to the highest data rate with any chip-scale frequency comb source at the time of the publication.

Chapter 6 summarizes the main results of this thesis and gives an outlook on the use of chip-scale frequency comb sources for further WDM applications.

Achievements of the present work

This thesis investigates the potential of chip-scale frequency comb sources as multi-wavelength sources for massively-parallel WDM transmission. This study helps to compare different frequency comb sources and to benchmark them with respect to the achievable transmission performance. On the experimental side, the focus is put on two comb generator concepts that are of particular interest, the quantum-dash mode-locked laser diode (QD-MLLD) and the Kerr comb generator, which consists of a Kerr-nonlinear microresonator driven by a continuous-wave (CW) laser. With a series of transmission experiments, the potential of these two devices is demonstrated. In the following, the main achievements presented in this work are highlighted.

Formulation of a holistic model that allows estimating the transmission performance of comb-based WDM systems: This model can be used to estimate the transmission performance of comb-based WDM systems under the influence of optical carrier-to-noise ratio (OCNR) limitations and line-to-line power variations [J3]. Two distinctively different regimes are identified, where the transmission performance is either limited by the comb source or by the link itself. The model also considers the impact of the OCNR of the local oscillator (LO) comb.

First demonstration of 16QAM WDM transmission using a DC-driven QD-MLLD without the use of any hardware-based phase-noise reduction scheme: For the first time, the tones of the frequency comb generated in a QD-MLLD are used to transmit 16QAM signals at 38 GBd without the need for additional hardware for phase-noise reduction. The impact of the large phase noise of the comb lines is reduced at the receiver side by a dedicated digital symbol-wise blind phase search algorithm. A line rate of 11.55 Tbit/s is measured using 38 lines of the frequency comb.

First demonstration of WDM data transmission using the comb lines of a dissipative Kerr soliton (DKS) from a Kerr comb generator: The tones of a DKS frequency comb generated from a SiN microresonator driven by a CW-

laser, are used for the first time to demonstrate coherent massively parallel WDM data transmission at line rates of 37.2 Tbit/s through 75 km of a single-mode fiber [J1].

Highest data rate achieved with chip-scale frequency comb sources: Two interleaved DKS combs are used to transmit a data stream of 55.0 Tbit/s on a total of 179 individual optical carriers that span the entire telecommunication C and L bands. At the time of the publication, this represented the largest frequency span in a WDM link that was covered by a chip-scale frequency comb, and the highest data rate achieved with any chip-scale comb source.

1 Introduction

The internet of things (IoT) is a term coined in the late 90s, targeting at “integrating and automating everything from home appliances to entire factories”. Due to the huge leap in electronic and photonic integration technology witnessed over the last decades, the concept of IoT has evolved from a hypothetical idea to a reality. Already in 2017, the number of devices connected to the internet has surpassed that of humans on Earth [1]. A vast majority of devices, some of which are not as simple to recognize as smartphones and TVs, are now contributing to the fast growth of IoT. Some examples are smart meters for tracking energy consumption, cameras for video surveillance, and healthcare monitoring wearables.

In order to provide storage, communication, and transmission to the data generated by all the devices connected to the internet, service providers such as Google and Facebook are deploying hyper-scale data centers in large numbers around the world. Figure 1.1(a) shows the increase of the worldwide number of hyper-scale data centers over the last years, with a compound annual growth rate (CAGR) of 13% and a growth saturation not yet in sight [2]. Similarly, Figure 1.1(b), shows the traffic that flows from data center to data center which is projected to increase with a CAGR of 33 %, reaching 2.8 zettabyte/year in 2021.² This increase is particularly pronounced for high-capacity point-to-point interconnects with typical lengths of less than 100 km, [3],[4]. Despite the increase in demand for such short-reach systems, they are currently limited to relatively low data rates of at most a few hundreds of Gbit/s, when compared to long reach links already transmitting tens of Tbit/s over thousands of kilometers [5].

For short-reach systems, low-cost solutions are desired. Typically architectures based on direct-detection four-level pulse amplitude modulation (PAM-4) or discrete multi-tone modulation, or even low-cost coherent detection techniques are employed [3]. These architectures are, however, characterized by their low

² One zettabyte (ZB) corresponds to 10^{21} bytes.

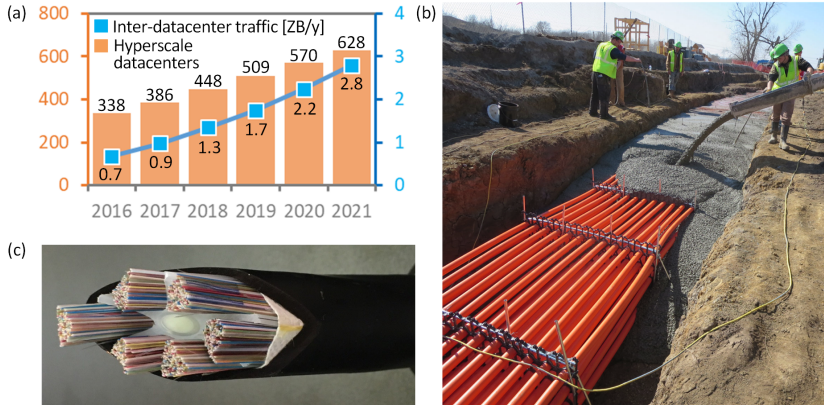


Figure 1.1: Growth of inter datacenter traffic. **(a)** Growth of the number of hyperscale data centers and growth of datacenter to datacenter traffic in zettabyte (ZB) per year [2]. **(b)** Buried fiber conduit containing tens of fiber bundles connecting two buildings on a datacenter campus. **(c)** Fiber cable comprising more than 1000 individual single-mode fibers (SMF). Figure adapted from Ch.2 in [B1].

data rate per optical fiber. Figure 1.1(b) shows an example of a buried fiber interconnect comprising tens of fiber conduits, each containing more than a thousand individual fibers connecting two facilities on a data-center campus. Nowadays, each of these fibers is still used to transmit data on a single carrier with typical data rates of a few hundreds of Gbit/s [6]. High data rates are only achieved using spatially separated channels in thousands of single-mode fibers (SMF), see Figure 1.1(c). It is, thus foreseeable that this concept of simple spatial parallelization will soon reach its scalability limits.

The capacity of each single-mode fiber can be increased by multiple orders of magnitude by spectral parallelization of data streams in each fiber using wavelength-division multiplexing (WDM) and high spectral efficiency coding. The following section motivates the need for highly parallel WDM systems in combination with spectrally efficient coherent modulation formats and introduces chip-scale frequency comb devices as the ideal multi-wavelength light sources for such WDM links. In Section 1.2, a short overview is given on how frequency comb technology evolved from macroscopic benchtop-type devices to chip-

scale assemblies, denoted as chip-scale frequency comb sources in this thesis. The section also reviews different types of frequency comb generators for their application in WDM transmission. This section is adapted from a book chapter [B1] that was published with equal contribution from the author of this thesis and Juned N. Kemal.

1.1 Need for coherent massively-parallel WDM with chip-scale frequency comb generators

High-speed optical fiber communication systems rely on wavelength-division multiplexing (WDM) schemes. While these schemes have been used since the 1990s for long-haul links over distances of thousands of kilometers [6], WDM is now becoming even more important also for shorter links ranging from few kilometers up to 100 km [7]. In combination with high spectral efficient coherent modulation formats, the capacity of each single-mode fiber can be increased to several tens of Tbit/s.

These short links are deployed in larger quantities and are much more sensitive to the cost and size of the optical transmitter and receiver [6]. Therefore, compact and cost-efficient optical transceivers are key for future WDM interconnects. In this context, optical frequency comb generators may play a key role as compact and robust multi-wavelength light sources that can provide large numbers of well-defined optical carriers. Among the various comb generator concepts, chip-scale frequency comb generators would enable cost-efficient mass production.

A particularly important advantage of frequency combs is the fact that comb lines are inherently equidistant in frequency, hence relaxing the requirements for inter-channel guard bands [38] and avoiding frequency control of individual lines as needed in conventional schemes that combine arrays of independent DFB lasers. These advantages do not apply only to the WDM transmitter, but also to the receiver, where an array of discrete local oscillators may be replaced by a single comb generator. Figure 1.2 depicts the basic architecture for a WDM communication system using either frequency combs or arrays of individually stabilized lasers at the receiver and at the transmitter. In the scheme shown in

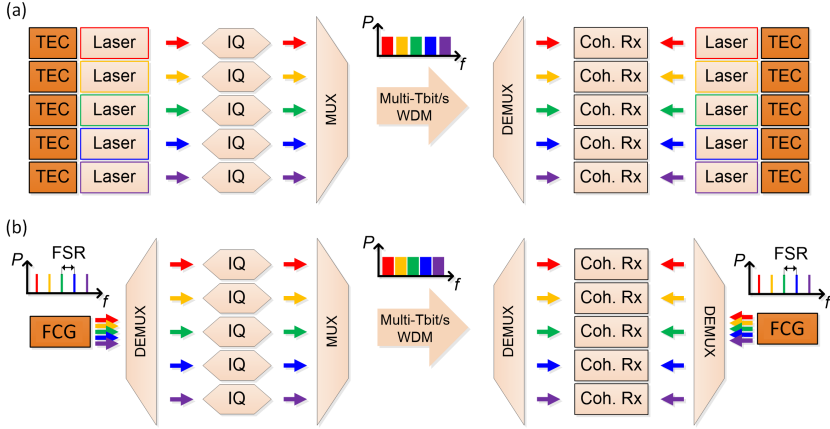


Figure 1.2: Scheme depicting the principle of WDM communications. **(a)** Conventional scheme for WDM communications using independent CW lasers as carriers at the transmitter and as LO at the receiver. The wavelength of each laser is individually stabilized with a thermo-electric cooler (TEC), each carrier is then modulated with an in-phase/quadrature (IQ) modulator and multiplexed to an optical fiber. At the receiver, the data stream is demultiplexed to the various channels and coherently received by using individual laser carriers as LO. **(b)** Comb-based scheme for WDM communications. The laser banks at the transmitter and receiver are replaced by a pair of frequency comb generators (FCG). The frequency combs are used either as a multi-wavelength carrier at the transmitter or as a multi-wavelength local oscillator at the receiver by demultiplexing their tones. MUX: wavelength multiplexer. DEMUX: wavelength demultiplexer.

Fig. 1.2(a), data are encoded on each carrier, derived from individually stabilized lasers, by means of in-phase/quadrature (IQ) modulators. The data channels are then multiplexed and transmitted through an optical fiber. At the receiver, the channels are demultiplexed and coherently detected using LO carriers, which are also derived from individually stabilized lasers. Fundamentals of coherent data transmission and reception are described in Chapter 2. In Fig. 1.2(b), the lasers arrays at the transmitter and receiver are replaced by a pair of frequency comb generators.

Using an LO comb further facilitates joint digital signal processing of the WDM channels, which may reduce receiver complexity and increase phase noise tolerance [41]. Moreover, parallel coherent reception with frequency-locked LO tones might even allow to reconstruct the time-domain waveform of the overall

WDM signal and thus permit compensation of impairments caused by optical nonlinearities of the transmission fiber [42]. These advantages make chip-scale frequency combs sources promising candidates for next-generation optical interconnects.

1.2 Evolution of optical frequency comb generators and their applications

Optical frequency combs became a topic of extensive research in the late 1990s after their successful use for measuring directly and accurately optical frequencies [8], culminating with the Nobel prize in Physics in 2005 for developing such a precision spectroscopy technique based on optical frequency combs [9]. This technique replaced previous absolute frequency measurements performed with complex RF-to-optical harmonic frequency chains built at, e.g., the Physikalisch-Technische Bundesanstalt (PTB) in Germany or the National Institute of Standards and Technology (NIST) in the USA [10]. The novel approach made use of an octave-spanning comb, whereby the frequency value of the comb line at the right edge of the spectrum, f_f , is at least twice the value of the comb line at the left edge, f_i , i.e., $f_f \geq 2f_i$. If this condition is fulfilled, a so-called $f - 2f$ self-referencing scheme can be used, in combination with measurements of the comb FSR, for stabilizing the frequency position of all of the tones of the frequency comb. This frequency stabilization allows the comb to be used as a frequency ruler to measure other optical frequencies.

Frequency combs have been conventionally generated with mode-locked femtosecond lasers using, e.g., Ti:sapphire or erbium-doped silica fibers as gain media, or with fiber-based electro-optic modulators, often in combination with highly nonlinear fibers. While these types of frequency comb generators offer high optical power and broadband comb spectra, they are technically complex, power-hungry, and not amenable to chip-scale integration, preventing low-cost mass production. Equally important, the lengthy gain media in mode-locked lasers limits the FSR of the corresponding frequency combs to rather low values of few hundreds of MHz, far away from the tens of GHz that are needed for WDM applications. Figure 1.3(a) shows an example of a state-of-the-art fiber-

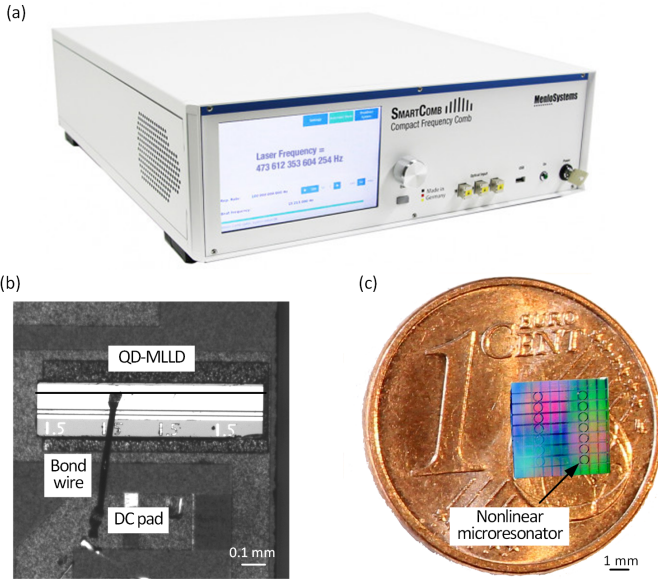


Figure 1.3. Size comparison of frequency comb generators. (a) Bench-top type frequency comb generator from Menlo Systems. The fiber-based setup is integrated into a 19-inch 3 rack-unit frame. (b) Image of a QD-MLLD mounted on a dielectric plate and contacted by a gold wire bond. (c) Image taken from a SiN chip, containing 16 microring resonators, lying on top of a one-cent coin. Each of the microresonators can be used as Kerr comb generator by driving them with a pump laser with properly chosen wavelength and optical power.

based frequency comb generator commercialized by Menlo Systems.³ In this device, the optical setup is integrated into a 19-inch 3 rack-unit frame.⁴

With the advent of integrated photonics technology, developing chip-scale frequency comb sources has been the focus of many research groups. Several types of frequency comb generators have been fabricated over the last years featuring low power consumption and small size. In this thesis, two highly-promising types of chip-scale comb sources are investigated, the QD-MLLD and the Kerr

³ <https://www.menlosystems.com/products/optical-frequency-combs/smartcomb/>

⁴ A rack unit (RU) is a unit of measure defined as 1 3/4 inches (44.45 mm). It is typically used as a measurement of the overall height of 19-inch rack frames, as well as the height of equipment that mounts in these frames and is expressed as multiples of rack units.

comb generator, which consists of a Kerr-nonlinear silicon nitride (SiN) microresonator driven by a continuous-wave (CW) laser. Figure 1.3(b) shows a QD-MLLD mounted on a dielectric plate and contacted by a gold wire bond, while Fig. 1.3(c) depicts an image of a millimeter-sized SiN chip containing 16 microresonators. Each microresonator can be used as a Kerr comb generator by driving them with a pump laser with properly adjusted wavelength and optical power [11]. In contrast to the benchtop-type comb generator of Fig. 1.3(a), these two chip-scale comb sources are characterized by their low footprint and by an FSR of the corresponding frequency comb of tens of GHz, compliant to the International Telecommunication Union (ITU) standard for WDM transmission.⁵

In the literature, other types of chip-scale comb sources have been investigated for their use as multi-wavelength light sources for WDM links. The basic setups for generating the corresponding frequency combs are depicted in Fig. 1.4(a)-(c) and are described in the following.

A frequency comb can be generated by a periodic modulation of a continuous-wave laser carrier using high-speed electro-optic modulators (EO mod.) that is driven by a sinusoidal RF signal [12], see Fig. 1.4(a). The limitation of this approach comes from the narrow bandwidth of the frequency comb at the output of the modulator. Although the bandwidth can be increased by cascading multiple EO mod., it still remains comparatively low [13]. A frequency comb can also be generated by gain switching of a semiconductor laser diode, labeled slave laser, that is injection-locked by a continuous wave (CW) master laser [14]–[17], see Fig. 1.4(b). The bandwidth of the frequency comb from the gain-switched laser diode (GSLD) is limited to a few hundred gigahertz. Frequency combs with a larger bandwidth can be obtained by spectrally broadening a seed frequency comb through third-order nonlinear processes such as self-phase modulation (SPM) and cross-phase modulation (XPM), see Fig. 1.4(c). This has been shown, e.g., using highly nonlinear waveguides (HNW) made of aluminum-gallium-arsenide-on-insulator (AlGaAsOI) [18]. Note that in [18] the seed frequency comb is based on a benchtop type pulsed fiber laser. Thus, to obtain

⁵ Carrier spacing grids ranging from 12.5 GHz to 100 GHz and integer multiples thereof are specified by the International Telecommunication Union (ITU) recommendation G.694.1 for dense WDM.

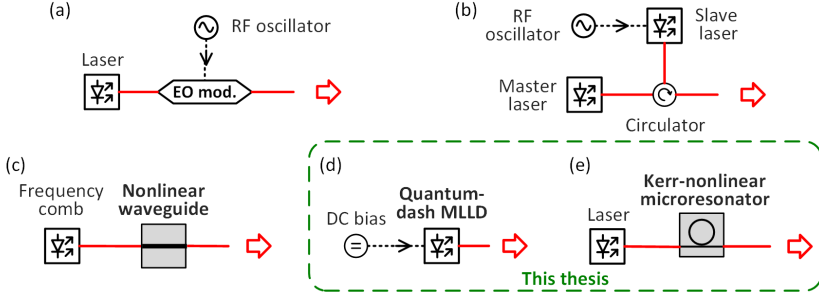


Figure 1.4: Basic setup for chip-scale frequency comb sources used in Tbit/s data transmission experiments. (a) Schematic setup of frequency comb generation using an electro-optic modulator (EO mod.). A frequency comb is generated by modulating a carrier emitted by a continuous-wave laser using an EO mod. that is driven by a sinusoidal RF signal. (b) Schematic setup of frequency comb generation by gain switching. In a gain-switched laser diode (GSLD), a frequency comb is generated by driving a slave laser by a sinusoidal signal from an RF oscillator. Injection locking a master laser to the slave laser improves the noise properties of the frequency comb. (c) Schematic setup of frequency comb broadening with Kerr-nonlinear waveguides. Spectral broadening of a seed frequency comb through nonlinear processes in a highly-nonlinear waveguide (HNW) leads to a broadband frequency comb. (d) Concept of frequency comb generation using a mode-locked laser diode (MLLD) with quantum-dash (QD) material as the active medium. An optical frequency comb can be generated by a QD-MLLD by simply driving the device with a direct current. (e) Microresonator-based Kerr comb generator. Coupling CW laser light with proper wavelength and sufficient optical power into a Kerr-nonlinear microresonator generates a frequency comb through four-wave mixing processes.

a fully integrated frequency comb generator, the source would also need to be on a chip.

Broadband frequency combs can be directly obtained from mode locked-laser diodes (MLLD). In particular, MLLD with quantum-dash (QD) gain material have been shown to generate frequency combs with bandwidths of more than 2 THz [19], see Fig. 1.4(d). An even broader frequency comb can be obtained by pumping a Kerr nonlinear microresonator with a sufficiently large power from a CW laser [21], [22], see Fig. 1.4(e). Among the various Kerr comb states, the so-called single dissipative Kerr solitons (DKS) are of particular interest for WDM applications. DKS combs are formed by an ultra-short soliton pulse circulating the microresonator, leading to broadband combs with particularly

smooth spectral envelopes. Despite the required pump laser, chip-scale assemblies generating DKS combs have been already demonstrated in the literature [23], [24].

Surrounded by a green dashed contour in Fig. 1.4 are the two frequency comb sources investigated in this thesis, the QD-MLLD and the Kerr comb generator. The main properties of these frequency comb sources are described in Sections 2.3 and 2.4, respectively. The transmission demonstrations with these frequency combs are detailed in Chapters 4 and 5, respectively.

2 Theoretical background

This chapter provides the required background to better understand the investigations and experimental demonstrations described in this thesis. Section 2.1 introduces the fundamental concepts of optical communication systems and the associated signal processing. The section focuses on high-capacity links based on coherent WDM systems, relevant to the experimental demonstrations of this thesis. Section 2.2 describes the relevant properties of frequency combs for coherent data transmission. This section is edited from a book chapter [B1] that was published with equal contribution from the author of this thesis and Juned N. Kemal. Section 2.3 and Section 2.4 discuss the theory and technology of the two chip-scale comb sources investigated in this thesis, namely a QD-MLLD and a Kerr comb generator, respectively. These sections introduce the mechanism behind frequency generation in QD-MLLD and Kerr comb generators and describe the properties of their output frequency combs. Regarding Kerr comb generators, special emphasis is laid on so-called dissipative Kerr solitons (DKS), which can be obtained from a SiN microresonator.

2.1 Coherent data transmission setups and signal processing

The building blocks of the coherent optical communication system used for the experimental demonstrations in this thesis are depicted in Figure 2.1. This system relies on transmitting spectrally-efficient K -ary quadrature amplitude modulation (QAM) signals through a fiber link consisting of fiber section and optical amplifiers.

At the transmitter, a digital binary signal is first mapped into K symbols and shaped for spectrally efficient transmission by means of digital signal processing (DSP). Next, the signal is converted to the analog domain by a digital-to-analog converter (DAC) and encoded onto one or more optical carriers using electro-optic (EO) in-phase/quadrature (IQ) modulators.

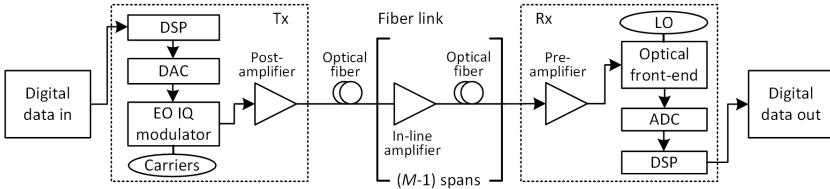


Figure 2.1: Main blocks of the coherent communications system used in this thesis for the transmission experiments.

Once in the optical domain, the signal is amplified by the so-called post-amplifier and launched into the first optical fiber section. The signal can then be transmitted across hundreds to thousands of kilometers by $M - 1$ additional fiber sections. In-line amplifiers are used to compensate for the fiber losses of the respective fiber sections.

The spacing between amplifiers is directly related to the achievable optical signal-to-noise ratio (OSNR).⁶ As the fiber length between amplifiers is increased, the OSNR decreases. This decrease results from using lumped amplifiers, such as the erbium-doped fiber amplifier (EDFA), and leads to the engineering tradeoff that shorter spans provide higher OSNR while longer spans lead to the use of fewer amplifiers and lower cost [25]. In practice, amplifier spacings in the range of 50 to 90 km are used [26]. In this thesis, a fiber span of 75 km is used.

At the receiver, the signal is boosted by a pre-amplifier and coherently detected. Different coherent receiver schemes can be employed to detect the signal and recover the data. In this thesis, an intradyne detection scheme is employed, consisting of a 90° optical hybrid (OH), balanced photodetectors (BPD), and analog-to-digital converters (ADC). In the last step, digital signal processing (DSP) is necessary to correct for impairments suffered by the signal through the system and to recover the transmitted binary signal.

⁶ The OSNR is defined as the ratio of the signal power to the amplified spontaneous emission (ASE) noise power within a reference bandwidth $B_{\text{ref}} = 12.5$ GHz, corresponding to a reference wavelength span of 0.1 nm at a center wavelength of 1.55 μm

2.1.1 Signal encoding and shaping

The electric field of an optical carrier with angular frequency ω_c , phase $\phi_c(t)$, and amplitude $E_c(t)$ can be expressed as

$$E(t) = E_c(t) \cos(\omega_c t + \phi_c(t)). \quad (2.1)$$

In coherent communications, data can be encoded onto the optical carrier by modulating its phase and amplitude with the phase $\phi(t)$ and amplitude $A(t)$ of a baseband complex signal $\underline{A}(t)$,⁷ given by

$$\underline{A}(t) = A(t) e^{j\phi(t)}. \quad (2.2)$$

Considering an optical carrier with no phase noise, $\phi_c(t) = \phi_c$, and no amplitude noise, $E_c(t) = E_c$, and further considering without loss of generality that $\phi_c = 0$ and $E_c = 1$, i.e., $E(t) = \cos(\omega_c t)$, the modulated optical carrier $E_m(t)$ can be expressed as the time-harmonic wave

$$E_m(t) = A(t) \cos(\omega_c t + \phi(t)). \quad (2.3)$$

Alternatively, rather than using the amplitude and phase representation of the complex baseband signal $\underline{A}(t)$, $E_m(t)$ can be represented by the real and imaginary parts of the baseband signal $\underline{A}(t)$, also known as in-phase $A_I(t)$ and quadrature $A_Q(t)$ components,

$$A_I(t) = \text{Re}\{\underline{A}(t)\} = A(t) \cos(\phi(t)), \quad (2.4)$$

$$A_Q(t) = \text{Im}\{\underline{A}(t)\} = A(t) \sin(\phi(t)). \quad (2.5)$$

By applying the compound angle formula to Eq. (2.3) and using Eqs. (2.4) and (2.5), the modulated carrier can be expressed as

$$\begin{aligned} E_m(t) &= A(t) \cos(\phi(t)) \cos(\omega_c t) - A(t) \sin(\phi(t)) \sin(\omega_c t) \\ &= A_I(t) \cos(\omega_c t) - A_Q(t) \sin(\omega_c t) \end{aligned} \quad (2.6)$$

Thus, complex baseband signals $\underline{A}(t)$, can be transmitted by mixing $A_I(t)$ with the carrier $\cos(\omega_c t)$ and $A_Q(t)$ with the carrier $-\sin(\omega_c t)$. This is the concept

⁷ In this thesis, the underscore “_” indicates a complex quantity.

behind quadrature amplitude modulation (QAM).⁸ The mixing and combining expressed in Eq. (2.6) can be achieved with the so-called in-phase/quadrature (IQ) modulator, which is described in the next section.

Each of the possible $\phi(t)$ and $A(t)$, or $A_I(t)$ and $A_Q(t)$, pairs represents a symbol that is typically visualized in the complex plane, leading to a so-called constellation diagram. Figure 2.2(a) depicts the constellation diagram, where the real and imaginary axis is expressed by $A_I(t)$ and $A_Q(t)$. The group of K different symbols used to transmit the data constitute the symbol alphabet and are associated with a given modulation format. Figure 2.2(b) depicts the constellation diagrams for the modulation formats which are relevant for this thesis, namely quadrature phase-shift keying (QPSK), 16-state quadrature amplitude modulation (16QAM), and 32-state QAM (32QAM). Each symbol of a given modulation format represents $\log_2 K$ bits. To map bits to symbols, two-dimensional Gray coding is used. This mapping scheme minimizes the number of bit errors by having adjacent symbols that differ by only a single bit, while diagonal adjacent symbols differ by 2 bits [27]. For QPSK and 16QAM, Figure 2.2(b) also displays the corresponding Gray coding.

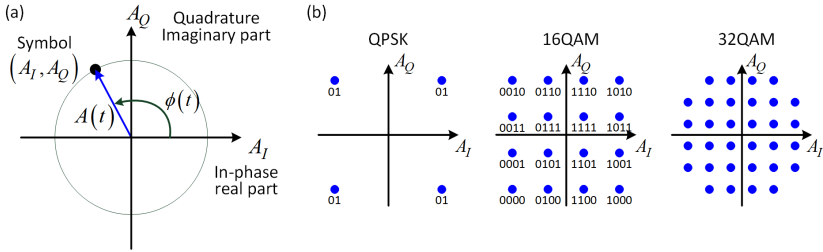


Figure 2.2: Complex representation of coherent modulation formats. **(a)** Representation of the complex electric field by $A_I(t)$ and $A_Q(t)$ components in the complex plane. **(b)** Constellation diagram of quadrature phase-shift keying (QPSK), 16-state quadrature amplitude modulation (16QAM), and 32-state (QAM).

⁸ In a QAM signal, two carriers shifted in phase by $\pi/2$ (90°), are modulated and combined. As a result of their 90° phase difference, they are in quadrature which gives rise to the name.

In this thesis, pseudorandom binary sequences (PRBS) are used to emulate a continuous random sequence of bits. The PRBS exhibits the same statistical behavior as a truly random sequence.

The number of encoded bits per symbol will determine the spectral efficiency of the communication system. For example, 32QAM is spectrally more efficient than QPSK. However, for WDM systems, the channel bandwidth also impacts the spectral efficiency. Traditionally, signals with rectangular time-domain pulse shapes were used. In the frequency domain, these signals correspond to a sinc-shaped spectrum with sidelobes, and a main lobe bandwidth that is twice the symbol rate $R_S = 1/T_S$, where T_S denotes the duration of a symbol. To avoid inter-channel interference in WDM systems, relatively wide guard bands are needed to be kept between channels, thereby considerably reducing the spectral efficiency. For a given symbol rate, the spectral separation of the channels can be minimized by shaping the time-domain pulses. To this end, raised-cosine (RC) pulse shapes are often chosen. In the frequency domain, the RC filter is described according to [28]

$$H(f) = \begin{cases} 1, & |f| \leq \frac{(1-\beta)R_S}{2} \\ \frac{1}{2} \left[1 + \cos \left(\frac{\pi}{\beta R_S} \left[|f| - \frac{(1-\beta)R_S}{2} \right] \right) \right], & \frac{(1-\beta)R_S}{2} < |f| \leq \frac{(1+\beta)R_S}{2} \\ 0, & \frac{(1+\beta)R_S}{2} < |f| \end{cases} \quad (2.7)$$

In Eq. (2.7), β is the roll-off factor, where $0 \leq \beta \leq 1$. The roll-off factor is a measure of the occupied spectral bandwidth beyond the Nyquist bandwidth of $B_S/2$. For $\beta = 0$, the spectrum is rectangular and leads to high spectral efficiency. However, low β values lead to an increase of the peak to average power ratio (PAPR), which is the ratio of the instantaneous power to the mean power, and a decrease of the signal quality in real transmission systems [29]. In contrast, high β values lead to a broader spectrum but make the received signal more tolerant to timing recovery errors. In practice, a value of β is chosen for each transmission system to balance these two effects. In this thesis, β values

of 0.05 and 0.1 are chosen, leading to excess bandwidths of 5% and 10%, respectively.

2.1.2 In-phase/quadrature (IQ) modulator

The complex baseband signal $\underline{A}(t)$ can be encoded onto an optical carrier following Eq. (2.6). The real $A_I(t)$ and imaginary $A_Q(t)$ components of $\underline{A}(t)$ are encoded onto two copies of an optical carrier which are de-phased by 90° and then combined together. This is accomplished by an in-phase/quadrature (IQ) modulator which is described in the following.

An IQ modulator consists of two Mach-Zehnder modulator (MZM) structures. An MZM is an interferometer used to change the intensity of the light by modifying, or shifting, the phase of the light propagating through the MZM arms. The phase of the light propagating in each arm of the MZM is manipulated through the Pockels effect. The Pockels effect is a second-order nonlinear effect in which an electric signal changes the refractive index of the material composing the MZM. Typically, lithium niobite (LiNbO_3) is chosen as second-order nonlinear material to generate the electro-optic effect.

Figure 2.3(a) depicts the structure of the IQ modulator. The signal $A_I(t)$ drives the upper MZM, MZM_I , and the signal $A_Q(t)$ drives the lower MZM, MZM_Q . For MZM_I , the phase of the carrier propagating through the upper arm is shifted by $\varphi_{I,1}(t)$ while the phase shift for the carrier propagating through the lower arm is $\varphi_{I,2}(t)$. Similarly, the phase shifts are $\varphi_{Q,1}(t)$ and $\varphi_{Q,2}(t)$ for MZM_Q . Each of the MZM is operated in a push-pull configuration, i.e., the phase shifts $\varphi_{I,1}(t)$ and $\varphi_{I,2}(t)$ introduced in each arm of the MZM_I are equal but have different signs, i.e. $\varphi_{I,1}(t) = -\varphi_{I,2}(t)$, likewise $\varphi_{Q,1}(t) = -\varphi_{Q,2}(t)$ for MZM_Q . Under these conditions, the MZM behaves as a pure amplitude modulator. For MZM_I , the amplitude and power transfer function can be written as

$$T_I = \cos\left(\frac{A_I(t)}{U_{I,\pi}}\pi + \varphi_{I,\text{DC}}\right) \quad |T_I|^2 = \cos^2\left(\frac{A_I(t)}{U_{I,\pi}}\pi + \varphi_{I,\text{DC}}\right). \quad (2.8)$$

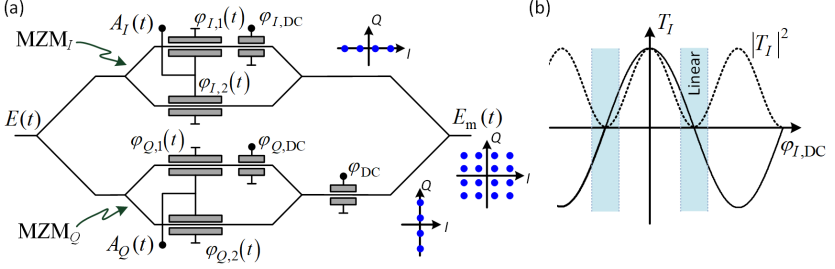


Figure 2.3: In-phase/quadrature (IQ) modulator. **(a)** Scheme of an IQ modulator consisting of two nested MZM. The upper MZM, MZM_I , is driven by $A_I(t)$ and the lower MZM, MZM_Q , by $A_Q(t)$. Both MZM are driven in push-pull configuration, i.e. the phase shifts introduced in each arm of the MZM fulfill $\varphi_{I,1}(t) = -\varphi_{I,2}(t)$ and $\varphi_{Q,1}(t) = -\varphi_{Q,2}(t)$. Phase shifts $\varphi_{I,DC}$ and $\varphi_{Q,DC}$ are applied to one of the arms of each MZM to adjust the operation point to the null transmission point. In addition, a phase shift $\varphi_{DC} = \pi/2$ is applied to the output from MZM_Q to place the output signals from MZM_I and MZM_Q into quadrature. **(b)** Amplitude and power transfer function of MZM_I as a function of the phase shift $\varphi_{I,DC}$. The blue shaded area indicates the linear regime of operation of the MZM, which is centered at the null transmission point.

In these relations, $\varphi_{I,DC}$ is a phase shift applied to adjust the operation point of MZM_I , and $U_{I,\pi}$ is the so-called half-wave voltage of the MZM and is a property of the modulator indicating the required voltage to achieve a phase difference of π between the upper and the lower arm. Equivalent relations can be expressed for MZM_Q . In coherent communication systems, the phase $\varphi_{I,DC}$ is chosen such that the output power is null when there is no driving signal, $A_I(t) = 0$. This operation point of the MZM is called the null point and leads to a suppression of the undesired optical carrier. Figure 2.3(b) shows the amplitude and power transfer function of MZM_I as a function of $\varphi_{I,DC}$ for $A_I(t) = 0$. The null point is located where $|T_I|^2 = 0$.

In addition to the null point, the MZM is typically operated within the linear regime, i.e., with drive signal $A_I(t) \ll U_{I,\pi}$. In the linear regime of the MZM, the output optical field from MZM_I can simply be expressed as

$$E_I(t) = \pi \frac{A_I(t)}{U_{I,\pi}} E(t). \quad (2.9)$$

Thus, the output field $E_I(t)$ is proportional to the signal $A_I(t)$. A similar expression is obtained for the output of MZM_Q

$$E_Q(t) = \pi \frac{A_Q(t)}{U_{Q,\pi}} E(t). \quad (2.10)$$

Note that Eqs. (2.9) and (2.10) neglect amplitude factors from the couplers.

Typically, both upper and lower MZM are nominally identical and it is reasonable to consider $U_{I,\pi} = U_{Q,\pi} = U_\pi$. In this thesis, the amplitude of $A_I(t)$ and $A_Q(t)$ is usually kept at approximately $0.2U_\pi$

The lower arm of the IQ modulator applies a phase shift φ_{DC} to the output $E_Q(t)$ of MZM_Q . The phase shift is chosen as $\varphi_{\text{DC}} = \pi/2$ such that the signals in the upper and lower arm of the IQ modulator are placed in quadrature. The output of the IQ modulator can then be expressed as

$$E_m(t) = \frac{\pi}{U_\pi} \left(A_I(t) \cos(\omega_c t) - A_Q(t) \sin(\omega_c t) \right). \quad (2.11)$$

The difference between Eq. (2.6) and Eq. (2.11) is due to the proportionality factors.

2.1.3 Wavelength-division multiplexing (WDM) and polarization-division multiplexing (PDM)

For relatively low data rate transmissions of, e.g., 200 Gbit/s, it is sufficient to use a single optical carrier. For example, 16QAM signals with a symbol rate of 50 GBd lead to 200 Gbit/s. In addition, polarization-division multiplexing (PDM) can double the transmitted data rate by making use of both independent polarizations of the optical field. However, to reach Tbit/s data rates, it is practically impossible to use a single optical carrier. This restriction originates from the limited bandwidth of the state-of-the-art DAC and IQ modulators. Thus, to reach Tbit/s data rates, an additional multiplexing technique is implemented, namely wavelength-division multiplexing (WDM). In WDM, data is encoded onto multiple optical carriers using independent IQ modulators. A multiplexer

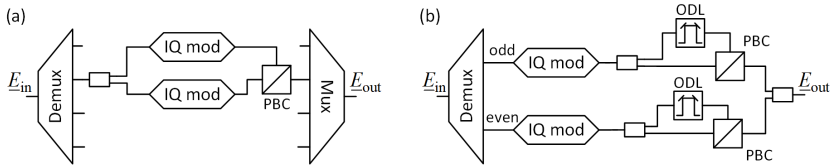


Figure 2.4: Frequency comb based WDM and PDM schemes. **(a)** Conventional comb-based WDM and PDM implementation. A demultiplexer (Demux) separates the carriers before modulation. An optical coupler splits the signal into two copies, and two IQ modulators (IQ mod) are used to encode independent data onto each carrier. A polarization beam combiner (PBC) joins the two signals with different orthogonal polarizations. Lastly, a multiplexer (Mux) combines the signals from each dual-polarization (DP) modulator stage. **(b)** Laboratory emulation of the conventional comb-based WDM and PDM. A Demux separates the comb carriers into two groups, referred to as “odd” and “even” channels according to their respective comb indices. These two groups of carriers are encoded with independent data. For each IQ modulator, PDM is emulated employing the split-and-combine method. In this technique, the data signal is split, decorrelated in time using an optical delay line (ODL), and combined with different polarizations using a PBC.

(Mux) combines all channels into a single fiber, thereby enabling Tbit/s communications. Other multiplexing techniques, such as spatial division multiplexing (SDM) can also be implemented to further scale the data rates. However, this requires the use of specialized fibers and complex multiplexing and demultiplexing setups. In this thesis, we consider only propagation through single-mode fibers.

For each wavelength carrier, PDM is typically implemented with a dual-polarization (DP) IQ modulator. In the DP IQ modulator, the incoming carrier is first power split into two copies, which are then sent through independent IQ modulators and finally combined into different orthogonal polarizations with, e.g., a polarization beam combiner (PBC), see Fig. 2.4(a). In the case of using a frequency comb source to generate the multi-wavelength carriers, a demultiplexer (Demux) is required to separate the carriers prior to modulation. The signals after the DP IQ modulator are combined using a channel multiplexer (Mux). The number of DP IQ modulators will thus scale linearly with the channel count. In this thesis, due to the limited number of IQ modulators, PDM is emulated with a single IQ modulator by employing the split-and-combine method. In this

technique, the data signal is split, decorrelated in time and combined with different polarizations. In addition, WDM is emulated by separating the optical carriers into two groups using a demultiplexer. These two groups of carriers, which are referred to as “odd” and “even” channels according to their respective integer indices, are encoded with independent data streams, see Fig. 2.4(b). In this way, neighboring channels will carry independent data such that the impact of cross-talk between neighboring channels can be realistically investigated.

After the Mux, the WDM channels are transmitted through an SSMF with relatively low optical power levels per channel to operate the optical fiber below the threshold for nonlinear impairments [30]. Nonlinear effects, such as cross-phase modulation (XPM) and self-phase modulation (SPM), would lead to detrimental interactions of different WDM channels thereby limiting the achievable OSNR and the associated bit error ratio (BER). In the next section, the impact of nonlinearities on the OSNR is examined, and a technique to overcome the impact of nonlinearities using a frequency comb is discussed.

2.1.4 Transmission link

A major element of coherent optical communication systems is the transmission medium, the optical fiber. For metro, regional and long-haul communications, standard single-mode fiber (SSMF) is the type of fiber recommended by the International Telecommunication Union (ITU).⁹ Silica-based SSMF are widely available and offer low attenuation as compared to other fibers such as multi-mode fibers. This section discusses the maximum capacity that can be transmitted through a link affected by linear and nonlinear impairments, and describes the most important linear properties of an SSMF when transmitting a WDM signal, namely, attenuation, chromatic dispersion, and polarization mode dispersion.

2.1.4.1 Linear and nonlinear Shannon capacity

The Shannon capacity of a transmission link expresses the data rate that can be achieved with arbitrarily low BER and arbitrarily complex modulation format. From Shannon’s theory, for a link that adds white Gaussian noise, i.e., additive

⁹ <https://www.itu.int/rec/T-REC-G.652/en>

noise, the capacity C of a channel with limited bandwidth, B , is given by the relation [31]

$$C = B \log_2(1 + \text{SNR}). \quad (2.12)$$

In this relation, the signal-to-noise ratio (SNR) is the signal average power divided by the noise average power in the signal bandwidth B . For a dual-polarization signal, the SNR is related to the OSNR by the relation

$$\text{OSNR} = \frac{R_s}{B_{\text{ref}}} \text{SNR}, \quad (2.13)$$

where R_s is the symbol rate of the channel and $B_{\text{ref}} = 12.5 \text{ GHz}$ is the reference bandwidth. From Eq. (2.12), the capacity or spectral efficiency (SE), $\text{SE} = C/B$, measured in bit/s/Hz, can be arbitrarily increased by increasing the signal power for a fixed noise power. However, optical fibers exhibit Kerr nonlinearity. As a result, increasing the optical power of the signal will ultimately lead to strong nonlinearities and a reduction of the SNR [32]. The magnitude of the nonlinear distortion will determine the maximum achievable capacity under nonlinear impairment, also known as nonlinear Shannon capacity. The impact of nonlinearities on the signal can be numerically calculated by solving the nonlinear Schrödinger equation as the light propagates through the fiber. This differential equation is commonly solved using the split-step Fourier method [30]. Considering parameters such as the nonlinear coefficient of the fiber, the dispersion, and the number of WDM channels, the maximum achievable capacity or SE can be calculated for each propagation distance. In Ref. [32], the authors use this technique to evaluate the SE after transmission for various link distances and compare it to the linear Shannon SE from Eq. (2.12). The results of their analysis are displayed in Fig. 2.5, taken from [32].

For links affected only by additive noise Eq. (2.12) holds and the channel capacity increases with the launch optical power due to an increase of the SNR. In contrast, for a link affected by nonlinearities, at high optical powers the impact of nonlinear distortions will overcome the SNR capacity gain leading to a decrease of the channel capacity with the SNR. Thus, the channel capacity will feature a maximum at a finite optical power or SNR [32], see Fig. 2.5.

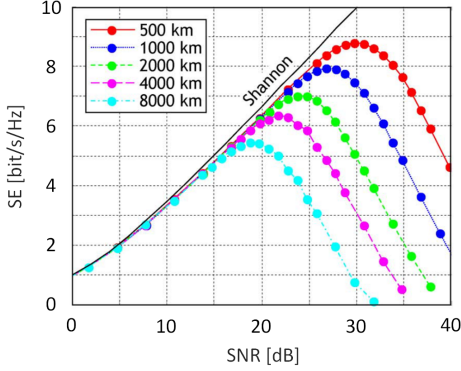


Figure 2.5: Numerical investigation of the channel spectral efficiency (SE) as a function of the signal-to-noise ratio (SNR) for different link distances under the influence of fiber nonlinearities. The straight line, labeled “Shannon” is derived from the Shannon channel capacity, Eq. (2.12), which only considers additive noise. Figure adapted from [32].

Figure 2.5 displays how under nonlinear impairments the maximum SE that can be achieved in a WDM link is reduced by approximately 1 bit/s/Hz when doubling the link distance. For example, the maximum SE for a link of 500 km is approximately 9 bit/s/Hz, while for a distance of 2000 km, the SE is reduced to approximately 7 bit/s/Hz. In addition, the SNR at which the channel capacity is maximized decreases with the link distance due to the larger accumulation of nonlinear distortions.

Nonlinear impairments in a WDM system represent the main limitation for increasing the link capacity. However, there are several approaches to mitigate nonlinear effects [33], [34]. These techniques rely on the precise knowledge of the carrier spacing and the relative phase between carriers. Frequency combs, thus, inherently fulfill this requirement. In Ref. [34], the authors demonstrate the cancellation of nonlinear impairments with the use of a frequency comb source at the transmitter. In this approach, the time-domain waveform of the overall WDM signal is reconstructed in the first step. The signal is then digitally back-propagated through the fiber simulating the nonlinear effects of the link with the inverse-signed physical properties.

2.1.4.2 Losses, chromatic dispersion, and polarization mode dispersion

Optical signals propagating through a fiber will suffer attenuation, chromatic dispersion, and polarization mode dispersion. If the optical power from the signal is kept below the threshold for Kerr nonlinearities, nonlinear effects can be disregarded.

Optical attenuation is caused by different loss mechanisms in the fiber, namely, absorption, radiative loss, and scattering. Optical losses are typically expressed in decibels per kilometer (dB/km) employing the fiber-loss parameter α ,

$$\alpha = \frac{1}{L} 10 \log_{10} \left(\frac{P(0)}{P(L)} \right), \quad (2.14)$$

Where $P(0)$ is the optical power at the input of the optical fiber, $P(L)$ is the optical power at the output of the fiber, and L is the length of the fiber. For SSMF, which are used in this thesis, typical attenuation values are approximately 0.18 dB/km at the wavelength of 1550 nm [35].

Chromatic dispersion in optical fibers is caused by the wavelength dependence of the effective group refractive index of the fiber. The effective group index determines the group velocity or the velocity with which the envelope of a pulse propagates in a medium. Different frequency components of the signals will propagate at different velocities, leading to intersymbol interference at the receiver. Chromatic dispersion in optical fibers is typically expressed in picoseconds per nanometer per kilometer (ps/nm/km) through the dispersion parameter C_λ ,

$$C_\lambda = -\frac{2\pi c}{\lambda^2} \beta^{(2)}, \quad (2.15)$$

where $\beta^{(2)}$ is the second derivative of the propagation constant leading to group velocity dispersion (GVD), c is the speed of light, and λ is the center wavelength of the channel. For SSMF, the dispersion parameter is typically 18 ps/nm/km [35]. For a propagation distance of 75 km using a symbol rate of 50 GBd, and assuming an RC spectrum with a 50 GHz separation, the delay between the highest and lowest frequency component of the channel would be

approximately 0.5 ns, causing intersymbol interference. Due to the linear nature of chromatic dispersion, the intersymbol interference is typically compensated digitally at the receiver.

Polarization mode dispersion (PMD) in optical fibers is mainly caused by the slight ellipticity of real fiber cores. This asymmetry breaks the degeneracy of orthogonally polarized modes and leads to different group velocities for these two modes, commonly referred to as slow and fast mode with group delays $t_{g,\text{slow}}$ and $t_{g,\text{fast}}$, respectively. The delay difference is then $\Delta t_g = t_{g,\text{slow}} - t_{g,\text{fast}}$. Having the same probability of coupling from one mode to the other one, the coupling is described by the binomial distribution. After a transmission length L with $n \square 1$ coupling points, the signal width is proportional to \sqrt{L} , see Eq. (19) in [36]. The broadening of the signal $\Delta\tau$ is thus proportional to \sqrt{L} with the PMD parameter D being the proportionality factor,

$$\Delta\tau = D\sqrt{L} . \quad (2.16)$$

The PMD parameter D is typically expressed in picoseconds per square root of kilometer ($\text{ps}/\sqrt{\text{km}}$). For SSMF, the dispersion parameter is lower than $0.04 \text{ ps}/\sqrt{\text{km}}$ [35]. For short link distances, it can be neglected.

2.1.5 Optical receiver front-end and ADC

After the transmission link, the optical power of the WDM signal is boosted by a pre-amplifier and the signal is then sent through a demultiplexer which routes each of the WDM channels to different outputs. Each channel is then sent to a dual-polarization coherent intradyne receiver, see Fig. 2.6. The receiver consists of a polarization beam splitter (PBS) and a 90° optical hybrid (OH) together with four BPDs. The PBS separates the signal \underline{E}_s into two orthogonal polarizations, i.e., $\underline{E}_{s,X}$ and $\underline{E}_{s,Y}$. Each polarized signal is sent to a dedicated 90° OH where they are split in power by a 3-dB coupler, with a 50:50 power ratio. In addition, an LO signal \underline{E}_{LO} is input into each of the 90° OH, where it is also split in power. A similar description follows for both polarizations, thus, in the following the subscripts ‘‘X’’ and ‘‘Y’’ are not considered. In the 90° OH, the signal \underline{E}_s is superimposed with the LO \underline{E}_{LO} using an optical 2x2 coupler and

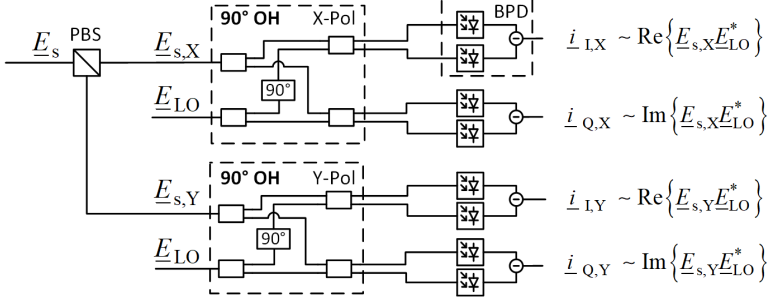


Figure 2.6: Dual-polarization coherent intradyne receiver. A polarization beam splitter (PBS) separates the signal \underline{E}_s into two orthogonal polarizations, i.e., $\underline{E}_{s,X}$ and $\underline{E}_{s,Y}$. Each polarized signal is sent to a dedicated 90°OH where they are split in power. An LO $\underline{E}_{s,X}$ is input into each 90°OH and also split in power. In each 90°OH , the signal is superimposed with the LO using a 2×2 coupler and the other copy of the signal is superimposed with a 90° phase-shifted copy of the LO with a 2×2 coupler. The four outputs of each 90°OH are sent in pair to two BPD.

the other copy of the signal \underline{E}_s is superimposed with a 90° phase shifted copy of the LO \underline{E}_{LO} , leading to four outputs. Provided that the superimposed signal and LO share the same polarization, the electric fields at the four outputs can be expressed as

$$\begin{aligned}
 \underline{E}_1(t) &\propto \frac{1}{2}(\underline{E}_s(t) + \underline{E}_{LO}(t)) \\
 \underline{E}_2(t) &\propto \frac{1}{2}(\underline{E}_s(t) - \underline{E}_{LO}(t)) \\
 \underline{E}_3(t) &\propto \frac{1}{2}(\underline{E}_s(t) + j\underline{E}_{LO}(t)) \\
 \underline{E}_4(t) &\propto \frac{1}{2}(\underline{E}_s(t) - j\underline{E}_{LO}(t))
 \end{aligned} \tag{2.17}$$

The four signals are then sent in pairs to two BPD. The photocurrent at the output of the BPDs can be expressed as

$$\begin{aligned}
 i_I(t) &\propto |\underline{E}_1(t)|^2 - |\underline{E}_2(t)|^2 \propto \text{Re}\{\underline{E}_s(t) \underline{E}_{LO}^*(t)\} \\
 i_Q(t) &\propto |\underline{E}_3(t)|^2 - |\underline{E}_4(t)|^2 \propto \text{Im}\{\underline{E}_s(t) \underline{E}_{LO}^*(t)\}
 \end{aligned} \tag{2.18}$$

These photocurrents are related to the real and imaginary part of the complex signal

$$\underline{i}(t) = i_I(t) + j i_Q(t) \propto \underline{E}_s(t) \underline{E}_{LO}^*(t). \quad (2.19)$$

Considering $\underline{E}_s(t) = \underline{A}(t)e^{j(\omega_c t + \phi(t))}$ and $\underline{E}_{LO}(t) = e^{j\omega_{LO}t}$, i.e., neglecting phase and amplitude noise of the carrier and the LO, the complex photocurrent from Eq. (2.19) can be written as

$$\underline{i}(t) = \underline{A}(t)e^{j(\omega_{IF}t + \phi(t))}. \quad (2.20)$$

In Eq. (2.20) $\omega_{IF} = \omega_c - \omega_{LO}$ is the intermediate frequency (IF) at which the complex photocurrent oscillates. In an intradyne receiver, the frequency offset between the frequency of the carrier and that of the LO is kept below the bandwidth B of the signal, i.e., $|\omega_{IF}| < B$. Note that in practice, the phase of the LO is not known and the in-phase and quadrature components in Eq. (2.19) are not the same as those from Eq. (2.3).

Next, the photocurrents $\underline{i}(t) = i_I(t) + j i_Q(t)$ are sent to a 50-ohm-terminated ADC, where they are sampled and digitized. The digital signals are then further processed using dedicated DSP algorithms for reconstructing the original digital signal and recovering the associated data, see the next section.

2.1.6 Digital signal processing algorithms

The basic DSP algorithms used to demodulate and recover the original digital signal are illustrated in Fig. 2.7. The signal digitized by the ADC consists of a discrete number of samples. In general, these samples do not coincide with the center of the transmitted symbol slots. In addition, the DAC, which generates the symbols, and the ADC, which records the symbols, may have different clock frequencies. Thus, a timing recovery algorithm is implemented to retrieve the symbols. In this thesis, timing recovery is based on the Godard algorithm [37], [38]. This algorithm requires resampling the signal to two samples per symbol.

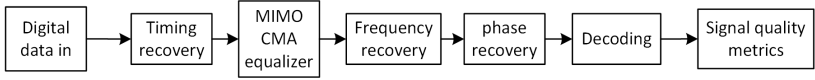


Figure 2.7: Digital signal processing (DSP) steps undergone by the detected signal to retrieve the original digital signal. After demodulation, the bit error ratio (BER) and the error vector magnitude (EVM) metrics are used to quantify the signal quality. MIMO: multiple-input multiple-output. CMA: constant modulus algorithm.

After recovering the symbols, a multiple-input multiple-output (MIMO) equalizer is used to both demultiplex the two orthogonal polarizations of the signal and to compensate for linear transmission impairments [39], such as chromatic dispersion and polarization mode dispersion. This equalizer is based on the constant-modulus algorithm (CMA). Due to the intermediate frequency, or carrier frequency offset $\omega_{\text{IF}} \neq 0$ for an intradyne receiver, the symbols obtained from the CMA equalizer will suffer from a linear phase increase in time with a slope of ω_{IF} . This translates into a fast phase rotation in the complex plane. To decode the signal, the rapidly increasing phase needs to be determined and compensated. In this thesis, the Viterbi-Viterbi algorithm is implemented to recover the carrier frequency offset. For K -ary phase-shift-keying (K -PSK), the frequency offset can be effectively recovered by taking the symbols to the power of K . In general, the received K -PSK symbol can be written as

$$\underline{E} = E e^{jk \frac{\pi}{K} + j\phi_{c-\text{LO}}}. \quad (2.21)$$

with k being an odd integer from 1 to K , and E being the symbol modulus. Taking the symbol to the power of K results in

$$\underline{E}^K = -E^K e^{jK\phi_{c-\text{LO}}}. \quad (2.22)$$

The phase modulation is removed, and only the phase $\phi_{c-\text{LO}}$ caused by the frequency offset between the carrier and the LO remains. The frequency offset is compensated by fitting a linear curve to the unwrapped $\phi_{c-\text{LO}}$ as a function of time and by subtracting the fitted curve from the measured phase offset. In the case of 16QAM signaling, the 4th-power scheme can be adapted by the so-called QPSK-partitioning [40].

Once the carrier frequency offset is compensated, carrier phase noise compensation is carried out by a digital phase-tracking technique. In this thesis, two different digital phase-tracking techniques are employed. For the transmission experiments with Kerr comb generators, Chapter 5, the conventional “block-wise” phase recovery is employed. For the transmission experiments with quantum-dash (QD) mode-locked laser diodes (MLLD), Chapter 4, the digital phase-tracking relies on a “symbol-wise” blind phase search technique. This technique is key to enable 16QAM transmission with QD-MLLD devices. These techniques are explained thoroughly in Section 4.4.2 and are therefore not discussed further in this section.

These techniques for phase noise compensation are affected by so-called phase cycle-slips. Phase slips happen when the phase noise of either the carrier or the LO line changes considerably over a short period, typically of the order of the symbol duration. In this case, phase compensation algorithms may reconstruct the symbol in the wrong quadrant of the constellation diagram. When phase slips occur, the following symbols will be wrongly reconstructed. Thus, to reliably track the phase over long symbol sequences, either advanced FEC schemes [41] or pilot symbols [42] should be considered. When using pilot symbols, a sequence of several known symbols is added in a periodic manner such that it can be observed if any cycle slip has occurred during signal reconstruction and therefore compensate it. These techniques lead to a slightly lower net data rate but prevent the loss of all symbols after a cycle slip.

Finally, hard decision decoding is performed to associate the recovered symbols to bits by associating them to the closest constellation symbol in the complex plane. The recovered symbols are then compared to the transmitted symbol with the use of different signal quality metrics such as the BER and the error vector magnitude (EVM), which are discussed in the following section.

2.1.7 Quality metrics for K -ary QAM signals

To quantify the performance of a coherent data transmission, the most relevant metric is the bit error ratio (BER). The BER is the number of erroneously decoded bits divided by the total number of bits transmitted. In coherent optical communications, several BER thresholds are defined. These thresholds are

related to the so-called forward error correction (FEC) scheme. Forward error correction is a technique used in telecommunications to detect erroneous bits and to correct them by using some amount of redundancy in the transmitted information. For a given FEC scheme, these BER thresholds define the maximum BER of the raw data channel that can still be corrected to a BER of less than 10^{-15} , which is considered error-free [43].

In the literature, the BER threshold values commonly considered are approximately 4.5×10^{-3} and 1.5×10^{-2} and we adopt these thresholds in this thesis as well. A system performing with a BER lower than 1.5×10^{-2} would require an FEC scheme with 20% overhead, while a system with a BER lower than 4.5×10^{-3} would require an FEC scheme with an overhead of only 7% [43]. While a low BER is an indication of good signal quality, it also indicates that the capacity of the transmission system is not fully exploited. For example, a higher modulation format or a higher symbol rate could be used. Therefore, a communications system is typically designed to maximize throughput while keeping the resulting BER below the targeted threshold.

To directly measure the BER, a known data sequence has to be transmitted. For very low BER values, it is thus necessary to take extremely long recordings. To measure a statically reliable BER reaching a confidence level of 99 % within a confidence interval of 100 %, at least 13 erroneous bits have to be found in each recording [44]. In this case, to reliably measure a $\text{BER} = 10^{-11}$ of a 50 GBd 16QAM signal, a recording length of 6.5s is necessary. For the transmission experiments performed in this thesis, the limited memory of the ADC constrains the length of the recorded waveforms. In this situation, other metrics such as the error vector magnitude (EVM), are typically used.

When transmitting K -ary QAM signals, the received symbol is typically represented by a complex phasor, which can be represented by a vector in the complex plane. Due to noise, the symbol in the complex plane will deviate from that corresponding to the ideal transmitted symbol, see Fig. 2.8. The vector between these two complex values is named error vector. The EVM is computed by taking the root mean square of each error vector $\underline{E}_{\text{err}}$ for N randomly transmitted symbols [44],

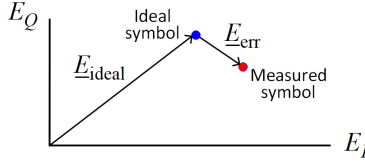


Figure 2.8: Error vector magnitude (EVM), illustrated in the complex plane of the received IQ signals. The EVM is a signal quality metric that quantifies the deviation $\underline{E}_{\text{err}}$ of a measured symbol from its ideal position in the constellation diagram $\underline{E}_{\text{ideal}}$.

$$\text{EVM} = \frac{1}{E_{\text{norm}}} \sqrt{\frac{1}{N} \sum_{n=1}^N |E_{\text{err},n}|^2}. \quad (2.23)$$

The EVM is normalized by E_{norm} , which is either the vector length $|E_{\text{max}}|$ of the ideal symbol with the largest amplitude, leading to EVM_{max} , or to the average amplitude $|\underline{E}_{\text{avg}}|$ of all K possible symbols, leading to EVM_{avg} , where,

$$|\underline{E}_{\text{avg}}| = \sqrt{\frac{1}{K} \sum_{k=1}^K |E_{\text{ideal},k}|^2}. \quad (2.24)$$

$$\text{EVM}_{\text{avg}} = \frac{1}{|\underline{E}_{\text{avg}}|} \sqrt{\frac{1}{N} \sum_{n=1}^N |E_{\text{err},n}|^2}. \quad (2.25)$$

The BER can be estimated from the EVM under certain conditions, namely, the system errors are mainly due to optical additive white Gaussian noise (AWGN), the reception is data-aided, i.e., the transmitted data is known – for measurement purposes –, and quadratic-QAM signal constellations with K symbols are considered, such as QPSK and 16QAM. Under these assumptions, if the EVM is known, the BER can be approximated by [44]

$$\text{BER} = 2 \frac{1 - K^{-1/2}}{\log_2 K} \text{erfc} \sqrt{\frac{3}{2(K-1)\text{EVM}_{\text{avg}}^2}}. \quad (2.26)$$

For large OSNR values, the EVM_{avg} can be approximated as [12]

$$\text{OSNR} = \text{EVM}_{\text{avg}}^{-2}. \quad (2.27)$$

Combining Eq. (2.26) and Eq. (2.27) it is possible to either estimate the achievable BER for a given OSNR, or determine the required OSNR for a specific BER, e.g. for a BER value of 4.5×10^{-3} . For QPSK, $K = 4$, and 16 QAM, $K = 16$, the BER as a function of the OSNR is given as

$$\begin{aligned} \text{BER}_{\text{QPSK}} &= \frac{1}{2} \text{erfc} \sqrt{\frac{\text{OSNR}}{2}} \\ \text{BER}_{16\text{QAM}} &= \frac{3}{8} \text{erfc} \sqrt{\frac{\text{OSNR}}{10}} \end{aligned} \quad (2.28)$$

From Eq. (2.28) it is possible to determine the required OSNR to achieve a given BER. In a transmission experiment, additional signal impairments such as electronic noise or nonlinear effects will increase this required OSNR by the so-called OSNR penalty. The OSNR penalty is a measure of the performance of the transmission system. For example, it can be used to compare the performance of a frequency comb based WDM system with a WDM system based on individual lasers, see Fig. 5.2(f). In Appendix B.4, Fig. B4., the setup for measuring the OSNR penalty is presented and further details are included.

2.2 Optical frequency combs

A frequency comb is a spectrum of phase-coherent, evenly-spaced, narrow-band lines [45]. The frequency position f_ν of all the comb lines is completely specified by only two parameters, the free spectral range (FSR) or comb line spacing f_r , and the center frequency f_c ,

$$f_\nu = f_c + \nu f_r, \quad (2.29)$$

where ν is an integer, see Fig. 2.9. In the time domain, a frequency comb corresponds to a periodic signal that usually consists of a sequence of well-defined equidistant pulses with repetition frequency f_r . In the following, the most relevant metrics for optical frequency combs in coherent WDM communications are described and are indicated in Fig. 2.9. This information is extracted from a book chapter [B1] that was published with equal contribution from the author of this thesis and Juned N. Kemal.

- **Free spectral range.** The FSR or line spacing, f_r , should be compliant with the bandwidth of state-of-the-art transmitters, i.e., a few tens of gigahertz, and it should adhere to the pertinent industry standards such as those defined by the international telecommunication union (ITU).
- **Number of lines and bandwidth.** In WDM, data are encoded on each of the comb tones, thus the data rate increases with the number of available lines. Ideally, a frequency comb should have a bandwidth f_{BW} , defined by the full width at half maximum (FWHM) of the spectral envelope of the frequency comb, covering the conventional (C) and long (L) telecommunication bands, from approximately 1520 nm to 1620 nm. This frequency range is typically used for optical communications due to the low loss of silica-based SSMF at these wavelengths, see Fig. 2.10(a). State-of-the-art SSMF show loss coefficients as low as 0.2 dB/km, i.e., after 100 km the light will be attenuated by 20 dB. These losses can be brought to as low as 0.14 dB/km lower by using pure-silica-core fiber (PSCF) [46], [47], which are already commercially available [48]. A PSCF has a pure core and a doped cladding, typically with fluorine, to reduce the refractive index. In contrast, an SSMF has a pure cladding and a doped core, typically with germanium, to increase the refractive index. Other telecommunications bands, such as the S-band and U-band, have also been used for WDM data transmission [49], [50]. In these systems, thulium-doped fiber amplifiers (TDFA) or Raman amplifiers are used to amplify the signals for long links. Figure 2.10(b) depicts a frequency comb

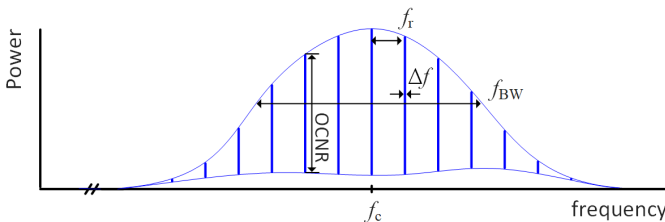


Figure 2.9: Sketch of the spectrum of an optical frequency comb indicating its relevant parameters: free spectral range (FSR), f_r ; center frequency, f_c , determined by f_r and the frequency offset, f_0 ; frequency comb bandwidth, f_{BW} ; optical carrier-to-noise ratio (OCNR) and optical linewidth, Δf .

generated from a Kerr-nonlinear SiN microresonator covering more than the telecommunications C- and L-band.

- **Comb-line power.** Comb line power is one of the most relevant parameters for WDM systems. For low comb line powers, an optical amplifier is required prior to modulation, which will directly impact the achievable OSNR and therefore the maximum data rate and link distance. Therefore, higher comb line power is desired. Section 3 provides an analysis of the impact of the comb-line power on the OSNR per channel. In particular, for chip-scale frequency combs, the total comb power is limited, such that in many cases of practical interest, the devices are subject to a trade-off between the number of lines the power per comb line.
- **Optical phase noise and intrinsic linewidth.** The optical phase noise dictates the linewidth, Δf , of the individual optical carriers. Typically, discrimination between long-term and short-term phase noise is made. The short-term phase noise is characterized by the spectrally white part

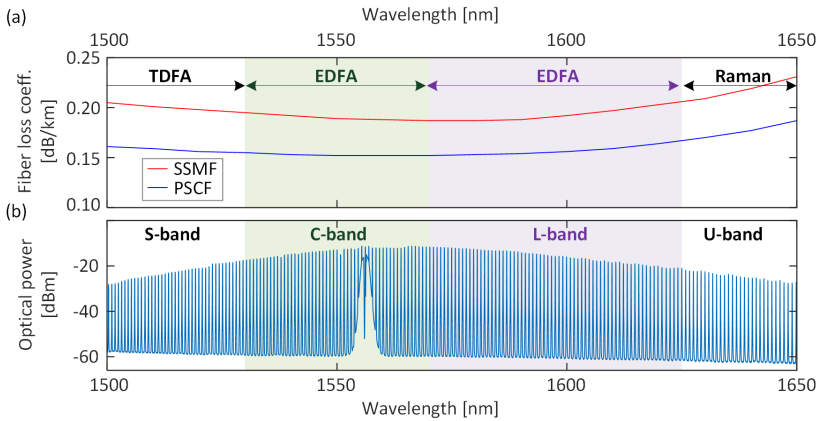


Figure 2.10: Bandwidth for coherent WDM optical communications. (a) Fiber loss coefficient of standard single-mode fiber (SSMF), red, and of pure-silica-core fiber (PSCF), blue [46], [47]. The lowest fiber loss occurs at the telecommunications C- and L-bands, where the bandwidth of erbium-doped fiber amplifiers (EDFA) are located. S-band and U-band are used in some WDM communication systems [49], [50], and for these systems, thulium-doped fiber amplifiers (TDFA) or Raman amplifiers need to be used. (b) Spectrum of a frequency comb generated in a Kerr comb generator, covering more than the telecommunication C- and L-band.

of the frequency-noise power spectral density [51]. Following the Wiener–Khintchine theorem, the laser line shape is obtained from the Fourier transform of the autocorrelation function of the laser light field. In the case of white frequency noise, the line shape can be analytically derived and corresponds to a Lorentzian function whose full width at half maximum (FWHM) is referred to as the intrinsic linewidth. The long-term phase noise typically leads to a Gaussian line shape [52]. In coherent WDM communications, the impact of long-term phase noise can be typically accounted for by digital phase tracking such that usually, only the intrinsic linewidth is relevant for transmission performance. The impact of phase noise depends on the symbol duration and the modulation format – the shorter the symbol duration, the lower the impact of phase noise for a given intrinsic linewidth. In addition, the more complex the modulation format is, the lower its tolerance with respect to phase noise [6], [53]. A detailed analysis of the measurement and impact of phase noise in coherent WDM systems is given in Section 4.3.

- **Relative intensity noise (RIN).** Besides phase noise, any laser also features amplitude or intensity noise. Unlike phase noise, which follows a random walk process with a variance that increases monotonically with time, amplitude fluctuations are bounded to a finite variance due to the inherent nonlinear amplitude control of the laser oscillator. The intensity noise can be modeled by considering a small perturbation $\delta I(t)$ of the mean intensity \bar{I} . The intensity noise is generally expressed in terms of the relative intensity noise (RIN), which is the ratio of the variance of the laser intensity or power fluctuations $\overline{\delta I^2}$ and the square of the mean intensity signal \bar{I}^2 ,

$$\text{RIN} = \frac{\overline{\delta I^2}}{\bar{I}^2}. \quad (2.30)$$

For coherent communications, the RIN of the LO dominates, since the LO tones are much stronger than the signal. A balanced receiver is typically used, which removes this component. However, the mixing of the carrier RIN with the LO RIN remains. In the case of using a single photodetector, the RIN of the carrier does not have to be considered as long

as the LO tone has at least 20 dB more power than the incoming signal [54]. Typically, mode-partition noise that results from the distribution of the saturated gain into different longitudinal modes leads to individual modes having a RIN level much higher than that of the total comb power. In short, a power increase in one mode is compensated by a power decrease in other modes.

- **Optical carrier-to-noise ratio (OCNR).** The OCNR relates the comb line power to the power of the optical background noise centered at the comb line frequency derived from the amplified stimulated emission (ASE) of the amplifier or the gain media. The ASE noise is typically measured with a reference bandwidth of 0.1 nm. A more detailed analysis of the impact of the comb line power and OCNR is given in Section 3.
- **RF linewidth.** The radio-frequency (RF) linewidth is an indication of the coherence of the frequency comb. The narrower the RF linewidth, the higher the coherence between the comb lines. In a frequency comb, the phase noise of the various lines is strongly correlated, therefore the RF linewidth is smaller than the optical linewidth. The RF linewidth is not of critical importance for coherent communications, since the phase noise of each comb line is individually compensated at the receiver. However, a low RF linewidth value could result in an improvement of the performance of the digital signal processing (DSP) necessary for demodulating the signal. For example, a low RF linewidth facilitates the use of joint carrier phase recovery, which reduces DSP complexity [55]. . In addition, digital backpropagation techniques for the cancellation of fiber nonlinearities work better for a small RF linewidth [34].

In the following Sections 2.3 and 2.4, the properties of the two frequency comb sources investigated in this thesis, namely a QD-MLLD and a microresonator-based Kerr comb generator, and their mechanism for frequency comb generation are detailed.

2.3 Frequency comb generation in QD-MLLD

Quantum-dash (QD) mode-locked laser diodes (MLLD) are compact low-cost frequency comb generators featuring low RF linewidth and high repetition rates. QD-MLLDs have been used mainly in the field of optical communications [56], [57]. In general, mode-locking of a laser diode requires an active medium with an inhomogeneously broadened gain spectrum which allows different longitudinal modes to oscillate simultaneously in the laser cavity, in combination with an additional mechanism that establishes a fixed phase relationship between the longitudinal modes [6].

In QD-MLLD, quantum-dash, or elongated-dot, nanostructures grown with molecular beam epitaxy (MBE) are used as the active medium [19]. Lasers with QD-based gain medium stand out due to their low threshold current densities and low-intensity noise [58]. The shape distribution of the QD leads to an inhomogeneously broadened gain spectrum [59], i.e. many longitudinal modes are excited simultaneously.

These devices can be operated by a simple direct current and provide a relatively flat comb spectrum that may span a 3 dB-bandwidth of more than 1 THz [20]. These features make QD-based MLLD highly attractive for WDM optical communications. QD-MLLD devices emitting at the telecommunication C-band wavelength of 1.55 μm were first reported using Fabry Perot (FP) cavities based on a single gain section, i.e., without the need of a saturable absorber typically used in other MLLD-type devices [60]. In single-section QD-MLLD devices, a frequency comb is generated through four-wave mixing, possibly in combination with cross-gain modulation as a passive mode-locking mechanism [19], [61].

This thesis explores and experimentally proves the potential of QD-MLLD for coherent WDM transmission. The following Section 2.3.1 describes the properties of the QD-MLLD and the associated frequency comb which are relevant for coherent communications. In particular, the optical phase noise of the individual comb lines has been so far the limiting factor preventing the use of spectrally efficient modulation formats. In this context, Section 2.3.2 describes different approaches that have been considered in the literature to either reduce the

optical phase noise or to minimize its impact on the performance of coherent optical communication systems.

2.3.1 Frequency comb properties

In a QD-MLLD, the line spacing of the frequency comb or FSR, dictated by the round-trip time of the cavity, can reach tens of GHz, which is compatible with ITU standards for WDM applications, see Section 2.2. So far, QD-MLLD devices have been realized with repetition rates ranging from 10 GHz [62], [63] to more than 300 GHz [64].

For WDM applications, it is important to be able to adjust the FSR and the central frequency of the frequency comb. In a QD-MLLD, this can be achieved by properly adjusting the temperature and the pump current applied to the device. While the FSR remains practically constant for different current values, the radio frequency beat signal, or RF linewidth, changes considerably as a function of the injection current, see Fig. 2.11(a).

Measuring the RF linewidth for different injection current values is a method to determine favorable operation regimes of the QD-MLLD. The RF linewidth can be measured by detecting the self-beating of the comb tones at an RF frequency equal to the FSR, f_r , using a photodiode (PD) with a bandwidth larger than f_r and an electrical spectrum analyzer (ESA).

Depending on the injection current, the RF linewidth is either broad, if the phase of the comb lines are weakly correlated, or narrow, if the phase values of the comb lines are strongly correlated. The beat spectrum may feature multiple peaks around the FSR frequency, if two or more frequency combs with slightly different FSR are co-existing within the cavity [65]. In this case, no RF linewidth can be associated. For best performance, the QD-MLLD should be operated at a current where the beat spectrum features only one peak and where the RF linewidth associated to this peak is narrow. Even when the current is optimized, the RIN of the individual comb lines is still relatively high when compared, e.g., to the RIN measured from high-quality external-cavity lasers (ECL). This is attributed to mode partition noise [66],[67], see Section 2.2. In

Chapter 4, Section 4.2 further details of the impact of the injection current on the bandwidth and optical output power of the frequency comb are discussed.

In addition, QD-MLLD suffer from both amplitude and phase noise. However, well above the laser threshold, the amplitude fluctuations are relatively small because of the inherent nonlinear amplitude control of the laser oscillator. In contrast to this, there is no mechanism to control the phase of the laser, which follows a diffusion process, or random walk, described by an instationary Gaussian process [68]. In QD-MLLD frequency combs, the intrinsic linewidth of individual comb lines can reach values of the order of a few MHz. These high linewidth values have required the use of either hardware or software techniques to enable data transmission with high-spectral efficient modulation formats. The following section details the techniques used so far for minimizing the impact of phase noise

2.3.2 Phase noise reduction techniques

The optical phase noise of individual comb lines from a QD-MLLD leads to linewidths values typically of the order of several MHz. Different techniques have been considered to either reduce the phase noise $\phi_0(t)$ of the individual lines of the frequency comb or to minimize the impact of the phase noise of the recovered signal [69]–[72]. The most relevant techniques are detailed below.

Feed-forward heterodyne scheme

For feed-forward phase-noise compensation, the center comb line with phase noise $\phi_0(t)$ is mixed with a low-noise local oscillator (LO) in a heterodyne receiver. The resulting electrical signal is thus proportional to $\cos(\omega_{\text{IF}}t + \phi_0(t))$, where ω_{IF} is the intermediate frequency between the center comb line and the LO. Next, the phase noise $\phi_0(t)$ is encoded on each of the comb lines by sending the frequency comb through a Mach-Zehnder modulator (MZM) biased at zero transmission and driven by the electrical signal from the heterodyne receiver. Operating the MZM in the linear regime, two sidebands will be generated for each comb line; the lower modulation sidebands will have the term $\phi_0(t)$ compensated, while the upper modulation sidebands will feature enhanced phase noise [69]. This scheme allows reducing the phase noise and thus

the linewidth of the central lines, while the comb lines with increasing line index ν will still present large phase noise. A direct drawback of this approach is the system complexity. Besides, the upper sidebands need to be suppressed to allow for maximum bandwidth usage. This technique was employed to demonstrate an overall net data rate of 0.97 Tbit/s with QPSK signals at 18 GBd.

Self-homodyne detection

In this scheme, the frequency comb of the QD-MLLD is split in power such that a portion is used to transmit the signal and the rest is used as LO tones [70]. Both LO comb and modulated signals are transmitted through the same single-mode fiber using polarization multiplexing, thereby limiting the signal to just one polarization. Using this technique, an aggregate data rate of 1.56 Tbit/s was achieved. A drawback of this scheme is the reduced spectral efficiency since one polarization is used for transmitting the LO tones. In addition, the LO tones will experience the different impairments caused by the transmission link.

Phase-noise reduction by resonant optical feedback

In this scheme, an external optical cavity is used to re-inject a small fraction of the emitted light into the MLLD, thereby considerably reducing the phase noise of the comb lines [71]–[73]. Simultaneous coherent feedback for all lines shows to preserve the flat and broadband spectral envelope of the original frequency comb. Thanks to a strong reduction of the linewidth of individual comb lines, using this technique, a net data rate of 11.22 Tbit/s was demonstrated using 32QAM symbols at 20 GBd. This scheme, however, requires to match the group delay to an integer multiple of the cavity round-trip time, which can only be achieved by a careful alignment of the external cavity if realized by discrete optical components. This limits the practical viability of the approach.

Dedicated schemes for digital phase-noise compensation

The aforementioned techniques for phase noise compensation either require additional hardware or greatly reduce the transmission performance. This raises the question of whether phase noise could simply be compensated by dedicated digital techniques. As will be shown in more detail in Chapter 4, this approach is indeed possible by using a dedicated blind phase search technique. Chapter 4 shows that coherent transmission with QD-MLLD becomes also possible by

using a dedicated digital phase tracking technique that can handle the strong phase noise fluctuations of the QD-MLLD comb lines. With this method, a net data rate of 10.68 Tbit/s was demonstrated using 16QAM symbols at 38 GBd. The transmission performance is on par with that of using resonant optical feedback [72], and corresponds to the highest data rate achieved without any hardware-based phase-noise reduction schemes.

2.4 Frequency comb generation with Kerr-nonlinear microresonators

Kerr frequency comb generation in nonlinear microresonators has become a field of research of its own, initiated after a seminal paper by Del’Haye et al. [68]. This publication reported on the first experimental demonstration of a frequency comb which is generated from a high-Q microcavity driven by a CW-laser. Kerr comb generators offer a wide variety of FSR values, ranging from a few GHz to beyond THz. In addition, they are particularly compact devices, making them suitable for a variety of applications.

The following Section 2.4.1 describes the mechanism behind frequency comb formation in Kerr-nonlinear microresonators, with emphasis on soliton generation, while Section 2.4.2 describes the properties and fabrication techniques of SiN microresonators, which is the most widely used microresonator platform for Kerr comb generation.

2.4.1 Kerr comb formation: From Turing patterns to solitons

Kerr frequency combs are generated by coupling a strong CW laser into a high- Q Kerr nonlinear microresonator that features anomalous group velocity dispersion (GVD). Under appropriate pumping conditions, i.e., sufficient optical power and precise offset of the pump wavelength relative to the pumped cavity resonance, a multitude of spectral lines can be generated by modulation instability and subsequent cascaded four-wave mixing [74].

In general, GVD in a microresonator leads to a non-equidistant separation between the resonances. For anomalous GVD, the FSR increases with frequency,

as depicted by the blue trace in Fig. 2.11. In a Kerr nonlinear microresonator, the non-equidistant spacing of the resonances is compensated by Kerr nonlinearities. The pump induces self-phase modulation (SPM) for the pumped resonance as well as cross-phase modulation (XPM) for the other resonances, which leads to a shift of the resonances. The „hot“ resonances of a pumped cavity hence deviate from the „cold“ resonances of the unpumped cavity. The cavity will also heat up when resonantly pumped, leading to an additional thermal shift of the entire resonance spectrum. As a result, XPM and SPM shift the resonance towards lower frequencies, compensating for the detuning of the sidebands induced by the dispersion.

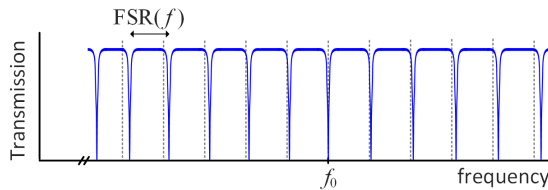


Figure 2.11. Transmission profile of a microresonator with anomalous GVD, for which the FSR increases with frequency. Dashed gray lines represent a regular grid, that corresponds to the position of the resonances in absence of GVD.

Different techniques for Kerr comb generation have been experimentally shown in the literature. These involved either tuning the wavelength of the CW pump-laser [74] or using a fixed wavelength while shifting the resonance frequency, e.g., by temperature tuning through the optical pump power [75] or through integrated microheaters [76], [77], or by electro-optic tuning [78][79]. In the majority of experiments involving Kerr comb generation, the method of choice is to tune the wavelength of a CW laser at a fixed pump power. In this thesis, wavelength tuning is the technique employed for Kerr comb generation, see Section 5.2 and Appendix B.2 for details of the experimental setup for Kerr comb generation.

The resonance shift due to thermal and nonlinear optical effects should lead to a configuration in which small perturbations of the spectral spacing between the pump wave and the pumped resonance will be compensated. This can only be achieved when the pump wavelength (frequency) is slightly smaller (higher) than the hot resonance wavelength (frequency), also referred to as a blue-

detuned pump. In case of an instantaneous reduction of the spacing between the pump and the resonance, e.g., due to a thermal fluctuation, thermal and nonlinear effects push the resonance away from the pump, i.e., towards higher wavelengths, and therefore counteract the perturbation. Similarly, in case of an instantaneous increase of the spacing between the pump and the resonance, thermal and nonlinear effects will pull the resonance back towards the pump. This mechanism is known as thermal and Kerr locking of the microresonator to the pump wavelength. For a red-detuned pump, thermal and nonlinear effects will lead to an increase of small perturbations – this configuration is hence not stable.

When tuning the laser wavelength with respect to the position of the hot resonance, the Kerr comb will evolve through several stages. Adjusting the detuning allows to access each of these stages. Figure 2.12(a) shows different Kerr comb stages accessed by increasing the laser wavelength and sweeping it from the left-side (blue-detuned) of the pumped resonance to the right (red-detuned) side. This leads to a gradual increase of the intracavity power. In each state, the system is stable due to thermal and Kerr locking. Figure 2.12(b) depicts the power spectrum for each of these states.

Once the intracavity power reaches the threshold for parametric oscillations, modulation instability enables the generation of sidebands when the parametric gain from four-wave mixing overcomes the cavity decay-rate [80]. Cascaded non-degenerate four-wave mixing (FWM) from the initial sidebands leads to the formation of a *primary frequency comb*, which in the time domain corresponds to periodic temporal patterns named *Turing patterns*, see state **A** in Fig. 2.12(a) and (b). These periodic waveforms are stationary solutions of the Lugiato-Lefever equation [81]. Turing patterns have already been used in many applications, e.g., in optical communications [82], however, the strong line to line power variations do not allow them to be used for massively parallel WDM communications.

Reducing further the detuning of the pump laser from the hot resonance leads to a further increase of the intracavity power. This results in the generation of frequency combs from the comb lines of the primary frequency comb and eventually gives rise to multiple comb lines oscillating in the same microresonator's resonance. This results in a frequency comb with no coherence, known as *chaotic state* or *noisy Kerr comb*, see state **B** in Fig. 2.12 (a) and (b).

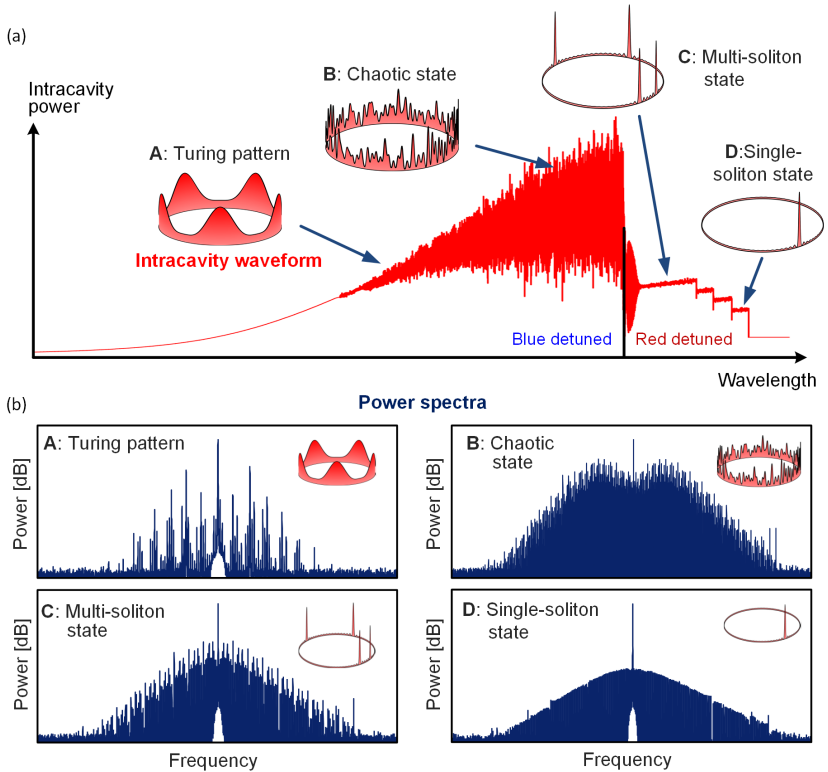


Figure 2.12: Kerr comb generation by tuning the pump wavelength through the hot resonance from an initial blue detuning side to the red detuning side. (a) Evolution of the intracavity power as the wavelength of the pump laser is scanned from the blue to the red side of the hot cavity resonance, and intracavity waveform snapshots at various stages. Turing patterns (A) are generated through four-wave mixing (FWM) when the intracavity power reaches the threshold for parametric oscillation. Tuning the wavelength close to the hot resonance from the blue detuned side leads to the formation of a chaotic state (B), where multiple comb lines oscillate in the same resonance. Increasing the wavelength from the blue-detuned to the red-detuned regime causes the system to enter a bistable regime where multiple- or single-soliton states (C,D) can be stabilized. At higher red-detuning values, the multi-soliton state can collapse into a single-soliton state (D). (b) Power spectra and associated intracavity waveform of the various Kerr comb stages depicted in panel (a).

Increasing the wavelength of the pump laser further from the blue-detuned to the red-detuned regime leads the system to enter a bistability regime, where

solitons can be stabilized, i.e., thermal and Kerr locking of the microresonator to the pump wavelength also holds. In this bistable regime, a single or multiple localized pulses that circulate the cavity coexist with a CW background [83]. These pulses are called *dissipative Kerr solitons* (DKS), see states **C** and **D** in Fig.2.12(a) and (b). The term *soliton* refers to a pulse that keeps its shape while propagating inside a Kerr nonlinear medium with losses and dispersion. The term *dissipative* refers to the fact that these pulses can only exist while the microresonator is pumped. At higher red-detuning values, the multi-soliton state can collapse into a single-soliton state, featuring a particularly smooth optical spectrum, see state **D** in Fig. 2.12(b). Solitons are often represented as pulses with sech amplitude profile.

The stability of solitons, or dissipative Kerr solitons, emerges from a double balance between second-order cavity dispersion and Kerr nonlinearities, as well as between the cavity losses and parametric gain from the coupling of the pump laser into the cavity [21]. Among these states, single-solitons are of particular interest for WDM communications as they provide a smooth and broadband spectrum with small power variations between comb lines.

To avoid large thermal shifts of the resonances when tuning from the blue side to the red side of the hot cavity, a high-speed wavelength tuning procedure is required, such that the thermal state of the cavity before tuning and after landing into the existence range of the soliton is practically the same [21].

Note that the soliton pulses cannot develop from noise fluctuations by simply setting the pump wavelength at the detuning corresponding to soliton existence. The transition from the blue- to the red-detuned regime is necessary to generate the pulse seeds from the chaotic states which will then evolve into soliton pulses when the pump wavelength crosses the effective zero-detuning region.

Recently, soliton states have been also observed in microresonators with normal GVD [84]. These states are known as dark pulses, as opposed to the bright pulses generated in microresonators with anomalous GVD. These pulses can be excited through locally anomalous GVD caused by the interaction of different mode families, so-called avoided mode crossings. In contrast to bright solitons, the excitation of dark pulses follows a deterministic pathway, avoiding a chaotic

state. In addition, dark solitons have a higher conversion efficiency from the pump wave to the frequency comb than their bright counterparts, which is typically associated with a smaller effective detuning of the pump with respect to the hot resonance [85], [86]. However, these states feature a wider pulse, leading to a narrower spectrum. Dark solitons have been already used in optical communication applications [85].

2.4.2 Dissipative Kerr solitons in SiN microresonators

Dissipative Kerr solitons have been generated for different material platforms [87]. So far, the most advanced platforms where solitons have been generated are CMOS-compatible materials such as silicon [88] and silicon nitride (SiN) [75]. Silicon nitride is the mainstream material of choice for fabricating microresonators where solitons can be generated. At telecommunication wavelengths of 1.5 μm , SiN does not suffer from two-photon absorption and the resulting free-carrier absorption which affects silicon waveguides. In addition, SiN features low optical insertion loss.

There are two established fabrication processes for SiN microresonators, namely subtractive and Damascene [6]. In the subtractive process, the SiN waveguides are etched using a patterned mask layer. In the Damascene process, which takes its name from the art of damascene used for centuries in the fabrication of jewelry [89], the process order is inverted and the SiN is deposited onto a pre-patterned substrate [6]. While the subtractive process is the most convenient because of its simplicity, the photonic Damascene process allows the fabrication of thick waveguides with smoother sidewalls leading to average Q -factors above 10^7 [90]. Recently, combining the photonic Damascene process with a novel reflow process has led to Q -factor values in excess of 10^7 [91].

The massively parallel WDM transmission detailed in Section 5 makes use of SiN microresonators fabricated with the photonic Damascene process. These microresonators have also been used over the last years for other major applications [6], such as ultrafast distance measurements [92], dual-comb spectroscopy, and low-noise microwave generation.

3 Performance of chip-scale optical frequency comb generators in coherent WDM communications

This chapter investigates the potential of using chip-scale comb sources as a multi-wavelength source at the transmitter (Tx) and as a multi-wavelength local oscillator (LO) at the receiver of coherent WDM links. The derived holistic model allows estimating the transmission performance of comb-based WDM systems. Additional information on the underlying models can be found in Appendix A. The content of this chapter is taken from a paper that was published in Optics Express [J3]. In order to fit the structure and layout of this document, the content of the paper has been adapted accordingly.

The concept of the holistic model was developed by the author of this thesis together with J. N. Kemal and C. Koos. The model described in Section 3,2 was derived by the author with the support of J.N. Kemal and C. Koos. The study of the impact of line-to-line power variations on the achievable capacity was performed by the authors with the support of S. Randel. The manuscript was written by the author with the support of W. Freude, T. J. Kippenberg, S. Randel, and C. Koos.

[start of paper [J3]]

Copyright © 2020 Optical Society of America

Performance of chip-scale optical frequency comb generators in coherent WDM communications

Optics Express, Volume 28, pages 12897-12910 (2020)

DOI: 10.1364/OE.380413

P. Marin-Palomo¹, J. N. Kemal¹, T. J. Kippenberg², W. Freude¹, S. Randel¹, C. Koos^{1,3}

¹ Karlsruhe Institute of Technology, Institute of Photonics and Quantum Electronics, 76131 Karlsruhe, Germany

- ² Laboratory of Photonics and Quantum Measurements (LPQM), École Polytechnique Fédérale de Lausanne (EPFL), Lausanne, Switzerland
- ³ Karlsruhe Institute of Technology, Institute of Microstructure Technology 76344 Eggenstein-Leopoldshafen, Germany

Optical frequency combs have the potential to become key building blocks of wavelength-division multiplexing (WDM) communication systems. The strictly equidistant narrow-band spectral lines of a frequency comb can serve either as carriers for parallel WDM transmission or as local-oscillator (LO) tones for parallel coherent reception. When it comes to highly scalable WDM transceivers with compact form factor, chip-sale comb sources are of particular interest, and recent experiments have demonstrated the viability of such devices for high-speed communications with line rates of tens of Tbit/s. However, the output power of chip-scale comb sources is generally lower than that of their conventional discrete-element counterparts, thus requiring additional amplifiers and impairing the optical signal-to-noise ratio (OSNR). In this paper, we investigate the influence of the power and optical carrier-to-noise ratio (OCNR) of the comb lines on the performance of the WDM link. We identify two distinctively different regimes, where the transmission performance is either limited by the comb source or by the link and the associated in-line amplifiers. We further investigate the impact of line-to-line power variations on the achievable OSNR and link capacity using a soliton Kerr frequency comb as a particularly interesting example. We believe that our findings will help to compare different comb generator types and to benchmark them with respect to the achievable transmission performance.

3.1 Introduction

Frequency comb generators (FCG) have emerged as light sources for wavelength-division multiplexing (WDM) communications [16], [17], [82], [85], [93]–[98]. A frequency comb consists of a multitude of inherently equidistant spectral lines, hence relaxing the requirements for inter-channel guard bands and avoiding individual frequency control of each line as needed in conventional schemes that use arrays of independent lasers. This advantage also applies to the WDM receiver, where an array of discrete local oscillators (LO) might be

replaced by a single FCG [17], [96], [98]. Using an LO comb for parallel coherent reception of WDM signals further facilitates joint digital signal processing of the channels and can thus reduce receiver complexity and increase phase-noise tolerance [55], [78], [99]. Moreover, parallel coherent reception with frequency-locked LO tones might even allow to reconstruct the time-domain waveform of the overall WDM signal and thus permit compensation of impairments caused by optical nonlinearities of the transmission fiber [34].

Among the various FCG concepts, chip-scale devices are of particular interest [12], [16], [103], [20], [82], [85], [96], [97], [100]–[102]. Combined with advanced photonic integrated circuits for modulation, multiplexing, routing, and reception of data signals, chip-scale FCG offer a path towards highly scalable, compact and energy-efficient WDM transceivers that can offer multi-terabit transmission capacities per fiber. However, chip-scale FCG are also subject to specific limitations when compared to arrays of individual tunable lasers [104] or to discrete-element comb generators that rely, e.g., on highly nonlinear optical fibers [93]–[95]. In particular, the tones of a chip-scale FCG usually feature comparatively low optical power, in some cases combined with limited optical carrier-to-noise ratio (OCNR). For large line counts, optical amplifiers are then needed to boost the optical power prior to modulation, which might further decrease the OCNR. In addition, comb lines generated by chip-scale devices may exhibit pronounced spectral power variations and thus often require spectral flattening, which can lead to further degradation of the optical signal-to-noise ratio (OSNR). However, while these aspects can lead to severe performance limitations, a quantitative analysis of the impact of OCNR limitations and line-to-line power variations on the transmission performance of comb-based WDM transceivers is still lacking.

In this paper, we formulate a model that allows to estimate the transmission performance of comb-based WDM systems under the influence of OCNR limitations and line-to-line power variations. Our model builds upon previous studies of WDM systems in general [105] and of comb-based WDM transmission [78] and extends them to quantify the OSNR at the receiver of the WDM link for different comb-source parameters and transmission distances. We identify two distinctively different operation regimes for such links: For low line powers

or low OCNR levels, the transmission performance is limited by the comb source and the associated amplifiers, whereas the in-line amplifiers along the link turn out to be the main limitation for high line powers and high OCNR. We further investigate the impact of line-to-line power variations on the performance of the WDM link. To this end, we use a soliton Kerr frequency comb generator as an example of a comb source that offers a large number of narrow-band tones [106]. We also analyze the achievable capacity as a function of the link distance for a soliton Kerr frequency comb. For metropolitan-area links of up to 400 km, our model predicts capacities of around 80 Tbit/s. We believe that our findings will help to broadly compare and benchmark different chip-scale comb generator concepts with respect to achievable transmission performance in a given use case.

This paper is structured as follows: In Section 3.2, we introduce the model of the comb-based transmission link that represents the base of our investigation. Section 3.3 describes the results of this investigation and formulates requirements with respect to comb-line power and OCNR that should be fulfilled by chip-scale comb generators to ensure link-limited transmission. Section 3.4 is dedicated to investigating the impact of spectral flattening.

3.2 OSNR limitations in a comb-based WDM system

In comb-based WDM systems, one of the main aspects leading to limited transmission performance is the fact that the overall output power of the comb source is limited and that spectral splitting of the comb lines leads to additional optical loss. This may lead to low powers per line, which often requires additional amplifiers to boost the power prior to modulation, thereby decreasing the OCNR of the lines entering the modulator array. In the following, we analyze these effects and quantify their impact on the overall transmission performance.

The performance of a WDM link is often described by the OSNR measured at the receiver input. The OSNR is defined as the ratio of the signal power to the amplified spontaneous emission (ASE) noise power within a reference

bandwidth $B_{\text{ref}} = 12.5$ GHz, corresponding to a reference wavelength span of 0.1 nm at a center wavelength of 1.55 μm . The OSNR can be translated into the signal-to-noise ratio (SNR) that refers to the actual bandwidth of a specific signal [32]. For a coherent system limited by ASE noise,

$$\text{SNR} = \frac{2B_{\text{ref}}}{pR_s} \text{OSNR}, \quad (3.1)$$

where R_s is the symbol rate, $p=1$ for a single polarization signal and $p=2$ for a polarization-multiplexed signal [32]. In the following, we will consider polarization-multiplexed signals.

In a comb-based WDM system, the OSNR of a WDM channel will depend on the comb line power P_{line} and the OCNR of the comb line, $\text{OCNR}_{\text{line}}$. In analogy to the OSNR, the OCNR relates the comb line power to the power of the background noise, measured again within a reference bandwidth B_{ref} centered at the comb line frequency. The sum of the noise power in both polarizations at the output of the FCG is given by

$$P_{\text{noise}} = N_0 B_{\text{ref}} = \frac{P_{\text{line}}}{\text{OCNR}_{\text{line}}}. \quad (3.2)$$

Here, N_0 is the noise spectral power density. Thus, P_{line} and $\text{OCNR}_{\text{line}}$ impact the OSNR of a WDM channel and can limit the achievable spectral efficiency for a given reach. Note that we disregard the impact of the optical linewidth in our analysis. The linewidth of the individual comb lines is not altered by the link and it only becomes relevant after the channel is coherently detected. At the receiver, the channels are analyzed individually and the linewidth may be treated as the property of an individual carrier tone rather than as a frequency comb property. The associated limitations have been discussed in the literature for different modulation formats and can be readily applied to frequency-comb transmission [53], [99].

For a quantitative analysis, consider the WDM link depicted in Fig. 3.1 consisting of a WDM transmitter, a link with M fiber spans, and a WDM receiver [78]. Note that the comb line powers P_{line} of most chip-scale FCG are usually much weaker than the power levels emitted by state-of-the-art continuous-wave laser

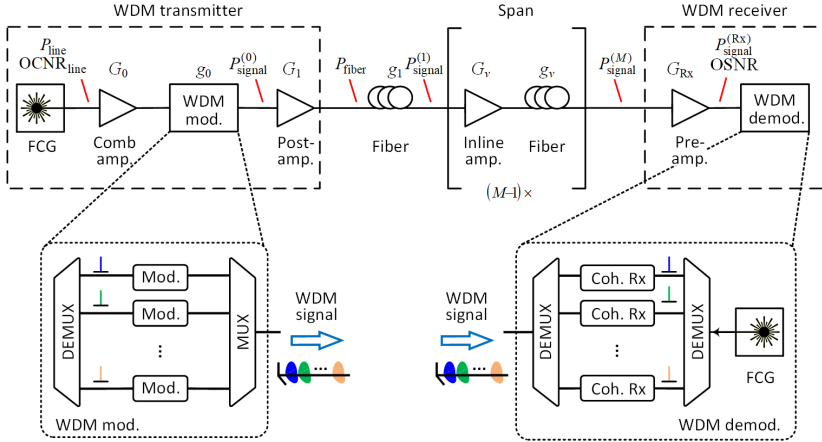


Figure 3.1. Schematic of a comb-based WDM transmission and reception system. The tones of a chip-scale frequency comb generator (FCG) are first amplified by an optical amplifier (Comb amp.) before data are encoded on each line in the WDM modulation unit (WDM mod.), which comprises a WDM demultiplexer (DEMUX), an array of dual-polarization I/Q modulators (Mod.), and a WDM multiplexer (MUX). The polarization multiplexed WDM signal is then boosted by an optical amplifier (Post-amp.) and transmitted through the fiber link consisting of at least one span. Each of the $M - 1$ additional spans contains an in-line amplifier (In-line amp.) which compensates the loss of the corresponding fiber section. The data from each WDM channel are recovered at the WDM receiver, which contains a pre-amplifier (Pre-amp.) and a WDM demodulation unit (WDM demod.). The WDM demodulation unit uses a multitude of LO tones derived from a second FCG.

diodes used in conventional WDM systems. For practical transmission systems, it is therefore necessary to amplify the comb lines prior to modulation by

sending them through a dedicated optical amplifier with gain $G_0 > 1$. Data are encoded onto the various carriers by a WDM modulation unit comprising a WDM demultiplexer (DEMUX), an array of dual-polarization in-phase/quadrature (I/Q) modulators, and a WDM multiplexer (MUX). The power transmission factor of the WDM modulation unit is denoted as $g_0 < 1$ and accounts for the insertion losses of the multiplexer and the demultiplexer as well as for the insertion and modulation losses of the I/Q modulators. In our analysis we consider the bandwidth of the WDM DEMUX filter to be equal to the line spacing

of the frequency comb. It can, however, be advantageous to reduce the filter bandwidth in order to suppress unwanted additive noise between the carriers. Note that the modulator will act as a polarizer and thus only the noise co-polarized with the laser carrier is considered. The signal and noise power at the output of the WDM modulation unit are given by

$$P_{\text{signal}}^{(0)} = g_0 G_0 P_{\text{line}}, \quad P_{\text{noise}}^{(0)} = \frac{g_0}{2} \left[\underbrace{G_0 N_0 B_{\text{ref}}}_{\text{amplified OFC noise}} + \underbrace{F_0 h f (G_0 - 1) B_{\text{ref}}}_{\text{ASE noise of comb amplifier}} \right]. \quad (3.3)$$

In these relations, F_0 is the noise figure of the comb amplifier, and hf is the photon energy [105]. For simplicity, we consider a frequency comb with equal power P_{line} for each spectral line, in Section 3.4, we investigate the impact of line-to-line power variations. Note that in our analysis, the noise is considered to be stationary, i.e., we do not account for any modulation of the noise contributions of the comb source and the comb amplifier. In the typically used link-limited regime, the effect of modulated noise can be disregarded since the stationary ASE noise added in the link dominates. In the source-limited regime, neglecting the amplitude modulation of the noise might lead to a slight overestimation of the performance.

The polarization-multiplexed WDM signal is then boosted by a post-amplifier with gain G_1 and launched into the first fiber section, which attenuates the power by $g_1 < 1$,

$$P_{\text{signal}}^{(1)} = g_1 G_1 P_{\text{signal}}^{(0)}, \quad P_{\text{noise}}^{(1)} = g_1 [G_1 P_{\text{noise}}^{(0)} + F_1 h f (G_1 - 1) B_{\text{ref}}]. \quad (3.4)$$

The first fiber span may be followed by $M - 1$ additional fiber sections, each attenuating the power by $g_m < 1$ and by the same number of additional in-line amplifiers with gain G_m .

These in-line amplifiers are used to compensate the loss of the respective fiber section such that $G_m g_m = 1$, $m = 2 \dots M$. Setting $G_m = G$, and $F_m = F$ for $m = 2 \dots M$, and $g_m = g$ for $m = 1 \dots M$, the signal power and the noise power after the transmission link are given as

$$P_{\text{signal}}^{(M)} = P_{\text{signal}}^{(1)}, \quad P_{\text{noise}}^{(M)} = P_{\text{noise}}^{(1)} + g(M - 1)F h f (G - 1)B_{\text{ref}}. \quad (3.5)$$

The data from each WDM channel are recovered at the WDM receiver, which contains an optical pre-amplifier with gain G_{Rx} and noise figure F_{Rx} and a WDM demodulation unit. The WDM demodulation unit uses a multitude of LO tones derived from a second FCG to recover the transmitted data with an array of IQ detectors. The signal power and the noise power at the output of the pre-amplifier are given by

$$P_{\text{signal}}^{(\text{Rx})} = G_{\text{Rx}} P_{\text{signal}}^{(M)}, \quad P_{\text{noise}}^{(\text{Rx})} = G_{\text{Rx}} P_{\text{noise}}^{(M)} + F_{\text{Rx}} h f (G_{\text{Rx}} - 1) B_{\text{ref}}. \quad (3.6)$$

To obtain the OSNR for a single WDM channel, the ratio of the received signal power and the noise power in the reference bandwidth B_{ref} needs to be calculated,

$$\text{OSNR} = \frac{P_{\text{signal}}^{(\text{Rx})}}{P_{\text{noise}}^{(\text{Rx})}}. \quad (3.7)$$

Introducing Eqs. (3.3) to (3.6) into Eq. (3.7) for a given line power P_{line} and $\text{OCNR}_{\text{line}}$ the OSNR per channel can be expressed as

$$\text{OSNR} = g_0 G_0 P_{\text{line}} \underbrace{\left(\frac{g_0 G_0 P_{\text{line}}}{2 \text{OCNR}_{\text{line}}} \right)}_{\text{ampl. FCG noise}} + h f B_{\text{ref}} \underbrace{\left(\frac{g_0}{2} (G_0 - 1) F_0 + \frac{G_1 - 1}{G_1} F + \right)}_{\text{amplifier noise}} \underbrace{\left((M-1) \frac{G-1}{G_1} F + \frac{G_{\text{Rx}} - 1}{G_{\text{Rx}} g G_1} F_{\text{Rx}} \right)}_{\text{amplifier noise}}^{-1}. \quad (3.8)$$

Note that for a high number of spans, i.e., $M \gg 1$, the noise of the receiver pre-amplifier does not play a role any more, since the noise background is dominated by the noise contribution from the various amplifiers along the link.

In Section 3.3, we apply Eq. (3.8) to a comb-based WDM system to derive the OSNR as a function of the line power P_{line} and the number M of fiber spans, see Fig. 3.2. In this analysis, we assume a spectrally flat comb where all tones have the same power. In addition, the gain G_1 of the post-amplifier is assumed to be the same as the gain G of the in-line amplifiers, and the gain G_0 of the

comb amplifier is adjusted such that a launch power into each fiber section of $P_{\text{fiber}} = 0$ dBm is reached after the post-amplifier. This launch power is commonly used in 32 GBd WDM links for keeping the nonlinear impairments low while maintaining high OSNR levels [107], [108]. In Section 3.4, we expand this consideration and analyze the more practical case where P_{line} varies from line to line. In this case, the resulting OSNR will depend on the comb line. As an example of a chip-scale FCG with large line count, we investigate a soliton Kerr comb generated in an integrated optical microresonator [85], [96], [106] and consider the OSNR variations from line to line as a function of P_{line} and $\text{OCNR}_{\text{line}}$, see Fig. 3.3. In this analysis, we set the G_0 such that a fixed output power of 25 dBm is obtained, and we adjust G_1 such that $P_{\text{fiber}} = 0$ dBm.

3.3 OSNR limitations considering frequency combs with flat spectra

In this section, we make use of Eq. (3.8) to estimate the OSNR as a function of P_{line} and $\text{OCNR}_{\text{line}}$ for different numbers M of fiber spans, see Fig. 3.2. The various parameters used for this study are specified in Table 3.1. For the WDM modulation unit, an overall insertion loss of 25 dB is assumed, comprising 3.5 dB of insertion loss each for the WDM demultiplexer and the multiplexer [109], 13 dB of loss for the dual-polarization IQ modulators [110], and an additional 5 dB of modulation loss, which are assumed to be independent of the modulation format for simplicity. Note that the results shown in Fig. 3.2 do not change significantly when varying these losses by a few dB while compensating the variation by an adjustment of the gain G_0 of the comb amplifier. The fiber spans are assumed to feature a power loss of 15 dB each, corresponding to 75 km of single-mode fiber with a propagation loss of 0.2 dB/km. The power loss of each span is exactly compensated by the 15 dB gain of the corresponding in-line amplifier such that a signal launch power of $P_{\text{fiber}} = 0$ dBm per channel is maintained for all spans. For simplicity, the gain and the noise figure of the receiver pre-amplifier is assumed to be identical to that of the in-line amplifiers, leading to a signal power of 0 dBm per wavelength channel at the input of the receiver DEMUX. Figure 3.2(a) shows the OSNR as a function of P_{line} for various span counts M . The $\text{OCNR}_{\text{line}}$ of the comb lines is assumed to be infinite,

i.e., the FCG itself does not introduce any practically relevant additive noise background. This can, e.g., be accomplished by soliton Kerr comb generators, see Fig. 3.3, where most of the comb lines do not contain relevant additive noise background. For low line powers P_{line} , Fig. 3.2(a) shows that the noise level at the receiver is dominated by the contribution of the comb amplifier. As a consequence, the OSNR increases in proportion to P_{line} and is essentially independent of the span count M . In this regime, transmission performance is limited by the comb source and its associated amplifier (“source-limited”). For high comb line powers P_{line} , in contrast, the noise level at the receiver is dominated by the contributions of the various amplifiers along the link (“link-limited”). In this regime, the OSNR is essentially independent of P_{line} and decreases with each additional span. For a given number of spans, the transition between both regimes is indicated by black circles in Fig. 3.2(a), indicating the points where the OSNR has decreased by 1 dB in comparison to its limit at high line power P_{line} . When using frequency combs in WDM systems, operation in the link-limited regime is preferred. Depending on the number of spans, this requires a minimum comb line power between approximately -25 dBm and -15 dBm. Note that, in principle, the gain G_1 of the post amplifier could be decreased while increasing the gain G_0 of the comb amplifier. For source-limited transmission, the overall impact would be small since the OSNR is mainly dictated by the comparatively low line power P_{line} that enters the comb amplifier. For link-limited transmission over a small number of spans, the OSNR can be slightly improved by decreasing the gain G_1 and increasing the gain G_0 while maintaining power levels of about 10 dBm per line at the output of the comb amplifier. In our analysis, we assume equal noise figures of 5 dB for all optical amplifiers. This is a realistic assumption since gain values of the amplifiers do not differ considerably, even when considering additional measures for spectral flattening, see Table 3.2 in Section 3.4.

Figure 3.2(a) can be used as a guide for estimating the performance requirements for comb sources in WDM applications. As a reference, the plot indicates the minimum OSNR required for transmission of a net data rate of 400 Gbit/s or 600 Gbit/s per WDM channel using 16QAM or 64QAM as a modulation format, respectively. In both cases, advanced forward-error correction (FEC) schemes with 11 % overhead and a BER threshold of 1.2×10^{-2} [111] are

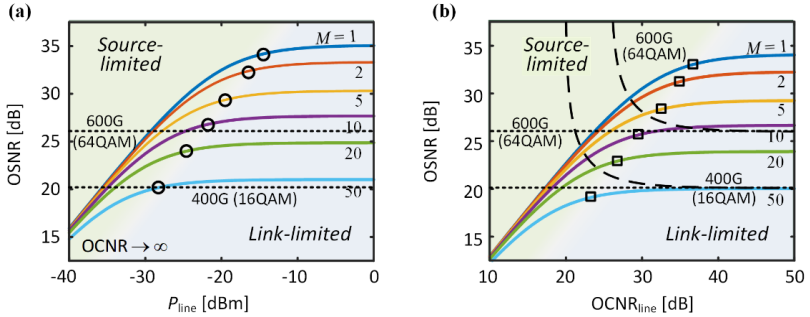


Figure 3.2. Influence of the comb-line power P_{line} and of its carrier-to-noise ratio $\text{OCNR}_{\text{line}}$ on the achievable optical signal-to-noise ratio OSNR at the WDM receivers for different values M of 75 km-long spans with 0.2 dB/km loss, see Table 1 for the model parameters used. **(a)** OSNR as a function of P_{line} in the limit of a high $\text{OCNR}_{\text{line}}$. The plot reveals two regimes: For source-limited transmission at low line powers, the OSNR is dominated by the contribution of the comb amplifier, whereas the contributions of the various amplifiers along the link dominates for link-limited transmission at high line powers. The transition between both regimes is indicated by black circles which mark the points where the OSNR has decreased by 1 dB in comparison to its limit at high comb line powers. The dotted horizontal lines indicate the minimum OSNR required for transmission of a net data rate of 400 Gbit/s using 16QAM and of 600 Gbit/s using 64QAM as a modulation format [111]. **(b)** OSNR at the WDM receiver as a function of $\text{OCNR}_{\text{line}}$ for comb line powers P_{line} that correspond to the transition points marked by circles in (a). For low $\text{OCNR}_{\text{line}}$, OSNR is dominated by the noise of the comb source, and the transmission performance is source-limited. For high $\text{OCNR}_{\text{line}}$, the OSNR is independent of the $\text{OCNR}_{\text{line}}$ and the transmission performance is link-limited. The dotted horizontal lines indicate again the minimum OSNR required for transmission of a net data rate of 400 Gbit/s using 16QAM and of 600 Gbit/s using 64QAM as a modulation format, assuming an ideal LO comb with infinite $\text{OCNR}_{\text{line}}$. In case of a real LO comb with finite $\text{OCNR}_{\text{line}}$, the OSNR requirements for a given BER become more stringent when approaching the link-limited regime, see dashed lines, which were derived from Eq. (3.9).

assumed, requiring a symbol rate of 56 GBd to provide the specified net data rates. Note that we do not account for the format-dependent modulation losses, but assume an overall insertion loss of the modulator of 25 dB both for 16QAM and 64QAM. This loss includes both the optical insertion loss of the device and the modulation loss.

Table 3.1. Model parameters used for generating Fig. 3.2(a) and 3.2(b) from Eq. (3.8). The fiber attenuation g_m , amplifier gain G_m , and noise figures F_m are assumed to be the same for all M fiber links denoted by subscript $m = 1 \dots M$. For the spectral flattening considered in Section 3.4, we adjust the power transmission factor g_0 of the WDM modulation unit or the gain G_0 individually for each channel, and we choose the gain G_1 of the post-amplifier to maintain a constant power per channel of 0 dBm at the input of the first fiber span. Specifically, for the variable-gain scenario, g_0 is varied such that $g_0 P_{\text{line}}$ is constant across all comb lines, whereas for the variable-gain scenario, G_0 is varied from channel to channel such that $G_0 P_{\text{line}}$ is constant.

Variable	Description	Value	
B_{ref}	Reference bandwidth for OSNR and OCNR calculation	12.5 GHz	
$G_m P_{\text{signal}}^{(m)} = P_{\text{fiber}}$	Signal power per WDM channel at the input of each fiber span	1 mW	0 dBm
g_0	Power transmission factor of WDM modulation unit	3.2×10^{-3}	-25 dB
G_0	Power gain factor of comb amplifier	$P_{\text{fiber}} / (P_{\text{line}} g_0 G_1)$	
F_0	Noise figure of comb amplifier	3.2	5 dB
G_1	Power gain factor of post-amplifier	32	15 dB
F_1	Noise figure of post-amplifier	3.2	5 dB
$g_m = g$	Power transmission factor of fiber section	3.2×10^{-2}	-15 dB
$G_m = G = g^{-1}$	Power gain factor of post- and inline-amplifier	32	15 dB
$F_m = F$	Noise figure of post- and inline-amplifiers	3.2	5 dB
G_{Rx}	Power gain factor of pre-amplifier	32	15 dB
F_{Rx}	Noise figure of pre-amplifier	3.2	5 dB

For many practically relevant comb sources, the $\text{OCNR}_{\text{line}}$ is finite, which also impairs the transmission performance. Figure 3.2(b) shows the OSNR at the receiver as a function of $\text{OCNR}_{\text{line}}$ for various span counts M . In this plot, the comb line power is the minimum value required for link-limited transmission, as indicated by the corresponding transition points in Fig. 3.2(a). For low $\text{OCNR}_{\text{line}}$, the noise level at the receiver is dominated by the amplified noise background of the comb source, and the $\text{OCNR}_{\text{line}}$ and OSNR are essentially identical. In this case, the link performance is again source-limited. For high $\text{OCNR}_{\text{line}}$, the OSNR is dictated by the accumulated ASE noise of the post-amplifier and the in-line amplifiers and is thus independent of the $\text{OCNR}_{\text{line}}$.

In this regime, the transmission performance is link-limited. Depending on the number of spans, the minimum $\text{OCNR}_{\text{line}}$ values needed for link-limited transmission range between approximately 25 dB and 35 dB. The transition between both regimes is marked by black squares in Fig. 3.2(b), indicating the points where the OSNR has decreased by 1 dB in comparison to its respective limit at high $\text{OCNR}_{\text{line}}$.

Note that finite OCNR can also become relevant at the receiver in case a frequency comb is used as multi-wavelength LO. In a simplified consideration, we may assume that the transmitter and the receiver rely on comb sources with identical OCNR. In this case, the OCNR of the LO comb is always higher than the OSNR of the received signal, which is affected by the ASE noise of the post-amplifier at the transmitter, the pre-amplifier at the receiver and the inline amplifiers along the link. In the link-limited transmission regime, the noise accumulated along the link dominates, and the noise of the LO comb can hence be neglected. The only case for which the impact of LO noise becomes important is the source-limited transmission regime, i.e., the left-hand part of Fig. 3.2(b). In this region, the LO comb noise additionally impairs the reception, thereby increasing the OSNR of the data signal that is required for a given BER. This is indicated by the dashed lines for the 400 Gbit/s 16QAM signal and for the 600 Gbit/s 64QAM signal. Neglecting noise-noise beating in the coherent receiver and defining OCNR_{∞} as the OSNR required for a given BER in case of an ideal noise-less LO comb (dotted line in Fig. 3.2(b)), the OSNR in case of a non-ideal LO-comb with finite $\text{OCNR}_{\text{line}}$ can be expressed as

$$\text{OSNR} = \left(\frac{1}{\text{OCNR}_{\infty}} - \frac{1}{\text{OCNR}_{\text{line}}} \right)^{-1}. \quad (3.9)$$

Note that the underlying BER can only be achieved for $\text{OCNR}_{\text{line}} > \text{OCNR}_{\infty}$ and that the achievable OSNR is always worse than the $\text{OCNR}_{\text{line}}$ of the transmitter comb, i.e., $\text{OSNR} \leq \text{OCNR}_{\text{line}}$ if the transmitter and the receiver rely on comb generators with identical.

3.4 OSNR limitations considering frequency combs with line-to-line power variations

Chip-scale comb sources, relying on different comb generation approaches, have been used in a variety of WDM transmission experiments covering a wide range of data rates, channel counts, and line spacings [12], [16], [101]–[103], [17], [20], [82], [85], [96]–[98], [100]. In these WDM transmission experiments, the line to line variations of P_{line} and $\text{OCNR}_{\text{line}}$ lead to a channel-dependent OSNR. In the following, we will analyze the impact of line-to-line power variations on the transmission performance of the WDM link for different transmission distances. To this end, we consider a Kerr frequency comb generated in a silicon nitride (SiN) microresonator [106] as an illustrative example. Kerr frequency combs are generated by pumping a high-Q microresonator with a strong CW laser, see Fig. 3.3(a). Under appropriate pumping conditions, cascaded four-wave mixing leads to the formation of a multitude of spectral lines. As a technically attractive example, we consider so-called single-Kerr-soliton states, which rely on a double balance of parametric gain and cavity loss as well as second order dispersion and nonlinearity and which consist of a single ultra-short pulse circulating in the micro-resonator [105]. This leads to broadband frequency combs providing tens or even hundreds of high-quality tones for massively parallel WDM transmission [96]. Note that single-soliton Kerr combs are considered for illustrative purposes only and that other comb sources or other comb states in Kerr-nonlinear microresonators can also be used for WDM transmission. As an example, Turing rolls and dark solitons can achieve high power conversion efficiencies and have been used in WDM transmission [82], [85]. However, the number of comb lines is rather limited and the line-to-line power variations may be strong. Solitons generated in microresonators with higher-order dispersion, such as quartic solitons [112] may provide frequency combs with broad and smooth spectra and might thus lend themselves to massively parallel WDM transmission.

An example of a measured single-soliton Kerr comb spectrum is shown in Fig. 3.3(b), which is measured after equalizing the residual pump power with a notch filter (not shown in Fig. 3.3). This spectrum comprises around 110

carriers spaced by approximately 100 GHz within the telecommunication C and L band (1530 nm ... 1610 nm). The line powers range from -11 dBm near the center to -20 dBm at the edges of the telecommunication window, and the OCNr values range from 48 dB to 40 dB, which would safely permit link-limited transmission in realistic WDM systems, see Fig. 3.2. While the on-chip pump power used to generate the comb in the originally experiment was approximately 29 dBm, recent advances in fabrication technology and system design have shown the possibility to significantly reduce the required pump power for soliton generation and increase the power conversion efficiency, e.g., by increasing the quality factor of the microresonator [113] or incorporating the microresonator into the cavity of the pump laser [76]. Using Eq. (3.8) with the P_{line} and $\text{OCNR}_{\text{line}}$ values measured from the carriers of the soliton frequency comb and with the model parameters from Table 3.1 and Table 3.2, we calculate the optical signal-to-noise ratio OSNR_{ℓ} , $\ell=1\dots L$, for each individual channel as a function of the link distance, see Fig. 3.3(c)-3.3(e). For this analysis, we assume an output power of 25 dBm provided by the comb amplifier, which corresponds to a power of approximately 5 dBm per line at the input of the WDM modulation unit. The gain of the post-amplifier is set such that a power per line of 0 dBm is launched into each fiber span.

We investigate three different WDM transmission scenarios, refer to Table 3.2 for the gain G_0 and G_1 of the comb amplifier and the post-amplifier for each of these scenarios as well as for the corresponding power transmission factor g_0 of the WDM modulation unit. In the first scenario, the comb lines are not equalized in power (“No equalization”), and all amplifiers are assumed to have a spectrally flat gain. Note that this scenario is typically not implemented in practical WDM transmission systems, and it is used here as a reference. In our analysis we assume the power $P_{\text{fiber}} = 0$ dBm to be the average signal power per WDM channel at the input of each fiber span. The individual per-channel launch powers vary from -7 dBm to 3 dBm. In the second scenario, the power per line is equalized at the first amplifier stage of Fig. 3.1 by using, e.g., a wavelength-dependent gain G_0 such that the comb lines at the edge of the telecommunication windows are amplified more than those at the center to reach a spectrally uniform per-channel launch power of 0 dBm into the first fiber span. This can be achieved, e.g., by adapting the gain profile of the optical amplifiers to the spectral variations of the

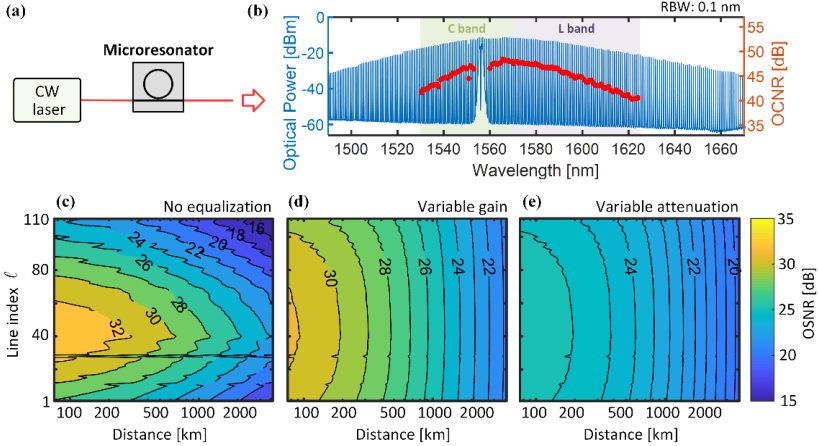


Figure 3.3. Single-soliton Kerr frequency combs and impact of line-to-line P_{line} and $\text{OCNR}_{\text{line}}$ variations on the OSNR. **(a)** Kerr comb generation: A high-Q Kerr nonlinear microresonator is pumped by a CW laser. Under appropriate conditions, cascaded degenerate and non-degenerate four-wave mixing leads to formation of new spectral lines. For single-soliton states, the superposition of the phase-locked optical tones forms an ultra-short soliton pulse circulating in the cavity. This leads to a comb spectrum with a broadband envelope. **(b)** Spectrum of a single-soliton Kerr frequency comb generated in a SiN microresonator [96]. The comb offers 110 carriers in the telecommunication C and L band (1530 nm ... 1625 nm), spaced by approximately 100 GHz. In the center of the spectrum, the comb line power amounts to -11 dBm, and the OCNR is approximately 48 dB. Towards the wings of the comb, both line power and OCNR decrease. **(c-e)** OSNR as a function of the link distance and the comb line index, ℓ , **(c)** without equalizing the power per line (“No equalization”); **(d)** for equalizing the power per line by using a spectrally variable gain in first amplifier stage of Fig. 3.1 (“Variable gain”); **(e)** for equalizing the power per line by introducing individual power attenuations for each channel (“Variable loss”) at the WDM modulation unit from Fig. 3.1.

frequency comb. For simplicity, we assume the noise figure of all amplifiers to be wavelength-independent. We refer to this scheme as variable-gain equalization (“Variable gain”). In the third scenario, the power per line is equalized at the WDM modulator stage of Fig. 3.1 by considering a channel dependent power transmission g_0 . This can, e.g., be accomplished by using optical attenuators or by adjusting the drive voltages of the IQ modulators, such that the channels at the center of the comb spectrum experience a higher attenuation. In

this scenario, we assume again amplifiers with spectrally flat gain and noise figure. The gain G_1 of the post-amplifier is increased such that $P_{\text{fiber}} = 0$ dBm. We refer to this scheme as variable-loss equalization (“Variable loss”).

Table 3.2. Model parameters for each WDM transmission scenario in Fig. 3.3 and Fig. 3.4. The gain G_0 of the comb amplifier is adjusted to reach a fixed output power of 25 dBm fed into the WDM modulation unit, while the gain G_1 of the post-amplifier is adjusted to obtain a power per channel of 0 dBm at the input of the first fiber span. The quantity g_0 denotes the power transmission of the WDM modulation unit and of the associated variable attenuators used for spectral flattening.

	No equalization	Variable gain	Variable attenuation
g_0	−25 dB	−25 dB	−35 dB ... −25 dB
G_0	19 dB	16 dB ... 26 dB	19 dB
G_1	21 dB	21 dB	27 dB

If no power equalization to the comb lines is performed, strong channel-to-channel OSNR variations can be observed for all transmission distances, see Fig. 3.3(c) “No equalization”. Note that these channel-dependent OSNR variations do not decrease with propagation distance since the amplifier noise term in Eq. (3.8) dominates the noise power in the denominator such that the difference in P_{line} at the output of the frequency comb will determine the OSNR_ℓ . If the comb line powers are equalized at the first amplification stage, see Fig. 3.3(d) “Variable gain”, all channels will exhibit the same OSNR_ℓ for large transmission distances. This can be understood by the fact that, at large distances, the accumulated ASE noise from the in-line amplifiers will dominate the noise power in all channels such that the initial OSNR differences become irrelevant. The same is true if the comb line powers are equalized at the WDM modulation stage, see Fig. 3.3(e) “Variable attenuation” – also here the accumulated ASE noise will dominate the noise power with increasing distance. In addition, the initial attenuation of the center channels will decrease the associated OSNR for short transmission distances, but this difference disappears for longer links as the accumulated ASE noise of the in-line amplifiers dominates. As a consequence, the performance of the second and the third transmission scenario converge with increasing transmission distance.

To quantitatively compare the transmission performance of the three different schemes, we estimate the maximum capacity for a given reach [114],

$$C = f_r \sum_{\ell=1}^L \log_2(1 + \text{SNR}_{\ell}), \quad (3.10)$$

where f_r is the comb line spacing, L is the number of comb lines, and SNR_{ℓ} is obtained from the OSNR_{ℓ} through Eq. (3.1) with a bandwidth $B = f_r$. Equation (3.9) considers the maximum capacity for each channel which can be theoretically achieved by using an arbitrarily complex modulation format [114]. The link capacity according to Eq. (3.10) for $f_r = 100$ GHz and $L = 110$, as well as the spectral efficiency, $\text{SE} = C / (L f_r)$ are indicated as solid lines in Fig. 3.4. The line spacing was chosen to maximize the per-channel symbol rate while still being compatible with the bandwidth of available signal generators [115] and IQ modulators [116].

For Metro links, both the scheme without equalization (“No equalization”) and the scheme with spectrally variable gain (“Variable gain”) lead to a higher capacity than the scheme based on spectrally variable attenuation (“Variable attenuation”), offering link capacities of around 80 Tbit/s. For longer reach, the capacity decreases, and the differences between the three schemes become negligible. Note that our consideration does not account for the impact of fiber non-linearity, which might lead to further limitations at longer transmission distances [30].

Another scenario of practical interest is the case where all modulators of the various WDM channels are operated with the same modulation format and same FEC overhead is applied to all channels. The maximum capacity is then dictated by the channel with the lowest SNR, SNR_{\min} , leading to

$$C = L f_r \log_2(1 + \text{SNR}_{\min}), \quad (3.11)$$

The results of this consideration are indicated as dashed lines in Fig. 3.4. For metro links, the variable-gain scheme provides the highest SNR_{\min} and thus the highest capacity and spectral efficiency. For longer links, the performance of carriers of a soliton Kerr frequency the variable-gain scheme approaches that of

the variable-attenuation scheme. The capacity is then the same as the one obtained from Eq. (3.10). As a comparison, Fig. 3.4 also shows the case of using individual lasers instead of the comb. For this analysis, we have assumed a fixed

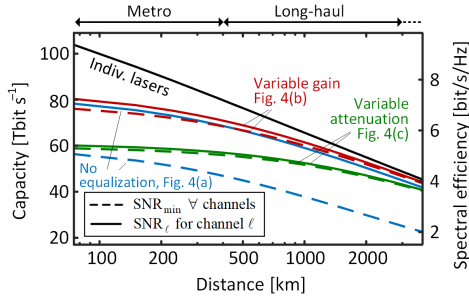


Figure 3.4. Total capacity and spectral efficiency of a WDM transmission link using individual lasers (black line) single-soliton Kerr frequency combs with $L = 110$ comb lines and a comb line spacing $f_r = 100$ GHz (colored traces). Blue traces: No equalization done (“No equalization”). Red traces: Flattening of the frequency by spectrally variable gain in the first amplifying stage (“Variable gain”). Green trace: Flattening of the frequency comb by spectrally variable attenuation in the WDM modulation unit (“Variable attenuation”). Black trace: Individual lasers each with 13 dBm of optical power and 60 dB of OCNR. Solid lines: The capacity is optimized individually for each channel. Dashed lines: The per-channel capacity is derived from the smallest SNR, SNR_{\min} in the WDM link.

power per line of 13 dBm fed directly into the modulator along with an OCNR of 60 dB. For short transmission distances, the performance of the comb-based scheme is source limited due to the low power per line. The analysis also shows that the spectral flatness and the gain flattening technique have a direct impact on the achievable capacity. For longer reach, all schemes with flat spectra approach the same link-limited performance.

Regarding technical realizations of chip-scale WDM transceivers, it should be noted that integration of high-power comb amplifiers might represent a challenge, in particular when it comes to massively parallel transmission with tens of even hundreds of comb lines [96], [97]. For the example of an input power of approximately 3 mW per line measured at the input of the modulator, a high-power semiconductor optical amplifier (SOA) with a saturation output power

of 23 dBm [117] could be used to handle approximately 70 lines. For bigger line counts or higher powers per line, the tones have to be amplified in separate groups or fiber amplifiers have to be used. For Kerr combs, another challenge might arise from the fact that the residual pump after the resonator may be much stronger than the other comb tones. Suppressing the pump leads to additional energy loss. Note, however, that in all of these cases, the power consumption of the comb generator and the comb amplifier is shared by all comb lines such that the power consumption per line still remains reasonable [96].

3.5 Summary

We have investigated the influence of the comb line power and optical carrier-to-noise ratio (OCNR) on the optical signal-to-noise ratio (OSNR) for comb-based WDM transmission systems. We identify two regimes of operation depending on whether the transmission performance is limited by the comb source (“source-limited”) or by the link and the associated in-line amplifiers (“link-limited”). Our analysis indicates that, depending on the number of spans, minimum comb line powers between -25 dBm and -15 dBm and minimum $\text{OCNR}_{\text{line}}$ values between 25 dB and 35 dB are needed for link-limited transmission. In addition, we investigated the impact of line-to-line power variations on the achievable OSNR and the overall link capacity for WDM system that relies on single-soliton Kerr frequency combs as a particularly interesting example. We find that OSNR levels of around 30 dB for Metro links lead to capacities of around 80 Tbit/s. We believe that our findings will help to broadly compare different comb generator types and to benchmark them with respect to the achievable transmission performance.

[end of paper [J3]]

4 DC-driven quantum-dash mode-locked laser diode for Tbit/s WDM transmission

This chapter details the data transmission experiments performed with a DC-driven quantum-dash (QD) mode-locked laser diode (MLLD) as a multi-wavelength light source at the transmitter. The content of this chapter is taken from a paper that has been published in Optics Express [J2]. In order to fit the structure and layout of this document, it was adapted accordingly.

The idea of the experiment was developed by P. Marin-Palomo and C. Koos. P. Marin-Palomo developed and implemented the experimental setups with the support of J. N. Kemal, P. Trocha, and S. Wolf. K. Merghem, and F. Lelarge developed and fabricated the QD-MLLDs for comb generation, under the supervision of A. Ramdane. The DSP required for the analysis of the received waveforms was performed by the author of this dissertation with the support of S. Randel. The manuscript was written by the author with the support of W. Freude, S. Randel, and C. Koos.

[start of paper [J2]]

Copyright © 2020 Optical Society of America

Comb-based WDM transmission at 10 Tbit/s using a DC-driven quantum-dash mode-locked laser diode

Optics Express, Volume 27, pages 31110-31129 (2019)

DOI: 10.1364/OE.27.031110

P. Marin-Palomo,¹ J. N. Kemal,¹ P. Trocha,¹ S. Wolf,¹ K. Merghem,² F. Lelarge,³ A. Ramdane,² W. Freude,¹ S. Randel,¹ and C. Koos^{1,4}

¹ Karlsruhe Institute of Technology, Institute of Photonics and Quantum Electronics, 76131 Karlsruhe, Germany

2. Centre de Nanosciences et de Nanotechnologies (CNRS), Univ. Paris-Sud, Univ. Paris-Saclay, C2N–Avenue de la Vauve, 91220 Palaiseau cedex, France
3. Almae Technologies, Route de Nozay, 91140 Marcoussis, France
4. Karlsruhe Institute of Technology, Institute of Microstructure Technology 76344 Eggenstein-Leopoldshafen, Germany

Chip-scale frequency comb generators have the potential to become key building blocks of compact wavelength-division multiplexing (WDM) transceivers in future metropolitan or campus-area networks. Among the various comb generator concepts, quantum-dash (QD) mode-locked laser diodes (MLLD) stand out as a particularly promising option, combining small footprint with simple operation by a DC current and offering flat broadband comb spectra. However, the data transmission performance achieved with QD-MLLD was so far limited by strong phase noise of the individual comb tones, restricting experiments to rather simple modulation formats such as quadrature phase shift keying (QPSK) or requiring hardware-based compensation schemes. Here we demonstrate that these limitations can be overcome by digital symbol-wise blind phase search (BPS) techniques, avoiding any hardware-based phase-noise compensation. We demonstrate 16QAM dual-polarization WDM transmission on 38 channels at an aggregate net data rate of 10.68 Tbit/s over 75 km of standard single-mode fiber. To the best of our knowledge, this corresponds to the highest data rate achieved through a DC-driven chip-scale comb generator without any hardware-based phase-noise reduction schemes.

4.1 Introduction

With the explosive growth of data rates across all network levels [2], wavelength-division multiplexing (WDM) schemes are becoming increasingly important for short transmission links that connect, e.g., data centers across metropolitan or campus-area networks. In this context, optical frequency combs have emerged as particularly attractive light sources, providing a multitude of narrowband optical carriers at precisely defined frequencies that may replace tens or even hundreds of actively stabilized laser diodes [78], [82], [85], [93]–[97]. Among the various comb generator concepts, chip-scale devices are of special interest, in particular when it comes to short-distance WDM links, for

which compactness and cost-efficient scalability to high channel counts is of utmost importance.

Over the previous years, a variety of chip-scale comb generators have been shown to enable high-speed WDM transmission at Tbit/s data rates. The highest performance was achieved by exploiting Kerr nonlinearities in integrated optical waveguides, either for spectral broadening of initially narrowband frequency combs [97] or for Kerr comb generation in high-Q microresonators [82], [85], [96]. While these approaches allow to generate hundreds of spectral lines distributed over bandwidths of 10 THz or more, the underlying setups are rather complex, require high pump power levels along with delicate operation procedures, and still comprise discrete components such as fiber amplifiers or external light sources. Other approaches to chip-scale comb generators rely on gain switching of injection-locked DFB lasers [14], [16], [17], which may be integrated into chip-scale packages with all peripheral components but suffer from the rather small bandwidth of the overall comb, which typically spans less than 500 GHz [14].

These limitations may be overcome by so-called single-section quantum-dash (QD) mode-locked laser-diodes (MLLD) [19], [61], [122]–[125], [69], [70], [101], [102], [118]–[121]. These devices combine an inhomogeneously broadened gain spectrum of the QD material with passive mode-locking through four-wave mixing and self-induced carrier density modulation [19], [61], [118] and allow for generation of broadband flat frequency combs without requiring a saturable absorber. QD-MLLD can be operated by a simple DC current while producing combs that can comprise 50 carriers or more, spaced by tens of GHz and distributed over a spectral range of more than 2 THz. However, the devices suffer from large optical linewidth of the individual tones, which strongly impairs transmission of signals that rely on advanced modulation formats [101], [119]–[122]. As a consequence, data transmission demonstrations with QD-MLLD have so far relied on intensity modulation of the optical carriers using, e.g., on-off-keying (OOK) [119] or electrical orthogonal frequency division multiplexing (OFDM) signals [120], were limited to rather simple modulation phase formats such as quadrature phase-shift keying (QPSK) [101], [121], [122], or

required dedicated hardware schemes for reducing the optical linewidth of the comb tones [69], [70], [102], [123].

In this work, we show that the phase-noise limitations of QD-MLLD-based WDM transmission schemes can be overcome by a continuous feed-forward algorithm based on symbol-wise blind phase search (BPS) [53] without the need for any additional optical hardware. Expanding on our earlier demonstrations [121], our concept allows for data transmission using 16-state quadrature amplitude modulation (16QAM), even in the presence of strong phase noise of the QD-MLLD tones. The viability of our concept is demonstrated in a series of transmission experiments. In a first experiment, we transmit 52 channels over 75 km of standard single-mode fiber (SSMF) using QPSK as a modulation format at a symbol rate of 40 GBd. By exploiting polarization-division multiplexing (PDM), we achieve an aggregate line rate (net data rate) of 8.32 Tbit/s (7.83 Tbit/s). In a second experiment, we use 38 carriers to transmit PDM-16QAM signals at a symbol rate of 38 GBd over 75 km of SSMF, leading to an aggregate line rate (net data rate) of 11.55 Tbit/s (10.68 Tbit/s). To the best of our knowledge, this is the highest data rate achieved by a DC-driven chip-scale comb generator that does not require any hardware-based phase-noise reduction schemes. Our investigation is supported by an in-depth analysis of the phase-noise characteristics of the QD-MLLD, revealing a strong increase of the FM-noise spectrum at low frequencies as the main problem that has prevented 16QAM transmission so far. Our results combined with the robustness and the ease of operating QD-MLLD show the great potential of such devices as light sources for highly scalable WDM transceivers.

4.2 Quantum-dash mode-locked laser diodes

The frequency comb sources used in our data transmission experiments consist of InAs/InGaAsP quantum-dash (QD) structures, which are grown by molecular beam epitaxy (MBE) on InP substrates [126]. The active region consists of six stacked layers of InAs QD, embedded into InGaAsP barriers, see Fig. 4.1(a). The InGaAsP composition is designed to have a bandgap corresponding to a photon energy $\lambda_g = 1.17 \mu\text{m}$, and the emission wavelength of the device used in

our experiments is approximately $1.55 \mu\text{m}$. Details of the dash-in-a-barrier design can be found in [19]. The thickness of the barrier between the QD layers amounts to 40 nm , and the structure is terminated by 80-nm -thick separate confinement heterostructure (SCH) layers of InGaAsP towards the top and bottom InP regions. Electrons are injected into the SCH layer from the n -side, corresponding to the bottom contact in Fig. 4.1(a), and are then trapped in the QD, emitting photons with a wavelength of approximately $1.55 \mu\text{m}$. The photons are guided in a buried ridge waveguide of $1.5 \mu\text{m}$ width [19]. Cleaved facets act as broadband front and backside mirrors, thereby forming a Fabry-Perot (FP) laser cavity with a total length of $980 \mu\text{m}$, corresponding to a free spectral range (FSR) of approximately 42 GHz . Due to the inhomogeneously broadened gain originating from the shape distribution of the QD, multiple longitudinal modes can coexist in the laser cavity. According to [126], mode-locking in QD-MLLD does not require a saturable absorber, but relies on mutual sideband injection due to four-wave mixing and self-induced carrier density modulation at the FSR frequency – similar to actively mode locked laser diodes, but induced by the signal generated from the beating among the laser cavity modes rather than by an external radio frequency (RF) source. This leads to a comb of equally spaced spectral lines with strongly correlated phases [127], thereby forming a periodic output signal with a period corresponding to the cavity round-trip time. The strong phase correlation of neighboring modes leads to a narrow RF beat note measured at the FSR frequency when detecting the periodic output signal with a high-speed photodetector.

To identify favorable parameters for operating the QD-MLLD in transmission experiments, we performed a thorough characterization of the devices using the setup shown in Fig. 4.1(b). The light emitted by the DC-driven QD-MLLD is collected by a lensed single-mode fiber (LF), which features an anti-reflection coating to avoid distortions by optical back-reflection into the laser cavity. The collected light is sent to an optical spectrum analyzer (OSA) and to a photodiode (PD), which is connected to an electrical spectrum analyzer (ESA) for extracting the RF beat note at the FSR frequency. In our experiment, we swept the pump current and recorded the fiber-coupled output power of the device along with the linewidth of the RF beat note and the optical spectrum, from which we extract the optical carrier-to-noise power ratio (OCNR) and the number of lines

within a 3-dB bandwidth of the comb, see Fig. 4.1(c) – 4.1(d). Figure 4.1(c) shows the full width half maximum (FWHM) linewidth of the RF beat note at the FSR frequency and the number of comb lines within the 3-dB bandwidth of the comb as a function of the injection current. The linewidth of the RF beat note decreases with higher injection current and reaches a constant value of approximately 10 kHz at high currents. Note that this decrease of the RF linewidth with injection current has been described in the literature [127], [128] and is attributed to the fact that mode-locking in the QD-MLLD relies on nonlinear interaction of the various modes, e.g., through four-wave mixing and carrier density modulation [126]. This interaction increases for higher optical power levels, i.e., higher injection currents, which leads to a decreased RF linewidth. Figure 4.1(d) shows the fiber-coupled output power and the average OCNR. The OCNR values are first determined individually for each comb line based on the optical spectrum of the frequency comb. As a reference bandwidth for specifying the OCNR, we choose 12.5 GHz, which corresponds to a wavelength span of 0.1 nm at a center wavelength of 1550 nm. Within the 3 dB-bandwidth of the comb, the OCNR of the lines exhibit only small variations of approximately ± 1 dB. The plot in Fig. 4.1(d) shows the mean OCNR averaged over all lines within the 3-dB bandwidth of the comb. The average OCNR increases with injection current and reaches an essentially constant level of approximately 40 dB above 300 mA.

From Fig. 4.1(c) and Fig. 4.1(d), we find that the output power, the number of lines and the OCNR monotonically increase with injection current, while the linewidth of the RF beat note decreases. For the transmission experiment, the injection current is hence chosen as high as possible without exceeding the current limit of the diode. As a favorable operation regime, we identify the range between 300 mA and 420 mA, which is shaded in red in Fig. 4.1(c) and Fig. 4.1(d). We repeated the measurement for other temperatures between 20 and 25 °C, observing a similar trend. Figure 4.1(e) shows the resulting frequency comb spectrum for an injection current of 390 mA at a stabilized temperature of 21.2 °C. Throughout the subsequent experiments, the injection current and operation temperature of the laser are kept constant to avoid drift of the center frequency of the generated combs. The accuracy of this stabilization

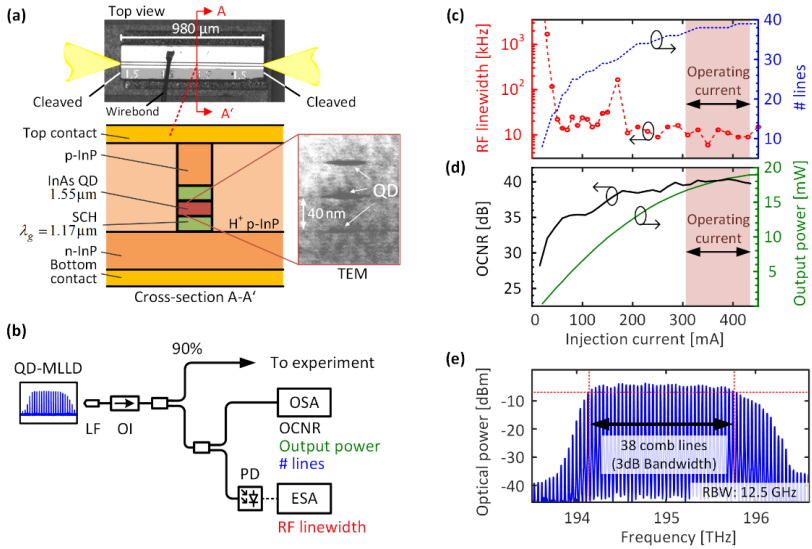


Figure 4.1. Frequency-comb generation in quantum-dash mode-locked laser diodes (QD-MLLD). **(a)** Top view and cross-section schematic of a QD-MLLD consisting of a ridge waveguide of $1.5 \mu\text{m}$ width and $980 \mu\text{m}$ length. The active region comprises six stacked layers of InAs QD separated by 40 nm -thick InGaAsP barriers, see transmission-electron microscope (TEM) image in the Inset [19]. Carriers are injected into the active region through 80-nm -thick separate confinement heterostructure (SCH) layers of InGaAsP, designed to have a bandgap corresponding to a photon energy $\lambda_g = 1.17 \mu\text{m}$. The emission wavelength of the devices used in our experiments is approximately $1.55 \mu\text{m}$. **(b)** Setup for frequency comb characterization. The QD-MLLD is driven by a DC current. LF: Lensed fiber. OI: Optical isolator. PD: Photodiode. ESA: Electrical spectrum analyzer. OSA: Optical spectrum analyzer. **(c)** Number of lines within the 3-dB bandwidth of the comb (blue) and FWHM of the RF beat note (“RF linewidth”, red) at the FSR frequency of 42 GHz as a function of injection current. **(d)** Optical output power (green) and average OCNR (black) of the comb lines as a function of injection current. Shaded region: Range of favorable operating currents for low RF linewidth, high output power and OCNR, and large number of lines. **(e)** QD-MLLD frequency comb spectrum for an injection current of 390 mA at a stabilized temperature of $21.2 \text{ }^\circ\text{C}$.

amounts to $\pm 0.1 \text{ K}$ for the operating temperature and to $\pm 0.1 \text{ mA}$ for the injection current. For coherent communications, the carriers used to transmit data need to have high OCNR and narrow optical linewidths, or, equivalently, low phase noise. The recorded OCNR level would in principle safely allow for

transmission of 16QAM signals at symbol rates of 50 GBd or more [129]. However, the individual comb tones exhibit strong phase noise, which inhibits the use of advanced modulation formats with high spectral efficiency. In the case of strong phase noise, there is a high probability that the induced phase change causes a wrong recovery of the symbol, thus dramatically increasing the bit-error ratio (BER), even at high OCNR. In the next section, we present a more detailed analysis of the phase noise for individual carriers of the QD-MLLD, whilst Section 4.4 contains an analysis of the impact of phase noise on the measured BER for QPSK and 16QAM signaling.

4.3 Phase noise characteristics of QD-MLLD

The optical tones of the QD-MLLD are broadened by several effects [130]. Fundamentally, laser linewidth broadening is caused by the coupling of spontaneous emission into the oscillating mode, leading to spectrally white frequency noise. Other effects such as flicker and random-walk frequency noise contribute to linewidth broadening, too, and occur at longer time scales [51], [52], i.e., lower frequencies. Influences of temperature fluctuations and mechanical vibrations happen on an even larger time scale and are disregarded. In the following, we differentiate between short-term and long-term phase noise, leading to a short-term and a long-term linewidth of the comb tone. Short-term phase fluctuations are characterized by a white frequency-noise spectrum and lead to a Lorentzian laser line shape with a FWHM Δf_L , while long-term phase fluctuations lead to a Gaussian spectrum with FWHM Δf_G [51]. For the devices used in our measurements, the long-term linewidth is observed when considering the frequency fluctuations for observation times $\tau_0 \square 1 \mu\text{s}$, whereas the short-term linewidth is obtained for observation times $\tau_0 \square 1 \mu\text{s}$, see Section 4.3.1 for a more detailed discussion.

For measuring the short-term and long-term optical linewidths of the individual comb lines, we follow two different heterodyne approaches, which are illustrated in Fig. 4.2(a), Setup I and Setup II. In Setup I, the QD-MLLD output is superimposed with the output of a highly stable tunable local-oscillator laser (LO I) and then sent to a photodetector connected to an ESA for recording the beat-note spectrum and the long-term linewidth. In Setup II, we use a second

tunable local oscillator laser (LO II) along with a coherent receiver and high-speed analog-to-digital converter (ADC). The ADC is used to record the RF beat note, from which the intrinsic Lorentzian, i.e., short-term linewidths are extracted by offline processing of the signals [51], see Section 4.3.2. Both LO I and LO II are external-cavity lasers (ECL, Keysight N7714A) with a specified linewidth below 100 kHz, i.e., the LO linewidths are much smaller than the expected linewidth of the comb lines. This is verified by connecting LO I to Input II (Inp II) of Setup II, and LO II to Input I (Inp I) of Setup I and by observing that in both cases the resulting linewidths of the beat notes are much smaller than those obtained from the QD-MLLD tones, see Fig. 4.2(b). Note that these measurements can only reveal the relative phase fluctuations of LO II with respect to LO I, which can be considered as an upper boundary of the phase noise of each of the sources. In the following sections, we detail a quantitative phase-noise model, Section 4.3.1, and use it to extract the QD-MLLD phase-noise characteristics from the measurements obtained from Setup I and Setup II, Sections 4.3.2 and 4.3.3.

4.3.1 Phase-noise and linewidth model

In the following, we give a short overview on the model used for quantitatively describing the phase noise of the MLLD tones. More details of the underlying theoretical background and a derivation of the mathematical relationships can be found in [131]. The complete statistical characteristics of the phase noise or, equivalently, the frequency noise of a laser oscillator can be obtained from the so-called FM-noise spectrum $S_{f_{\text{inst}}}$, i.e., the power-spectral-density function of the instantaneous optical frequency fluctuations $f_{\text{inst}}(t)$, which can be modeled by [132], [133]

$$S_{f_{\text{inst}}}(f) = S_L + S_1 f^{-1} + S_2 f^{-2} \quad (4.1)$$

This power spectral density is composed of spectrally constant white frequency noise $S_L f^0$, flicker frequency noise $S_1 f^{-1}$, and random-walk frequency noise $S_2 f^{-2}$. In these relations, the quantities S_L , S_1 and S_2 are constant coefficients quantifying the various frequency noise contributions.

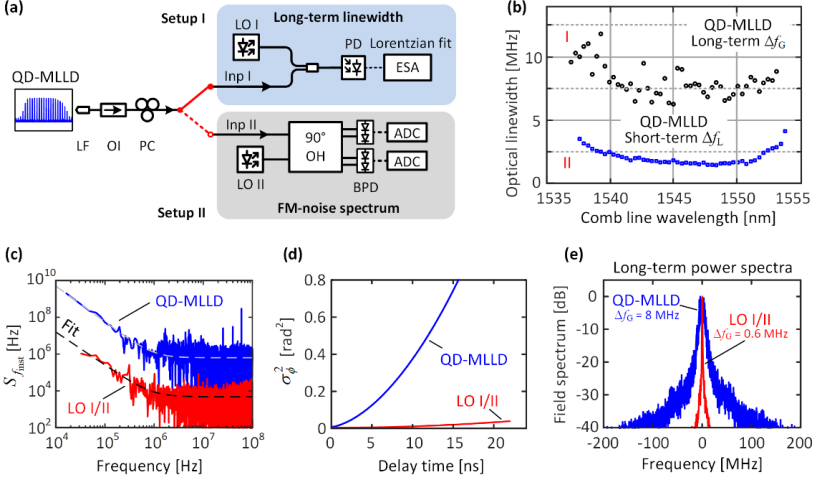


Figure 4.2. Linewidth measurement and phase-noise characterization for selected comb lines of the QD-MLLD. **(a)** Experimental setups: In Setup I, the QD-MLLD output is superimposed with the output of a narrowband local oscillator laser (LO I) and detected by a single photodiode (PD) and an electrical spectrum analyzer (ESA) to extract the long-term linewidth Δf_G . In Setup II, a second LO laser (LO II) is used along with a coherent receiver and a high-speed analog-to-digital converter (ADC) for measuring the temporal phase-noise characteristics, from which we extract the FM-noise spectrum that reveals the intrinsic Lorentzian linewidth Δf_L . LF: Lensed fiber. OI: Optical isolator. PC: Polarization controller. LO I, LO II: Tunable external cavity lasers (ECL). OH: Optical hybrid. BPD: Balanced photodiodes. Inp I, Inp II: Auxiliary inputs for verification of the LO laser linewidths. **(b)** Long-term and short-term optical linewidths of the different comb lines. The long-term linewidths were recorded with an effective ESA observation time of $\tau_{0, \text{ESA}} \approx 150 \mu\text{s}$. **(c)** Power spectra $S_{f_{\text{inst}}}$ of instantaneous frequency fluctuations (FM noise) along with model fits according to Eq. (4.1). The length of the recorded time-domain beat signal is 125 μs . The data were obtained by testing a QD-MLLD tone with Setup II (QD-MLLD, blue) or by connecting LO I to Inp II of Setup II (LO I/II, red). In both cases, the wavelength of the tested tone was 1547.3 nm. Note that the second measurement can only reveal the relative phase fluctuations of LO II with respect to LO I, which can be considered as an upper boundary of the phase noise of each of the sources. Since the linewidth of LO I is much smaller than that of the QD-MLLD tone, the phase fluctuations in the first measurement can be attributed to the QD-MLLD tone. **(d)** Phase-noise variance σ_ϕ^2 as a function of measurement time τ , both for LO I and for the QD-MLLD tone. **(e)** Power spectra as a function of the frequency offset from the carrier for LO I and for the QD-MLLD tone (resolution bandwidth $\delta f = 400 \text{ kHz}$).

The FM-noise spectrum can be separated into two areas that influence the measured line shape in distinctively different ways, depending on the observation time. For long observation times, the measured linewidth will be dictated by FM-noise components at low Fourier frequencies, where flicker and random-walk frequency noise dominates. Specifically, the resulting line can be approximated by a Gaussian if the line shape is dominated by frequency noise at Fourier frequencies f smaller than a frequency f_{high} defined by [131]

$$S_{f_{\text{inst}}}(f_{\text{high}}) = (8f_{\text{high}} \ln 2) / \pi^2. \quad (4.2)$$

The spectral power of the frequency noise beyond this point does usually not influence the center part of the line shape [131]. Towards smaller Fourier frequencies, the lowest frequency f_{low} that can be considered in a given measurement is dictated by the observation time $\tau_0 = 1/f_{\text{low}}$. For $f_{\text{high}} > 5f_{\text{low}}$, a good approximation of the long-term FWHM linewidth is then [131]

$$\Delta f_G = [8 \ln(2) A]^{1/2}, \quad (4.3)$$

where the parameter A corresponds to the spectral power of the frequency noise between f_{low} and f_{high} ,

$$A = \int_{f_{\text{low}}}^{f_{\text{high}}} S_{f_{\text{inst}}}(f) df \quad (4.4)$$

Note that in the presence of flicker or random-walk frequency noise, A increases with decreasing lower frequency limit f_{low} , i.e., the measured long-term linewidth increases with increasing measurement duration $\tau_0 = 1/f_{\text{low}}$.

In contrast to that, the observed line shape is Lorentzian if the observation time is chosen short enough, i.e., if the lower frequency limit f_{low} is high enough to exclude the impact of flicker and random-walk frequency noise. The relevant part of the FM-noise spectrum can then be considered white, and the intrinsic Lorentzian linewidth Δf_L is directly proportional to the constant spectral power density S_L of the frequency noise [51],

$$\Delta f_L = \pi S_L. \quad (4.5)$$

Note that in this case, the measured linewidth is independent of the exact observation time τ_0 .

These considerations allow us to give a more precise definition of the terms “long-term linewidth” and “short-term linewidth” introduced earlier. The long-term linewidth Δf_G is observed for observation times $\tau_0 \gg \tau_{\text{low}} = 1/f_{\text{high}}$ (usually $\tau_0 > 5\tau_{\text{low}}$), where f_{high} is obtained from Eq. (4.2). For $\tau_0 \ll \tau_{\text{low}}$, the short-term linewidth, i.e., the intrinsic Lorentzian linewidth Δf_L is found. Measuring the FM-noise spectrum of the QD-MLLD tones and fitting Eq. (4.1) to the measurement allows us to obtain both the intrinsic linewidth Δf_L , see Section 4.3.2, the long-term linewidth Δf_G , see Section 4.3.3, and the parameter $\tau_{\text{low}} \approx 1 \mu\text{s}$, which corresponds to the observation time that roughly marks the transition between the two regimes. Alternatively, the long-term linewidth Δf_G can be extracted by means of an ESA that records the beat-note spectrum of the comb tone with the tone emitted by LO I, see Section 4.3.3.

The results of the linewidth measurements are shown in Fig. 4.2(b) with short-term linewidths Δf_L ranging from approximately 1.5 MHz at the center of the frequency comb to 4 MHz at the edges, and long-term linewidths Δf_G ranging from 7 MHz at the center to 12 MHz at the edges. The increase of the linewidths towards the edges of the comb spectrum is related to the timing jitter of the periodic signal generated by the QD-MLLD [118]. The long-term linewidths in the comb center are in good agreement with the values found in [118].

4.3.2 Short-term linewidth from measured FM-noise spectrum

The intrinsic Lorentzian linewidth Δf_L for each line of the frequency comb is obtained from the FM-noise spectrum $S_{f_{\text{inst}}}$ using Eqs. (4.1) and (4.5). To measure $S_{f_{\text{inst}}}$, we first recover the in-phase (I) and quadrature (Q) component of the electric field of individual comb carriers with a coherent receiver [51], [134], [135] using Setup II of Fig. 4.2(a). In these measurements, LO II is tuned to generate an I and a Q beat signal with the respective comb line at an intermediate frequency of approximately 1 GHz. This choice of intermediate frequency guarantees that the beat note with an FWHM of the order of a few tens of MHz does not extend to negative frequencies, thereby avoiding impairment by spectral foldback. The time-dependent phase differences between the LO tone and

the comb tone are derived from the I and the Q signals, and the frequency offset is removed by fitting the time-dependent increase of the phase with a linear function. The time-dependent random phase fluctuations $\phi(t)$ are then obtained from the difference of the measurement data and the linear fit. To extract the associated instantaneous frequency fluctuation $f_{\text{inst}}(t)$, we compute the time-derivative of the measured phases,

$$2\pi f_{\text{inst}}(t) = \frac{d\phi(t)}{dt} \approx \frac{\phi(t + \tau_s) - \phi(t)}{\tau_s}, \quad (4.6)$$

where $\tau_s = 12.5$ ps denotes the sampling period of our ADC (Keysight, DSO-X 93204A). The length of the recorded time-domain beat signal is 125 μ s. The FM-noise spectrum $S_{f_{\text{inst}}}$ is obtained by computing the autocorrelation function of $f_{\text{inst}}(t)$ and by taking its Fourier transform [51], see Fig. 4.2(c), blue trace. As a reference, we also record the relative phase fluctuations of LO I with respect to LO II, see Fig. 4.2(c), red trace. The relative phase fluctuations of LO I and LO II are significantly smaller than the phase fluctuations observed in the QD-MLLD measurement, and we can conclude that the linewidth of the LO does not deteriorate our measurements.

To extract the model parameters S_L , S_1 and S_2 of Eq. (4.1) from our measurements, we perform a parameter fit of the model prediction to the measured data. The fitting procedure comprises several steps: For smoothing the measured FM-noise spectrum, we used a moving-average filter for which the length increases with frequency. We start from a filter length of 1 tap, i.e., no averaging, at Fourier frequencies of up to 70 kHz and then increase the filter length exponentially to 800 taps at a Fourier frequency of 100 MHz. This approach was necessary to maintain the strong increase of the FM-noise spectrum towards low frequencies (< 100 kHz) while effectively reducing the uncertainties at higher frequencies (> 1 MHz). Prior to fitting the smoothed data, we re-sample it to obtain points that are equidistant with respect to the logarithm of the Fourier frequency. This avoids a situation where the least-squares errors of the fit are dominated by the noisy high-frequency part of the spectrum while the physically relevant low-frequency part does not play a role. The results of the fit are robust with respect to the choice of initial fitting parameters and of the tap number that the averaging filter uses towards high frequencies. For the MLLD tone, we obtain

$S_L = 5.9 \times 10^5$ Hz, $S_1 = 9.4 \times 10^{11}$ Hz² and $S_2 = 2.3 \times 10^{17}$ Hz³, leading to an intrinsic Lorentzian linewidth $\Delta f_L = 1.9$ MHz. We repeat the measurement for different QD-MLLD lines, see Fig. 4.2(b). For the beat of LO I with LO II, we find $S_L = 4.0 \times 10^3$ Hz, $S_1 = 3.2 \times 10^9$ Hz², and $S_2 = 2.2 \times 10^{15}$ Hz³, leading to an intrinsic linewidth of the measured beat note of 12 kHz.

Note that the intrinsic linewidth Δf_L can also be inferred from the delay-dependent phase differences $\Delta\phi_\tau(t) = \phi(t + \tau) - \phi(t)$ and the associated phase-noise variance [51]

$$\sigma_{\Delta\phi}^2(\tau) = \left\langle \Delta\phi_\tau(t)^2 \right\rangle. \quad (4.7)$$

This involves calculating the slope of $\sigma_{\Delta\phi}^2(\tau)$ close to $\tau = 0$ [51],

$$\Delta f_L = \lim_{\tau \rightarrow 0} \frac{\sigma_{\Delta\phi}^2(\tau)}{2\pi\tau}. \quad (4.8)$$

To reliably extract this slope, we first fit a parabola to the measured phase-noise variances $\sigma_{\Delta\phi}^2(\tau)$ of the QD-MLLD (blue) and of LO I/II (red) in Fig. 4.2(d) and then take the derivative of the fitted function at $\tau = 0$. The values are consistent with the linewidths obtained from the measured FM-noise spectra according to Eqs. (4.1) and (4.5).

4.3.3 Long-term linewidth measurement

The long-term linewidth Δf_G is measured using the heterodyne setup shown in Fig. 4.2(a), Setup I. To this end, we tune LO I close to a comb line of the QD-MLLD and detect the superposition of both on a PD. The spectrum of the resulting photocurrent is centered about the difference frequencies of the comb line and the tone emitted by LO I and is measured using an electrical spectrum analyzer (ESA).

For better comparison of the results obtained from the ESA measurement to the long-term FWHM linewidths extracted from Eq. (4.3), we estimate the effective observation time $\tau_{0,\text{ESA}}$ that has to be assigned to the ESA measurement. For a given frequency span Δf , the effective observation time $\tau_{0,\text{ESA}}$ that is needed

to record this span using the ESA is dictated by the resolution bandwidth δf [136],

$$\tau_{0,\text{ESA}} = \kappa \frac{\Delta f}{\delta f^2}, \quad (4.9)$$

where κ denotes the proportionality constant that depends on the specific ESA model. For our system (Keysight N9030A), a value between $\kappa = 2$ and $\kappa = 3$ is specified [136], and we assume $\kappa = 2.5$. Thus, for a resolution bandwidth of $\delta f = 400 \text{ kHz}$, we obtain an effective observation time of approximately $\tau_{0,\text{ESA}} = 150 \mu\text{s}$ that is needed to record the approximately 10 MHz-wide beat note between the comb tone and LO I.

In our measurements, we select different comb lines by tuning LO I, see Fig. 4.2(b). In these measurements, two important requirements need to be fulfilled: First, the resulting intermediate frequency must be much larger than the expected spectral half width of the investigated comb line. This is ensured by choosing an intermediate frequency of approximately 1 GHz. Second, the phase fluctuations of the LO must be much smaller than those expected for the investigated comb line. The validity of this assumption was already assured when recording the frequency noise spectrum, see Section 4.3.2.

The long-term linewidth is extracted by evaluating the FWHM of a model function that is fit to the measured spectra. In general, the line-shape is described by a Voigt function, i.e., a convolution of a Lorentzian and a Gaussian [52], [137]. This function, however, may be approximated by a Gaussian near the line center [52]. In our analysis we have investigated the impact of fitting both types of curves to the measured data. Both fits lead to virtually the same results for Δf_G with deviations of less than 5%. The long-term linewidths indicated in Fig. 4.2(b) are obtained from the Voigt function. For a QD-MLLD tone close to 1547.3 nm, we obtain a long-term linewidth Δf_G of approximately 8 MHz, Fig. 4.2(e), blue curve.

As a check, we also re-confirm that the linewidth of LO I can be neglected by measuring the long-term optical linewidth of the beat note between LO I and LO II using Setup I, leading to $\Delta f_G = 0.6 \text{ MHz}$ for an ESA resolution bandwidth of $\delta f = 400 \text{ kHz}$, see Fig. 2(e), red curve. We further compare the long-

term linewidth obtained from the ESA measurement to that extracted from the fitted FM-noise spectrum. To this end, we use Eqs. (4.3) and (4.4) which, for $S_L = 4.0 \times 10^3$ Hz, $S_1 = 3.2 \times 10^9$ Hz², $S_2 = 5.0 \times 10^{17}$ Hz³, $f_{\text{low}} = 1/\tau_{0,\text{ESA}} = 8$ kHz, and $f_{\text{high}} = 1/\tau_{\text{low}} = 2$ MHz lead to a long-term linewidth Δf_G of approximately 14 MHz. This is in good agreement with the width obtained from the directly measured line shape.

4.4 Coherent transmission using QD-MLLD

In this section, we first investigate the effect of the inherent phase noise of QD-MLLD carriers on coherent data transmission for different modulation formats and symbol rates, see Section 4.4.1. We show that symbol-wise blind phase search (BPS) [53], relying on continuous feed-forward estimation and correction of the instantaneous phase difference between the LO tone and the carrier, substantially improves the transmission performance of the QD-MLLD and finally enables the use of 16QAM signaling, see Fig. 4.3. Details of the phase tracking algorithm are described in Section 4.4.2.

As a reference, we use the transmission performance obtained by block-wise carrier phase recovery (CPR) which is part of the Vector Signal Analyzer (VSA) software offered by Keysight Technologies (89600 series VSA software) [138]. In this approach, received symbols are processed in blocks, within which a certain frequency offset and an otherwise constant phase difference between the LO tone and the carrier are corrected. To this end, the phases of symbols in a block are extracted and unwrapped. The frequency offset is then extracted from a linear regression of the time dependence of the unwrapped phases. Details can be found in [138]. Note that this block-wise CPR does not allow for dynamic phase tracking. We further benchmark the results obtained from the MLLD by replacing the comb tone by an ECL carrier with an intrinsic linewidth of approximately 10 kHz. For optical signal-to-noise power ratios (OSNR) of 25 dB or less that are typically found at the receivers of 16QAM transmission links [139], the transmission performance achieved with QD-MLLD tones in combination with BPS is comparable to that offered by high-quality ECL carriers.

In Sections 4.4.3 and 4.4.4, we present a series of transmission experiments demonstrating the ability of the symbol-wise BPS scheme to compensate for the phase noise of the QD-MLLD tones. In a first experiment, we transmit 52 channels spaced by 42 GHz over 75 km of standard single-mode fiber (SSMF) using QPSK as a modulation format, see Section 4.4.3. Using polarization-division-multiplexing (PDM), we achieve an aggregate line rate of 8.32 Tbit/s, which reduces to a net data rate of 7.83 Tbit/s when considering a 6.25 % overhead necessary for hard-decision forward error correction (FEC) of BER values below 4.7×10^{-3} [140]. In a second experiment, we use 38 carriers to transmit PDM-16QAM signals over 75 km of SSMF at an aggregate line rate of 11.55 Tbit/s, which corresponds to a net data rate of 10.68 Tbit/s when accounting for a FEC overhead of 6.25 % for 32 channels and of 20 % for the remaining six channels [140], see Section 4.4.4. This corresponds to the highest data rate achieved by a DC-driven chip-scale comb generator without any additional hardware-based phase-noise reduction [69], [70], [102], [123].

4.4.1 Influence of comb-carrier linewidth and OSNR on coherent communications

To quantify the influence of the linewidth of the QD-MLLD comb lines on coherent transmission, we measure the BER at different symbol rates for both QPSK and 16QAM. The experimental setup is depicted in Fig. 4.3(a). After amplification of the frequency comb by EDFA1 to an output power of 17 dBm, we filter the comb line of interest using a programmable optical filter (POF). A 3dB-bandwidth of approximately 10 GHz of the POF is chosen to effectively suppress all neighboring comb lines. The filtered carrier, centered at a wavelength of 1540.4 nm, is amplified to a power of 24 dBm and sent through an IQ modulator. The phase-noise properties of this carrier are essentially the same as those of the carrier at 1547.3 nm, which is analyzed in detail in Figs. 4.2(c) – 4.2(e). The modulator drive signal is synthesized by an arbitrary-waveform generator (AWG) based on a pseudo-random bit sequence (PRBS) of length $2^{11} - 1$. The bit sequence is mapped to either QPSK or 16QAM symbols with pulses having a raised-cosine (RC) spectrum with a 5 % roll-off for QPSK and 10 % for 16QAM. PDM is emulated by splitting the data signal and decorrelating the split signals in time by approximately 5.3 ns using a delay line

(DL) [82]. Finally, both signals are combined in orthogonal polarization states using a polarization beam combiner (PBC). To adjust the OSNR of the signal, a noise-loading stage (ASE source) is used. The signal is then sent to the receiver, where it is further amplified by EDFA3 and EDFA4. Bandpass filters (BPF) are used to suppress out-of-band noise after each amplifier. The signal is finally detected by an optical modulation analyzer (OMA, Keysight N4391A) acting as a dual-polarization coherent receiver (DP-CR) with built-in local oscillator (LO) laser. The intrinsic linewidth of the LO is approximately 10 kHz. The output of the DP-CR is digitized by a 4-channel 80 GSa/s real-time oscilloscope (two synchronized Keysight DSO-X 93204A) and recorded for offline digital signal processing (DSP). The digitized signal undergoes a number of DSP steps, comprising timing recovery, MIMO equalization, frequency offset compensation, carrier phase compensation, and decoding, see Section 4.4.2 for details.

The measured signal quality parameters are summarized in Fig. 4.3(b) and 4.3(c) for QPSK and 16QAM signals. In these plots, green traces represent the results obtained from using block-wise CPR ('MLLD/block-wise CPR') as implemented in Keysight's VSA software [138]. In this analysis, the block length was varied between 100 and 200 symbols, depending on the symbol rate. The blue traces are obtained using continuous feed-forward symbol-wise BPS algorithm ('MLLD/symbol-wise BPS') [53], see Section 4.4.2 for details. The red traces ('ECL') are obtained by repeating the experiment using a narrowband ECL as an optical source. The ECL is tuned to the same wavelength as the comb tone and has an intrinsic linewidth of approximately 10 kHz, and we can hence assume that the transmission performance is not impaired by phase noise. This is confirmed by observing that block-wise CPR and symbol-wise BPS lead to the same result for the ECL-based transmission. For QPSK, Fig. 4.3(b), the limited recording length did not contain enough errors for a statistically reliable measurement of the BER. We therefore use the error vector magnitude (EVM) rather than the BER as a performance metric [129]. Assuming that the signals are impaired by additive white Gaussian noise only, the measured EVM would correspond to BER values below 10^{-10} [129]. Note that the EVM can be defined in two different ways depending on the normalization, which either refers to the maximum field in the constellation, or to the average field resulting from

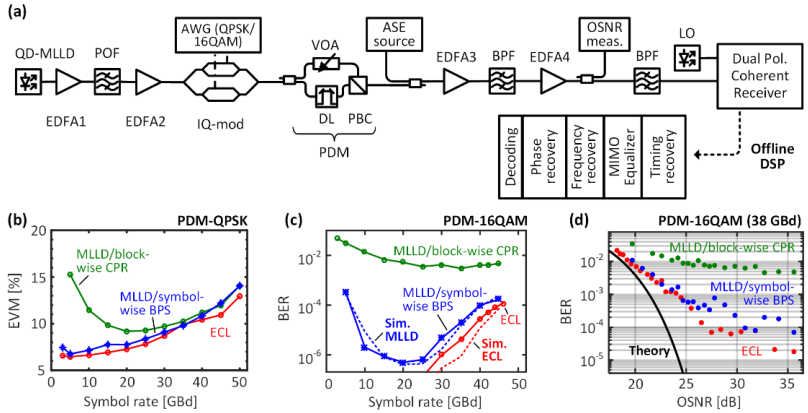


Figure 4.3. Influence of phase noise on coherent transmission at different symbol rates, modulation formats, and OSNR values. The analysis relies on using a single comb line with an intrinsic linewidth of 1.9 MHz as a carrier at a wavelength of 1540.4 nm. As a reference, we use a narrowband optical carrier provided by an ECL with an intrinsic linewidth of ~ 10 kHz. The transmission performance of the ECL tone is compared to that of the QD-MLLD tone using either block-wise CPR (MLLD/block-wise CPR) or symbol-wise BPS (MLLD/symbol-wise BPS). **(a)** Experimental setup. EDFA: Erbium-doped fiber amplifier. POF: Programmable optical filter. IQ-mod: In-phase/quadrature (IQ) modulator. AWG: Arbitrary waveform generator. PDM: Polarization division multiplexing. VOA: Variable optical attenuator. OSNR meas.: Optical signal-to-noise-ratio measurement unit. DL: Delay line. PBC: polarization beam combiner. ASE: Amplified spontaneous emission. BPF: Band-pass filter. LO: Local oscillator. **(b)** Error-vector magnitude (EVM) measured for PDM-QPSK signaling at different symbol rates. For QPSK, we did not find a sufficient number of errors within our limited recording lengths and can hence only provide the EVM. We find that symbol-wise BPS algorithm can essentially overcome the phase-noise-related limitations observed for block-wise CPR and bring the transmission performance of the MLLD tone close to that of a narrowband ECL tone. **(c)** BER results for PDM-16QAM signaling for different symbol rates. In these measurements, the OSNR was around 35 dB. For practically relevant symbol rates beyond 30 GBd, symbol-wise BPS can essentially overcome the phase-noise-related impairments. The measured BER values fit well to the simulation results (dashed lines) labelled “Sim. MLLD” and “Sim. ECL”. **(d)** BER results for PDM-16QAM signaling at 38 GBd for different OSNR values. The OSNR values are measured after EDFA 4, see Subfigure (a). For OSNR values of 25 dB or less, symbol-wise BPS allows the QD-MLLD tone to perform nearly as good as a narrowband ECL carrier with OSNR penalties of approximately 0.5 dB.

summing the power of all possible symbols [44]. Here, we refer to the second definition, i.e., we normalize the EVM to the average field. For 16QAM, we measure the BER directly.

Generally, the impact of phase noise increases with decreasing symbol rates, i.e., longer optical symbol periods, which leads to an increase of the EVM or the BER at low symbol rates for the QD-MLLD experiments with block-wise CPR, see green traces in Fig. 4.3(b) and 4.3(c). At high symbol rates, the signal quality is impaired by the decreasing SNR and by the bandwidth limitations of our AWG, leading to higher EVM and BER. Using the symbol-wise feed-forward BPS, the impact of phase noise can be greatly reduced, both for QPSK and 16QAM, see blue traces. For QPSK, the transmission performance comes close to that of the narrowband ECL, illustrated by the red trace. 16QAM is generally more sensitive to phase noise than QPSK, since more phases need to be discriminated. In this case, at low symbol rates, even the symbol-wise BPS is not capable of compensating the complete impact of phase noise. Still, the performance of the QD-MLLD experiments with symbol-wise BPS does not show any substantial penalty compared to that of the ECL-based transmission at practically relevant symbol rates of 30 GBd or more.

To quantitatively confirm the results depicted in Fig. 4.3(c), we have performed simulations of 16QAM transmission at different symbol rates. In these simulations, we neglect low-frequency FM noise and only consider the spectrally white part of the FM-noise spectrum. To this end, we model the underlying phase fluctuations as a Wiener process where the variance of the stochastic phase increments is chosen to produce an intrinsic linewidth of 1.9 MHz for the QD-MLLD carrier and of 10 kHz for the ECL carrier. We further consider additive white Gaussian noise (AWGN), modeling the noise contributions of the optical amplifiers and the receiver electronics. The AWGN level used in each simulation is obtained from the signal-to-noise ratio (SNR) of the measured data signals. The dashed lines in Fig. 4.3(c) show the simulation results, which are in good agreement with their measured counterparts.

Finally, we measure the BER as a function of the OSNR, see Fig. 4.3(d), for 16QAM and a symbol rate of 38 GBd, which is used for the high capacity WDM transmission experiment, see Section 4.4.4. In this measurement, we again

compare the QD-MLLD with block-wise phase recovery (green trace) and symbol-wise phase tracking (blue trace) as well as the ECL reference (red trace). For a BER of 4.7×10^{-3} , corresponding to the threshold for hard-decision FEC with 6.25 % overhead [140], the implementation penalty amounts to approximately 0.9 dB for ECL-based transmission and to approximately 1.4 dB for the MLLD tone. The penalty of the MLLD tone with respect to the ECL carrier hence amounts to approximately 0.5 dB. This value is not only found at the FEC threshold, but more generally for all OSNR values of less than 25 dB. Thus, under realistic transmission conditions [139], the carriers of the QD-MLLD comb source perform similarly as a high-quality individual ECL carrier. The slightly lower performance of the MLLD tone observed at high OSNR beyond 25 dB, see Fig.4.3(d), is attributed to residual phase noise that is still left after phase tracking [53]. This is confirmed by the simulation results shown in Fig. 4.3(c), which reproduce the measured BER performance both for the MLLD and the LO carrier by accounting for the measured linewidth of the respective carrier and by assuming OSNR levels between 20 dB and 25 dB. For the simulation, the OSNR level of each channel is derived from the SNR of the measured data signal.

4.4.2 Data recovery using feed-forward symbol-wise blind phase search

The continuous feed-forward algorithm for symbol-wise phase tracking was implemented in Matlab following the scheme introduced by Pfau *et al.* [53]. It is part of a multi-step DSP procedure, see Inset of Fig. 4.3(a). First, the signal is resampled to two samples per symbol followed by timing recovery [37], [38]. A 30-tap MIMO equalizer based on the constant-modulus algorithm (CMA) is then used to demultiplex the two orthogonal polarizations of the signal and to compensate for linear transmission impairments [39]. The received symbols from the MIMO equalizer then undergo frequency-offset correction [141]. For QPSK, the 4th-power of the received symbols is calculated to remove the information of the modulated phase. This leaves only the rapidly increasing phase caused by the frequency offset between signal carrier and LO. The frequency offset is then corrected by fitting a linear curve to the unwrapped phase as a function of time and by subtracting the fitted curve from the measured phase

offset. For the case of 16QAM signaling, the 4th-power scheme can be adapted by QPSK-partitioning [40]. Once the carrier frequency offset is compensated, carrier phase noise compensation is carried out based on a “symbol-wise” BPS algorithm [53].

The BPS algorithm starts with selecting a group of N complex symbols which are centered around the symbol of interest. The phases of these complex symbols are then modified by adding identical test phases ϕ_t . The test phases are varied, and the sum of the squares of the N Euclidean distances of the measured symbols to their closest constellation points in the complex plane is measured. The optimum phase is determined by searching the minimum value of this sum [53]. Note that for symbol-wise BPS, the group of symbols used for phase estimation is slid along with the symbol of interest such that an individual phase correction term is computed for each symbol. This is in contrast to “block-wise” phase recovery, where all symbols within a block are treated with the same phase-correction parameter. For evaluating our measurements, we apply 45 equidistant test phases for covering an unambiguity range of $\pm 45^\circ$ for an M -QAM signal with a quadratic constellation.

As a rough estimate, a symbol-wise phase tracking technique relying on averaging of measured phases over a moving group of N symbols can effectively suppress frequency noise components occurring at Fourier frequencies up to $f = 1/NT_S$, where T_S corresponds to the symbol duration. This is confirmed by simulating 16QAM transmission at a symbol rate of 38 GBd, an intrinsic linewidth of the carrier of $\Delta f_L = 1.9$ MHz, and an OSNR of 35 dB, see Fig. 4.4. In this simulation, we perform BPS with different averaging lengths N and then extract the residual phase error of the various symbols with respect to the respective ideal constellation point. The residual instantaneous frequency fluctuations $f_{\text{inst}}(t)$ are then extracted from this time series of phase errors using the relation given in Eq. (4.6), and the FM-noise spectrum is derived by taking the Fourier transform of the autocorrelation function of $f_{\text{inst}}(t)$. The FM-noise spectra for different averaging lengths are then compared to the FM-noise spectrum of the carrier prior to modulation, indicated by a blue trace in Fig. 4.4. For $N = 10$ (red trace) we find that the frequency noise is effectively suppressed for Fourier frequencies smaller than approximately 4 GHz, whereas for $N = 100$

symbols (green trace), the suppression is only effective up to approximately 400 MHz, thus confirming the above-mentioned rule. Note that for $N = 10$, we observe a slight increase of the frequency noise level towards higher Fourier frequency. We attribute this to the impact of additive white Gaussian noise which may distort the phase recovery for small N . Note that Flicker and random-walk frequency would occur at Fourier frequencies below 1 MHz, see Fig. 4.2(c), and would hence also be effectively suppressed by BPS.

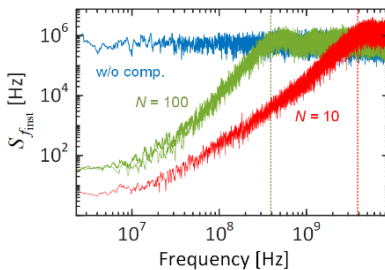


Figure 4.4. FM- noise compensation by blind-phase search (BPS) for different averaging lengths N : In the simulation, we assume 16QAM transmission at a symbol rate of 38 GBd, an intrinsic linewidth of the carrier of $\Delta f_L = 1.9$ MHz, and an OSNR of 35 dB. The traces show the residual FM-noise spectrum of the received signal after blind phase search, relying on averaging of measured phases over a moving group of $N=10$ (red trace) and $N = 100$ (green trace) symbols. The blue trace indicates the spectrally white FM-noise spectrum of the carrier prior to modulation. As a rough estimate, BPS relying on a moving group of N symbols can effectively suppress frequency noise components occurring at Fourier frequencies up to $f = 1/NT_S$, where $T_S \approx 26$ ps corresponds to the symbol duration. Flicker and random-walk frequency would occur at Fourier frequencies below 10^6 Hz and would hence also be effectively suppressed by BPS.

For a carrier with given phase noise and a fixed OSNR, an optimum number N of symbols within a group exists that provides an ideal trade-off between strong resilience to noise when averaging over many symbols for large N and the ability to track fast phase fluctuations, which requires small N . For a symbol rate of 38 GBd, an intrinsic linewidth of the QD-MLLD tone of 1.9 MHz, and OSNR levels of approximately 25 dB, best values of N are typically between 20 and 40. For $N = 40$ and symbol rates of 2 GBd or more, the overall averaging time of the phase-tracking scheme amounts to at most 20 ns. This is much shorter

than the limit $\tau_{\text{low}} \approx 1\mu\text{s}$ of the observation time, beyond which flicker and random-walk frequency noise start to become noticeable, see Section 4.3.1. We may hence conclude that the phase-noise-related impairments that remain after symbol-wise phase tracking are solely dictated by the intrinsic (short-term) linewidth of the device related to the spectrally white component of the FM-noise.

Note that there is a residual probability that cycle slips occur in the BPS algorithm. To check this aspect, we have investigated our 16QAM recordings with OSNR values of 19.8 dB, 20.6 dB and 21.3 dB and with lengths of 6×10^5 symbols without finding any cycle slips. We hence conclude that the BPS phase recovery is able to reliably track the phase over long symbol sequences. In a real system, this might have to be backed up by advanced FEC schemes [41] or pilot symbols [42].

In our experiments, the length of the PRBS was limited to $2^{11} - 1$ due to the memory size and the memory granularity of the arbitrary waveform generator (AWG) that was used to generate the data signals. However, we do not expect that a longer PRBS would lead to different results. For a symbol rate of 38 GBd, the duration of a single PRBS sequence amounts to 50 ns. In comparison to that, the averaging time used for BPS is much shorter and amounts to less than 1 ns ($N < 40$). Any phase drifts occurring over a longer time scale will be suppressed by the phase-noise compensation, and the associated signal impairments will vanish. Increasing the PRBS length beyond the currently used 50 ns will hence not have any impact on the phase-noise-related signal impairments.

Note that BPS is not the only phase tracking technique that allows to compensate impairments introduced by optical carriers with strong phase noise. Comparative study of other phase-tracking techniques such as digital phase-locked loops, Viterbi & Viterbi phase estimation, or algorithms based on Kalman filtering can, e.g., be found in Refs. [142]–[144]. In these studies, one conclusion is that feed-forward techniques such as BPS are more phase-noise tolerant and better suited for high symbol rates than feedback phase tracking such as digital phase-locked loops or algorithms based on Kalman filtering. Regarding feed-forward methods, it has also been shown that BPS outperforms other algorithms such as Viterbi & Viterbi phase estimation in terms of phase-noise tolerance, and previous studies indicate that the Viterbi & Viterbi algorithm is not well

suited for compensating the phase noise of QD-MLLD carriers at rather low symbol rates of 12.5 GBd [101].

It should also be noted that the performance advantages of symbol-wise BPS come at the price of increased computational complexity when compared to block-wise phase recovery. A more detailed discussion of the trade-off between the computational effort and the performance of BPS can, e.g., be found in [144]. Despite this complexity increase of the phase-tracking algorithm, the overall DSP complexity at the receiver does not change to a substantial degree, since the computational effort is mainly dominated by chromatic-dispersion (CD) compensation and FEC decoding [145].

4.4.3 42 GBd PDM-QPSK 7.83 Tbit/s data transmission

To demonstrate the viability of QD-MLLD in WDM transmission, we perform an experiment at a symbol rate of 40 GBd using QPSK as modulation format. The experimental setup is shown in Fig. 4.5(a). The total QD-MLLD output power is boosted by EDFA1 to 17 dBm. Using a programmable optical filter (POF), we select 52 tones from the frequency comb, marked in blue in Fig. 4.5(b), and separate them into odd and even carriers. The two sets of carriers are later encoded with independent data streams to emulate a realistic WDM signal [82], [95]. The POF additionally flattens the power spectrum of the carriers. After amplification and flattening, the OCNR of the comb lines amounts to approximately 35 dB. The even and odd carriers are amplified by subsequent EDFA2 and EDFA3 and sent through a pair of IQ modulators. Both modulators are driven by QPSK signals with RC spectrum pulses with a 5 % roll-off, generated by an AWG using a PRBS of length $2^{11}-1$ at a symbol rate of 40 GBd. After combining the signals, PDM is emulated by a split-and-combine method, described in Section 4.4.1. The data stream is amplified and transmitted over 75 km of SSMF, see Fig. 4.5(c) for the power spectrum before and after modulation. At the receiver, we amplify the signal and select each channel using a 0.6 nm tunable BPF followed by EDFA6 and a second tunable 1.5 nm BPF to suppress out-of-band ASE noise. The signal is detected with a DP-CR and

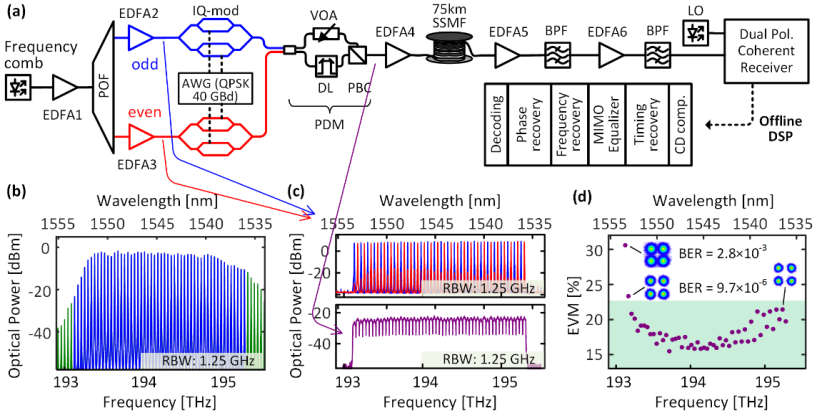


Figure 4.5. PDM-QPSK data transmission with QD-MLLD. **(a)** Experimental setup used to emulate the WDM transmission experiment. EDFA: Erbium-doped fiber amplifier. POF: Programmable optical filter. AWG: Arbitrary-waveform generator. PDM: Polarization division multiplexing. VOA: Variable optical attenuator. DL: Delay line. PBC: Polarization beam combiner. SSMF: Standard single-mode fiber. BPF: Band-pass filter. LO: Local oscillator. **(b)** Optical spectrum of the QD-MLLD frequency comb. The 52 lines selected for WDM experiment are colored in blue. **(c)** Top: Superimposed spectra of odd and even carriers before modulation. Bottom: Spectrum of 52 modulated carriers. **(d)** EVM of the transmitted WDM channels. The maximum recording length of 2×10^6 bit leads to a minimum BER of 6.5×10^{-6} that can be measured in a statistically reliable way. This corresponds to an EVM of 22.9 %. Below this value, the expected BER is smaller and cannot be measured within our recordings of 10^6 symbols – the associated range of EVM values is shaded in green. Importantly, all 52 channels fall below an EVM of 38.5 %, which corresponds to a BER of 4.7×10^{-3} , representing the threshold for hard-decision FEC with 6.25 % overhead [140].

undergoes a number of DSP steps, as described in Sections 4.4.1 and 4.4.2. To undo the dispersive effect of the 75 km-long fiber link, we additionally perform CD compensation.

The measured EVM values are shown in Fig. 4.5(d). For evaluating the recorded signals, the averaging length N used for BPS is optimized individually for each channel, and amounts to approximately 30 symbols. For QPSK transmission, the signal quality is comparatively high with EVM levels down to 16 %, which would correspond to a BER of 2×10^{-10} assuming that the signals are impaired by additive white Gaussian noise (AWGN) only. To measure a

statically reliable BER reaching a confidence level of 99 % within a confidence interval of 100 %, at least 13 erroneous bits have to be found in each recording [44]. This would lead to recording lengths of more than 6×10^{10} , which is far beyond the storage capabilities of our oscilloscope. We hence limited our recordings to a practically well manageable length of approximately 2×10^6 bit and rely on the EVM as a quality metric. For this length, the smallest BER that can be measured with the above-mentioned confidence amounts to 6.5×10^{-6} , which would correspond to an EVM of approximately 22.9 %. Recordings with EVM values below this value are not accessible to direct BER measurements and fall into the green shaded area in Fig. 4.5(d). A statistically reliable measurement of the BER was hence only possible for the two channels at the lowest carrier frequency – the measured BER values are indicated in Fig. 4.5(d) and are in good agreement with the BER estimated from the EVM assuming that the signals are impaired by AWGN only. Importantly, all 52 channels fall below an EVM of 38.5 %, which corresponds to a BER of 4.7×10^{-3} [44], representing the threshold for hard-decision FEC with 6.25 % overhead [140]. This leads to an aggregate line rate of 8.32 Tbit/s and a net data rate of 7.83 Tbit/s, transmitted over 75 km of SSMF with a net spectral efficiency of 3.8 bit/s/Hz.

4.4.4 38 GBd PDM-16QAM 10.68 Tbit/s data transmission

We also perform a 16QAM transmission demonstration to prove the viability of symbol-wise blind phase search (BPS) for more complex modulation formats. We use the same setup as for the QPSK experiments, see Fig. 4.5(a). The symbol rate amounts to 38 GBd, and we use 38 carriers from our QD-MLLD frequency comb for WDM transmission, see Fig. 4.6(a) for the flattened power spectrum before and after modulation. We use pulses with RC spectrum having a 10 % roll-off. The WDM transmission experiments relies on the central 38 comb lines, which offer a spectral flatness of better than 3 dB. The measured BER for each of the transmitted WDM channels is depicted in Fig. 4.6(b). For each channel, five signal sequences were recorded, each containing 10^6 bit. This recording length is sufficient to provide more than 100 erroneous bits in each of our measurements, hence allowing for a statistically reliable BER estimation, see Section 4.4.3. Also here, the averaging length N used for BPS is optimized for each channel, see Section 4.4.2. Out of the 38 channels, 32 fall below the

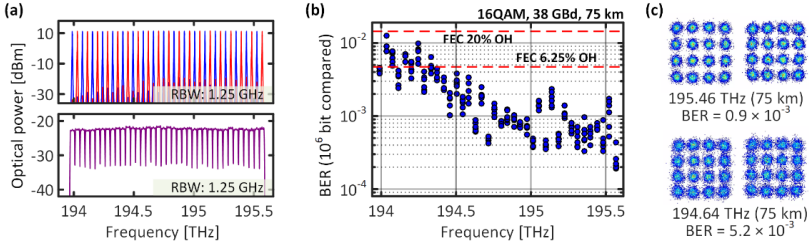


Figure 4.6. Data transmission results of 38 channels carrying PDM-16QAM signals at 38 GBd. **(a)** Top: Combined odd and even carriers prior to modulation. Bottom: 38 modulated carriers prior to transmission. The line rate amounts to 304 Gbit/s per channel. **(b)** Measured BER of the transmitted channels. The BER increase towards lower carrier frequencies is attributed to an increase of the noise figures of EDFA5 and EDFA6 with decreasing optical frequency. **(c)** Exemplary constellation diagrams recorded at different optical carrier frequencies.

BER threshold of 4.7×10^{-3} for hard-decision FEC with 6.25 % overhead, while the remaining six channels fall below the BER threshold of 1.44×10^{-2} for FEC with 20 % overhead [140]. This leads to an aggregate line rate of 11.55 Tbit/s and a net data rate of 10.68 Tbit/s with a net spectral efficiency of 6.7 bit/s/Hz. To the best of our knowledge, our experiments represent the first demonstration of optical 16QAM signal transmission using multiple carriers from a DC-driven chip-scale comb generator without any hardware-based phase-noise reduction schemes, leading to the highest data rate achieved in such an experiment. From Fig. 4.6(b) one can observe that channels at higher frequencies have a better signal quality. This is due to the fact that our preamplifiers EDFA5 and EDFA6 have a higher noise figure for decreasing optical frequency. Exemplary constellation diagrams for dual polarization channels at carrier frequencies 195.46 THz and 194.64 THz are shown in Fig. 4.6(c).

Note that the FSR of 42 GHz of the MLLD comb generator was deliberately chosen for our experiments to enable transmission at maximum spectral efficiency with the available transmitter equipment. Specifically, the AWG (Keysight M8195) used for driving the I/Q modulators was limited to a bandwidth of approximately 20 GHz, which led to high penalties when utilizing 16QAM at symbol rates beyond 40 GBd, see Fig. 4.3(c). Other FSR can be

obtained by cleaving the devices at a different length to achieve line spacings of, e.g., 25 GHz [122] or 50 GHz that comply to ITU standards.

4.5 Summary

We have shown that the strong low-frequency FM noise of QD-MLLD can be overcome by feed-forward symbol-wise phase tracking, thus making the devices usable as particularly simple and attractive multi-wavelength light sources for WDM transmission at data rates beyond 10 Tbit/s. We perform an in-depth analysis of the phase-noise characteristics of QD-MLLD, which reveals a strong increase of the FM-noise spectrum at low frequencies as the main problem that has prevented the use of higher-order modulation formats such as 16QAM so far. To overcome these limitations, we implement and test a digital phase tracking technique using a symbol-wise blind phase search (BPS) technique that finally allows transmission of 38 GBd dual-polarization (DP) 16QAM signals on a total of 38 carriers. This leads to a line rate of 11.55 Tb/s and a net data rate of 10.68 Tbits/s. To the best of our knowledge, this is the highest data rate so far achieved by a DC-driven chip-scale comb generator without any hardware-based phase-noise reduction schemes. We show that under realistic transmission conditions the QD-MLLD tones show a penalty of less than 0.5 dB with respect to a 10 kHz-wide high-quality laser carrier.

5 Microresonator-based Kerr comb generators for massively parallel coherent optical communications

This chapter devotes itself to the demonstration of massively parallel WDM coherent communications using the tones of microresonator-based dissipative Kerr solitons (DKS) both at the transmitter and at the receiver. The contents of this chapter correspond to the publication [J1], which was published with equal contribution from me, Juned N. Kemal, and M. Karpov. In this work, I contributed and lead the DKS generation and the data transmission experiments using DKS generators as multi-wavelength light sources at the transmitter, see Sections 5.2 and 5.3., and to the analysis of the power conversion efficiency of DKS in Section 5.5. To maintain a logical structure of the contents of this thesis, the complete publication is reproduced in this chapter. In order to fit the structure and layout of this document, the content of the publication was adapted accordingly. Methods and Supplementary Information associated with this publication are to be found in Appendix B.

In this publication, the author of this thesis, Juned N. Kemal and M. Karpov contributed equally. The idea of the experiment was developed jointly by the author together with J. Kemal, and C. Koos. The author of this thesis and J. N. Kemal jointly developed and implemented the experimental setups, discussed in detail in Appendices B.3, B.4 and B.5, with the support of P. Trocha, S. Wolf, R. Rosenberger, J. Pfeifle, and K. Vijayan. The transmission experiments with DKS combs as multi-wavelength carrier source at the transmitter, Section 5.3, were lead by the author of this thesis, while the transmission experiment using DKS solitons both as multi-wavelength carriers and multi-wavelength LO was lead by J. N. Kemal. The investigation of power conversion efficiency of the DKS source, Section 5.5, was developed by the author together with J. N. Kemal with the support of C. Koos, M. Karpov, M.H.P. Pfeiffer, V. Brasch, M. H. Anderson, and A. Kordts from the Laboratory of Photonics and Quantum Measurements at École Polytechnique Fédérale de Lausanne (EPFL) developed,

fabricated, and characterized the Kerr-nonlinear microresonators for comb generation as well as the soliton-generation technique described in Appendices B.1 and B.2. Section 5.2 and Appendix B.7 under supervision of T. J. Kippenberg. The DSP required for the analysis of the recordings was performed by the author of this dissertation together with J. N. Kemal. Sections 5.2, 5.3, and 5.5 were written by the author with the support of J. N. Kemal, W. Freude, and C. Koos. The work was jointly supervised by W. Freude, T.J. Kippenberg, and C. Koos.

[start of paper [JI]]

Microresonator solitons for massively parallel coherent optical communications

Nature, Volume 546, Issue 7657, pp. 274-279, 2017
DOI: 10.1038/nature22387

Pablo Marin-Palomo^{1,†}, Juned N. Kemal^{1,†}, Maxim Karpov^{2,†}, Arne Kordts², Joerg Pfeifle¹, Martin H. P. Pfeiffer², Philipp Trocha¹, Stefan Wolf¹, Victor Brasch², Miles H. Anderson², Ralf Rosenberger¹, Kovendhan Vijayan¹, Wolfgang Freude^{1,3}, Tobias J. Kippenberg², Christian Koos^{1,3}

1 Institute of Photonics and Quantum Electronics (IPQ), Karlsruhe Institute of Technology (KIT), 76131 Karlsruhe, Germany

2 École Polytechnique Fédérale de Lausanne (EPFL), 1015 Lausanne, Switzerland

3 Institute of Microstructure Technology (IMT), Karlsruhe Institute of Technology (KIT), 76131 Karlsruhe, Germany

† These authors contributed equally to this work

Optical solitons are waveforms that preserve their shape while propagating, relying on a balance of dispersion and nonlinearity [146], [147] Soliton-based data transmission schemes were investigated in the 1980s, promising to overcome the limitations imposed by dispersion of optical fibers. These approaches, however, were eventually abandoned in favor of wavelength-division multiplexing (WDM) schemes that are easier to implement and offer improved scalability to higher data rates. Here, we show that solitons may experience a comeback in optical communications, this time not as a competitor, but as a key element of massively parallel WDM. In-stead of encoding data on the soliton itself, we exploit continuously circulating dissipative Kerr solitons (DKS) in a

microresonator [21], [148]. DKS are generated in an integrated silicon nitride microresonator [149] by four-photon interactions mediated by Kerr nonlinearity, leading to low-noise, spectrally smooth and broadband optical frequency combs [75]. In our experiments, we use two interleaved soliton Kerr combs to transmit a data stream of more than 50 Tbit/s on a total of 179 individual optical carriers that span the entire telecommunication C and L bands. Equally important, we demonstrate coherent detection of a WDM data stream by using a pair of microresonator Kerr soliton combs – one as a multi-wavelength light source at the transmitter, and another one as a corresponding local oscillator (LO) at the receiver. This approach exploits the scalability advantages of microresonator soliton comb sources for massively parallel optical communications both at the transmitter and receiver side. Taken together, the results prove the significant potential of these sources to replace arrays of continuous-wave lasers in high-speed communications. In combination with advanced spatial multiplexing schemes [94], [150] and highly integrated silicon photonic circuits [151], DKS combs may bring chip-scale petabit/s transceivers into reach.

5.1 Introduction

The first observation of solitons in optical fibers [147] in 1980 was immediately followed by major research efforts to harness such waveforms for long-haul communications [146]. In these schemes, data was encoded on soliton pulses by simple amplitude modulation using on-off-keying (OOK). However, even though the viability of the approach was experimentally demonstrated by transmission over one million kilometers [152], the vision of soliton-based communications was ultimately hindered by difficulties in achieving shape-preserving propagation in real transmission systems [146] and by the fact that nonlinear interactions intrinsically prevent dense packing of soliton pulses in either the time or frequency domain. Moreover, with the advent of wavelength-division multiplexing (WDM), line rates in long-haul communication systems could be increased by rather simple parallel transmission of data streams with lower symbol rates, which are less dispersion sensitive. Consequently, soliton-based communication schemes have moved out of focus over the last two decades.

More recently, frequency combs were demonstrated to hold promise for revolutionizing high-speed optical communications, offering tens or even hundreds of well-defined narrowband optical carriers for massively parallel WDM [93]–[95]. Unlike carriers derived from a bank of individual laser modules, the tones of a comb are intrinsically equidistant in frequency, thereby eliminating the need for individual wavelength control and for inter-channel guard bands [94], [95]. In addition, when derived from the same comb source, stochastic frequency variations of optical carriers are strongly correlated, permitting efficient compensation of impairments caused by nonlinearities of the transmission fiber [34].

For application in optical communications, frequency comb sources must be compact. In recent years, a wide variety of chip-scale comb generators have been demonstrated [12], [16], enabling transmission of WDM data streams with line rates of up to 12 Tbit/s [123]. Transmission at higher line rates however, requires more carriers and lower noise levels, and still relies on spectral broadening of narrowband seed combs using dedicated optical fibers [93]–[95] or nanophotonic waveguides [97]. In addition, generating uniform combs with a broadband spectral envelope often requires delicate dispersion management schemes, usually in combination with intermediate amplifiers [93]. Such schemes are difficult to miniaturize and not readily amenable to chip-scale integration. Moreover, with a few exceptions at comparatively low data rates [17], all advanced comb-based transmission experiments exploit the scalability advantages only at the transmitter, but not at the receiver, where individual continuous-wave (CW) lasers are still used as optical local oscillators (LO) for coherent detection.

In this paper, we show that dissipative Kerr solitons [21] (DKS) generated in integrated photonic microresonators via Kerr-nonlinear four-photon interactions, allow for generation of highly stable broadband frequency combs that are perfectly suited to overcome scalability limitations of massively parallel optical transmission both at the transmitter and receiver. Microresonator-based Kerr comb sources [153], [154] intrinsically offer unique advantages such as small footprint, large number of narrow-linewidth optical carriers, and line spacings of tens of GHz, which can be designed to fit established WDM frequency grids.

However, while these advantages were recognized, previous transmission experiments were limited to aggregate line rates of 1.44 Tbit/s due to strong irregularities of the optical spectrum associated with the specific Kerr comb states [82].

These limitations can be overcome by using DKS combs generated in a CW-driven microresonator. The technique exploits four-wave mixing, a process that converts two pump photons into a pair of new photons. In a microresonator, the strength of this interaction is given by the single-photon Kerr frequency shift of $g = \hbar\omega_0^2 cn_2/n^2 V_{\text{eff}}$, where n_2 (n) is the nonlinear (linear) refractive index, c the speed of light in vacuum, \hbar the reduced Planck constant, V_{eff} the nonlinear optical mode volume and ω_0 the angular frequency of the pump mode. For pump powers that cause the cavity Kerr frequency shift to exceed the linewidth of the resonance, parametric oscillations lead to the emergence of Kerr frequency combs (modulation instability, MI Kerr combs). Bright DKS can be formed in this process when the microresonator has a locally anomalous group velocity dispersion (i.e. a Taylor expansion for cavity modes $\omega_\mu = \omega_0 + \sum_{i=1}^{\infty} \mu^i D_i/i!$ has $D_2 > 0$) and a CW laser excitation (frequency ω_L) that is red detuned from the cavity resonance (i.e. $\delta\omega = \omega_0 - \omega_L > 0$). Mathematically, DKS states appear as specific solutions of the Lugiato-Lefever equation [155] and consist of an integer number of discrete secant-hyperbolic-shaped pulses on a CW background circulating in the cavity [21]. Stability of such states relies on the double balance of dispersion and Kerr nonlinearity as well as of nonlinear parametric gain and cavity loss. Theoretically predicted in Ref. [148] and first reported to spontaneously form in microresonators made from crystalline MgF₂ [21], DKS have been observed in different types of material systems including silica-on-silicon [156] and silicon nitride [75] (Si₃N₄) as well as silicon [157]. Of particular interest are single-soliton states, which consist of only one ultra-short pulse circulating around the cavity, leading to a broadband comb spectrum with a smooth and numerically predictable envelope given by

$$p(\mu) \approx \frac{\kappa_{\text{ex}} D_2 \hbar \omega_0}{4g} \text{sech}^2 \left(\frac{\pi\mu}{2} \sqrt{\frac{D_2}{2\delta\omega}} \right) \quad (5.1)$$

where κ_{ex} represents the external coupling rate to the bus waveguide [21] (see Appendix B.6.2 for more details). DKS have already been used in applications such as self-referencing of optical frequency combs [11], [158], low noise microwave generation [159] and dual soliton comb spectroscopy [156], [160].

Our demonstration comprises a series of three experiments that exploit the extraordinarily smooth and broadband spectral envelope and the inherently low phase noise of DKS combs for massively parallel coherent communications. In a first experiment, we transmit data on 94 carriers that span the entire telecommunication C and L bands with a line spacing of ~ 100 GHz. Using 16-state quadrature amplitude modulation (16QAM) to encode data on each of the lines, we achieve an aggregate line rate of 30.1 Tbit/s. In a second experiment, we double the number of carriers by interleaving two DKS combs. This gives a total of 179 carriers and an aggregate line rate of 55.0 Tbit/s transmitted over a distance of 75 km – the highest data rate achieved to date with a chip-scale frequency comb source. In a third experiment, we demonstrate coherent detection using a DKS comb as a multi-wavelength LO. We use 93 carriers to transmit and receive an aggregated line rate of 37.2 Tbit/s. In these experiments, the LO comb is coarsely synchronized to the transmitter comb, and digital signal processing is used to account for remaining frequency differences. The results prove the tremendous potential of Kerr soliton combs, both as multi-wavelength optical sources and as LO for massively parallel WDM transmission.

5.2 Generation of dissipative Kerr soliton frequency combs in SiN microresonators

Our work relies on integrated Si_3N_4 microresonators for generation of DKS frequency combs [21], cf. Fig. 5.1(a). The Si_3N_4 platform is chosen due to its low optical losses and its compatibility with large-scale silicon-based processing [149]. The microresonators feature a waveguide height of 800 nm to achieve anomalous group velocity dispersion (GVD) and are fabricated using the photonic Damascene process [161]. Neighboring resonances are spaced by 100 GHz while featuring intrinsic Q -factors exceeding 10^6 . DKS combs are obtained by sweeping of the pump laser through the resonance from a blue-

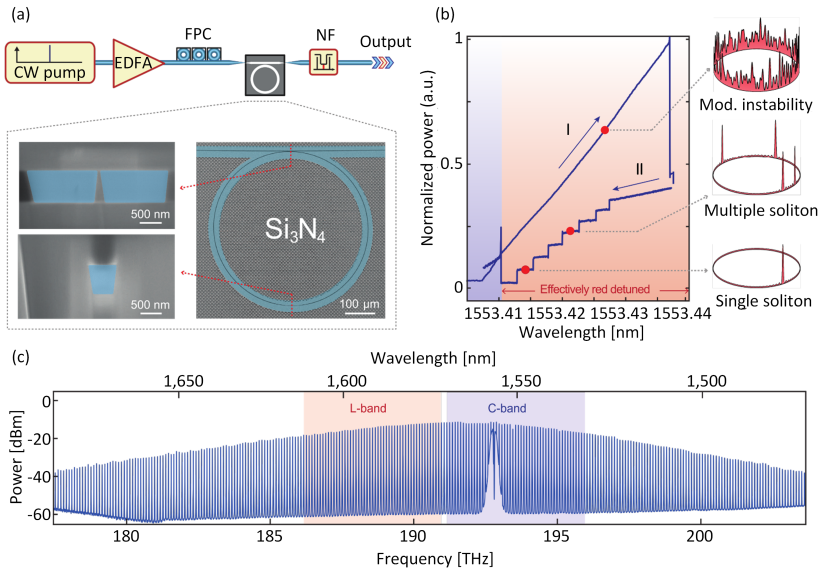


Figure 5.1: Broadband frequency comb generation using dissipative Kerr solitons in high-Q silicon nitride (Si_3N_4) microresonators. **(a)** Principle of soliton frequency comb generation: The integrated photonic microresonator is pumped by a tunable CW laser amplified by an erbium-doped fiber amplifier (EDFA). Lensed fibers are used to couple light to the chip (FPC – fiber polarization controller). After the microresonator, a notch filter (NF) suppresses the remaining pump light. The insets show scanning electron microscopy images of a Si_3N_4 microresonator with a radius of 240 μm . Right inset: Top view. The checker-board pattern results from the photonic Damascene fabrication process [161], see Appendix B.1. Left insets: Cross sections of the resonator waveguide (dimensions $0.8 \times 1.65 \mu\text{m}^2$) at the coupling point (top) and at the tapered section (bottom, dimensions $0.8 \times 0.6 \mu\text{m}^2$). The tapered section is used for suppressing higher order modes families [162], while preserving a high optical quality factor ($Q \sim 10^6$), see Appendix B.1. **(b)** Pump tuning method for soliton generation in optical microresonator, showing the evolution of the generated comb power versus pump laser wavelength: (I) The pump laser is tuned over the cavity resonance from the blue-detuned regime, where high-noise modulation instability (MI) combs are observed, to the red-detuned regime, where cavity bistability allows for the formation of soliton states (here a multiple soliton state); (II) Upon having generated a multiple soliton state, the pump laser is tuned backwards to reduce the initial number of solitons down to a single one. The insets on the right schematically show the corresponding intracavity waveforms in different states (MI, multiple and single soliton state). **(c)** Measured spectrum of a single-soliton frequency comb after suppression of residual pump light. The frequency comb features a smooth spectral envelope with a 3 dB bandwidth of 6 THz comprising hundreds of optical carriers extending beyond the telecommunication C and L bands (blue and red, respectively).

detuned wavelength to a predefined red-detuned wavelength [21], [75]. This leads initially to the generation of MI Kerr combs followed by DKS states once the resonance is crossed, cf. Fig. 5.1. Importantly, once a multiple-soliton comb state is generated, the transition to a single-soliton state can be accomplished in a reliable and deterministic manner by adjusting the laser frequency [22], cf.

Fig. 5.1(a),(b) and Appendix B.1. The measured power spectrum of the DKS comb state is shown in Fig. 5.1(c), which exhibits a 3dB spectral bandwidth of ~ 6 THz. The soliton comb states are remarkably stable for many hours in a laboratory environment, which is key to the transmission experiments presented in this work. Massively-parallel data transmission using dissipative Kerr solitons.

5.3 Soliton Kerr comb generators for as multi-wavelength carriers for WDM transmission

The general concept of massively parallel data transmission using a frequency comb as a multi-wavelength light source is depicted in Figure 5.2(a). For emulating massively parallel WDM transmission in our laboratory, we rely on a simplified scheme using only two independent data streams on neighboring channels along with an emulation of polarization division multiplexing, see Appendix B.3 for details. We use 16QAM at a symbol rate of 40 GBd along with band-limited Nyquist pulses that feature approximately rectangular power spectra, Figure 5.2(b). At the receiver, each channel is individually characterized using a CW laser as LO and an optical modulation analyzer, which extracts signal quality parameters such as the error-vector magnitude (EVM) or the bit-error ratio (BER). The BER of the transmission experiment are depicted in Figure 5.2(e) with different BER thresholds indicated as horizontal dashed lines. Out of the 101 carriers derived from the comb in the C and L band, a total of 94 channels were used for data transmission. This leads to a total line rate of 30.1 Tbit/s, see Appendix B.1 for details on data rate calculations. The transmission capacity is restricted by the fact that the line spacing of ~ 100 GHz significantly exceeds the signal bandwidth of ~ 40 GHz, leading to unused frequency bands

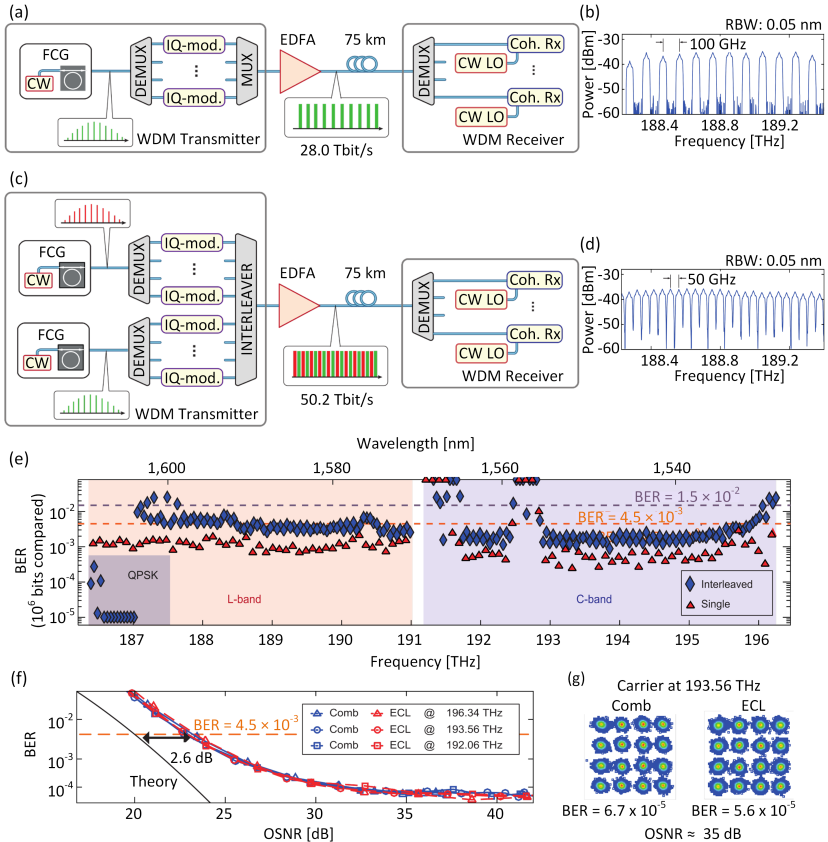


Figure 5.2: Data transmission using microresonator soliton frequency comb generators as optical sources for massively parallel WDM. **(a)** Principle of data transmission using a single DKS comb generator as optical source at the transmitter. A demultiplexer (DEMUX) separates the comb lines and routes them to individual dual-polarization in-phase/quadrature (IQ) modulators, which encode independent data on each polarization. The data channels are then recombined into a single-mode fiber using a multiplexer (MUX) and boosted by an erbium-doped fiber amplifier (EDFA) before being transmitted. At the receiver, the wavelength channels are separated by a second DEMUX and detected using digital coherent receivers (Coh. Rx) along with individual CW lasers as local oscillators (CW LO). In our laboratory experiment, we emulate WDM transmission by independent modulation of even and odd carriers using two IQ modulators, see Appendix B.3. We use 16-state quadrature amplitude modulation (16QAM) at a symbol rate of 40 GBd per channel. (Caption continued on next page)

Figure 5.2 continued: (b) Section of the optical spectrum of the WDM data stream. Nyquist pulse shaping leads to approximately 40 GHz wide rectangular power spectra for each of the carriers, which are spaced by approximately 100 GHz. **(c)** Principle of data transmission using interleaved DKS combs. At the transmitter, two combs of practically identical line spacing are interleaved. The resulting comb features a carrier spacing of approximately 50 GHz, which enables dense spectral packing of WDM channels and hence high spectral efficiency. At the receiver, this scheme still relies on individual CW lasers as LO for coherent detection, see Appendix B.3 for details. **(d)** Section of the optical spectrum of the WDM data stream. **(e)** Measured bit-error ratios (BER) of the transmitted channels for the single-comb and the interleaved-comb experiment, along with the BER thresholds for error-free propagation when applying forward error correction schemes with 7% overhead (4.5×10^{-3} , dashed orange line) and 20% overhead (1.5×10^{-2} , dashed blue line) [43], see Appendix B.1 for details. For the interleaved-comb experiment, the outer 14 lines at the low-frequency edge of the L band were modulated with quadrature phase-shift keying (QPSK) signals rather than 16QAM due to the low OSNR of these carriers. **(f)** Measured BER vs. optical signal-to-noise ratio OSNR of three different channels derived from a DKS frequency comb (blue) and a high-quality ECL (red), all with 16QAM signaling at 40 GBd. A total of 10^6 bits were compared. The comb lines do not show any additional penalty in comparison the ECL tones. Similar results were obtained at other symbol rates such as 28 GBd, 32 GBd, or 42.8 GBd. **(g)** Constellation diagrams obtained for an ECL and DKS comb tone at 193.56 THz.

between neighboring channels, see Figure 5.2(b), and hence to a rather low spectral efficiency (SE) of 2.8 bit/s/Hz. These restrictions can be overcome by using interleaved frequency combs, see Figure 5.2(c). The scheme relies on a pair of DKS combs with practically identical line spacing, but shifted with respect to each other by half the line spacing by thermal tuning. At the receiver, this scheme still relies on individual CW

lasers as LO for coherent detection. The interleaved comb features a line spacing of ~ 50 GHz, which allows for dense packing of 40 GBd data channels in the spectrum, see Fig. 5.2(d). The BER results of the transmission experiment are depicted in Fig. 5.2(e) with different thresholds indicated as horizontal dashed

lines. For a given forward-error correction (FEC) scheme, these thresholds define the maximum BER of the raw data channel that can still be corrected to a BER level below 10^{-15} , which is considered error-free [43], see Appendix B.1

We find a total of 204 tones in the C and L band, out of which 179 carriers could be used for data transmission. The remaining channels were not usable due to

technical limitations, see Appendix B.1. The transmission performance is slightly worse than in the single-comb experiment since twice the number of carriers had to be amplified by the same EDFA, which were operated at their saturation output power such that the power per data channel reduced accordingly. Nevertheless, data was successfully transmitted over 75 km of standard single-mode fiber at a symbol rate of 40 GBd using a combination of 16QAM and QPSK. The total line rate amounts to 55.0 Tbit/s, and the net data rate is 50.2 Tbit/s. This is the highest data rate so far achieved with a chip-scale frequency comb source, and compares very well to the highest capacity of 102.3 Tbit/s ever transmitted through a single-mode fiber core using more than 200 discrete DFB lasers as optical sources at the transmitter [163]. In addition, we achieve an unprecedented spectral efficiency of 5.2 bit/s/Hz, owing to the densely packed spectrum, Fig. 5.2(d). In the experiments, limited saturation output power of the employed EDFA is the main constraint of signal quality and BER, see Appendices B.3 and B.6.3 for details. The presented data rates are hence not limited by the DKS comb source, but by the components of the current transmission setup, leaving room for further improvement.

To confirm the outstanding potential of DKS combs for data transmission, we compare the transmission performance of a single comb line to that of a reference carrier derived from a high-quality benchtop-type external-cavity laser featuring an optical linewidth of approximately 10 kHz, an optical output power of 15 dBm, and an optical carrier-to-noise power ratio (OCNR) in excess of 60 dB. As a metric for the comparison, we use the OSNR penalty at a BER of 4.5×10^{-3} , which corresponds to the threshold for FEC with 7 % overhead [43]. The results for 40 GBd 16QAM transmission are shown in Fig. 5.2(f) for three different comb lines and for ECL reference transmission experiments at the corresponding comb line frequencies. The OSNR_{ref} values are defined for a reference bandwidth of 0.1 nm, see Appendix B.4. As shown, no additional OSNR penalty is observed for the frequency comb when compared with the high-quality ECL: For both sources, we observe an OSNR penalty of 2.6 dB with respect to the theoretically required OSNR (black line) for a BER of 4.5×10^{-3} . DKS-based light sources can hence dramatically improve scalability of WDM systems without impairing the signal quality under realistic transmission conditions. The error floor in Fig. 5.2(f) is attributed to transmitter nonlinearities and electronic

receiver noise in our setup. Fig. 5.2(g) shows the measured constellation diagrams for the ECL and the comb line at 193.56 THz, both taken at the same OSNR of 35 dB.

5.4 Data transmission using DKS combs both at the transmitter and at the receiver

To demonstrate the potential of DKS frequency combs as multi-wavelength LO at the receiver, we perform a third experiment shown schematically in Fig. 5.3(a). At the transmitter, a first DKS comb generator with an FSR of ~ 100 GHz serves as an optical source. At the receiver, a second DKS comb source having approximately the same FSR is used to generate the corresponding LO tones, each featuring an optical linewidth below 100 kHz. Fig. 5.3(b),(c) show a section of the transmitted data spectrum along with the corresponding section of the LO comb. As a reference, the same experiment was repeated using a high-quality ECL with a 10 kHz linewidth as an LO for channel-by-channel demodulation. Overall, an aggregate data rate of 34.6 Tbit/s is obtained. The resulting BER values of all 99 channels for both methods are shown in Fig. 5.3(d). Some of the channels showed signal impairments due to limitations of the available equipment, see Appendix B.1. However, we cannot observe any considerable penalty that could be systematically attributed to using the DKS comb as an LO.

5.5 Power conversion efficiency of dissipative Kerr solitons

While frequency combs offer fundamental technical advantages compared to discrete lasers, they can also contribute to reduce the power consumption of the transmission system. In this context, the power conversion efficiency of the DKS comb generator is an important metric, defined as the ratio between the power of the pump and that of the generated comb lines. The power conversion efficiency of our current comb sources is limited to rather small values between 0.1 % and 0.6 % due to the fundamental principle that bright soliton generation

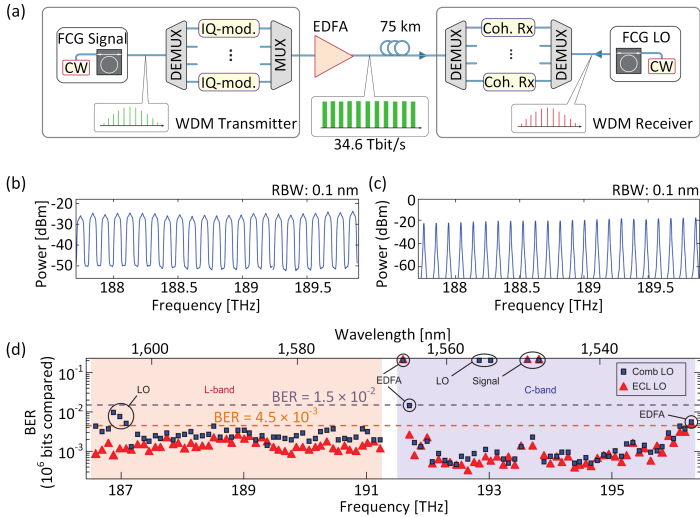


Figure 5.3: Coherent data transmission using microresonator soliton frequency combs both at the transmitter and at the receiver side. **(a)** Massively parallel WDM data transmission scheme using DKS frequency combs both as multi-wavelength source at the transmitter and as multi-wavelength local oscillator (LO) at the receiver. In contrast to Figure 5.2, a single optical source provides all required LO tones for coherent detection. An extra DEMUX is used to route each LO tone to the respective coherent receiver (Coh. Rx). **(b)** Section of the spectrum of the transmitted channels. **(c)** Corresponding section of the spectrum of the LO frequency comb. Note that the comparatively large width of the depicted spectral lines is caused by the resolution bandwidth of the spectrometer ($\text{RBW} = 0.1 \text{ nm}$) and does not reflect the sub-100 kHz optical linewidth of the LO tones. **(d)** Measured BER for each data channel. Blue squares show the results obtained when using a DKS comb as multi-wavelength LO, and red triangles correspond to a reference measurement using a high-quality ECL as LO. Dashed lines mark the BER thresholds of 4.5×10^{-3} (1.5×10^{-2}) for hard-decision (soft-decision) FEC with 7% (20%) overhead. Black circles show the channels with BER above the threshold for 7% FEC and specify the reasons for low signal quality: low OCNR of the carriers from the LO comb (“LO”) and the signal comb (“Signal”), as well as bandwidth limitations of the C-band EDFA (“EDFA”), see Appendix B.1 for more details.

only occurs with the pump laser being far detuned from the optical resonance. Still, the overall power consumption can already now compete with massively parallel arrays of commercially available integrated tunable laser assemblies (ITLA), see Appendices B.1 and B.6 for details. The analysis also shows that

improvement of more than one order of magnitude compared to ITLA is possible by optimizing the microresonator dispersion, by making use of tailored amplifiers with optimum efficiency, and by increasing the power conversion efficiency via recently demonstrated high- Q Si_3N_4 microresonators with Q -factors of 6×10^6 .

5.6 Summary

In summary, we have demonstrated the potential of chip-scale DKS frequency combs for massively parallel WDM at data rates of tens of terabit/s. We use them both as multi-wavelength source at the transmitter and as LO at the receiver, and we show in both cases that there is no systematic penalty compared to using high-quality ECL. While our experiments achieve the highest data rate with chip-scale frequency comb sources to date, there is still room for increasing the transmission capacity by optimizing the transmission system or by using the adjacent S and U bands for telecommunications in the near infrared. For long transmission distances, comb-based transmission schemes might allow for compensation of nonlinear impairments and hence lead to an improved signal quality compared to conventional WDM schemes [34]. The results prove the tremendous potential of DKS comb generators for high-speed data transmission, both in petabit/s intra-datacenter networks [164] and in inter-datacenter connections.

[end of paper [J1]]

6 Summary and Outlook

6.1 Summary

This thesis aims at investigating and verifying the potential of chip-scale frequency comb sources for coherent WDM transmission both from a fundamental and an experimental approach.

In this context, a holistic model is derived to estimate the transmission performance of comb-based WDM links. The findings extracted from this model helped to compare different comb generator types and to benchmark them against the achievable transmission performance. When using chip-scale comb sources both at the transmitter side and at the receiver side, the analysis leads to transmission capacities reaching 80 Tbit/s for metropolitan-area links of up to 400 km.

From an experimental standpoint, two highly-promising chip-scale comb sources are characterized and their potential for massively parallel WDM transmission is verified by performing various data transmission experiments. These comb generators are the so-called quantum-dash mode-locked laser diode (MLLD) and the microresonator-based Kerr comb generator which consists of a Kerr-nonlinear silicon nitride (SiN) microresonator driven by a continuous-wave (CW) laser.

The main properties of these comb generators and the key data transmission achievements are summarized below.

Quantum-dash mode-locked laser diodes (QD-MLLD) stand out due to their compactness and simple operation by a direct current along with the ability to generate a flat and broadband frequency comb comprising dozens of equidistant lines spaced by tens of GHz and distributed over more than 2 THz. These properties make QD-MLLD devices promising candidates to be used as multi-wavelength light sources in WDM links. However, these devices suffer from the large optical linewidth of the individual carriers, which impairs the signal quality and

limits their use to rather low spectral efficient modulation formats. This thesis demonstrates spectrally efficient coherent transmission with QD-MLLD by using a dedicated digital phases tracking technique that can deal with the strong phase noise fluctuations of the comb lines. With this technique, a data stream of 11.55 Tbit/s was transmitted over 75 km of single-mode fiber by using 16QAM symbol at a symbol rate of 38 GBd.

Microresonator-based Kerr comb generators stand out due to their ability to produce a stable ultra-short pulse sequence, or soliton train, which corresponds to a broadband frequency comb, so-called dissipative Kerr soliton (DKS) comb, with hundreds of comb lines which are distributed over more than 10 THz. The tones of a DKS comb feature low phase noise levels which allow them to be used to transmit spectral efficient modulation formats without dedicated phase tracking techniques. Using DKS combs, a 55 Tbit/s data stream spanning the entire telecommunication C and L band is transmitted over a fiber length of 75 km, corresponding to the highest data rate with any chip-scale frequency comb source at the time of the publication.

Taken together, these results demonstrate the significant potential of these two comb sources to replace arrays of continuous-wave lasers in multi-Tbit/s communications.

6.2 Outlook

The transmission experiments performed in this thesis relied on the use of a coherent receiver with an external cavity laser (ECL) as a local oscillator (LO). To leverage the full potential of the chip-scale comb sources investigated in this thesis, a second chip-scale comb source should be used at the receiver as multi-wavelength LO, as depicted in Fig. 1.2. For Kerr comb sources, a first proof-of-principle transmission experiment has been demonstrated using two DKS combs, one as a multi-wavelength carrier at the receiver and another as a multi-wavelength LO at the transmitter. The results of the transmission experiment are discussed in Section 5.4 and are part of the work of Juned N. Kemal. Similarly, QD-MLLD devices have been also used in a transmission experiment both as multi-wavelength carrier source and multi-wavelength LO source [J7]. In

these two demonstrations, the LO comb is coarsely synchronized to the transmitter comb, and digital signal processing is used to account for the remaining frequency differences between the carriers and the corresponding LO tones. In this context, further investigations are necessary to continuously synchronize the center frequency and the free spectral range of the receiver comb to the transmitter comb.

In this thesis, the DKS comb is generated by driving a silicon nitride (SiN) microresonator with high optical powers of more than 1 W. Such high optical powers are achieved by amplifying the output from an ECL with a high-power optical amplifier. Future investigations towards Kerr-comb-based multi-Tbit/s transceivers should focus on the co-integration of the CW laser source and the microresonator. For this to happen, the threshold power for DKS generation should be reduced considerably. In this context, recent improvements of the microresonator technology by the group of T. J. Kippenberg,¹⁰ and the group of M. Lipson and A. L. Gaeta,¹¹ has demonstrated DKS generation with optical powers below the 50 mW [76], [113]. Such advances lead to the first demonstrations of packaged Kerr-comb generators co-integrating the CW laser with the microresonator [23], [24]. In these demonstrations, however, the tones of the associated frequency combs feature comparatively low optical powers, which would impact data transmission performance considerably. The small optical powers are associated with the low power conversion efficiency from the pump laser to the comb lines, which is characteristic of DKS generation. Further investigations could focus on the use of so-called dark-solitons, which offer improved power conversion efficiencies [86], or on the use of quartic solitons, which are solitons generated in a microresonator with quartic group velocity dispersion (GVD) and lead to frequency combs with smoother spectra [112].

Future investigations regarding the use of QD-MLLD devices in WDM transceivers should focus on further paths to reduce the phase noise of the comb lines. In this context, the group of J. Witzens,¹² has demonstrated RF linewidth

¹⁰ At the *Ecole Polytechnique Fédérale de Lausanne*, <https://www.epfl.ch/labs/k-lab/>

¹¹ At the *Columbia University*, <https://lipson.ec.columbia.edu/>

¹² At *RWTH Aachen University*, <http://www.iph.rwth-aachen.de/>

and optical linewidth reduction with optical feedback from a photonic integrated chip (PIC) [73]. Further investigations are required to understand the limitations of this approach, and its applicability for massively-parallel WDM transmission is the subject of ongoing research.

The focus of future work should be placed on packaged comb-based coherent WDM transceivers. For example, on the transmitter side, this would require multi-chip integration of modulators, (de)multiplexers and light sources. In this context, the group of C. Koos,¹³ has demonstrated coherent data transmission with a silicon photonics transmitter, where the silicon photonics modulators are connected to InP lasers by employing 3D nano-printing of freeform optical waveguides, so-called photonic wire bonding, for efficient coupling between the photonic chips [165]. Multi-chip integration of a frequency comb source with modulators and multiplexers is the subject of ongoing research. Future work could thus build upon the investigations presented in this thesis.

¹³ At the Karlsruhe Institute of Technology, <https://www.ipq.kit.edu/index.php>

Appendices

A. Performance of chip-scale optical frequency comb generators in coherent WDM communications: Additional information

This section includes additional information on the underlying models introduced in Chapter 3.

A.1 OSNR penalty when using frequency comb sources at the receiver side

This section details the derivation of Eq. (3.9) in Section 3, which describes the OSNR penalty of using a frequency comb source as a multi-wavelength local oscillator at the receiver side. The impact of the local oscillator is typically neglected, however, when using a frequency comb, the impact of a finite OCNR of the tones can become relevant.

Equation (3.9) is derived considering the coherent receiver from Fig. A.5, and assuming the signal is impaired by additive white Gaussian noise: The signal and the LO can be expressed as

$$\begin{aligned} \underline{E}_1 &= \underline{E}_s + \underline{n}_s \\ \underline{E}_2 &= \underline{E}_{LO} + \underline{n}_{LO} \end{aligned} \quad (\text{A.1})$$

where $|\underline{E}_s| \ll |\underline{n}_s|$ and $|\underline{E}_{LO}| \ll |\underline{n}_{LO}|$. Similar to Eq. (2.11), the photocurrent at the output of the two BPDs can be expressed as

$$\begin{aligned}
 i_I &\sim \text{Re}\left\{E_1 E_2^*\right\} = \text{Re}\left\{\underbrace{E_s E_{LO}^*}_{\text{signal}} + \underbrace{E_s n_{LO}^* + E_{LO}^* n_s + n_s n_{LO}^*}_{\text{noise}}\right\} \\
 i_Q &\sim \text{Im}\left\{E_1 E_2^*\right\} = \text{Im}\left\{\underbrace{E_s E_{LO}^*}_{\text{signal}} + \underbrace{E_s n_{LO}^* + E_{LO}^* n_s + n_s n_{LO}^*}_{\text{noise}}\right\}.
 \end{aligned} \tag{A.2}$$

Neglecting the noise-noise mixing terms $n_s n_{LO}^*$ and adding the photocurrents from both BPDs, the complex value signal can be constructed as

$$i \sim E_s E_{LO}^* + E_s n_{LO}^* + E_{LO}^* n_s. \tag{A.3}$$

Equation (A.3) can be separated into signal intensity $i_{\text{signal}} = E_s E_{LO}^*$ and noise intensity $i_{\text{noise}} = E_s n_{LO}^* + E_{LO}^* n_s$. Next, the signal and noise powers are computed. Assuming that the noise terms are uncorrelated, the powers are added, resulting in

$$\begin{aligned}
 i_{\text{signal}}^2 &\sim |E_s E_{LO}^*|^2 \\
 i_{\text{noise}}^2 &\sim |E_s n_{LO}^*|^2 + |E_{LO}^* n_s|^2.
 \end{aligned} \tag{A.4}$$

Eq. (A.4) can be modified by using the OCNR relation for the LO

$$\text{OCNR} = \frac{|E_{LO}|^2}{|n_{LO}|^2}, \tag{A.5}$$

and the OSNR relation for the signal

$$\text{OSNR} = \frac{|E_s|^2}{|n_s|^2}. \tag{A.6}$$

Introducing Eqs. (A.5) and (A.6) into Eq. (A.4),

$$i_{\text{noise}}^2 = |E_s|^2 |E_{LO}|^2 \left(\frac{1}{\text{OCNR}} + \frac{1}{\text{OSNR}} \right). \tag{A.7}$$

Defining the OSNR for $\text{OCNR} \rightarrow \infty$ as

$$\text{OSNR}_\infty = \frac{|E_s|^2 |E_{\text{LO}}|^2}{I_{\text{noise}}^2}, \quad (\text{A.8})$$

the OSNR can be extracted from Eq. (A.7) leading to

$$\text{OSNR} = \left(\frac{1}{\text{OSNR}_\infty} - \frac{1}{\text{OCNR}_{\text{line}}} \right)^{-1}. \quad (\text{A.9})$$

For simplification, in Section 3 it is assumed that the OCNR of the carrier is the same as the OCNR of the LO. This assumption is reasonable when the same type of frequency comb source is used both at the transmitter side and at the receiver side.

A.2 Omission of modulated noise

The noise power given by Eq. (3.3) in Chapter 3 is modulated. The simple analysis in Chapter 3, however, does not take this effect into account. Considering modulated noise would make the analysis data dependent. This section justifies why a modulated noise is not considered in the analysis of Chapter 3.

In the case of amplitude modulation, the noise will be modulated and is therefore not stationary. For PSK formats, the model in Chapter 3 works fine and the results would not change. If comparing different QAM formats, the noise modulation will have a certain impact, which is related to the peak-to-average-power ratio. Also, the shape of MUX and DEMUX filters will have an impact. In the typically used link-limited regime, the effect of modulated noise can be disregarded since the dominating ASE noise is added after modulation. In the source-limited regime, neglecting the amplitude modulation of the noise might lead to a slight overestimation of the performance. A quantitative analysis of this effect, however, would depend on the modulation format and the associated modulation loss and would require exact knowledge of the spectral transmission characteristics WDM DEMUX and MUX used for separating and combining the comb lines. Although it is an interesting and important aspect, a detailed analysis of this effect would go beyond the main focus of this thesis.

In addition, format-dependent modulation losses are not considered in the analysis, but an overall insertion loss of the modulator of 25 dB both for 16QAM and 64 QAM is assumed. This loss includes both the optical insertion loss of the device and the modulation loss.

B. Microresonator-based solitons for WDM communications (Tx, Rx)

The content of this section has been published in the Methods and Supplementary Information of the journal publication [J1] that was published with equal contribution from the author of this thesis and Juned N. Kemal. The contributions of the various co-authors are explained in the introduction of Chapter 5 on page 97. To fit the structure and layout of this document, it was adapted accordingly.

[start of Methods and Supplementary Information of paper [J1]]

Microresonator solitons for massively parallel coherent optical communications

Nature, Volume 546, Issue 7657, pp. 274-279, 2017

DOI: 10.1038/nature22387

Pablo Marin-Palomo^{1,†}, Juned N. Kemal^{1,†}, Maxim Karpov^{2,†}, Arne Kordts², Joerg Pfeifle¹, Martin H. P. Pfeiffer², Philipp Trocha¹, Stefan Wolf¹, Victor Brasch², Miles H. Anderson², Ralf Rosenberger¹, Kovendhan Vijayan¹, Wolfgang Freude^{1,3}, Tobias J. Kippenberg², Christian Koos^{1,3}

1 Institute of Photonics and Quantum Electronics (IPQ), Karlsruhe Institute of Technology (KIT), 76131 Karlsruhe, Germany

2 École Polytechnique Fédérale de Lausanne (EPFL), 1015 Lausanne, Switzerland

3 Institute of Microstructure Technology (IMT), Karlsruhe Institute of Technology (KIT), 76131 Karlsruhe, Germany

† These authors contributed equally to this work

B.1 Methods

B.1.1 Fabrication of high-Q Si_3N_4 microresonator

We use Si_3N_4 microresonators for generation of DKS frequency combs. These devices lend themselves to co-integration with other photonic devices, using either monolithic approaches on silicon [151] or indium phosphide (InP) [166], hybrid InP-on-silicon approaches [167], or multi-chip concepts [16], [168]. A particularly attractive option is to co-integrate DKS comb generators with advanced multiplexer and demultiplexer circuits [151] and with highly power-efficient IQ modulators [169], [170] to realize chip-scale transceivers that can handle tens of terabit/s of data traffic, as already envisioned in Ref. [16]. For soliton formation, anomalous group velocity dispersion (GVD) is required, necessitating Si_3N_4 waveguide heights of approximately 800 nm for a width of 1.65 μm . These dimensions are achieved by using the recently developed photonic Damascene process [161], along with a waveguide filtering section to achieve a smooth dispersion profile [162]. A mode-filtering section was incorporated into the microrings in order to suppress higher-order modes [162], see Inset of Fig. 5.1(a). This allows to minimize the number of avoided mode crossings and facilitates soliton comb generation.

Fabrication reproducibility was investigated, leading to a yield of chips enabling DKS generation per batch of approximately 40 %. For resonators taken from the same wafer, we measured an average line spacing of 95.75 GHz with a standard deviation of approximately 70 MHz. We attribute such differences to variations of both the waveguide width and the thickness of the Si_3N_4 layer between distant micro-resonators within the same wafer. These variations are approximately 20 nm and may be reduced by increasing the uniformity of the fabrication process over the entire wafer. In particular, we expect that the use of highly developed large-scale fabrication equipment such as 193 nm deep-UV lithography and thin-film tools with improved uniformity will overcome these shortcomings in device reproducibility, as already demonstrated in the context of silicon photonics [171]. Note that the line spacing difference between frequency combs can be compensated through thermal tuning, which allows us to adapt the microresonators' FSR over a tuning range of more than 40 MHz, with

a precision of approximately 200 kHz. The same technique can be applied to precisely match the line spacing to established ITU grids.

In addition, we measured the differences in power conversion efficiency of the DKS comb generators used in our experiment, leading to values that range from 0.1 % to 0.6 %. These differences in power conversion efficiency are attributed to variations of the quality factors of the pumped resonances, which may be influenced by interactions of the fundamental mode with higher-order modes. Even though mode-filtering sections are used to suppress the propagation of higher order modes within the waveguide, we can still observe slight variations of the spectral envelope with respect to the theoretical sech^2 envelope shape. This fact hints to the presence of avoided mode crossings which are characteristic of multimode waveguides. We expect that these limitations can be overcome by optimized device design.

For DKS comb generators with improved power efficiency, high-Q factors are of great importance. Recently, Si_3N_4 resonators have been demonstrated [172], [173] to reach Q-factors of more than 6×10^6 both in devices with normal [172] and anomalous [173] GVD. Along with tailored optical amplifiers, such devices allow to reduce the electrical power consumption by more than an order of magnitude compared to state-of-the-art ITLA laser arrays, see Section B.6.1.

B.1.2 Soliton comb generation

The DKS combs are generated by pumping the microresonators with an ECL and a subsequent EDFA, which is operated at an output power of approximately 35 dBm, see Section B.2 and Fig. B1 for a more detailed description of the comb generation setup. A high-power band-pass filter with a 3 dB bandwidth of 0.8 nm is used to suppress the ASE noise originating from the pump amplifier. The soliton state is excited by well-controlled wavelength tuning of the pump ECL from low to high wavelengths across the resonance at a rate of approximately 100 pm/s [75]. Once a multiple-soliton state is obtained, the transition to a single-soliton state is accomplished by fine-tuning of the pump laser towards lower wavelengths [22]. This slow sweep is performed at a rate of approximately 1 pm/s. Light is coupled into and out of the on-chip Si_3N_4 waveguides by means of lensed fibers, featuring spot sizes of 3.5 μm and coupling

losses of 1.4 dB per facet. The pump power in the on-chip waveguide amounts to approximately 32 dBm. The frequency comb used in the single-comb transmission experiment exhibits a line spacing of 95.80 GHz and a 3-dB bandwidth of more than 6 THz. The optical linewidth of individual comb carriers is limited by the optical linewidth of our tunable pump lasers (TLB-6700, New Focus and TSL-220, Santec), which is below 100 kHz. This value is well below that of telecommunication-grade DFB lasers [174] and hence perfectly suited for coherent data transmission [53]. No additional linewidth broadening relative to the pump is measured, i.e., the phase noise of the comb lines is entirely dominated by the pump. Note that an alternative approach to DKS generation has recently been demonstrated [77] where the detuning of the pump laser with respect to the resonance is adjusted by thermally shifting the resonance by means of integrated heaters rather than by tuning the wavelength of the pump laser. This technique allows to replace the tunable pump lasers by much more stable CW pump lasers with sub-kHz linewidths. At the output of the microresonator, a tunable fiber Bragg grating (FBG) acts as a notch filter to suppress residual pump light to a power level that matches the other comb carriers. After the FBG, the measured optical power of the entire comb spectrum, see Fig. 5.1(c), amounts to 4 dBm. For the experiments using interleaved transmitter (Tx) frequency combs or a separate receiver (Rx) LO comb, a second DKS comb generator with similar performance is used. The frequency comb from the second device for the interleaved Tx combs (for the Rx LO) features a slightly different line spacing of 95.82 GHz (95.70 GHz) and overall optical power of 0 dBm (8 dBm). For the transmission experiments, an EDFA is used to amplify the combs to an approximate power of 5 dBm per line prior to modulation. The carriers next to the pumped resonance are superimposed by strong amplified stimulated emission (ASE) noise that originates from the optical amplifier. In future implementations, ASE noise can be avoided by extracting the comb light from the microresonator using a drop-port geometry [175]. This would avoid direct transmission of broadband ASE noise through the device and, in addition, would render the notch filter for pump light suppression superfluous.

B.1.3 Dissipative Kerr soliton comb tuning and interleaving

Precise interleaving of the frequency combs in the second transmission experiment is achieved by adjusting the temperature of each microresonator, thereby changing the refractive index and shifting the resonance frequencies while leaving the FSR essentially unchanged [176]. A detailed sketch of the experimental setup is given in Section B.2. The resonance frequencies of the cavity can be tuned at a rate of approximately -2.5 GHz/K with an accuracy of approximately 200 MHz, limited by the resolution of the heater of approximately 0.1 K. In addition, as a consequence of intra-pulse Raman scattering [177], the center frequency of the comb can also be tuned by slowly changing the pump frequency during operation at a constant external temperature. The associated tuning range is limited to approximately ± 500 MHz before the comb state is lost; the tuning resolution is given by the pump laser and amounts to approximately 10 MHz for our devices (TLB-6700, New Focus; TSL-220, Santec). These tuning procedures are used both for precise interleaving of DKS combs in the second transmission experiment and for synchronizing the LO comb to the Tx comb in the third transmission experiment.

B.1.4 Data transmission experiments

For the data transmission experiments [178]–[180], the single or interleaved frequency comb is amplified to 26.5 dBm by a C/L-band EDFA, before the lines are equalized and dis-interleaved into odd and even carriers to emulate WDM. In the laboratory experiment, the de-multiplexer (DEMUX) depicted in Fig. 5.2(a) is implemented by two programmable filters (Finisar WaveShaper, WS) along with C- and L-band filters, that act as dis-interleavers to separate the combs into two sets of “even” and “odd” carriers, see Section B.3 for a more detailed description of the experimental setup. After separation, the carriers are routed to individual dual-polarization in-phase/quadrature modulators (IQ-mod), which encode independent data streams on each polarization using both the amplitude and the phase of the optical signal as carriers of information. To this end, we use two optical IQ modulators which are driven with pseudo-random bit sequences of length $2^{11} - 1$ using QPSK or 16QAM signaling and raised-cosine (RC) pulse shaping with a roll-off factor $\beta = 0.1$. The drive signals

were generated by arbitrary-waveform generators (AWG). For the transmission experiment using frequency combs as optical source at the Tx, the symbol rate was 40 GBd, and the sampling rate of the AWG was 65 GSa/s (Keysight M8195A). For the experiment with a DKS comb as a multi-wavelength LO, symbol rates of 50 GBd and sampling rates of 92 GSa/s (Keysight M8196A) were used. We refrained from using higher symbol rates since the limited electrical bandwidth of our transmitter and receiver hardware would have led to significantly worse signal quality. In all experiments, polarization division multiplexing (PDM) is emulated by a split-and-combine method, where the data stream of one polarization is delayed by approximately 240 bits with respect to the other to generate uncorrelated data [181]. The data channels are then recombined into a 75 km long standard single-mode fiber (SSMF) fiber using a multiplexer (MUX) and boosted by an erbium-doped fiber amplifier (EDFA), before being transmitted. At the receiver, we select each channel individually by a BPF having a 0.6 nm passband, followed by a C-band or an L-band EDFA, and another BPF with a 1.5 nm passband. The signal is received and processed by means of an optical modulation analyzer (OMA, Keysight N4391A), using either a high-quality ECL line or a tone of another DKS comb as local oscillator. In the latter case, we use an optical band-pass filter to extract the tone of interest from the LO comb, see Section B.5 for details. In all experiments, we perform offline processing including filtering, frequency offset compensation, clock recovery, polarization demultiplexing, dispersion compensation, and equalization.

B.1.5 Transmission impairments and data rates

In our transmission experiments, performance was impaired by specific limitations of the available laboratory equipment, which can be avoided in real-world transmission systems. For the transmission experiment using a single DKS comb generator as optical source, Fig. 5.2(a), a total of 101 tones were derived from the comb in the C and L band. Out of those, 92 carriers performed better than the BER threshold of 4.5×10^{-3} for widely used second-generation forward-error correction (FEC) with 7 % overhead see Fig. 5.2(e). The pump tone at approximately 192.66 THz and two neighbouring carriers could not be used for data transmission due to strong amplified spontaneous emission (ASE)

background from the pump EDFA. Two more directly adjacent channels exceeded the threshold of 4.5×10^{-3} , but were still below the BER threshold of 1.5×10^{-2} for soft-decision FEC with 20 % overhead [43]. Another four channels at the low-frequency end of the C-band were lost due to a mismatch on the transmission band of the C-band filters used to realize the demultiplexer, see Section B.3 for a more detailed description. This leads to an overall net data rate (line rate) of 28.0 Tbit/s (30.1 Tbit/s).

For the transmission experiment using interleaved DKS combs as optical source at the transmitter, Fig. 5.2(c), we use a combination of 16QAM and QPSK, depending on the optical signal-to-noise power ratio (OSNR) of the respective carrier, see Fig. 5.2(e). For 16QAM transmission, a total of 126 channels exhibit a BER of less than 4.5×10^{-3} , requiring an FEC overhead of 7 %, and 39 additional channels showed a BER below 1.5×10^{-2} , which can be corrected by FEC schemes with 20 % overhead. For the 14 channels at the low-frequency edge of the L band, the modulation format was changed to QPSK due to the low power of these carriers caused by a decrease of amplification of the L-band EDFA in this wavelength range. This leads to an overall net data rate (line rate) of 50.2 Tbit/s (55.0 Tbit/s).

For the transmission experiment using DKS frequency combs both at the transmitter and at the receiver side, Fig. 5.3(a), 99 tones were transmitted and tested. Out of those, a total of 89 channels perform better than the BER threshold for hard-decision FEC with 7 % overhead (4.5×10^{-3}), and additional four channels are below the BER limit of 1.5×10^{-2} for soft-decision FEC with 20 % overhead. For the remaining channels, coherent reception was inhibited by low OSNR. This leads to an overall net data rate (line rate) of 34.6 Tbit/s (37.2 Tbit/s). The black circles in Fig. 5.3(d) show the channels with BER above the threshold for 7 % FEC and specify the reasons for low signal quality: low optical carrier-to-noise power ratio (OCNR) of the carriers from the LO comb (LO) and the signal comb (Signal) as well as bandwidth limitations of the C-band EDFA (EDFA).

It is further worth noting that field-deployed WDM systems rely on statistically independent data channels rather than on transmitting identical data streams on the “even” and the “odd” channels. As a consequence, real-world signals will

suffer much less from coherent addition of nonlinear interference noise than the signals used in our experiments [182]. With respect to nonlinear impairments, our experiments hence represent a bad-case scenario with further room for improvement.

B.1.6 Characterization of the OSNR penalty of frequency comb source

For comparing the transmission performances of a single comb line to that of a high-quality external cavity laser (Keysight N7714A) reference carrier, we measure the OSNR penalty at a BER of 4.5×10^{-3} , which corresponds to the threshold for FEC with 7 % overhead [43]. For a given BER, the OSNR penalty is given by the dB-value of the ratio of the actually required OSNR to the OSNR that would be theoretically required in an ideal transmission setup [129].

A detailed description of the associated experimental setup is given in Section B.4. The carrier under test is selected by a band-pass filter with a 1.3 nm (160 GHz) wide passband. The carrier is then amplified to 24 dBm by an EDFA (EDFA2 in Fig. B.3 and modulated with a PDM-16QAM signal at 40 Gbd. Next, an ASE noise source together with two VOA is used to set the OSNR of the channel while keeping its optical power constant. As an ASE generator, we use a second EDFA (EDFA3 in Fig. B.3(a)). An optical spectrum analyzer (OSA, Ando AQ6317B) is used for measuring the OSNR at the input of the receiver. For each OSNR value, the quality of the channels is determined by measuring the BER using our previously described receiver configuration, see the Section “Data transmission experiments” above in Appendix B.1.4. At a BER of 4.5×10^{-3} , a penalty of 2.6 dB with respect to the theoretical OSNR value is observed, see Fig. 5.2(f), which is a common value for technical implementations of optical 16QAM transmitters [139]. For high OSNR, an error floor caused by transmitter nonlinearities and electronic receiver noise is reached. The maximum achievable OSNR of 44 dB at 192.56 THz for transmission with the comb line is dictated by ASE noise of the C/L-band EDFA (EDFA1) right after the FCG, see Fig. B.3. As a reference, the same measurements are repeated using a high-quality ECL (Keysight N7714A) to generate the carrier, which leads to essentially the same OSNR penalty for a given BER as the transmission

with the comb line. For a symbol rate of 40 GBd, the results are shown in Fig. 5.2(f), similar results are obtained at other symbol rates such as 28 GBd, 32 GBd and 42.8 GBd. Note that for transmission with the ECL, only one EDFA (EDFA2) is needed to increase the power to 24 dBm before being modulated. As a consequence, a higher maximum OSNR of 58 dB can be achieved with the ECL than with the comb line. Note in addition that for transmission with a single line, the lowest BER reached at 40 GBd is below 10^{-4} , as depicted in Fig. 5.2(f). This value, however, is not reached in the WDM transmission experiment with the full comb, Fig. 5.2(a) and Fig. 5.3(d). For WDM transmission, a larger number of carriers are amplified by the EDFA in front of the modulator, which, together with the limited output power of the EDFA (EDFA 2-5 in Fig. B.2(a)), decreases the optical power per line and hence the OCNR. Moreover, when interleaving two frequency combs, a VOA and a directional coupler are inserted into the setup, thereby introducing additional loss which needs to be compensated by the subsequent EDFA. Using additional EDFA would therefore increase the quality of the received signal.

B.2 Kerr soliton frequency comb generation

Figure B.1(a) shows the detailed setup of the dissipative Kerr-soliton (DKS) frequency comb generators (FCG) used for the data transmission experiments discussed in the main paper. The DKS frequency comb is generated by pumping a silicon nitride (Si_3N_4) microresonator with an external cavity laser (ECL). A polarization controller (PC) before the microresonator is adjusted for maximum coupling of pump light into the resonance. The pump light generated by the ECL is amplified by an erbium-doped fiber amplifier (EDFA) which is operated at an output power of approximately 35 dBm. After the EDFA, a high-power band-pass filter (BPF) is used to suppress amplified stimulated emission (ASE) noise. Since the passband of the BPF has finite non-zero width, noise near the pump frequency is not fully suppressed, thereby deteriorating the signal quality of the adjacent carriers. A pair of lensed fibers (LF) with a mode field diameter of $3.5 \mu\text{m}$ are used to couple light into and out of the microresonator, leading to 1.4 dB of insertion loss per facet. The temperature of the microresonator is adjusted and stabilized by a thermoelectric controller (TEC), while an optical

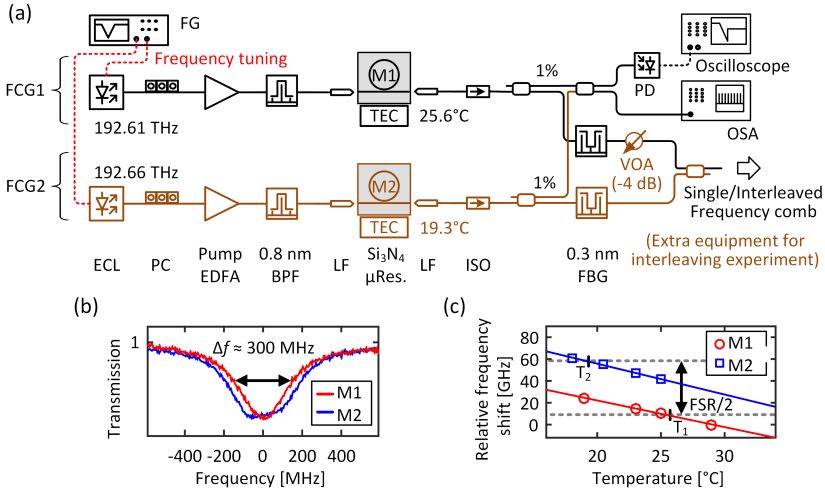


Figure B.1: Generation of single and interleaved DKS frequency combs. **(a)** Setup for generation of single and interleaved DKS frequency combs. The frequency comb generator (FCG) for single-comb generation is depicted in black (FCG1); for dual-comb generation and interleaving, a second FCG (FCG2) is used, depicted in brown. The microresonators (M1, M2) are driven by a pair of linearly polarized continuous-wave (CW) external-cavity lasers (ECL) whose output powers are boosted by erbium-doped fiber amplifiers (EDFA). The frequency of each ECL is controlled via an analog signal generated by a function generator (FG) for tuning into a soliton state. Amplified spontaneous emission (ASE) noise from the power booster EDFA is suppressed by two band-pass filters (BPF) with 0.8 nm passbands. Pump light is coupled to and from the resonator chips by lensed fibers (LF) having a mode field diameter of $3.5 \mu\text{m}$, which leads to 1.4 dB of losses per facet, measured at the pump wavelength. After the microresonators, optical isolators (ISO) avoid back reflection of light into the chip. Fiber Bragg gratings (FBG), acting as notch filters with a 0.3 nm bandwidth, are used to attenuate the residual pump light to a power level comparable to that of the adjacent carriers. Prior to the interleaving of both frequency combs with a directional coupler, a variable optical attenuator (VOA) with an attenuation of 4 dB adapts the power level of one comb to the other. A real-time oscilloscope connected to a photodiode (PD) and an optical spectrum analyzer (OSA) are used to track the change of transmitted power and to measure the comb spectrum. **(b)** Transmitted optical power measured by the PD as a function of the ECL frequencies, around the center frequency of the cold resonances from M1 (red) and M2 (blue). A width of about 300 MHz is measured for both microresonators, corresponding to a loaded quality factor of approximately 7×10^5 . The different shape of the resonances is attributed to spurious coupling of counter-propagating waves in M2. (Caption continued on next page)

Figure B.1 continued: (c) Temperature-induced frequency shift of the comb carriers from M1 and M2 relative to the frequencies of the comb carriers from M1 at 28 °C. A dependence of -2.2 GHz/K and -2.7 GHz/K is measured for M1 and M2, respectively. Temperatures $T_1 = 25.6^\circ\text{C}$ and $T_2 = 19.3^\circ\text{C}$ are chosen for M1 and M2 such that the frequency difference of the carriers near the center of the interleaved comb is half the line spacing of the frequency comb from M1.

isolator (ISO) at the output avoids back-reflection of light into the chip. A fiber Bragg grating (FBG) acts as a notch filter with a 0.3 nm bandwidth to suppress the remaining pump laser up to a level comparable to that of the adjacent frequency comb carriers.

DKS frequency combs are generated by operating the microresonator in the effectively red-detuned regime with respect to the cavity resonance, i.e., the pump wavelength is bigger than the wavelength of the thermally shifted resonance. This regime is accessed by fast sweeping of the pump ECL through the cavity resonance from a blue-detuned wavelength to a predefined red-detuned wavelength (forward-tuning), where a multiple-soliton comb state is generated [21], [75], see trace I of Fig. 5.1(b). The transition to a single-soliton state is accomplished in a reliable and deterministic manner by adiabatically reducing the wavelength of the pump laser (backward-tuning) thereby approaching the hot-cavity resonance from the red side [22], see trace II of Fig. 5.1(b). In both sweeps, the ECL wavelength is controlled via an analogue voltage signal generated by a function generator (FG). The forward-tuning is performed at a speed of approximately 100 pm/s and is fast enough to avoid excess heating of the microresonator, which would lead to loss of the soliton comb state due to a too strong thermal shift of the cavity resonance. The backward-tuning is performed at a speed of approximately 1 pm/s and is slow enough to adiabatically switch between different multiple-soliton states. A real-time oscilloscope and an optical spectrum analyzer (OSA) are used to track the change of transmitted power and to measure the comb spectrum, respectively, while sweeping the pump wavelength along the resonance.

For the interleaved-comb experiment, Fig. 5.2(c), two DKS comb sources, namely M1 and M2, with comparable free spectral ranges (FSR) are used in parallel. The equipment required for the second FCG (FCG2) and for

interleaving the soliton Kerr combs of the two microresonators is marked in brown in Fig. B.1(a). FCG2 is setup similar to FCG1 as discussed above. For interleaving, the two DKS frequency combs from FCG1 and FCG2 are superimposed by a directional coupler. Note that for the microresonator M2, a lower conversion efficiency of optical pump power to soliton power is observed as compared to that of microresonator M1. This can be attributed to spurious coupling of counter-propagating waves in M2, which also explains the difference in the shape of the resonances from M1 and M2 depicted in Fig. B.1(b). Therefore, the power level of the frequency comb from M1 is adapted to that of M2 by a variable optical attenuator (VOA) before interleaving with the directional coupler. This results in a uniform power spectral envelope of the interleaved frequency comb. To obtain an interleaved comb with evenly spaced carriers, the working temperatures of the microresonators are set such that one of the frequency combs is offset by half the line spacing with respect to the other. Figure B.1(c) shows the frequency shift of the carriers of M1 (red) and M2 (blue), relative to the frequency of the carriers from M1 at 28 °C, as a function of the microresonator temperature. Both frequency combs follow a linear trend with a shift of -2.2 GHz/K and -2.7 GHz/K for M1 and M2, respectively [176]. At the temperature T_1 (T_2) for microresonator M1 (M2) the frequency difference between the central carriers of both combs is half the line spacing. The pump frequency for the microresonator M1 (M2) is set to 192.61 THz (192.66 THz) for the chosen chip temperature of $T_1 = 25.6$ °C ($T_2 = 19.3$ °C). At such temperatures, the measured line spacing is 95.80 GHz (95.82 GHz) for M1 (M2), leading to a difference of approximately 20 MHz, or 0.02% of the line spacing. Such a difference would lead to a variation of the line spacing by ± 1 GHz at the edges of the interleaved frequency comb as compared to the line spacing near the center of the comb. This mismatch can be avoided by carefully matching the line spacing of the two combs, e.g., by improving the uniformity of the fabrication process, see Appendix B.1.1 for details. In the transmission experiment, the variation of line spacing did not have any significant influence on the quality of the received signal.

B.3 Data transmission experiments using Kerr-soliton frequency combs in the transmitter

The setup used for massively parallel wavelength-division multiplexing (WDM) data transmission is depicted in Fig. B.2(a). The single (interleaved) frequency comb generated by FCG1 (FCG1 and FCG2) is amplified by a C/L-band EDFA (EDFA 1) to a level of approximately 5 dBm (2 dBm) per carrier. For a realistic emulation of massively parallel WDM transmission, neighboring carriers need to be encoded with independent data streams [183], [184]. To this end, the comb is divided into even and odd carriers by a de-interleaver (DI) stage. The DI stage contains a directional coupler (CPL1) that divides the optical power into two parts, which are fed to a C-band and an L-band programmable filter (Finisar WaveShaper; WS). The WS splits even and odd carriers within the respective band. After the C- and the L-band WS, each set of carriers is amplified by EDFA 2-5 to compensate for optical losses caused during de-interleaving. Next, the C- and L-band odd carriers are recombined by the use of a C/L-band multiplexer (C/L MUX) before being coupled into an optical in-phase/quadrature (IQ) modulator (IQ1). The even carriers are also recombined and sent through IQ2. The WS are adjusted to compensate for the power differences of the comb carriers and for the spectral variations of the EDFA gain profile, thereby producing an overall flat spectrum at the inputs of IQ1 and IQ2. Both modulators are driven by either 16QAM or QPSK drive signals generated by a high-speed arbitrary waveform generator (AWG, Keysight M8195A 65 GS/s) using pseudo-random bit sequence (PRBS) of length $2^{11} - 1$, to encode data on each frequency comb carrier at a symbol rate of 40 GBd. Raised-cosine pulse shaping at a roll-off factor of $\beta = 0.1$ is used for improved spectral efficiency. After modulation, odd and even channels are combined by a directional coupler (CPL2). Polarization-division multiplexing (PDM) is emulated by splitting the data stream into two paths and recombining them on orthogonal polarizations with a decorrelating delay of approximately 1.5 ns (60 symbols) in one path and an attenuator in the other one for maintaining the same power levels. Hence, even if both polarizations contain the same PRBS sequence, they are detected as uncorrelated data streams at the coherent receiver. The signal is then amplified and transmitted through 75 km of standard

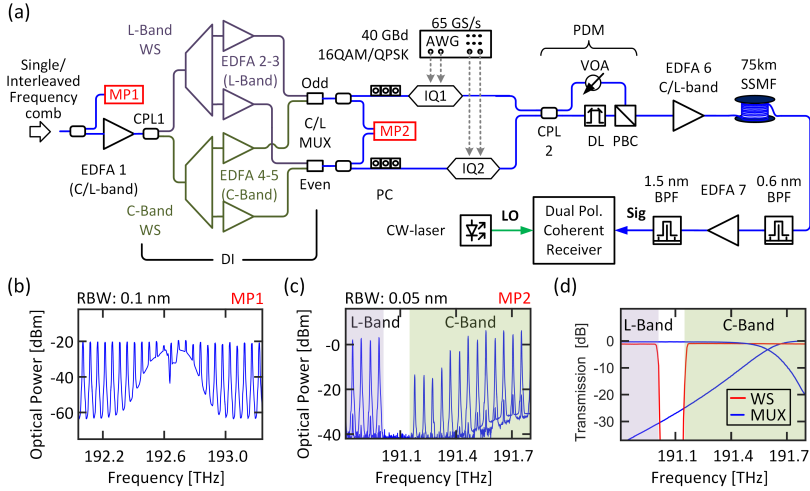


Figure B.2: Data transmission with single and interleaved DKS frequency combs as WDM carriers at the transmitter. **(a)** Data transmission setup: The single (interleaved) frequency comb generated by FCG1 (FCG1 and FCG2) from Fig. B.1(a) is amplified by EDFA 1 to a level of approximately 5 dBm (2 dBm) per carrier. Afterwards, WDM is emulated by encoding independent data into neighboring carriers. To this end, the comb is divided into even and odd carriers by a de-interleaver (DI) stage. The DI stage contains a directional coupler (CPL1) that divides the optical power into two parts, which are fed to a C-band and an L-band programmable filters (WS). The WS split the input comb lines into even and odd carriers within their respective bands. Each set of carriers is amplified by an EDFA to compensate for the optical losses caused by the de-interleaving. Next, C- and L-band carriers from each set are recombined by the use of a C- and L-band multiplexer (C/L MUX) and coupled into two optical IQ modulators (IQ1, IQ2), driven by 16QAM or QPSK drive signals generated by a high-speed AWG. We use a symbol rate of 50 GBd. After combining the modulated signals by a directional coupler (CPL2), PDM is emulated by splitting the data stream into two paths and recombining them on orthogonal polarizations using a polarization beam combiner (PBC) with a delay line (DL) in one path and a variable optical attenuator (VOA) in the other one to decorrelate the data while maintaining the same power levels. The signal is amplified and transmitted through a 75 km long standard single mode fiber (SSMF). At the receiver, a tunable BPF with a 0.6 nm passband selects the channel under test, which is amplified by a C- or L-band EDFA (EDFA 7), depending on which channels are being investigated. A second BPF (1.5 nm passband) suppresses the ASE noise from the EDFA. The modulated channels are received on a dual-polarization coherent receiver using a conventional external-cavity laser as optical local oscillators (LO). (Caption continued on next page)

Figure B.2 continued: An optical modulation analyzer (OMA) comprising two real-time oscilloscopes is used to record and process the data signals. Labels MP1 and MP2 represent monitor ports where the spectra shown in b and c, respectively, were recorded. These spectra show impairments of the OCNR which limit the signal quality. **(b)** Frequency comb spectrum in the vicinity of both pump frequencies showing the ASE noise coming from the pump EDFA, see Fig. D.1. **(c)** Frequency comb spectrum of the carriers at the gap between the C- and L-band WS. The low optical power of the carriers at the low-frequency edge of the C-band is caused by a mismatch between the C-passbands of the C/L MUX and the WS. **(d)** Transmission profiles of the C- and L-band WS (red) and of the C- and L-band C/L MUX (blue). For decreasing frequency, the C-band of the C/L MUX shows a decreasing transmission already from 191.7 THz, whereas the transmission band of the C-band WS reaches to 191.2 THz. This mismatch causes strong attenuation of the carriers within this region.

single mode fiber (SSMF). At the receiver, a tunable BPF with a 0.6 nm passband selects the channel under test. The signal is then amplified by a C- or L-band EDFA (EDFA 7), depending on which frequency band is being investigated, and is passed through a second 1.5 nm passband BPF to suppress the ASE noise from the EDFA. Afterwards, the channel is received on a dual-polarization coherent receiver which uses a conventional continuous-wave laser as an optical local oscillator (LO). An optical modulation analyzer (OMA, Keysight N4391A) comprising two real-time oscilloscopes (Keysight DSO-X 93204A, 80 GSa/s) is used to record and process the data signals. The constellation diagram for each channel is obtained after performing signal processing consisting of digital low-pass filtering, polarization demultiplexing, chromatic dispersion compensation, frequency offset estimation, carrier phase estimation, and adaptive equalization. The block length for performing the signal processing is chosen to be 1024 symbols, which is optimized to effectively track the changes of carrier phase and polarization of the received signal. The extracted bit error ratio (BER) is used as a metric to quantify the signal quality of each channel and it is shown in Fig. 5.2(e) of the main paper. Note that for the interleaved-comb experiment, we chose the approach of first recombining the unmodulated combs by means of a directional coupler, Fig. B.1(a), and then de-interleaving them again by means of the DI stage, Fig. B.2(a), to perform spectral flattening on the unmodulated carriers rather than on the densely packed spectrum of the data signals. Equalizing the data signals would unavoidably have led to distortions due to spectral variations of the attenuation within individual WDM channels.

Limitations of the transmission capacity of our experiments were identified by investigating the spectrum of the interleaved frequency comb at the monitor ports MP1 and MP2 in Fig. B.2(a). A fraction of the spectrum, measured at MP1 around the frequency of the pump lasers is shown in Fig. B.2(b). The spectrum exhibits strong residual ASE noise coming from the pump EDFA of FCG1 and FCG2, which passes the relatively wide 0.8 nm BPF centered at the pump frequencies of approximately 192.6 THz. This ASE noise directly deteriorates the optical carrier-to-noise power ratio (OCNR) of the tones adjacent to the pump frequencies, rendering these carriers unusable in the data transmission experiments. Figure B.2(c) depicts a fraction of the spectrum measured at MP2 and centered at the frequency gap between the C and the L bands near 191.4 THz. The gap originates from the limited bandwidth of the C- and the L-band WS. As can be seen in Fig. B.2(c), there is a strong attenuation of the carriers at the low-frequency edge of the C-band. This is caused by a mismatch between the passbands of the C/L MUX and the passbands of the WS, see Fig. B.2(d). For decreasing frequency, the C-band output of the C/L MUX shows a decreasing transmission starting already at 191.7 THz whereas the C-band WS features a flat transmission band that goes down to 191.2 THz. For the high-frequency edge of the L-band, the passband mismatch does not have any influence because the C/L MUX shows perfect transmission for all frequencies that can pass the L-band WS. All these impairments are not related to the comb sources and can be avoided by using optimized devices and filters with matched passbands. We hence believe that there is considerable room for improving signal quality and further increasing the overall transmission capacity.

Another constraint in the data transmission experiments was the limited saturation output power of EDFA 2-5. To quantify the influence of the power per tone on the BER, an extra experiment is performed with less channels but the same spectral efficiency (SE). To this end, we reduce the number of L-band channels from 97 to 48. These channels were located in the center of the L band, and the number of C-band channels were not changed. In this situation, an average BER of 2.3×10^{-3} was obtained for the L-band channels, corresponding to approximately half the averaged BER of 4.7×10^{-3} obtained when all L-band carriers were used for transmission. This proves that the current transmission capacity is not limited by the comb source, but by the components of the

transmission systems. Note, in addition, that for the interleaved-comb experiment the power per carrier at the input of EDFA 1 is reduced compared to the single Kerr soliton comb experiment due to an additional directional coupler for interleaving the combs and due to a variable optical attenuator (VOA) used to adapt the power levels of the two combs, see Fig. B.1(a). This explains the slightly worse performance in signal quality of the received channels using interleaved frequency combs at the transmitter as compared to the signal quality of the received channels when using a single Kerr soliton comb at the transmitter.

B.4 OSNR measurements

In this section we introduce the formalism used to calculate the theoretical BER obtained in a data transmission experiment as a function of the optical signal-to-noise power ratio measured at the reference bandwidth of 0.1 nm (OSNR_{ref}), see Fig. 5.2(f) of the main paper. We estimate the required theoretical OSNR_{ref} per channel as a function of the target BER for different symbol rates. Furthermore, we also examine our experimental measurement results.

B.4.1 Theoretical required OSNR for error free transmission with FEC

The BER of quadratic K -ary QAM signals with r bits per symbol can be analytically calculated from the OSNR_{ref} (measured for instance with an optical spectrum analyzer, OSA) [44], [129]. The basic assumptions are that optical additive white Gaussian noise (AWGN) is the dominant source of errors, thus neglecting nonlinear effects and electronic noise, and that reception is data-aided, which is required to measure directly the experimental BER. The relation for 16QAM, where $K = 2^r = 16$, is given by

$$\text{BER} = \frac{3}{8} \text{erfc} \sqrt{\frac{\text{OSNR}}{10}}, \quad (\text{B.1})$$

where OSNR is the signal-to-noise power ratio, where the noise power is measured within the signal bandwidth B_s for the same polarization as the signal. The

signal bandwidth B_s corresponds to the effective bandwidth of a receiver filter that is matched to the received pulse shape. For raised-cosine pulses as used in our experiments, this bandwidth corresponds to the symbol rate and does not depend on the roll-off-factor β . The OSNR is related to the commonly used signal-to-noise power ratio OSNR_{ref} , where the signal and noise powers are measured in both polarizations in a reference bandwidth B_{ref} .

$$\text{OSNR} = \frac{2B_{\text{ref}}}{p \cdot B_s} \text{OSNR}_{\text{ref}} , \quad (\text{B.2})$$

with $p = 1$ for a single-polarization signal and $p = 2$ for a polarization-multiplexed signal [32]. The reference bandwidth B_{ref} is taken to be 12.5 GHz, which corresponds to 0.1 nm resolution bandwidth of an OSA at 1550 nm carrier wavelength. If redundancy is included in the coding of the bit stream to reduce the BER, Eq. (B.2) is modified by the coding overhead, O_c , to:

$$\text{OSNR} = (1 + O_c) \frac{2B_{\text{ref}}}{p \cdot B_s} \text{OSNR}_{\text{ref}} . \quad (\text{B.3})$$

Combining Eqs. (B.1) and (B.3), we can derive the required OSNR_{ref} for a given symbol rate and coding overhead. Figure B.3 shows the theoretical required OSNR_{ref} per channel for a targeted raw BER of 4.5×10^{-3} with $O_c = 7\%$ coding overhead as a function of the net symbol rate. In this context, raw BER means the uncorrected BER obtained before applying forward-error correction (FEC) based on the 7% of redundancy. For example, at a symbol rate of 40 GBd, an OSNR_{ref} higher than 20 dB is required theoretically to achieve a raw BER below the targeted threshold BER of 4.5×10^{-3} , and FEC will allow to bring the BER further down to values below 10^{-15} . Note that the OSNR_{ref} values provided in Fig. B3 refer to the input of the coherent receiver, and hence must be considered as a minimum requirement for the OSNR_{ref} at the output of the transmitter discussed in Section B.6 and specified in Table B.1. Note that in field deployed systems, impairments such as electronic noise or nonlinear effects will increase the required OSNR_{ref} by the so-called OSNR penalty. The OSNR penalty has been experimentally measured for our system at different symbol rates, see Section B.4.2.

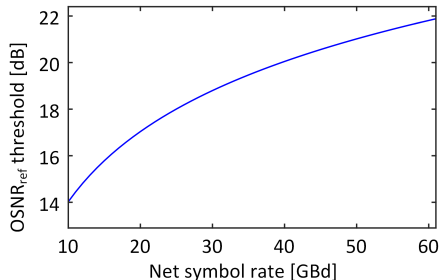


Figure B.3: Theoretical required OSNR_{ref} at the input of the coherent receiver as a function of the net symbol rate for a targeted raw BER of 4.5×10^{-3} . The plot refers to 16QAM signaling, dual-polarization transmission, and a 7 % coding overhead. Raw BER means the BER before applying FEC, which can bring the final BER down to values below 10^{-15} .

B.4.2 OSNR measurements

In an extra set of experiments, we compare the 16QAM transmission performance of individual comb lines of our Kerr soliton frequency comb, featuring optical linewidths below 100 kHz, to that of a high-quality ECL reference carrier (Keysight N7714A) with an optical linewidth of approximately 10 kHz. As a metric for the comparison we use the OSNR penalty. For a given BER, the OSNR penalty is given by the dB-value of the ratio of the actually required OSNR to the OSNR that would be theoretically required in an ideal transmission setup, see Section B.4.1 and Fig. B.3. The corresponding setup for OSNR penalty measurements is depicted in Fig. B.4(a). We use the frequency comb from FCG1, Fig. B.1(a), tap it directly after the FBG, and amplify it by a C/L-band EDFA (EDFA 1) to bring the comb to a level of approximately 5 dBm per carrier – just like in the transmission experiment. The carrier under test is then selected by operating the C-band WS as a band-pass filter with a 1.3 nm (160 GHz) wide passband and coupled to a C-band EDFA (EDFA 2). The bandwidth of the WS is chosen to effectively suppress all the neighboring comb lines. For the reference transmission experiments, an ECL with an output power of 16 dBm is directly connected to EDFA 2. In both cases, the carrier under test is amplified to 24 dBm by EDFA 2 before being modulated in IQ 1 using 40 GBd PDM-16QAM. To quantify the signal quality, we investigated the BER

of the received channel for different OSNR_{ref} values. The OSNR_{ref} of the signal is adjusted by using a noise-loading system, consisting of an ASE noise generator (EDFA 3) and two VOA. The VOA are used to modify the ASE noise power while feeding the preamplifier (EDFA 4) of the receiver with a constant optical input power. This assures that the same receiver sensitivity is maintained for all OSNR_{ref} values investigated. An optical spectrum analyzer (OSA, Ando AQ6317B) is used to measure the OSNR_{ref} at the input of the receiver. For each OSNR_{ref} level, signal quality is determined by using the OMA to measure the BER after EDFA4 and after an additional BPF.

A section of the comb spectrum recorded at MP3 and showing four carriers of the unmodulated frequency comb is depicted in Fig. B4(b). Here, the carriers still exhibit an OCNR_{ref} of approximately 50 dB, measured at a reference bandwidth of 0.1 nm (12.5 GHz). This value, however, cannot be maintained throughout the setup and is reduced by the noise of the subsequent amplifiers. After filtering by the 1.3 nm BPF, the carrier under test features an optical power of approximately 0 dBm. Note that this is a much lower power level than the 16 dBm of output power generated by the ECL. To enable a fair comparison that also accounts for the superior per-carrier power levels of the ECL, we decided to use the ECL at its full output power rather than attenuating it to the 0 dBm provided by the comb source. As a consequence, we find an OCNR_{ref} of 58 dB of the ECL carrier after EDFA 2, which is higher than the 42 dB achieved for the amplified comb line at 193.56 THz, see spectra in Fig. B4(c), measured at MP4. Note that two noise floor levels can be identified for the comb carrier. The high-power spectral shoulder around the carrier, which is used to calculate the OCNR_{ref} , is caused by the noise of EDFA 1 and is suppressed further away from the carrier by the 1.3 nm BPF, whereas the low-power background arises from the noise of EDFA 2. Hence, the maximum achievable OSNR_{ref} for transmission with the comb line is dictated by ASE noise of the C/L-band EDFA (EDFA 1) right after the FCG. Using comb sources with higher output levels can help to further increase the signal quality. An exemplary data signal spectrum for the ECL (red) and comb (blue) carriers before entering the coherent receiver is shown in Fig. B.4(d) as measured at MP5. Both signals are set to the same power and the same OSNR_{ref} using the VOA.

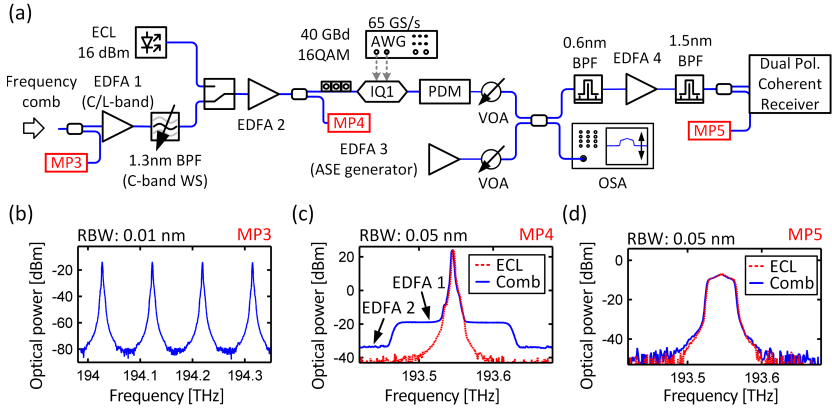


Figure B.4: Comparison of isolated frequency comb carriers with ECL carriers for data transmission. **(a)** Setup for OSNR penalty measurements: The frequency comb is generated by FCG1, see Fig. B.1(a), and amplified by a C/L-band EDFA (EDFA 1). A single carrier is either generated by an ECL or selected from the comb by operating the C-band programmable filter (WS) as a band-pass filter (BPF) with a 1.3 nm (160 GHz) passband. The carrier under test further amplified to 24 dBm by EDFA 2 before being modulated with PDM-16QAM at 40 Gb/s. To adjust the optical signal-to-noise ratio (OSNR) of the signal, a noise-loading system is used, consisting of an ASE noise generator (EDFA 3) and two VOA to modify the ASE noise power while feeding EDFA 4 with a constant optical input power. The signal is sent to the receiver where it is further amplified and analyzed by an OMA. Labels MP3, MP4 and MP5 represent monitor ports where the spectra shown in b, c and d, respectively, were recorded. These spectra have been corrected to take into account the tapping ratios of the respective power splitters. **(b)** Section of the frequency comb spectrum (resolution bandwidth RBW = 0.01 nm) as obtained from the output of FCG1. The carriers show an OCNR of approximately 50 dB at a reference bandwidth of 0.1 nm. **(c)** Frequency comb (blue) and ECL (red) carriers after EDFA 2. The frequency comb carrier shows two noise floor levels: The high-power spectral shoulder around the carrier is caused by ASE from the C/ L band EDFA (EDFA 1), which is suppressed further away from the carrier by the 1.3 nm-wide BPF, whereas the low-power ASE noise background arises from EDFA 2. The OCNR of the ECL carrier amounts to 58 dB, whereas an OCNR of 42 dB is achieved for the comb line at 193.56 THz, both measured at a reference bandwidth of 0.1 nm. **(d)** Spectrum of the received modulated data for both the frequency comb and ECL carriers with 40 Gb/s PDM-16QAM modulation.

Results of the OSNR penalty measurements are depicted in Fig. 5.2(f) of the main paper. The carriers derived from the frequency comb source do not exhibit any additional implementation penalty in comparison to those generated by the reference ECL. However, the higher achievable OCNR provided by the ECL may translate into longer transmission link, which makes DKS frequency comb sources more suitable for rather short metro and regional distances. Similar results were also obtained when comparing ECL and comb carriers at symbol rates of 28 GBd, 32 GBd and 42.8 GBd.

In our setup we observe an OSNR penalty of 2.6 dB with respect to the theoretical required OSNR_{ref} . This value compares well with similar transmission experiments [139], [185], [186]. In Ref. [185], an OSNR_{ref} penalty of approximately 2.5 dB is observed with respect to the theoretical required OSNR_{ref} when transmitting DP-16QAM at 43 GBd. It is reasonable therefore to consider a penalty of 2.5 dB, meaning that an OSNR_{ref} per channel of approximately 22.5 dB is required for error free transmission using FEC with 7% overhead [43] at 40 GBd and approximately 23 dB at 50 GBd. In our transmission experiment, described in Fig. 5.3 of the main paper, the minimum measured channel OSNR_{ref} amounts to 23 dB, measured at a reference bandwidth of 0.1 nm. The corresponding channel is at the high-frequency edge of the C-band. The measured raw BER for this channel corresponds to approximately 4.5×10^{-3} , which fits the expected required OSNR_{ref} derived in the previous section.

B.5 Coherent reception using a Kerr-soliton frequency comb LO

Figure B.5(a) shows the WDM data transmission setup with a DKS frequency comb generator (FCG) as a multi-wavelength source at the transmitter (signal) and as a multi-wavelength local oscillator at the receiver (LO). The microresonator used at the transmitter side (Tx) corresponds to M1 from Fig. B.1(a). To provide the multi-wavelength LO, an additional microresonator (M3) with similar line spacing is used at the receiver side. Both combs are matched in absolute frequency position by adjusting the microresonators' temperature.

The pump frequency for the signal (LO) comb is 193.56 THz (192.89 THz), the on chip pump power is 32.5 dBm (32 dBm) and the temperature is set to 16.4 °C (23.4 °C). We chose to pump the aforementioned resonances as they present the highest power conversion efficiency. The frequency comb obtained from M3 features a slightly lower line spacing of approximately 95.70 GHz as compared to that of M1, 95.80 GHz, due to fabrication inaccuracies. When using the carriers from M3 as LO for coherent intradyne detection, such difference in line spacing translates into a non-zero intermediate frequency (IF). The IF can be brought down to values below 100 MHz near the center of the frequency combs at around 191.5 THz but it reaches relatively high frequencies of approximately 4 GHz when coherently demodulating the signals at the low frequency edge of the L band and at the high frequency edge of the C band. The high IF, however, does not prohibit data transmission as it can be removed using digital signal processing after detection of the transmitted signal with our coherent receiver. However, for high IF, the received signal is slightly affected by the limited electrical bandwidth ($BW = 33$ GHz) of the analog-to-digital convertor (ADC) of our coherent receiver. This leads to a reduction of the electrical power, and thus of the electrical signal-to-noise ratio, of our baseband signal. The high IF, nonetheless, can be avoided by carefully matching the line spacing of the two Kerr soliton frequency comb sources during fabrication.

As in the previous experiments, WDM transmission is emulated by encoding independent data streams on adjacent channels, see Fig. B.2(a). To this end, the transmitter frequency comb (signal) is de-interleaved into even and odd carriers using two programmable filters (WS) for the C band and the L band. After amplifying the respective carriers by EDFA 2-5 operated at 24 dBm of output power, the C-band and L-band portions of the odd (even) carriers are combined by directional couplers and sent through optical IQ-modulators IQ1 (IQ2).

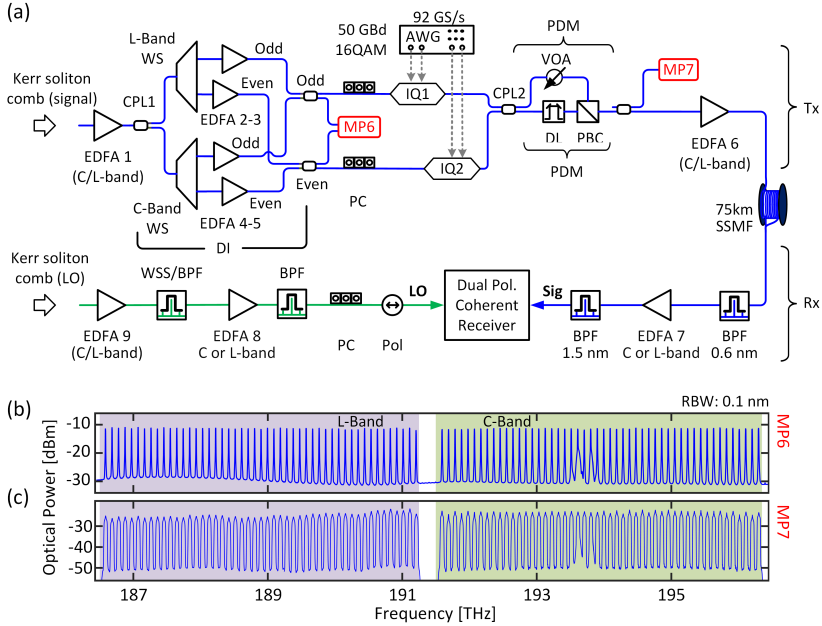


Figure B.5: All-soliton data transmission setup using a dissipative Kerr-soliton (DKS) frequency comb as a multi-wavelength local oscillator for coherent detection. **(a)** Data transmission setup: Two independent DKS frequency comb generators provide both the carriers for WDM coherent data transmission (signal) and for parallel intradyne detection (LO). At the transmitter side (Tx), WDM is emulated by encoding independent data into neighboring carriers. To this end, the comb is divided into even and odd carriers by a de-interleaver (DI) stage. As in the previous experiments, the DI stage contains a directional coupler (CPL1) that divides the optical power into two parts, which are fed to a C-band and an L-band programmable filter (WS) to select even and odd set of carriers within the respective band. Each set of carriers is amplified by an additional EDFA to compensate for the optical losses caused by the de-interleaving. Next, the C- and L-band carriers from each set are recombined by a directional coupler and sent through two different optical IQ-modulators (IQ1, IQ2). Both modulators are driven by 16QAM drive signals generated by a high-speed arbitrary waveform generator (AWG) using pseudo-random bit sequences (PRBS) of length $2^{11} - 1$. The symbol rate amounts to 50 GBd, and we use raised-cosine pulse shaping with a roll-off factor $\beta = 0.1$. After combining the signals by a directional coupler (CPL2), polarization division multiplexing (PDM) is emulated by splitting the data stream into two paths and recombining them on orthogonal polarizations with a decorrelating delay in one path and an attenuator in the other for maintaining the same power levels. The PDM signal is amplified and transmitted through a 75 km long standard single mode fiber (SSMF). (Caption continued on next page)

Figure B.5 continued: At the receiver side (Rx), the LO tones and the transmitted channels are filtered and amplified before being coupled to a dual-polarization coherent receiver which performs digital signal processing (DSP) to decode the data and to determine the BER. A polarization controller (PC) and polarizer are used to adjust the LO-line to the pre-defined input polarization of the coherent receiver. The spectra recorded at monitor ports (MP) 6 and 7 are shown in panels b and c. **(b)** Spectrum of the combined odd and even carriers prior to modulation. The flat spectrum is achieved by adjusting the WS to compensate for the power differences of the frequency comb carriers and the spectral variations of the EDFA gain profiles. **(c)** Spectrum of the data channels prior to fiber transmission. The spectrum was taken in eight segments with individually optimized bias points of the modulators to compensate for the wavelength dependence of the devices.

Note that the C/L MUX of the de-interleaver (DI) stage from Fig. B.2(a) has been replaced by a directional coupler to avoid the power attenuation of the carriers at the low-frequency edge of the C-band, which was described in Section B.3. The WS are also used to compensate the power differences of the carriers and the spectral variations of the EDFA gain profile, thereby producing an overall flat spectrum at the input of IQ1 and IQ2, which is to be seen in Fig. B.5(b), measured at monitor port MP6. The modulators are driven by 16QAM drive signals generated by a high-speed arbitrary waveform generator (AWG, Keysight M8196A) using pseudo-random bit sequences (PRBS) of length $2^{11}-1$. We use a symbol rate of 50 GBd with raised-cosine pulse shaping at a roll-off factor of $\beta = 0.1$. The larger analog bandwidth of this AWG (32 GHz) allowed us to use higher symbol rates as compared to the experiments described in Section B.3. Polarization-division multiplexing (PDM) is again emulated by temporally delaying one of the polarizations using a delay line (DL) and combining on orthogonal polarizations in a polarization beam combiner (PBC). The signal spectrum is shown in Fig. B.5(c), measured at monitor port MP7. The WDM data stream is amplified and transmitted over 75 km of standard single-mode fiber (SSMF). At the receiver (Rx), each transmitted channel is selected individually by an optical tunable band-pass filter (BPF), followed by an EDFA (EDFA 7) and a second BPF to suppress ASE noise. The selected channel is then sent to a dual-polarization coherent receiver which, in contrast to the data transmission experiment described in Section B.3, uses a spectral line from the Kerr soliton comb at the receiver side as a local oscillator

(LO). The portion of the setup that is related to generation and selection of the LO carrier is depicted in green in Fig. B.5(a). For detection of channels in the C-band, a wavelength-selective switch (WSS) is used to select the LO tone. For the L-band, the WSS could not be used for selecting LO tones due to its limited optical bandwidth, and we deploy a BPF instead. The selected LO tone is then amplified by EDFA 8, filtered by a second BPF to suppress the ASE from the EDFA, and fed to the dual-polarization coherent receiver which consists of an optical modulation analyzer (OMA, Keysight N4391A) together with two real-time oscilloscopes (Keysight DSO-X 93204A 80 GSa/s). The detected signal undergoes a number of digital post processing stages comprising digital low-pass filtering, polarization demultiplexing, chromatic dispersion compensation, frequency offset estimation, carrier phase estimation and adaptive equalization. The block length for performing signal processing is chosen to be 1024 symbols, which is optimized to track the varying physical quantities of the received signal, such as carrier phase and polarization. The measured BER (averaged from different recordings with a length of 10^6 bit) for all transmitted channels is given in Fig. 5.3(d) of the main paper.

B.6 Energy consumption analysis

In this section, we investigate the electrical power consumption of DKS-based frequency comb sources and compare our results with state-of-the-art integrated tunable laser assemblies (ITLA). In the proof-of-concept experiments presented in the main paper, the comb generator relies on general-purpose benchtop-type research equipment, for which the sum of all power ratings is approximately 1.3 kW. This number is of course not representative for an industrial implementation of the comb source in a real communication system, where components can be chosen to exactly match the specific requirements of the comb generation scheme. For a meaningful analysis of the power consumption, we hence consider dedicated components that correspond to the commercially available state of the art, and combine them with specifically designed Si_3N_4 microresonators which are optimized to achieve maximum power of the outermost comb lines that are still within the C- and L-band. This leads to an improved optical signal-to-noise power ratio (OSNR) after amplification and modulation of the

generated comb carriers. We conclude Section B.6 with the investigation and the comparison of the achievable OSNR for both DKS- and ITLA-based sources of carriers for WDM data transmission.

B.6.1 Electrical power consumption of comb generators and ITLA array

Our experiments described in the previous sections and in the main paper demonstrate that chip-scale DKS comb generators are well suited for massively parallel coherent WDM transmission, both as a multi-wavelength source at the transmitter and as multi-wavelength LO at the receiver. In particular, the concept allows the generation of hundreds of inherently equidistant highly stable optical tones, thereby eliminating the need for individual wavelength control of each carrier. In addition, DKS can dramatically reduce electrical power consumption as compared to a bank of individual laser modules despite the rather low power conversion efficiency of the nonlinear comb generation process. In the following section, we investigate the power consumption of different DKS comb generation schemes with resonators of different Q -factors in combination with either off-the-shelf optical amplifiers or tailored optical amplifiers that feature optimized power consumption. As a model system, we choose a comb source that can generate 114 discrete tones with a spacing of 100 GHz corresponding to the full number of ITU-channels in the C band (1530 nm to 1565 nm) and the L band (1565 nm to 1625 nm) [187]. We design the coupling and the dispersion of the microresonator to find an optimum trade-off between high comb power and large bandwidth. It turns out that DKS comb sources have the potential to reduce the power consumption by up to an order of magnitude in comparison to an array of state-of-the-art integrated tunable laser assemblies (ITLA).

In our analysis, we investigate the electrical power consumption, P_{el} , of three different implementations of DKS comb generators (DKS-1, DKS-2, DKS-3) and compare it to the power consumption of an array of state-of-the-art ITLA, see Table B.1. DKS-1, DKS-2, and DKS-3 are based on a power-optimized scheme depicted in Fig. B.6. The scheme is designed to feature low electrical power consumption while providing an optical output power per carrier of

13 dBm, which is comparable to the power levels provided by high-quality ITLA sources [188]. The DKS comb generator comprises a Si_3N_4 -based microresonator chip, which is driven by a CW laser and a subsequent pump amplifier [189], [190]. The wavelength of the pump laser is adjusted by a controller [191], and the temperature of operation of the microresonator is kept stable with the use of a thermoelectric controller (TEC) [192]. For DKS-1, we assume a microresonator that has the same characteristics, with respect to Q -factor and dispersion, as the devices used in our experiments and is pumped at the same power level. The frequency comb output from the microresonator is next split into C and L bands and amplified by the first comb amplifiers [190] (AMP 1 and 2). Tailored gain-equalizing filters are used to correct the power variations between the amplified carriers, leading to a flat spectrum.

Table B.1: Electrical power required for the generation of 114 carriers on the C and L bands having an optical power of approximately 13 dBm per carrier. DKS-based configurations are shown in columns 2-4, and the associated comb generation scheme is depicted in Fig. B.6(a) a. DKS-1: off-the-shelf equipment; DKS-2: Off-the-shelf equipment and optimized microresonators; DKS-3: Tailored amplifiers with optimized power consumption and optimized microresonators. The last column considers the use of 108 ITLA as source of WDM carriers. For each configuration, the last two rows show the minimum and maximum OCNR_{ref} (OSNR_{ref}) that occurs for any channel in the C- or L-band. OCNR_{ref} refers to the optical carrier-to-noise power ratio at the output of the comb generator, i.e., after the DEMUX depicted in Fig. B.6 OSNR_{ref} refers to the optical signal-to-noise power ratio measured after modulation, recombination and re-amplification of the WDM channels, i.e., after AMP 5 and AMP 6 in Figure B.9. Both parameters are measured for a reference bandwidth of 0.1 nm.

	DKS-1	DKS-2	DKS-3	ITLA
	$P_{\text{el}} \text{ (W)}$	$P_{\text{el}} \text{ (W)}$	$P_{\text{el}} \text{ (W)}$	$P_{\text{el}} \text{ (W)}$
Laser [188]	3.8	3.8	3.8	114×3.8
Controller [191]	1.0	1.0	1.0	-
Pump amp. [189], [190]	38.0	12.0	3.5	-
TEC [192][19]	0.6	0.6	0.6	-
AMP 1 & AMP 2 [190]	3.0 + 3.0	3.0 + 3.0	0.5 + 0.5	-
AMP 3 & AMP 4 [189]	25 + 38	25 + 38	12 + 20	-
Total $P_{\text{el}} \text{ (W)}$	112.4	86.4	41.9	433.2
Max/Min $\text{OCNR}_{\text{ref}} \text{ (dB)}$	39.0/35.0	39.0/35.0	39.0/35.0	55
Max/Min $\text{OSNR}_{\text{ref}} \text{ (dB)}$	38.3/34.6	38.3/34.6	38.3/34.6	46.9/45.8

These filters can be realized, e.g., by concatenating fiber Bragg gratings with different periodicities [193] or by using an acousto-optic tunable filter with multi-frequency acoustic signals generated by a single transducer [194]. To obtain the target power level of 13 dBm/carrier, high-power optical amplifiers (AMP 3 and 4) are used before separating the carriers by a wavelength demultiplexer (DEMUX) for independent modulation. The DEMUX [195] features a channel spacing of 100 GHz and supports 44 channels in the C-band and 70 channels in the L-band.

For the DKS-1 scheme, we assume a microresonator with the same Q -factor and under the same operation conditions as the LO comb of the transmission experiment depicted in Fig. 5.3 of the main paper. For estimating the OCNR_{ref} and OSNR_{ref} values, we use a comb spectral shape that mirrors the one measured during our experiment. To estimate the electrical power dissipation P_{el} associated with DKS-1, we assume state-of-the-art off-the-shelf amplifiers that match the requirements of gain and optical output power while featuring low electrical power consumption, see the corresponding references in first column of Table B.1. This leads to a total power consumption of approximately 110 W for generation of 114 carriers – less than one third of the power consumption obtained for 114 independent ITLA.

For the DKS-2 and DKS-3 scheme, we assume Si_3N_4 microresonators having intrinsic Q -factors of 6×10^6 with dispersion and coupling parameters that were optimized for maximizing the power of the outermost comb lines that are still within the C- and L-band, see Section 5.2 and Refs. [90], [173], [196] for details. The assumption of a Q -factor of 6×10^6 is based on recent reports about Si_3N_4 microresonators resonators, where optimized fabrication processes have led to Q -factors even exceeding 6×10^6 , both in devices with normal [172] and anomalous [173] GVD. While DKS-2 is still based on state-of-the-art off-the-shelf amplifiers, DKS-3 assumes tailored optical amplifiers that have the highest electrical-to-optical power conversion efficiency [197]. This results in DKS-3 having a total power consumption of approximately 42 W for generation of 114 carriers – more than an order of magnitude below the power consumption of the considered ITLA array.

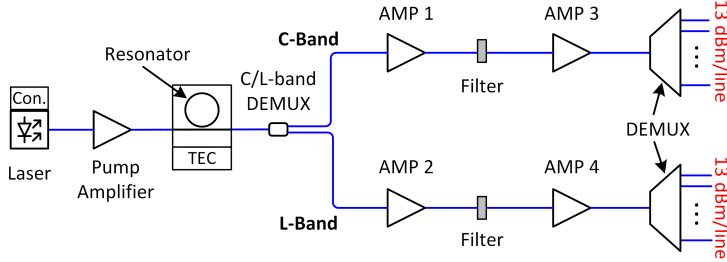


Figure B.6: Power-optimized setup for DKS frequency comb generation and amplification for data transmission. A tunable CW laser followed by a pump amplifier are used to drive the microresonator. The operation temperature of the microresonator is kept stable by a TEC. After separating the C and L band tones by a C/L-band DEMUX, the tones of each band are amplified by the comb amplifiers AMP 1 and 2. Optical filters compensate the spectral power variations among the carriers of the frequency comb in each band. High-power optical amplifiers AMP 3 and 4 are used before the wavelength demultiplexer (DEMUX) to obtain the target power level of ~ 13 dBm per carrier.

Naturally, the amplifiers used to boost the optical power of the comb lines reduce the optical carrier-to-noise power ratio (OCNR) with respect to the carriers from an ITLA, which do not need to be amplified prior to modulation. This reduction of the OCNR was investigated analytically, as discussed in Section B.6.3, and the results were verified by simulations using the commercial tool OptSim [198]. The last two rows of Table B.1 give the results of the investigation. The Max/Min OCNR_{ref} values of Table B.1 correspond to the maximum and minimum values of the OCNR for the DKS frequency comb carriers and for the ITLA carriers within the C- and L-band prior to modulation, measured at a reference bandwidth of 0.1 nm. For the DKS frequency comb carriers, OCNR_{ref} was measured at the output of the DEMUX, see Fig. B.6, whereas it was taken from the datasheet of a commercial device for the case of the ITLA carriers [188]. Using DKS sources leads to optical carriers with OCNR_{ref} values that range from 35.0 dB to 38.5 dB. The difference between the maximum and the minimum OCNR_{ref} values is due to the difference in power between the comb carriers over the whole C and L band and due to the difference in noise figure between the C and L band amplifiers. The Max/Min OSNR_{ref} values of Table B.1 give the maximum and minimum values of the OSNR, measured at a

reference bandwidth of 0.1 nm, for the DKS frequency comb and ITLA tones after modulation, multiplexing and re-amplification, prior to transmission through the single-mode fiber. Due to the amplified spontaneous emission (ASE) noise added during re-amplification of the DKS-based channels, the OSNR_{ref} of the DKS comb generator and the ITLA differ much less than the associated OCNR_{ref} . Furthermore, the DKS-based channels exhibit OSNR_{ref} values above 34.5 dB, which would correspond to theoretically achievable BER of less than 10^{-34} for 50 GBd 16QAM transmission assuming impairments only by additive white Gaussian noise, without inter-symbol interference [129]. This is a purely virtual value, much smaller than any BER relevant to real-world 16QAM systems which are deteriorated by noise and are typically operating at BER values of more than 10^{-6} . This analysis shows that DKS comb tones will not exhibit any practically relevant impairment of transmission performance in comparison to much more power hungry arrays of individually stabilized ITLA. For details on the analytical OSNR calculation, refer to Section B.6.3.

It is further worth noting that DKS comb generators are particularly advantageous when large numbers of carriers are to be generated. Fig. B.7 shows the dependence of the electrical power consumption per carrier on the total number of carriers for the implemented three DKS comb generation configurations. The power consumption per line for DKS comb sources decreases considerably with the number of lines. With only 20 lines, the DKS-3 scheme already exhibits a power consumption per line which is half of that required by ITLA sources. Note that Fig. B.7 is based on the assumption that the amplifiers used for DKS frequency comb generation consume constant electrical power. This may lead to an overestimation of the power consumption since the electrical pump power of the EDFA can be reduced if only a few comb lines are to be utilized. Moreover, we did not consider that the design of the microresonator can be adapted for power-efficient generation of narrowband combs, see Section B.2 below. In addition, the power consumption per carrier when using an ITLA array is considered constant. This may not be the case if techniques to synchronize all optical sources, e.g. through frequency locking, are employed. Fig. B.7 hence represents a rather conservative estimation of the performance that can be achieved with DKS comb sources.

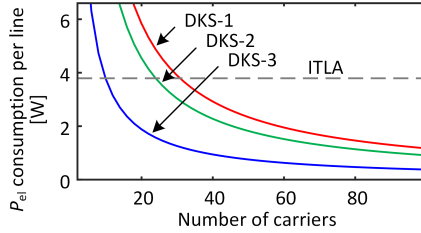


Figure B.7: Electrical power consumption per carrier as a function of the number of carriers. We compare the power consumption of the DKS comb generation schemes detailed in Table B.1 and Fig. B.6 (DKS-1, DKS-2, DKS-3) to that of an array of integrated tunable laser assemblies (ITLA).

B.6.2 Dispersion and coupling parameters of SiN microresonators

In this section, we explain the optimization of the microresonator carried out to maximize the achievable OSNR of a DKS frequency comb. For a given input power, such optimization is done by maximizing the optical power of the outermost lines of the C and L band of the frequency comb, which have the lowest power and hence limit the achievable OSNR. It turns out that for a moderate input power of $P_{\text{in}} = 400$ mW or 26 dBm, which allows the use of a pump amplifier with low power consumption, we obtain OSNR_{ref} values higher than 35 dB, which are more than sufficient for real-world communication systems, see discussion in Section B.6.1. In addition, we investigate the power conversion efficiency of the DKS comb source, and the bandwidth of the frequency comb.

To maximize the power of the weakest lines at the edges of the C and L band, the group velocity dispersion (GVD) and the coupling rate of the microresonator to the external waveguide, κ_{ex} , are varied within values that can be engineered by varying the Si_3N_4 waveguide dimensions as well as the resonator-to-waveguide distance in combination with specially designed coupling regions [173], [196]. The analytical expression for the line power, in Watts, of the DKS frequency comb at the output of the microresonator, solved in the limit of low resonator loss, is given by [21]:

$$P(\mu) = \frac{\kappa_{\text{ex}} D_2 \hbar \omega_0}{4g} \operatorname{sech}^2 \left(\frac{\kappa \mu}{2} \sqrt{\frac{D_2 \hbar \omega}{\kappa_{\text{ex}} g P_{\text{in}}}} \right), \quad (\text{B.4})$$

where $\mu = (\omega - \omega_0)/D_1$ is the comb mode index relative to the pumped mode, $D_1/2\pi$ is the free spectral range, $D_2/2\pi$ is the per-resonance frequency shift due to GVD, $g/2\pi$ is the nonlinear coupling constant or Kerr frequency shift per photon, P_{in} is the input pump power, and $\kappa = \kappa_0 + \kappa_{\text{ex}}$ is the total cavity loss-rate including the internal loss rate, κ_0 , and the coupling rate to the external waveguide, κ_{ex} . In our model, we set a realistic value of internal loss rate to $\kappa_0 = 2\pi \times 30$ MHz (which corresponds to the intrinsic $Q \sim 6 \times 10^6$) [173] and the nonlinear coefficient is assumed to amount to $g = 2\pi \times 0.27$ Hz. In addition, we assume that the soliton operates at the maximum pump-cavity resonance detuning, which corresponds to the maximum output power and the broadest comb spectrum available for the given pump power [21], [177]. Note that Eq. (B.4) is based on the assumption of high resonator finesse [199] and is hence not valid any more as the loss of the resonator κ is increased to large values. For a comprehensive study over a broader range of values, we therefore perform simulations using the Lugiato-Lefever equation to retrieve the spectral envelope of the DKS frequency comb [155]. Figure B.8a shows the optical power of the weakest line within the C and L-band attained through these simulations when the dispersion parameter $D_2/2\pi$ and the ratio between the external coupling and the intrinsic loss $\kappa_{\text{ex}}/\kappa_0$ are varied from 0.2 to 2.0 MHz and from 1 to 25, respectively. We find that there exists an optimal value for κ and $D_2/2\pi$ where the weakest line of the frequency comb within the C and L band is maximized. We find that for $\kappa_{\text{ex}}/2\pi = 525$ MHz and $D_2/2\pi = 0.4$ MHz the outermost line reaches a maximum power of 46 μW or -13.4 dB, which allows OCNR_{ref} values above 35 dB for the comb carriers obtained from DKS-2 and DKS-3 comb generation and amplification schemes. The power consumption, OCNR_{ref} and OSNR_{ref} values of Table B.1, for DKS-2 and DKS-3 configurations, have been derived considering such optimized microresonators. Figure B.8(b) depicts the values of the ratio, in dB, between the power of the strongest and the weakest comb line within the C and L band. For the optimum values of κ_{ex} and $D_2/2\pi$ a ratio of 5 dB is obtained, which is comparable to the approximately 6 dB of power ratio observed in our measurements.

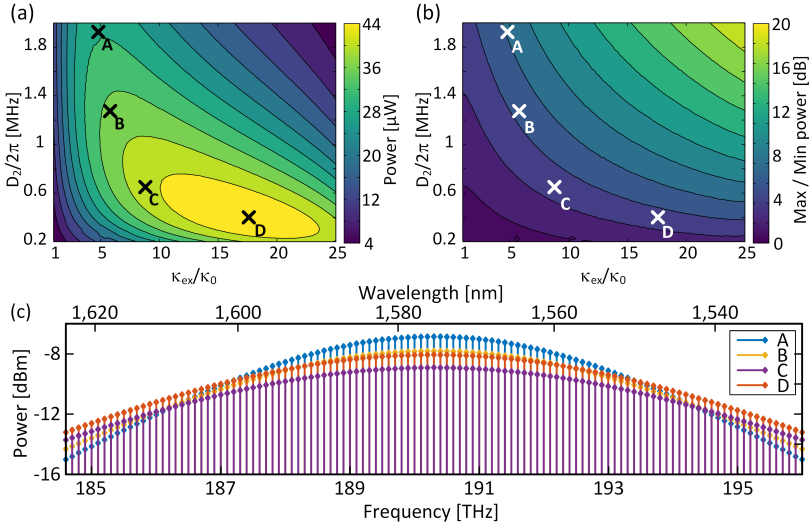


Figure B.8: Optimization of minimum comb line power by varying the cavity GVD parameter D_2 and the coupling rate κ_{ex} . **(a)** Heat map for minimum comb line power as a function of D_2 and κ_{ex} . The crosses mark the comb spectra depicted in c, with ‘D’ indicating the ideal point where a global maximum of the power of the weakest comb line within the C and L band is achieved. **(b)** Map of the comb line power variation as maximum/minimum comb power in dB as a function of D_2 and κ_{ex} , with the same highlighted points as in a. **(c)** Frequency comb spectrum corresponding to the data points A to D from panels a. and b. The plotted frequency range corresponds to C and L-band. Comb D exhibits an optimal balance between a high total output power as well as the broadest bandwidth, allowing for an increased OCNR and OSNR per carrier.

Figure B.8(c) contains four comb spectra taken from the points marked as crosses on Fig. B.8(a),(b). The interplay between spectral broadening and overall power increase is well demonstrated. In general, decreasing the dispersion D_2 tends to increase the bandwidth while reducing the total comb power. Conversely, increasing the resonator coupling κ_{ex} leads to an increase in total comb power but a reduction in the soliton bandwidth. This is due to more light escaping the cavity, and consequently reducing the conversion efficiency from the pump to the comb lines. Hence, for a given value of dispersion D_2 there exists an optimum value of κ_{ex} that maximizes the power of the weakest line at the edge of the C and L-band. In Fig. B.8(a), these values are indicated by points A

to D for four values of D_2 . Point D corresponds to the overall maximum that can be achieved by optimization of both parameters.

In addition, we have analyzed the power conversion efficiency, Γ , of the DKS comb sources for the same range of values for κ_{ex} and $D_2/2\pi$. The general expression can be calculated as [156], [200]

$$\Gamma = \frac{P_{\text{out}}^{\text{sol}}}{P_{\text{in}}} = \frac{\pi\kappa_{\text{ex}}}{\kappa} \sqrt{\frac{\kappa_{\text{ex}} D_2 \hbar \omega_0}{g P_{\text{in}}}}, \quad (\text{B.5})$$

where $P_{\text{out}}^{\text{sol}}$ is the total soliton power exiting the microresonator. For the optimum values κ_{ex} and $D_2/2\pi$, the power conversion efficiency amounts to 2.5%, greatly improving the maximum value of 0.6% observed in the experimental setup.

B.6.3 OSNR for DKS and ITLA WDM sources

The OCNR_{ref} and OSNR_{ref} values shown in Table B.1 have been obtained through an analytic study of the amplified stimulated emission (ASE) noise power generated after amplifying the initially low-noise frequency comb carriers using a chain of amplifiers. To verify the results of our analysis, the DKS frequency comb generation setup shown in Fig. B.6 has also been simulated. In both the analytical calculations and simulations, the gain of the optical amplifiers is assumed to be constant across the bandwidth occupied by the frequency comb. This assumption can be justified by the amplifier specifications of different EDFA manufacturers which assure variations of gain to be lower than 1 dB [201]. ASE noise was quantified by the noise figure of the comb amplifiers. Optical amplifiers for the L band are assumed to feature a 1 dB higher noise figure with respect to their counterparts in the C band [201], [202]. In our model, we consider a noise figure of 4 dB (5 dB) for the C band (L band) comb amplifier AMP 1 and a noise figure of 6 dB (7 dB) for the C band (L band) comb amplifier AMP 2, which are the maximum noise figure values specified for the corresponding amplifiers and should hence lead to a

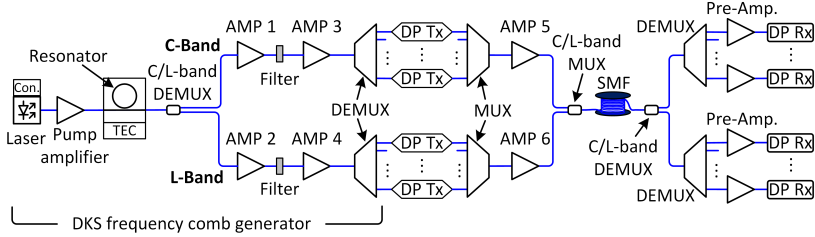


Figure B.9: Communication setup assumed for estimating the OSNR levels that can be achieved with the various DKS-based comb generation schemes discussed in Table B.1. The DKS frequency comb generator is described in more detail in Fig. B.6. The carriers are modulated by dual polarization coherent transmitters (DP Tx). The C- and L-band signals are re-amplified by separate booster amplifiers AMP 5 and AMP 6, combined by a C/L-band MUX, and transmitted through 75 km of single-mode fiber (SMF). At the receiver, the channels are demultiplexed and sent through a pre-amplifier before detection by a dual-polarization coherent receiver (DP Rx).

conservative estimate of the OSNR. The noise figure of the amplifiers is also assumed to be flat within the bandwidth occupied by the frequency comb. Moreover, insertion loss values of all the passive components were also taken into account. The C/L-band DEMUX feature a 0.5 dB insertion loss, the gain-equalizing filters, which compensate for the power difference between comb carriers, present an insertion loss of approximately 5 dB in addition to the wavelength-dependent attenuation profile required for gain flattening [203], and the wavelength DEMUX is considered to have 3 dB insertion loss [195]. For the calculation of the OSNR_{ref} obtained after modulation and re-amplification by booster amplifiers AMP 5 and 6 and prior to transmission through the single-mode fiber, we further need to quantify the optical losses associated with modulating data signals onto the carriers and with recombining these carriers into the transmission fiber, see Fig. B.9. To this end, we assume state-of-the-art dual-polarization IQ modulators with 13 dB of insertion loss for each polarization [110], [204] along with a modulation loss of 2.55 dB, corresponding to the peak-to-average symbol power ratio of 16QAM signals [205]. To recombine the channels into the single-mode transmission fiber, an optical multiplexer (MUX) and a C/L-band MUX with 3 dB and 0.5 dB of insertion loss, respectively, are considered. For re-amplification of the modulated signal by AMP 5 (6), we assume an amplifier with a noise figure of 5.5 dB (6.5 dB) for the C (L) band. The

output power is set such that the power per channel is 0 dBm, which is the typical launch power per channel into standard single mode fibers (SSMF) to reduce the nonlinear impairments while optimizing the channel OSNR [107], [108].

Note that the comb amplifiers AMP 1 ... AMP 4 in Fig. B.9 are deliberately placed between the comb generator and the respective DEMUX. In fully integrated schemes, it would be desirable to avoid amplifiers before the modulators. However, due to the low comb line powers directly after the resonator and the generally high insertion loss of the IQ modulators, such schemes would lead to low power levels at the input of the transmitter booster amplifiers AMP 5 and AMP 6 and the OSNR_{ref} of the transmitted signal would drop to values below 23 dB. For this reason, placing of an EDFA prior to modulation is a common approach in most comb-based transmission schemes [97].

Figure B.10 shows the spectrum obtained from our simulation using the commercial tool OptSim [198]. The spectrum exhibits a maximum OCNR_{ref} of 39 dB for the leftmost comb line in the C-band and a minimum OCNR_{ref} of 35 dB for the leftmost comb line in the L-band. These values are in accordance with the OCNR_{ref} values measured in our experiments, which amount to 35 ... 39 dB for the single comb, and to 30 ... 37 dB for the interleaved combs. In contrast to that, the experimentally measured OSNR_{ref} values of the data signal typically amount to 20 ... 24 dB (23 ... 27 dB) for the case of the interleaved-comb (single-comb) experiment. This is significantly below the values of more 34 dB that can be expected when using optimized equipment, see Table B.1. The low OSNR_{ref} in the experiment is caused by a rather high insertion loss of the electro-optic modulators that we used in our experiment, which lead to low power levels coupled into the subsequent EDFA (EDFA 6 in Fig. B.2).

The simulations are confirmed by an analytical estimation. To this end, we start from the input signal power P_0 to Comb Amplifiers #1 & #2 and derive the OSNR from the noise figure of the system.

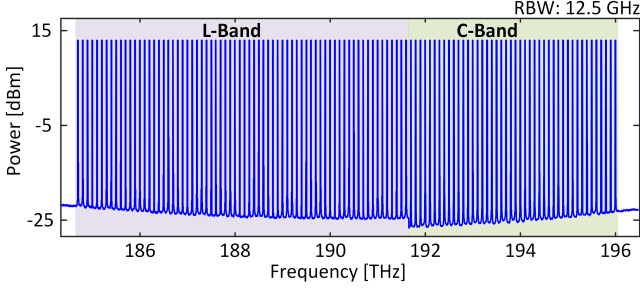


Figure B.10: Merged plot of the amplified frequency comb spectra, at the output of amplifiers AMP 3 and AMP 4, in Fig. B.9, after accounting for the subsequent DEMUX insertion loss. The spectra are obtained from our simulation using the commercial tool OptSim [198]. RBW: resolution bandwidth.

For an output signal power P_s and ASE noise power P_{ASE} , the OSNR is given by the equation:

$$\text{OSNR} = \frac{P_s}{P_{\text{ASE}}} \quad (\text{B.6})$$

with P_s and P_{ASE} given by [206]

$$P_s = G P_0, \quad (\text{B.7})$$

$$P_{\text{ASE}} = h\nu B_{\text{ref}} F (G - 1), \quad (\text{B.8})$$

where G is the EDFA gain, h is the Planck constant, ν is the input signal's center frequency, B_{ref} is the noise reference bandwidth (centered at ν) and F is the noise figure of the EDFA. For a chain of amplifiers connected by passive components with power transmission factor α , $0 < \alpha \leq 1$, the total gain G_t and the noise figure F_t of the system are given by

$$G_t = \prod_{n=1}^N G_n \alpha_n \quad (\text{B.9})$$

$$F_t = \frac{1}{G_t} + \left(F_1 + \frac{F_2}{G_1 \alpha_1} + \frac{F_3}{G_1 \alpha_1 G_2 \alpha_2} + \dots + \frac{F_n}{\prod_{n=1}^{N-1} G_n \alpha_n} \right). \quad (\text{B.10})$$

Using Eqs. (B.6) to (B.10), the maximum and minimum OCNR_{ref} and OSNR_{ref} values of the DKS frequency comb generation and amplification configurations given in Table B.1 are calculated analytically. These values are also found to be in accordance with the simulations results. Note that the DKS frequency comb generation setup assumed in Table B.1 already contains the booster EDFA (AMP 5 and AMP 6 in Fig. B.9) after the modulator. For transmission over a distance of 75 km, the OSNR_{ref} measured after a state-of-the-art preamplifier [207] (Pre-Amp. In Fig. B.9) would be 2 dB below the OSNR_{ref} values at the transmitter that are specified in Table B.1.

In addition to the ASE noise introduced by the various amplifiers, nonlinear interference noise will also influence the OSNR at the receiver. For a quantitative analysis, we consider the 50 GBd PDM-16QAM transmission experiment in which we use a DKS comb generator as a source of LO tones, see Fig. 5.3 of the main paper. We assume typical parameters for the transmission fiber such as a nonlinearity coefficient of $\gamma = 2 \text{ W}^{-1}\text{km}^{-1}$, a dispersion coefficient of $\beta_2 = 20 \text{ ps}^2/\text{km}$, and a fiber loss coefficient of $a = 0.2 \text{ dB/km}$. The average input power to the transmission fiber was assumed to be 0 dBm per channel, which matches our laboratory experiment. For the estimation, we use the model described in Ref. [30]. After the first 75 km transmission link, we estimate an effective OSNR_{NL} of approximately 32.5 dB, which would correspond to an $\text{OSNR}_{\text{ref,NL}}$ of 38.5 dB, taking into account nonlinear interference noise from self-phase modulation, cross-phase modulation, and four-wave mixing, but no ASE noise from any EDFA deployed in the system. After an additional 75 km link, the OSNR_{NL} ($\text{OSNR}_{\text{ref,NL}}$) reduces to 29 dB (35 dB). These OSNR_{ref} numbers are comparable to the values estimated at the output of the transmitter when taking into account only the ASE noise of the various EDFA, but no fiber nonlinearities. We hence conclude that in optimized systems, fiber nonlinearities may have significant impact even for transmission over rather short distances that are typically found in metro and regional networks. These impairments can be compensated by exploiting the strong correlation of frequency variations of the comb carriers [34] – another key advantage of comb-based transmission schemes, leading to better signal quality and allowing higher capacity and reach. Note that the $\text{OSNR}_{\text{ref,NL}}$ values estimated for nonlinear impairments are much higher than the OSNR_{ref} of approximately 23 dB that we actually measured in our current experiment.

We hence conclude that nonlinearities of the transmission fiber did not significantly impact signal quality of our experiment

[End of Methods and Supplementary Information of journal publication [J1]]

C. Bibliography

- [1] Cisco White Paper, “Cisco Annual Report (2018–2023).” [Online]. Available: https://www.cisco.com/c/en/us/solutions/collateral/executive_perspectives/annual-internet-report/white-paper-c11-741490.html.
- [2] Cisco White Paper, “Cisco Global Cloud Index: Forecast and Methodology, 2016–2021.” [Online]. Available: <https://www.cisco.com/c/en/us/solutions/collateral/service-provider/global-cloud-index-gci/white-paper-c11-738085.html>.
- [3] C. Xie, “Datacenter Optical Interconnects: Requirements and Challenges,” *6th IEEE Photonics Soc. Opt. Interconnects Conf. OI 2017*, pp. 37–38, 2017.
- [4] M. Chagnon, “Optical Communications for Short Reach,” *J. Lightw. Technol.*, vol. 37, no. 8, pp. 1779–1797, 2019.
- [5] J. X. Cai *et al.*, “70.4 Tb/s Capacity over 7,600 Km in C+L Band Using Coded Modulation with Hybrid Constellation Shaping and Nonlinearity Compensation,” *2017 Opt. Fiber Commun. Conf. OFC 2017 - Proc.*, pp. 12–14, 2017.
- [6] A. Willner, “Ch.2. Chip-Based Frequency Combs for Wavelength-Division Multiplexing Applications,” in *Optical fiber telecommunications VII*, Academic Press, 2019, pp. 51–94.
- [7] A. D. Maynard, “Navigating the Fourth Industrial Revolution,” *Nat. Nanotechnol.*, vol. 10, no. 12, pp. 1005–1006, 2015.
- [8] P. F. Moulton, “Spectroscopic and Laser Characteristics of Ti:Al₂O₃,” *J. Opt. Soc. Am. B*, vol. 3, no. 1, p. 125, 1986.
- [9] “The Nobel Foundation 2005 The Nobel Prize in Physics 2005.” [Online]. Available: <http://nobelprize.org/physics/laureates/2005/index.html>.
- [10] S. T. Ye, J. & Cundiff, *Femtosecond Optical Frequency Comb: Principle, Operation and Applications*. Springer, New York, 2005.
- [11] V. Brasch, E. Lucas, J. D. Jost, M. Geiselmann, and T. J. Kippenberg, “Self-Referenced Photonic Chip Soliton Kerr Frequency Comb,” *Light Sci Appl.*, vol. 6. p. e16202, 2017.
- [12] C. Weimann *et al.*, “Silicon-Organic Hybrid (SOH) Frequency Comb Sources for Terabit/s Data Transmission,” *Opt. Express*, vol. 22, no. 3, p.

- 3629, 2014.
- [13] C. Chen, C. Zhang, W. Zhang, W. Jin, and K. Qiu, “Scalable and Reconfigurable Generation of Flat Optical Comb for WDM-Based next-Generation Broadband Optical Access Networks,” *Opt. Commun.*, vol. 321, pp. 16–22, 2014.
 - [14] P. M. Anandarajah *et al.*, “Generation of Coherent Multicarrier Signals by Gain Switching of Discrete Mode Lasers,” *IEEE Photon. J.*, vol. 3, no. 1, pp. 112–122, 2011.
 - [15] M. D. G. Pascual, V. Vujicic, J. Braddell, F. Smyth, P. Anandarajah, and L. Barry, “Photonic Integrated Gain Switched Optical Frequency Comb for Spectrally Efficient Optical Transmission Systems,” *IEEE Photon. J.*, vol. 9, no. 3, pp. 1–8, Jun. 2017.
 - [16] J. Pfeifle *et al.*, “Flexible Terabit/s Nyquist-WDM Super-Channels Using a Gain-Switched Comb Source,” *Opt. Express*, vol. 23, no. 2, p. 724, 2015.
 - [17] J. N. Kemal *et al.*, “Multi-Wavelength Coherent Transmission Using an Optical Frequency Comb as a Local Oscillator,” *Opt. Express*, vol. 24, no. 22, p. 25432, 2016.
 - [18] H. Hu *et al.*, “Single-Source AlGaAs Frequency Comb Transmitter for 661 Tbit/s Data Transmission in a 30-Core Fiber,” in *Conference on Lasers and Electro-Optics*, 2016, p. JTh4C.1.
 - [19] F. Lelarge *et al.*, “Recent Advances on InAs/InP Quantum Dash Based Semiconductor Lasers and Optical Amplifiers Operating at 1.55 μm ,” *IEEE J. Sel. Top. Quantum Electron.*, vol. 13, no. 1, pp. 111–123, 2007.
 - [20] P. Marin-Palomo *et al.*, “Comb-Based WDM Transmission at 10 Tbit/s Using a DC-Driven Quantum-Dash Mode-Locked Laser Diode,” *Opt. Express*, vol. 27, no. 22, p. 31110, 2019.
 - [21] T. Herr *et al.*, “Temporal Solitons in Optical Microresonators,” *Nat. Photonics*, vol. 8, no. 2, pp. 145–152, Feb. 2014.
 - [22] H. Guo *et al.*, “Universal Dynamics and Deterministic Switching of Dissipative Kerr Solitons in Optical Microresonators,” *Nat. Phys.*, vol. 13, no. 1, pp. 94–102, Sep. 2016.
 - [23] B. Shen *et al.*, “Integrated Turnkey Soliton Microcombs,” *Nature*, vol. 582, no. 7812, pp. 365–369, 2020.
 - [24] A. S. Raja *et al.*, “Electrically Pumped Photonic Integrated Soliton Microcomb,” *Nat. Commun.*, vol. 10, no. 1, pp. 1–8, 2019.

- [25] N. S. Bergano, "Wavelength Division Multiplexing in Long-Haul Transoceanic Transmission Systems," *J. Lightw. Technol.*, vol. 23, no. 12, pp. 4125–4139, 2005.
- [26] T. Li, "The Impact of Optical Amplifiers on Long-Distance Lightwave Telecommunications," *Proc. IEEE*, vol. 81, no. 11, pp. 1568–1579, 1993.
- [27] J. Lu, "M-PSK and M-QAM BER Computation Using Signal-Space Concepts," *IEEE Trans. Commun.*, vol. 47, no. 2, pp. 181–184, 1999.
- [28] J. Proakis and M. Salehi, *Digital Communications*, Fifth Edit. New York: McGraw-Hill Higher Education, 2008.
- [29] J. Palicot and Y. Lou, "Power Ratio Definitions and Analysis in Singlecarrier Modulation," in *13th European Signal Processing Conference*, 2005.
- [30] R. Dar, M. Feder, A. Mecozzi, and M. Shtaif, "Accumulation of Nonlinear Interference Noise in Fiber-Optic Systems," *Opt. Express*, vol. 22, no. 12, pp. 14199–14211, 2014.
- [31] C. E. Shannon, "A Mathematical Theory of Communication," *Bell Syst. Tech. J.*, vol. 27, no. 3, pp. 379–423, Jul. 1948.
- [32] R.-J. Essiambre, G. Kramer, P. J. Winzer, G. J. Foschini, and B. Goebel, "Capacity Limits of Optical Fiber Networks," *J. Lightw. Technol.*, vol. 28, no. 4, pp. 662–701, 2010.
- [33] N. Alic, E. Myslivets, E. Temprana, B. P.-P. Kuo, and S. Radic, "Nonlinearity Cancellation in Fiber Optic Links Based on Frequency Referenced Carriers," *J. Light. Technol.*, vol. 32, no. 15, pp. 2690–2698, 2014.
- [34] E. Temprana *et al.*, "Overcoming Kerr-Induced Capacity Limit in Optical Fiber Transmission," *Science*, vol. 348, no. 6242, pp. 1445–1448, 2015.
- [35] Corning Incorporated, "Corning SMF-28 Ultra Optical Fiber." [Online]. Available: [https://www.corning.com/media/worldwide/coc/documents/Fiber/SMF-28 Ultra.pdf](https://www.corning.com/media/worldwide/coc/documents/Fiber/SMF-28%20Ultra.pdf). [Accessed: 10-Feb-2020].
- [36] S. Geckeler, "Pulse Broadening in Optical Fibers with Mode Mixing," *Appl. Opt.*, vol. 18, no. 13, p. 2192, 1979.
- [37] D. N. Godard, "Passband Timing Recovery in an All-Digital Modem Receiver," *IEEE Trans. Commun.*, vol. COM-26, no. 5, pp. 517–523, 1978.
- [38] C. W. Farrow, "A Continuously Variable Digital Delay Element," *IEEE*

- Int. Symp. Circuits Syst. IEEE*, pp. 2641–2645, 1988.
- [39] S. J. Savory, “Digital Filters for Coherent Optical Receivers,” *Opt. Express*, vol. 16, no. 2, pp. 804–817, 2008.
- [40] I. Fatadin, D. Ives, and S. J. Savory, “Laser Linewidth Tolerance for 16-QAM Coherent Optical Systems Using QPSK Partitioning,” *IEEE Photon. Technol. Lett.*, vol. 22, no. 9, pp. 631–633, 2010.
- [41] L. Schmalen, S. Ten Brink, and A. Leven, “Spatially-Coupled LDPC Protograph Codes for Universal Phase Slip-Tolerant Differential Decoding,” *Conf. Opt. Fiber Commun.*, p. Th3E.6, 2015.
- [42] M. Magarini *et al.*, “Pilot-Symbols-Aided Carrier-Phase Recovery for 100-G PM-QPSK Digital Coherent Receivers,” *IEEE Photon. Technol. Lett.*, vol. 24, no. 9, pp. 739–741, 2012.
- [43] F. Chang, K. Onohara, and T. Mizuoichi, “Forward Error Correction for 100 G Transport Networks,” *IEEE Commun. Mag.*, vol. 48, no. 3, pp. 48–55, 2010.
- [44] W. Freude *et al.*, “Quality Metrics for Optical Signals: Eye Diagram, Q-Factor, OSNR, EVM and BER,” *Int. Conf. Transparent Opt. Networks*, p. Mo.B1.5, 2012.
- [45] N. Picqué and T. W. Hänsch, “Frequency Comb Spectroscopy,” *Nat. Photonics*, vol. 13, no. 3, pp. 146–157, 2019.
- [46] Y. Kawaguchi, Y. Tamura, T. Haruna, Y. Yamamoto, and M. Hirano, “Ultra Low-Loss Pure Silica Core Fiber,” *SEI Tech. Rev.*, no. 80, pp. 50–55, 2015.
- [47] Y. Tamura *et al.*, “The First 0.14-DB/Km Loss Optical Fiber and Its Impact on Submarine Transmission,” *J. Lightw. Technol.*, vol. 36, no. 1, pp. 44–49, 2018.
- [48] “Sumimoto Electric. Fiber Optics Products. Fiber Line Up.” [Online]. Available: https://global-sei.com/ftx/product_e/opticalfibers_e/optical-fiber01.html.
- [49] K. Fukuchi, T. Kasamatsu, M. Morie, R. Ohhira, T. Ito, and K. Sekiya, “10.92-Tb/s (273 x 40-Gb/s) Triple-Band/Ultra-Dense WDM Optical-Repeated Transmission Experiment,” *Optical Fiber Communication Conference (OFC)*, pp. PD24-1, 2001.
- [50] T. K. and A. N. T. Matsuda, T. Kotanigawa, “54 x 42.7 Gbit/s L- and U-Band WDM Signal Transmission Experiments with in-Line Hybrid

- Optical Amplifiers,” *Electron. Lett.*, vol. 40, no. 6, 2004.
- [51] K. Kikuchi, “Characterization of Semiconductor-Laser Phase Noise and Estimation of Bit-Error Rate Performance with Low-Speed Offline Digital Coherent Receivers,” *Opt. Express*, vol. 20, no. 5, p. 5291, 2012.
- [52] L. B. Mercer, “ $1/f$ Frequency Noise Effects on Self-Heterodyne Linewidth Measurements,” *J. Lightw. Technol.*, vol. 9, no. 4, pp. 485–493, 1991.
- [53] T. Pfau, S. Hoffmann, and R. Noe, “Hardware-Efficient Coherent Digital Receiver Concept With Feedforward Carrier Recovery for M-QAM Constellations,” *J. Lightw. Technol.*, vol. 27, no. 8, pp. 989–999, 2009.
- [54] “Infinera Corp., White Paper: Coherent DWDM Technologies. Document n. WP-CT-10-2012.” [Online]. Available: http://www.hit.bme.hu/~jakab/edu/litr/Core/WDM/Infinera_Coherent_Tech.pdf.
- [55] L. Lundberg, M. Mazur, A. Lorences-Riesgo, M. Karlsson, and P. A. Andrekson, “Joint Carrier Recovery for DSP Complexity Reduction in Frequency Comb-Based Superchannel Transceivers,” in *2017 European Conference on Optical Communication (ECOC)*, 2017, p. Th1D.
- [56] M. G. Thompson, A. R. Rae, M. Xia, R. V. Penty, and I. H. White, “InGaAs Quantum-Dot Mode-Locked Laser Diodes,” vol. 15, no. 3, pp. 661–672, 2009.
- [57] M. M. H. Adib *et al.*, “24 GBd DP-QPSK Upstream and Downstream Operation of a Colourless Coherent PON Using an MLLD-Based Frequency Comb,” in *45th European Conference on Optical Communication*, 2019, p. Paper M1.F2.
- [58] M. Asada, Y. Miyamoto, and Y. Suematsu, “Gain and the Threshold of Three-Dimensional Quantum-Box Lasers,” *IEEE J. Quantum Electron.*, vol. 22, no. 9, pp. 1915–1921, 1986.
- [59] E. U. Rafailov, M. A. Cataluna, and W. Sibbett, “Mode-Locked Quantum-Dot Lasers,” *Nat. Photonics*, vol. 1, pp. 395–401, 2007.
- [60] C. Gosset *et al.*, “Subpicosecond Pulse Generation at 134 GHz Using a Quantum-Dash-Based Fabry-Perot Laser Emitting at $1.56\mu\text{m}$,” *Appl. Phys. Lett.*, vol. 88, no. 24, pp. 10–13, 2006.
- [61] Z. G. Lu, J. R. Liu, S. Raymond, P. J. Poole, P. J. Barrios, and D. Poitras, “312-Fs Pulse Generation from a Passive C-Band InAs/InP Quantum Dot Mode-Locked Laser,” *Opt. Express*, vol. 16, no. 14, p. 10835, Jul. 2008.
- [62] A. Shen *et al.*, “Low Confinement Factor Quantum Dash (QD) Mode-

- Locked Fabry-Perot (FP) Laser Diode for Tunable Pulse Generation,” in *OFC/NFOEC 2008 - Conference on Optical Fiber Communication /National Fiber Optic Engineers Conference*, 2008, p. OThK1.
- [63] A. Akrouf, A. Shen, A. Enard, G.-H. Duan, F. Lelarge, and A. Ramdane, “Low Phase Noise All-Optical Oscillator Using Quantum Dash Modelocked Laser,” *Electron. Lett.*, vol. 46, no. 1, p. 73, 2010.
- [64] K. Merghem *et al.*, “Pulse Generation at 346 GHz Using a Passively Mode Locked Quantum-Dash-Based Laser at 1.55 μ m,” *Appl. Phys. Lett.*, vol. 94, no. 2, p. 21107, 2009.
- [65] K. Merghem *et al.*, “Stability of Optical Frequency Comb Generated with InAs/InP Quantum-Dash-Based Passive Mode-Locked Lasers,” *IEEE J. Quantum Electron.*, vol. 50, no. 4, pp. 275–280, 2014.
- [66] G. P. Agrawal and N. K. Dutta, *Semiconductor Lasers*, 2nd ed. New York: Van Nostrand Reinhold, 1993.
- [67] Y. Ben M’Salleem *et al.*, “Quantum-Dash Mode-Locked Laser as a Source for 56-Gb/s DQPSK Modulation in WDM Multicast Applications,” *IEEE Photon. Technol. Lett.*, vol. 23, no. 7, pp. 453–455, Apr. 2011.
- [68] W. Freude *et al.*, “Phase-Noise Compensated Carriers from an Optical Frequency Comb Allowing Terabit Transmission,” in *2015 17th International Conference on Transparent Optical Networks (ICTON)*, 2015, p. TU.B5.1.
- [69] J. Pfeifle *et al.*, “Simultaneous Phase Noise Reduction of 30 Comb Lines from a Quantum-Dash Mode-Locked Laser Diode Enabling Coherent Tbit/s Data Transmission,” in *Optical Fiber Communication Conference*, 2015, p. Tu3I.5.
- [70] J. Pfeifle *et al.*, “Coherent Terabit Communications Using a Quantum-Dash Mode-Locked Laser and Self-Homodyne Detection,” in *Optical Fiber Communication Conference*, 2015, p. W2A.19.
- [71] K. Merghem, V. Panapakkam, Q. Gaimard, F. Lelarge, and A. Ramdane, “Narrow Linewidth Frequency Comb Source Based on Self-Injected Quantum-Dash Passively Mode-Locked Laser,” in *Conference on Lasers and Electro-Optics*, 2017, p. SW1C.5.
- [72] J. N. Kemal *et al.*, “32QAM WDM Transmission at 12 Tbit/s Using a Quantum-Dash Mode-Locked Laser Diode (QD-MLLD) with External-Cavity Feedback,” *Opt. Express*, vol. 28, no. 16, p. 23594, 2020.

-
- [73] J. Hauck *et al.*, “Semiconductor Laser Mode Locking Stabilization With Optical Feedback From a Silicon PIC,” *J. Lightw. Technol.*, vol. 37, no. 14, pp. 3483–3494, Jul. 2019.
- [74] T. Herr *et al.*, “Temporal Solitons in Optical Microresonators,” *Nat. Photonics*, vol. 8, no. 2, pp. 145–152, 2013.
- [75] V. Brasch *et al.*, “Photonic Chip-Based Optical Frequency Comb Using Soliton Cherenkov Radiation,” *Science*, vol. 351, no. 6271, pp. 357–360, Jan. 2016.
- [76] B. Stern, X. Ji, Y. Okawachi, A. L. Gaeta, and M. Lipson, “Battery-Operated Integrated Frequency Comb Generator,” *Nature*, vol. 562, no. 7727, pp. 401–405, 2018.
- [77] C. Joshi *et al.*, “Thermally Controlled Comb Generation and Soliton Modelocking in Microresonators,” *arXiv*, vol. 41, no. 11, pp. 1–5, 2016.
- [78] V. Torres-Company *et al.*, “Laser Frequency Combs for Coherent Optical Communications,” *J. Lightw. Technol.*, vol. 37, no. 7, pp. 1663–1670, 2019.
- [79] H. Jung, K. Y. Fong, C. Xiong, and H. X. Tang, “Electrical Tuning and Switching of an Optical Frequency Comb Generated in Aluminum Nitride Microring Resonators,” *Opt. Lett.*, vol. 39, no. 1, p. 84, 2014.
- [80] I. P. Kaminow, T. Li, and A. E. Willner, “Optical Fiber Telecommunications VIB Systems and Networks.”
- [81] A. Pasquazi *et al.*, “Micro-Combs: A Novel Generation of Optical Sources,” *Phys. Rep.*, vol. 729, pp. 1–81, 2018.
- [82] J. Pfeifle *et al.*, “Coherent Terabit Communications with Microresonator Kerr Frequency Combs,” *Nat. Photonics*, vol. 8, no. 5, pp. 375–380, 2014.
- [83] C. Godey, I. V. Balakireva, A. Coillet, and Y. K. Chembo, “Stability Analysis of the Spatiotemporal Lugiato-Lefever Model for Kerr Optical Frequency Combs in the Anomalous and Normal Dispersion Regimes,” *Phys. Rev. A*, vol. 89, no. 6, p. 63814, Jun. 2014.
- [84] X. Xue *et al.*, “Mode-Locked Dark Pulse Kerr Combs in Normal-Dispersion Microresonators,” *Nat. Photonics*, vol. 9, no. 9, pp. 594–600, Sep. 2015.
- [85] A. Fülöp *et al.*, “High-Order Coherent Communications Using Mode-Locked Dark-Pulse Kerr Combs from Microresonators,” *Nat. Commun.*,

- vol. 9, no. 1, p. 1598, 2018.
- [86] J. Gärtner, P. Trocha, R. Mandel, C. Koos, T. Jahnke, and W. Reichel, “Bandwidth and Conversion Efficiency Analysis of Dissipative Kerr Soliton Frequency Combs Based on Bifurcation Theory,” *Phys. Rev. A*, vol. 100, no. 3, p. 033819, Sep. 2019.
- [87] W. Wang, L. Wang, and W. Zhang, “Advances in Soliton Microcomb Generation,” *Adv. Photonics*, vol. 2, no. 03, p. 1, 2020.
- [88] M. Yu, Y. Okawachi, A. G. Griffith, M. Lipson, and A. L. Gaeta, “Mode-Locked Mid-Infrared Frequency Combs in a Silicon Microresonator,” *Optica*, vol. 3, no. 8, p. 854, Aug. 2016.
- [89] C. W. Kaanta *et al.*, “Dual Damascene: A ULSI Wiring Technology,” *Proc. 18th Int. IEEE VLSI Multilevel Interconnect. Conf.*, pp. 144–152, 1991.
- [90] M. H. P. Pfeiffer *et al.*, “Photonic Damascene Process for Low-Loss, High-Confinement Silicon Nitride Waveguides,” *IEEE J. Sel. Top. Quantum Electron.*, vol. 24, no. 4, pp. 1–11, Jul. 2018.
- [91] M. H. P. Pfeiffer, J. Liu, A. S. Raja, T. Morais, B. Ghadiani, and T. J. Kippenberg, “Ultra-Smooth Silicon Nitride Waveguides Based on the Damascene Reflow Process: Fabrication and Loss Origins,” *Optica*, vol. 5, no. 7, p. 884, Jul. 2018.
- [92] P. Trocha *et al.*, “Ultrafast Optical Ranging Using Microresonator Soliton Frequency Combs,” *Science*, vol. 359, no. 6378, pp. 887–891, 2018.
- [93] V. Ataie *et al.*, “Ultrahigh Count Coherent WDM Channels Transmission Using Optical Parametric Comb Based Frequency Synthesizer,” *J. Lightw. Technol.*, vol. 33, no. 3, pp. 694–699, 2015.
- [94] B. J. Puttnam *et al.*, “2.15 Pb/s Transmission Using a 22 Core Homogeneous Single-Mode Multi-Core Fiber and Wideband Optical Comb,” in *European Conference on Optical Communication, ECOC*, 2015, p. PDP3.1.
- [95] D. Hillerkuss *et al.*, “Single-Laser 32.5 Tbit/s Nyquist WDM Transmission,” *J. Opt. Commun. Netw.*, vol. 4, no. 10, pp. 715–723, 2012.
- [96] P. Marin-Palomo *et al.*, “Microresonator-Based Solitons for Massively Parallel Coherent Optical Communications,” *Nature*, vol. 546, p. 274, Jun. 2017.
- [97] H. Hu *et al.*, “Single-Source Chip-Based Frequency Comb Enabling

- Extreme Parallel Data Transmission,” *Nat. Photonics*, vol. 12, no. 8, pp. 469–473, 2018.
- [98] J. N. Kemal *et al.*, “Coherent WDM Transmission Using Quantum-Dash Mode-Locked Laser Diodes as Multi-Wavelength Source and Local Oscillator,” vol. 27, no. 22, pp. 31164–31175, 2019.
- [99] L. Lundberg *et al.*, “Frequency Comb-Based WDM Transmission Systems Enabling Joint Signal Processing,” *Appl. Sci.*, vol. 8, no. 5, 2018.
- [100] T. Shao, R. Zhou, V. Vujicic, M. D. Gutierrez Pascual, P. M. Anandarajah, and L. P. Barry, “100 Km Coherent Nyquist Ultradense Wavelength Division Multiplexed Passive Optical Network Using a Tunable Gain-Switched Comb Source,” *J. Opt. Commun. Netw.*, vol. 8, no. 2, pp. 112–117, 2016.
- [101] V. Vujicic *et al.*, “Tbit/s Optical Interconnects Based on Low Linewidth Quantum-Dash Lasers and Coherent Detection,” in *Conference on Lasers and Electro-Optics*, 2016, p. SF2F.4.
- [102] Z. Lu, J. Liu, L. Mao, C.-Y. Song, J. Weber, and P. Poole, “12.032 Tbit/s Coherent Transmission Using an Ultra-Narrow Linewidth Quantum Dot 34.46-GHz C-Band Coherent Comb Laser,” in *Next-Generation Optical Communication: Components, Sub-Systems, and Systems VIII (Vol. 10947, p. 109470J)*. International Society for Optics and Photonics, 2019.
- [103] J. Lin, H. Sephrian, Y. Xu, L. A. Rusch, and W. Shi, “Frequency Comb Generation Using a CMOS Compatible SiP DD-MZM for Flexible Networks,” *IEEE Photon. Technol. Lett.*, vol. 30, no. 17, pp. 1495–1498, Sep. 2018.
- [104] Lumentum, “Micro-Integrable Tunable Laser Assembly (ITLA), 100 KHz Linewidth, LambdaFLEX,” 2019. [Online]. Available: <https://www.lumentum.com/en/products/micro-itla-tunable-laser-100-khz>. [Accessed: 07-Oct-2019].
- [105] G. P. Agrawal, *Fiber-Optic Communication Systems*, 4th ed. Hoboken, NJ, USA. Wiley, 2011.
- [106] T. J. Kippenberg, A. L. Gaeta, M. Lipson, and M. L. Gorodetsky, “Dissipative Kerr Solitons in Optical Microresonators,” *Science*, vol. 361, no. 6402, 2018.
- [107] P. S. Cho, V. S. Grigoryan, Y. A. Godin, A. Salamon, and Y. Achiam, “Transmission of 25-Gb/s RZ-DQPSK Signals with 25-GHz Channel Spacing over 1000 Km of SMF-28 Fiber,” *IEEE Photon. Technol. Lett.*,

- vol. 15, no. 3, pp. 473–475, 2003.
- [108] G. Raybon, P. J. Winzer, and C. R. Doerr, “1-Tb/s (10 x 107 Gb/s) Electronically Multiplexed Optical Signal Generation and WDM Transmission,” *J. Lightw. Technol.*, vol. 25, no. 1, pp. 233–238, Jan. 2007.
- [109] Auxora, “Duplex DWDM MUX & DEMUX Module,” 2018. [Online]. Available: <http://www.auxora.com/product/info2.aspx?itemid=171&cid=45&ppid=7&pid=23>. [Accessed: 11-Oct-2019].
- [110] Fujitsu, “DP-QPSK 100G LN Modulator,” 2014. [Online]. Available: <http://www.fujitsu.com/downloads/JP/archive/imgjp/group/foc/services/100gln/l100gdpqpsk-e-141105.pdf>. [Accessed: 07-Jan-2019].
- [111] Y. Cai *et al.*, “FPGA Investigation on Error-Floor Performance of a Concatenated Staircase and Hamming Code for 400G-ZR Forward Error Correction,” in *Optical Fiber Communication Conference Postdeadline Papers*, 2018, p. Th4C.2.
- [112] A. Blanco-Redondo, C. M. De Sterke, J. E. Sipe, T. F. Krauss, B. J. Eggleton, and C. Husko, “Pure-Quartic Solitons,” *Nat. Commun.*, vol. 7, no. 10427, 2016.
- [113] J. Liu *et al.*, “Ultralow-Power Chip-Based Soliton Microcombs for Photonic Integration,” *Optica*, vol. 5, no. 10, p. 1347, 2018.
- [114] R. J. Essiambre and R. W. Tkach, “Capacity Trends and Limits of Optical Communication Networks,” *Proc. IEEE*, vol. 100, no. 5, pp. 1035–1055, 2012.
- [115] K. Technologies, “M8194A 120 GSa/s Arbitrary Waveform Generator.” [Online]. Available: <https://www.keysight.com/en/pd-2951700-pn-M8194A/120-gsa-s-arbitrary-waveform-generator?cc=US&lc=eng>. [Accessed: 15-Dec-2019].
- [116] Y. Ogiso *et al.*, “Ultra-High Bandwidth InP IQ Modulator for beyond 100-GBd Transmission,” in *Optical Fiber Communications Conference (OFC)*, 2019, p. M2F.2.
- [117] T. Akiyama *et al.*, “An Ultra-Band Semiconductor Optical Amplifier Having an Extremely High Penalty-Free Output Power of 23 DBm Achieved with Quantum Dots,” *IEEE Photon. Technol. Lett.*, vol. 17, no. 8, pp. 1614–1616, 2005.
- [118] R. Rosales, K. Merghem, A. Martinez, F. Lelarge, A. Accard, and A. Ramdane, “Timing Jitter from the Optical Spectrum in Semiconductor

- Passively Mode Locked Lasers,” *Opt. Express*, vol. 20, no. 8, p. 9151, 2012.
- [119] A. Akrouf *et al.*, “Separate Error-Free Transmission of Eight Channels at 10 Gb/s Using Comb Generation in a Quantum-Dash-Based Mode-Locked Laser,” *IEEE Photon. Technol. Lett.*, vol. 21, no. 23, pp. 1746–1748, 2009.
- [120] C. Calò *et al.*, “Single-Section Quantum Well Mode-Locked Laser for 400 Gb/s SSB-OFDM Transmission,” *Opt. Express*, vol. 23, no. 20, p. 26442, 2015.
- [121] P. Marin *et al.*, “8.32 Tbit/s Coherent Transmission Using a Quantum-Dash Mode-Locked Laser Diode,” in *Conference on Lasers and Electro-Optics*, 2016, p. STh1F.1.
- [122] J. N. Kemal *et al.*, “WDM Transmission Using Quantum-Dash Mode-Locked Laser Diodes as Multi-Wavelength Source and Local Oscillator,” in *Optical Fiber Communication Conference*, 2017, p. Th3F.6.
- [123] J. N. Kemal *et al.*, “32QAM WDM Transmission Using a Quantum-Dash Passively Mode-Locked Laser with Resonant Feedback,” in *Optical Fiber Communication Conference Postdeadline Papers*, 2017, p. Th5C.3.
- [124] J. Müller *et al.*, “Silicon Photonics WDM Transmitter with Single Section Semiconductor Mode-Locked Laser,” *Adv. Opt. Technol.*, vol. 4, no. 2, pp. 119–145, 2015.
- [125] A. Moscoso-Mártir *et al.*, “8-Channel WDM Silicon Photonics Transceiver with SOA and Semiconductor Mode-Locked Laser,” *Opt. Express*, vol. 26, no. 19, p. 25446, 2018.
- [126] R. Rosales *et al.*, “InAs / InP Quantum-Dot Passively Mode-Locked Lasers for 1.55-Mm Applications,” vol. 17, no. 5, pp. 1292–1301, 2011.
- [127] R. Rosales *et al.*, “High Performance Mode Locking Characteristics of Single Section Quantum Dash Lasers,” *Opt. Express*, vol. 20, no. 8, p. 8649, 2012.
- [128] R. Maldonado-Basilio, J. Parra-Cetina, S. Latkowski, and P. Landais, “Timing-Jitter, Optical, and Mode-Beating Linewidths Analysis on Subpicosecond Optical Pulses Generated by a Quantum-Dash Passively Mode-Locked Semiconductor Laser,” *Opt. Lett.*, vol. 35, no. 8, p. 1184, 2010.
- [129] R. Schmogrow *et al.*, “Error Vector Magnitude as a Performance Measure

- for Advanced Modulation Formats,” *IEEE Photon. Technol. Lett.*, vol. 24, no. 1, pp. 61–63, Jan. 2012.
- [130] Y. Takushima, H. Sotobayashi, M. E. Grein, E. P. Ippen, and H. a. Haus, “Linewidth of Mode Combs of Passively and Actively Mode-Locked Semiconductor Laser Diodes,” *Proc. SPIE*, vol. 5595, pp. 213–227, 2004.
- [131] G. Di Domenico, S. Schilt, and P. Thomann, “Simple Approach to the Relation between Laser Frequency Noise and Laser Line Shape,” *Appl. Opt.*, vol. 49, no. 25, pp. 4801–4807, 2010.
- [132] A. Godone, S. Micalizio, and F. Levi, “RF Spectrum of a Carrier with a Random Phase Modulation of Arbitrary Slope,” *Metrologia*, vol. 45, no. 3, pp. 313–324, 2008.
- [133] T. N. Huynh, L. Nguyen, and L. P. Barry, “Phase Noise Characterization of SGDBR Lasers Using Phase Modulation Detection Method with Delayed Self-Heterodyne Measurements,” *J. Lightw. Technol.*, vol. 31, no. 8, pp. 1300–1308, 2013.
- [134] G. Vedala, M. Al-Qadi, M. O’Sullivan, J. Cartledge, and R. Hui, “Phase Noise Characterization of a QD-Based Diode Laser Frequency Comb,” *Opt. Express*, vol. 25, no. 14, p. 15890, 2017.
- [135] K. Zanette, J. C. Cartledge, R. Hui, and M. O’Sullivan, “Phase Noise Characterization of a Mode-Locked Quantum-Dot Coherent Optical Frequency Comb Source Laser,” *Opt. Fiber Commun. Conf.*, p. Th2A.17, 2018.
- [136] "Keysight Technologies", “Spectrum Analysis Basics,” *Application note 150*. [Online]. Available: <http://literature.cdn.keysight.com/litweb/pdf/5952-0292.pdf>. [Accessed: 20-Sep-2006].
- [137] W. J. Thompson, “Numerous Neat Algorithms for the Voigt Profile Function,” *Comput. Phys.*, vol. 7, no. 6, p. 627, 1993.
- [138] R. Schmogrow *et al.*, “Real-Time Nyquist Pulse Generation beyond 100 Gbit/s and Its Relation to OFDM,” *IEEE Photon. Technol. Lett.*, vol. 24, no. 1, pp. 61–63, Jan. 2012.
- [139] P. J. Winzer, A. H. Gnauck, C. R. Doerr, M. Magarini, and L. L. Buhl, “Spectrally Efficient Long-Haul Optical Networking Using 112-Gb/s Polarization-Multiplexed 16-QAM,” *J. Lightw. Technol.*, vol. 28, no. 4, pp. 547–556, 2010.
- [140] L. M. Zhang and F. R. Kschischang, “Staircase Codes with 6% to 33%

- Overhead,” *J. Lightw. Technol.*, vol. 32, no. 10, pp. 1999–2002, 2014.
- [141] A. Leven, N. Kaneda, U. V. Koc, and Y. K. Chen, “Frequency Estimation in Intradyne Reception,” *IEEE Photon. Technol. Lett.*, vol. 19, no. 6, pp. 366–368, 2007.
- [142] S. M. Bilal, K. P. Zhong, J. Cheng, A. P. T. Lau, G. Bosco, and C. Lu, “Performance and Complexity Comparison of Carrier Phase Estimation Algorithms for DP-64-QAM Optical Signals,” *European Conference on Optical Communication (ECOC)*, pp. 25–27, 2014.
- [143] M. I. Olmedo *et al.*, “Carrier Recovery Techniques for Semiconductor Laser Frequency Noise for 28 Gbd DP-16QAM,” in *Conference on Optical Fiber Communication*, 2015, p. Th2A.10.
- [144] J. R. Navarro *et al.*, “Carrier Phase Recovery Algorithms Coherent Optical Circular MQAM Systems,” *Photonics*, vol. 3, no. 2, pp. 2717–2723, 2016.
- [145] B. S. G. Pillai *et al.*, “End-to-End Energy Modeling and Analysis of Long-Haul Coherent Transmission Systems,” *J. Lightw. Technol.*, vol. 32, no. 18, pp. 3093–3111, 2014.
- [146] A. Hasegawa and Y. Kodama, *Solitons in Optical Communications*. New York: Clarendon Press; Oxford Univ. Press, 1995.
- [147] L. F. Mollenauer, R. H. Stolen, and J. P. Gordon, “Experimental Observation of Picosecond Pulse Narrowing and Solitons in Optical Fibers,” *Phys. Rev. Lett.*, vol. 45, no. 13, pp. 1095–1098, 1980.
- [148] A. Ankiewicz and N. Akhmediev, *Dissipative Solitons: From Optics to Biology and Medicine*. 2008.
- [149] J. S. Levy, A. Gondarenko, M. A. Foster, A. C. Turner-Foster, A. L. Gaeta, and M. Lipson, “CMOS-Compatible Multiple-Wavelength Oscillator for on-Chip Optical Interconnects,” *Nat. Photonics*, vol. 4, no. 1, pp. 37–40, Jan. 2010.
- [150] N. Bozinovic *et al.*, “Terabit-Scale Orbital Angular Momentum Mode Division Multiplexing in Fibers,” *Science*, vol. 340, no. 6140, pp. 1545–1548, 2013.
- [151] D. Dai and J. E. Bowers, “Silicon-Based on-Chip Multiplexing Technologies and Devices for Peta-Bit Optical Interconnects,” *Nanophotonics*, vol. 3, no. 4–5, pp. 283–311, 2014.
- [152] M. Nakazawa, E. Yamada, H. Kubota, and K. Suzuki, “10 Gbit/s Soliton

- Data Transmission over One Million Kilometres,” *Electron. Lett.*, vol. 27, no. 14, pp. 1270–1272, 1991.
- [153] P. Del’Haye, a Schliesser, O. Arcizet, T. Wilken, R. Holzwarth, and T. J. Kippenberg, “Optical Frequency Comb Generation from a Monolithic Microresonator,” *Nature*, vol. 450, no. 7173, pp. 1214–7, Dec. 2007.
- [154] T. J. Kippenberg, R. Holzwarth, and S. A. Diddams, “Microresonator-Based Optical Frequency Combs,” *Science*, vol. 332, no. 6029, pp. 555–559, 2011.
- [155] L. A. Lugiato and R. Lefever, “Spatial Dissipative Structures in Passive Optical Systems,” *Phys. Rev. Lett.*, vol. 58, no. 21, pp. 2209–2211, 1987.
- [156] X. Yi, Q.-F. Yang, K. Y. Yang, M.-G. Suh, and K. Vahala, “Soliton Frequency Comb at Microwave Rates in a High-Q Silica Microresonator,” *Optica*, vol. 2, no. 12, p. 1078, 2015.
- [157] M. Yu, Y. Okawachi, A. G. Griffith, N. Picqué, M. Lipson, and A. L. Gaeta, “Silicon-Chip-Based Mid-Infrared Dual-Comb Spectroscopy,” *Nat. Commun.*, vol. 9, no. 1, p. 1869, 2018.
- [158] J. D. Jost, T. Herr, C. Lecaplain, V. Brasch, M. H. P. Pfeiffer, and T. J. Kippenberg, “Counting the Cycles of Light Using a Self-Referenced Optical Microresonator,” *Optica*, vol. 2, no. 8, pp. 706–711, 2015.
- [159] W. Liang *et al.*, “High Spectral Purity Kerr Frequency Comb Radio Frequency Photonic Oscillator,” *Nat. Commun.*, vol. 6, p. 7957, 2015.
- [160] M.-G. Suh, Q.-F. Yang, K. Y. Yang, X. Yi, and K. J. Vahala, “Microresonator Soliton Dual-Comb Spectroscopy,” *Science*, vol. 354, no. 6312, pp. 600–603, 2016.
- [161] M. H. P. Pfeiffer *et al.*, “Photonic Damascene Process for Integrated High-Q Microresonator Based Nonlinear Photonics,” *Optica*, vol. 3, no. 1, pp. 20–25, 2016.
- [162] A. Kordts, M. H. P. Pfeiffer, H. Guo, V. Brasch, and T. J. Kippenberg, “Higher Order Mode Suppression in High-Q Anomalous Dispersion SiN Microresonators for Temporal Dissipative Kerr Soliton Formation,” *Opt. Lett.*, vol. 41, no. 3, pp. 452–455, 2016.
- [163] A. Sano *et al.*, “102.3-Tb/s (224 x 548-Gb/s) C- and Extended L-Band All-Raman Transmission over 240 Km Using PDM-64QAM Single Carrier FDM with Digital Pilot Tone,” in *Optical Fiber Communication Conference*, 2012, p. PDP5C.3.

- [164] C. Kachris and I. Tomkos, "A Survey on Optical Interconnects for Data Centers," *IEEE Commun. Surv. Tutorials*, vol. 14, no. 4, pp. 1021–1036, 2012.
- [165] M. Blaicher *et al.*, "Hybrid Multi-Chip Assembly of Optical Communication Engines by in Situ 3D Nano-Lithography," *Light Sci. Appl.*, vol. 9, no. 1, p. 71, Dec. 2020.
- [166] R. Nagarajan *et al.*, "InP Photonic Integrated Circuits," *IEEE J. Sel. Top. Quantum Electron.*, vol. 16, no. 5, pp. 1113–1125, 2010.
- [167] D. Liang and J. E. Bowers, "Recent Progress in Lasers on Silicon," *Nat. Photonics*, vol. 4, pp. 511–517, 2010.
- [168] N. Lindenmann *et al.*, "Photonic Wire Bonding: A Novel Concept for Chip-Scale Interconnects," *Opt. Express*, vol. 20, no. 16, p. 17667, 2012.
- [169] M. Lauermaun *et al.*, "40 GBd 16QAM Signaling at 160 Gb/s in a Silicon-Organic Hybrid Modulator," *J. Lightw. Technol.*, vol. 33, no. 6, pp. 1210–1216, 2015.
- [170] C. Koos *et al.*, "Silicon-Organic Hybrid (SOH) and Plasmonic-Organic Hybrid (POH) Integration," *J. Lightw. Technol.*, vol. 34, no. 2, pp. 256–268, 2016.
- [171] S. K. Selvaraja, P. Jaenen, W. Bogaerts, D. Van Thourhout, P. Dumon, and R. Baets, "Fabrication of Photonic Wire and Crystal Circuits in Silicon-on-Insulator Using 193-Nm Optical Lithography," *J. Lightw. Technol.*, vol. 27, no. 18, pp. 4076–4083, 2009.
- [172] Y. Xuan *et al.*, "High-Q Silicon Nitride Microresonators Exhibiting Low-Power Frequency Comb Initiation," *Optica*, vol. 3, no. 11, pp. 1171–1180, 2016.
- [173] M. H. P. Pfeiffer, J. Liu, M. Geiselmann, and T. J. Kippenberg, "Coupling Ideality of Integrated Planar High-Q Microresonators," *Phys. Rev. Appl.*, vol. 7, no. 024026, 2017.
- [174] B. J. Puttnam *et al.*, "High-Capacity Self-Homodyne PDM-WDM-SDM Transmission in a 19-Core Fiber," *Opt. Express*, vol. 22, no. 18, pp. 21185–21191, 2014.
- [175] P.-H. Wang *et al.*, "Intracavity Characterization of Micro-Comb Generation in the Single-Soliton Regime," *Opt. Express*, vol. 24, no. 10, pp. 10890–10897, 2016.
- [176] T. Carmon, L. Yang, and K. Vahala, "Dynamical Thermal Behavior and

- Thermal Self-Stability of Microcavities.,” *Opt. Express*, vol. 12, no. 20, pp. 4742–4750, 2004.
- [177] M. Karpov *et al.*, “Raman Self-Frequency Shift of Dissipative Kerr Solitons in an Optical Microresonator,” *Phys. Rev. Lett.*, vol. 116, no. 10, p. 103902, 2016.
- [178] J. Pfeifle *et al.*, “Full C and L-Band Transmission at 20 Tbit / s Using Cavity-Soliton Kerr Frequency Combs,” in *Conference on Lasers and Electro-Optics*, 2015, p. JTh5C.8.
- [179] P. Marin *et al.*, “50 Tbit/s Massively Parallel WDM Transmission in C and L Band Using Interleaved Cavity-Soliton Kerr Combs,” in *Conference on Lasers and Electro-Optics*, 2016, p. STu1G.1.
- [180] P. Marin *et al.*, “34.6 Tbit/s WDM Transmission Using Soliton Kerr Frequency Combs as Optical Source and Local Oscillator,” in *European Conference on Optical Communication, ECOC*, 2016, p. PDP3.1.
- [181] D. Hillerkuss *et al.*, “26 Tbit S–1 Line-Rate Super-Channel Transmission Utilizing All-Optical Fast Fourier Transform Processing,” *Nat. Photonics*, vol. 5, no. 6, pp. 364–371, 2011.
- [182] R. Dar *et al.*, “Impact of WDM Channel Correlations on Nonlinear Transmission,” in *European Conference on Optical Communication, ECOC*, 2016, p. W.1.D.2.
- [183] N. S. Bergano and C. R. Davidson, “Circulating Loop Transmission Experiments for the Study of Long-Haul Transmission Systems Using Erbium-Doped Fiber Amplifiers,” *J. Lightw. Technol.*, vol. 13, no. 5, pp. 879–888, 1995.
- [184] J. Cai, M. Nissov, C. Davidson, and A. Pilipetskii, “Measurement Techniques for High-Speed WDM Experiments,” in *Optical Fiber Communications Conference (OFC)*, 2003, p. ThW1.
- [185] F. Buchali, A. Klekamp, L. Schmalen, and T. Drenski, “Implementation of 64QAM at 42.66 GBaud Using 1.5 Samples per Symbol DAC and Demonstration of up to 300km Fiber Transmission,” in *Conference on Optical Fiber Communication (OFC)*, 2014, p. M2A.1.
- [186] J. H. Ke, Y. Gao, and J. C. Cartledge, “400 Gbit/s Single-Carrier and 1 Tbit/s Three-Carrier Superchannel Signals Using Dual Polarization 16-QAM with Look-up Table Correction and Optical Pulse Shaping,” *Opt. Express*, vol. 22, no. 1, pp. 71–84, 2014.

- [187] L. Gasca, "From O to L: The Future of Optical Wavelength-Bands," *Broadband Prop.*, pp. 83–85, 2008.
- [188] Oclaro, "LambdaFLEX ITLA TL5000 Integrated Tunable Laser Assembly - C Band, Variable Output Power (2006)," 2006. [Online]. Available: <http://www.oclaro.com/product/tl5000vcj/>.
- [189] Emcore, "MAFA 3000 Series Erbium Doped Fiber Amplifier (2010)," 2010. [Online]. Available: http://www.eqphotonics.de/cms/cms/upload/datasheets/MAFA3000-08_2010.pdf. [Accessed: 20-Jul-2003].
- [190] Emcore, "MAFA 5000 Series Erbium Doped Fiber Micro Amplifier (2016)," 2016. [Online]. Available: <http://emcore.com/wp-content/uploads/2016/10/MAFA-5000-Series.pdf>. [Accessed: 20-Jul-2003].
- [191] Arduino, "Arduino/Genuino UNO (2016)," 2016. [Online]. Available: <https://www.arduino.cc/en/Main/ArduinoBoardUno>.
- [192] T. Analog, "ATE1-07 TEC Modules (2016)," 2016. [Online]. Available: <http://www.analogtechnologies.com/document/ATE1-07.pdf>.
- [193] A. M. Vengsarkar, N. S. Bergano, C. R. Davidson, J. R. Pedrazzani, J. B. Judkins, and P. J. Lemaire, "Long-Period Fiber-Grating-Based Gain Equalizers," *Opt. Lett.*, vol. 21, no. 5, pp. 336–338, 1996.
- [194] H. S. Kim, S. H. Yun, I. K. Kwang, and B. Y. Kim, "All-Fiber Acousto-Optic Tunable Notch Filter with Electronically Controllable Spectral Profile," *Opt. Lett.*, vol. 22, no. 19, pp. 1476–1478, 1997.
- [195] Auxora, "CATV Module (2009)," 2009. [Online]. Available: <http://www.auxora.com/doce/product-detail-pcid-68-page-2.html>.
- [196] J. Riemensberger, K. Hartinger, T. Herr, V. Brasch, R. Holzwarth, and T. J. Kippenberg, "Dispersion Engineering of Thick High-Q Silicon Nitride Ring-Resonators via Atomic Layer Deposition," *Opt. Express*, vol. 20, no. 25, pp. 27661–27669, 2012.
- [197] P. W. Juodawlkis *et al.*, "High-Power, Low-Noise 1.5-Mm Slab-Coupled Optical Waveguide (SCOW) Emitters: Physics, Devices, and Applications," *IEEE J. Sel. Top. Quantum Electron.*, vol. 17, no. 6, pp. 1698–1714, 2011.
- [198] OptSim, "Synopsys, Inc. (2016)," 2016. [Online]. Available: <https://optics.synopsys.com/rsoft/rsoft-system-network-optsim.html>.
- [199] S. Coen and M. Erkintalo, "Universal Scaling Laws of Kerr Frequency Combs.," *Opt. Lett.*, vol. 38, no. 11, pp. 1790–2, Jun. 2013.

- [200] C. Bao *et al.*, “Nonlinear Conversion Efficiency in Kerr Frequency Comb Generation,” *Opt. Lett.*, vol. 39, no. 21, pp. 6126–6129, 2014.
- [201] Optilab, “Gain Flattened EDFA for R&D Application (EDFA-GI-R),” 2016. [Online]. Available: http://www.optilab.com/products/category/gain_flattened_edfa/gain_flattened_booster_edfa_for_rd_networks/.
- [202] Optilab, “L-Band Inline EDFA with Mid-Stage Access (EDFA-L-M-R),” 2016. [Online]. Available: http://www.optilab.com/products/category/EDFA/l_band_inline_edfa_with_mid_stage_access/.
- [203] Finisar, “WaveShaper Series A Family of Programmable Optical Processors,” 2016. [Online]. Available: https://www.finisar.com/sites/default/files/downloads/waveshaper_12page_product_brochure_09_16_1.pdf.
- [204] Oclaro, “400G Lithium Niobate Modulator,” 2016. [Online]. Available: <http://www.oclaro.com/product/400g-lithium-niobate-modulator/>. [Accessed: 20-Jul-2004].
- [205] C. J. Meyer, “Measuring the Peak-to-Average Power of Digitally Modulated Signals,” *Boonton Application Note AN-50*, 1993.
- [206] P. C. Becker, N. A. Olsson, and J. R. Simpson, *Erbium-Doped Fiber Amplifiers : Fundamentals and Technology*. San Diego: Academic Press, 1999.
- [207] M. Communications, “EOA- μ Preamplifier,” 2017. [Online]. Available: http://mpbcommunications.com/en/site/products/gain_modules/EOA-Micro/preamplifiers/index.html. [Accessed: 20-Jul-2004].

D. Glossary

D.1 List of Abbreviations

16QAM	16-state quadrature amplitude modulation
32QAM	32-state quadrature amplitude modulation
ADC	Analog-to-digital converter
ASE	Amplified spontaneous emission
AWG	Arbitrary waveform generator
AWGN	Additive white Gaussian noise
BER	Bit-error ratio
BPD	Balanced photodetector
BPF	Band-pass filter
BPS	Blind phase search
CAGR	Compound annual growth rate
CD	Chromatic dispersion
CMA	Constant-modulus algorithm
CMOS	Complementary metal oxide semiconductor
CPL	Directional coupler
CPR	Carrier phase recovery
CW	Continuous wave
DAC	Digital-to-analog converter
DC	Data center, direct current

DEMUX	Wavelength demultiplexer
DFB	Distributed feedback
DKS	Dissipative Kerr soliton
DL	Delay line
DP	Dual-polarization
DSP	Digital signal processing
ECL	External-cavity laser
EDFA	Erbium-doped fiber amplifier
ENOB	Effective number of bits
EO	Electro-optic
ESA	Electrical spectrum analyser
EVM	Error-vector magnitude
FBG	Fiber Bragg grating
FCG	Frequency comb generator
FEC	Forward-error correction
FG	Function generator
FM	Frequency modulation
FP	Fabry-Perot
FPC	Fiber polarization controller
FWHM	Full width half maximum
FSR	Free spectral range
GSLD	Gain-switched laser diode
GVD	Group velocity dispersion

HNW	Highly-nonlinear waveguide
IF	Intermediate frequency
IoT	Internet-of-things
IQ	In-phase/quadrature
ITLA	Integrated tunable laser assembly
ITU	International telecommunication union
LF	Lensed fiber
LIDAR	Light detection and ranging
LO	Local oscillator
MBE	Molecular beam epitaxy
MI	Modulation instability
MIMO	Multiple-input multiple-output
MLLD	Mode-locked laser diode
MUX	Wavelength multiplexer
MZM	Mach-Zehnder modulator
NF	Notch filter
NIST	National Institute of Standards and Technology
OCNR	Optical carrier-to-noise ratio
OFDM	Orthogonal frequency division multiplexing
OH	Optical hybrid
OMA	Optical modulation analyzer
OOK	On-off-keying

OSA	Optical spectrum analyzer
OSNR	Optical signal-to-noise ratio
PAM-4	Four-levels pulse amplitude modulation
PBC	Polarization beam combiner
PBS	Polarization beam splitter
PC	Polarization controller
PD	Photodiode
PDF	Polarization-division multiplexing
PDM	Polarization division multiplexing
PMD	Polarization mode dispersion
POF	Programmable optical filter
PRBS	Pseudo-random bit sequence
PSCF	pure silica-core fiber
PSK	Phase-shift keying
PTB	Physikalisch-Technische Bundesanstalt
QD	Quantum dash
QPSK	Quadrature phase-shift keying
RC	Raised-cosine
RF	Radio-frequency
RIN	Relative intensity noise
SCH	Separate confinement heterostructure
SDM	Spatial division multiplexing
SE	Spectral efficiency

SiN	Silicon nitride
SMF	Single-mode fiber
SNR	Signal-to-noise ratio
SOA	Semiconductor optical amplifier
SOH	Silicon-organic hybrid
SPM	Self-phase modulation
SSMF	Standard single-mode fiber
TDFA	Thulium-doped fiber amplifier
TEM	Transmission-electron microscope
TEC	Thermo-electric cooler
USA	United states of America
VCSEL	Vertical-cavity surface-emitting laser
VOA	Variable optical attenuator
VSA	Vector signal analyzer
WDM	Wavelength division multiplexing
WSS	Wavelength-selective switch
XPM	Cross-phase modulation
ZB	Zettabyte

D.2 List of mathematical symbols

Greek symbols

α	Fiber attenuation coefficient in dB/km
β	Roll-off factor of raised-cosine signal

Γ	Power conversion efficiency
$\delta\omega$	Cold cavity detuning
$\Delta\phi$	Phase difference
δf	Resolution bandwidth
Δf	Optical linewidth
$\Delta\tau$	Differential group delay
κ_0	Cavity internal loss-rate
κ_{ex}	External coupling rate
λ	Wavelength
ν	Comb line index
$\sigma_{\Delta\phi}^2$	Phase noise variance
τ_0	Observation time
$\phi(t)$	Intrinsic time-varying phase of a carrier
$\phi_0(t)$	Phase noise of the center comb line
$\phi_R(t)$	Phase noise caused by fluctuations of the round-trip time
$\phi_s(t)$	Phase modulation of a carrier
ω	Angular frequency

Latin symbols

A	Spectral power of the frequency noise in a given range
B	Bandwidth
B_{ref}	Reference bandwidth for noise power evaluation
c	Speed of light

C	Shannon capacity
C_λ	Dispersion parameter
D_i	Taylor expansion coefficients for cavity modes
$E(t)$	Optical signal amplitude
$\underline{E}(t)$	Complex representation of the optical signal
f	Frequency
f_0	Frequency offset
f_{BW}	Bandwidth of the frequency comb
f_c	Center frequency of the frequency comb
f_f	Frequency of the right-most comb line
f_i	Frequency of the left-most comb line
f_r	Free spectral range
$f_{\text{inst}}(t)$	Instantaneous optical frequency fluctuations
F	Optical amplifier noise figure
g	Single-photon Kerr frequency shift
g	Power transmission factor
G	Optical amplifier gain
h	Planck's constant
$H(f)$	Raised-cosine filter
$\underline{i}(t)$	Complex time-domain photocurrent
K	Number of symbols or constellation size

L	WDM channels
M	Number of fiber spans in a transmission link
R_s	Symbol rate
n	Linear refractive index of a waveguide
n_2	Nonlinear refractive index of a waveguide
N	Number of processed symbols
N_0	Noise spectral power density
O_c	Coding overhead
p	1 (2) for single polarization (polarization multiplexed) signal
P	Optical power
P_{el}	Electrical power consumption
Q	Quality factor
R_s	Symbol rate
$S(t)$	Power-spectral-density-function
T_S	Symbol duration
V_{eff}	Nonlinear optical effective mode volume

Acknowledgments

This dissertation was written during my doctoral studies at the Institute of Photonics and Quantum Electronics (IPQ) at the Karlsruhe Institute of Technology (KIT). This work was integrated into the Erasmus Mundus doctorate program Europhotonics (grant number 159224-1-2009-1-FR-ERA MUNDUS-EMJD). I would like to dedicate this section to express my sincere gratitude to all people who have supported me during this important period of my life. I hereby acknowledge their contributions to the achievements of this work.

First, I would like to express my gratitude to my main advisor Prof. Christian Koos for granting me the opportunity to join his team at IPQ as a PhD student and be part of such a motivating and knowledgeable team. I thank Prof. Koos for guiding me through the different projects in which I participated. The success of this work would not have been possible without his extraordinary dedication and his ability to confront any challenge in a pragmatic way. Those late-evening paper discussion did pay off.

I would like to express my sincere appreciation to Prof. Wolfgang Freude for his effort and patience in supporting me through my PhD. Especially for his encouraging advice to improve my writing and presentation skills. Even at the end of my PhD, I still feel deeply impressed by his extraordinary linguistic skills.

I thank Prof. Randel for his guidance on the last stage of my PhD. In particular, his exceptional knowledge of signal processing has had a noticeable impact on the success of this work.

I would like to also thank Prof. Jens Biegert, who warmly welcomed me to his team at ICFO and made my short stay there pleasant and productive.

From a humble standpoint, I feel grateful for the supervision from such top-tier Professors and I hope to have taken hold of some of their knowledge throughout these years.

I would like to thank all IPQ colleagues who have made my stay at IPQ more enjoyable. I am honestly grateful to Jörg Pfeifle and Juned N. Kemal, who supervised me during my first months at IPQ and taught me all I needed to know regarding, e.g., optical communications and characterization of mode-locked lasers. Thanks to them, I could become quickly independent and take the lead in transmission experiments. Similarly, I would like to thank Stefan Wolf, who helped me numerous times to tackle unexpected issues with system lab equipment, and was always accessible for discussing measurement results. I also thank Philipp Trocha, not only for his assistance during tough experiments and for his discussions on soliton dynamics - which allowed me to understand some of the curious behavior of these states in the lab - but also for helping me many times deal with work-related and personal paperwork. I also thank Dengyang Fang for sharing exciting moments in the lab for the last year and a half, and making the last part of my PhD memorable.

I would like to thank all the colleagues with whom I had the pleasure to share the office and most part of my PhD. In this regard, I thank again Jörg Pfeifle, for the long discussion about soliton generation, and phase noise properties of MLLD, and Juned N. Kemal, for the uncountable discussions we had of every peculiar phenomenon we observed in the lab. Their experience and assistance were undoubtedly crucial for the success of this work. I also thank Alban Sherifaj, Tilahun Gutema, Sentayehu Wondimu, Jonas Krimmer, and Patrick Matalla for making the tea/coffee breaks interesting by sharing thoughts from politics and history to movies and videogames.

I would like to thank my PhD colleagues Aleksandar Nestic, Denis Ganin, Adib Hossain, Muhammad Rodlin Billah (aka, Oding), Yilin Xu, Stefan Singer, Philipp Dietrich, Heiner Zwickel, Simon Schneider, Claudius Weimann, Yasar Kutuvantavida, Matthias Lauermann, Carsten Eschenbaum, Mareike Trappen, and Pascal Maier for a great time we spent together at IPQ. I particularly thank Tobias Harter, not only for his advice and help during my PhD but also for the great moments we shared at the institute and especially at the memorable 2016 CLEO conference. I also thank my colleagues Christop Füllner, Clemens Kieninger, and Alexander Kotz for those late-afternoons table tennis games. I want to also thank my former Master students Vincent Lauinger, Yizhao Jia,

Raajib Ehsan, Alban Sherifaj, Daniel Drayss, and Erdem Cil, that I had the privilege to supervise during my PhD and with whom I shared important moments and allowed me to obtain supervision knowledge, quite important for academia.

I would like to thank my colleagues at ICFO, Daniel Rivas, Nicola di Palo, Ugaitz Elu, Aurelien Sanchez, and especially Tobias Steinle, who introduced me to CEP techniques and taught me valuable electronic knowledge. They made my stay at ICFO really valuable and enjoyable.

I would like to especially thank the group of Prof. Tobias Kippenberg at EPFL, whose collaboration made a great part of this Thesis possible. I want to especially thank Maxim Karpov, for teaching me how to generate solitons in the lab and for the countless discussions we had regarding the properties of their microresonators. I want to also thank Prof. Abderrahim Ramdane and his group for their valuable collaboration in this work.

I would like to thank Andrea Riemensperger, Marie-Luise Koch, Tatiana Gassmann, and Bernadette Lehmann, for providing such great administrative support and for making IPQ atmosphere more pleasant. I would also like to thank my Mentor, Dr. Martin Lauer, and the coordinators from the Erasmus program Sophie Brasselet, Crina Cojocaru, Jordi Mompert and Hugues Giovannini. I would like to thank David Guder, Oswald Speck, and Martin Winkeler, and Marco Hummel for always being available to help with spontaneous IT, mechanical or electro-optical needs.

This work would not have been possible if it wasn't for the unconditional support of my family and friends. I thank my siblings Laura and Carlos and I especially thank my parents Melchor and Ascensión which have made uncountable sacrifices to make my life cheerful and easier and to provide me with an excellent education. I especially want to thank my fiancée Öncü, which has spent all these years by my side and has enjoyed and suffered with me the good and bad moments of my PhD. Her joyful character, able to make me laugh and cheer me up, and our little adventures through Germany made this PhD easier to handle.

List of Publications

Book Chapter

- [B1] J. N. Kemal, **P. Marin-Palomo**, M. Karpov, M. H. Anderson, W. Freude, T. J. Kippenberg, and C. Koos, “Chip-Based Frequency Combs for Wavelength-Division Multiplexing Applications,” In: Willner A. E. (Ed): *Optical Fiber Telecommunications VII*, 7th ed. Elsevier (Imprint: Academic Press), Chapter 2, pp. 51–102, 2020.

Journal Publications

- [J1] **Marin-Palomo, P.**; Kemal, J. N.; Karpov, M.; Kordts, A.; Pfeifle, J.; Pfeiffer, M.; Trocha, P.; Wolf, S.; Brasch, V.; Anderson, M. H.; Rosenberger, R.; Vijayan, K.; Freude, W.; Kippenberg, T. J.; Koos, C., “Microresonator-based solitons for massively parallel coherent optical communications,” *Nature* **546**, 274–279 (2017), [DOI: 10.1038/nature22387](https://doi.org/10.1038/nature22387)
- [J2] **Marin-Palomo, P.**; Kemal, J. N.; Trocha, P.; Wolf, S.; Merghem, K.; Lelarge, F.; Ramdane, A.; Freude, W.; Randel, S.; Koos, C., “Comb-based WDM transmission at 10 Tbit/s using a DC-driven quantum-dash mode-locked laser diode,” *Opt. Express* **27**, 31110–31129 (2019), [DOI: 10.1364/oe.27.031110](https://doi.org/10.1364/oe.27.031110)
- [J3] **Marin-Palomo, P.**; Kemal, J. N.; Kippenberg, T. J.; Freude, W.; Randel, S.; Koos, C., “Performance of chip-scale optical frequency comb generators in coherent WDM communications,” *Opt. Express* **28**, 12897–12910 (2020), [DOI: 10.1364/OE.380413](https://doi.org/10.1364/OE.380413)

- [J4] Kemal, J. N.; **Marin-Palomo, P.**; Merghem, K.; Aubin, G.; Lelarge, F.; Ramdane, A.; Freude, W.; Randel, S.; Koos, C., “32QAM WDM transmission at 12 Tbit/s using a quantum-dash mode-locked laser diode (QD-MLLD) with external-cavity feedback,” *Opt. Express* **28**, 23594–23608 (2020), [DOI: 10.1364/oe.392007](https://doi.org/10.1364/oe.392007)
- [J5] Zazzi, A.; Müller, J.; Gudyriev, S.; **Marin-Palomo, P.**; Fang, D.; Scheytt, C.; Koos, J.; Witzens, J., “Fundamental limitations of spectrally-sliced optically enabled data converters arising from MLL timing jitter,” *Opt. Express* **28**, 18790–18813 (2020), [DOI: 10.1364/oe.382832](https://doi.org/10.1364/oe.382832)
- [J6] Blaicher, M.; Muhammad Rodlin, B.; Kemal, J.; Hoose, T.; Hoose, **Marin-Palomo, P.**; Hofmann, A.; Kutuvantavida, Y.; Kieninger, C.; Dietrich, P.-I.; Lauermaun, M.; Wolf, S.; Troppenz, U.; Moehrle, M.; Merget, F.; Skacel, S.; Witzens, J.; Randel, S.; Freude, W.; Koos, C., “Hybrid multi-chip assembly of optical communication engines by in situ 3D nano-lithography,” *Light: Science & Applications* **9**, (2020)
- [J7] Kemal, J. N.; **Marin-Palomo, P.**; Panapakkam, V.; Trocha, P.; Wolf, S.; Merghem, K.; Lelarge, F.; Ramdane, A.; Randel, S.; Freude, W.; Koos, C., “Coherent WDM transmission using quantum-dash mode-locked laser diodes as multi-wavelength source and local oscillator,” *Opt. Express* **27**, 3116431175 (2019), [DOI: 10.1364/oe.27.031164](https://doi.org/10.1364/oe.27.031164)
- [J8] Ummethala, S.; Harter, T.; Koehnle, K.; Li, Z.; Muehlbrandt, S.; Kutuvantavida, Y.; Kemal, J. N.; **Marin-Palomo, P.**; Schaefer, J.; Tessmann, A.; Garlapati, S. K.; Bacher, A.; Hahn, L.; Walther, M.; Zwick, T.; Randel, S.; Freude, W.; Koos, C., “THz-to-optical conversion in wireless communications using an ultra-broadband plasmonic modulator,” *Nature Photonics* **13**, 519–524 (2019), [DOI: 10.1038/s41566-019-0475-6](https://doi.org/10.1038/s41566-019-0475-6)
- [J9] Billah, M. R.; Blaicher, M.; Hoose, T.; Dietrich, P.-I.; **Marin-Palomo, P.**; Lindenmann, N.; Nesic, A.; Hofmann, A.; Troppenz, U.; Moehrle, M.; Randel, S.; Freude, W.; Koos, C., “Hybrid integration of silicon photonics circuits and InP lasers by photonic wire bonding,” *Optica* **5**, 876–883 (2018), [DOI: 10.1364/optica.5.000876](https://doi.org/10.1364/optica.5.000876)

- [J10] Trocha, P.; Karpov, M.; Ganin, D.; Pfeiffer, M. H. P.; Kordts, A.; Wolf, S.; Krockenberger, J.; **Marin-Palomo, P.**; Weimann, C.; Randel, S.; Freude, W.; Kippenberg, T. J.; Koos, C., “Ultrafast optical ranging using microresonator soliton frequency combs,” *Science* **359**, 887–891 (2018), DOI: [10.1126/science.aao3924](https://doi.org/10.1126/science.aao3924)
- [J11] Kemal, J. N.; Pfeifle, J.; **Marin-Palomo, P.**; Gutierrez Pascual, M. D.; Wolf, S.; Smyth, F.; Freude, W.; Koos, C., “Multi-wavelength coherent transmission using an optical frequency comb as a local oscillator,” *Opt. Express* **24**, 25432–25445 (2016), DOI: [10.1364/oe.24.025432](https://doi.org/10.1364/oe.24.025432)

Conference Publications

- [C1] **Marin-Palomo, P.**; Pfeifle, J.; Kemal, J. N.; Wolf, S.; Vijayan, K.; Chimot, N.; Martinez, A.; Ramdane, A.; Lelarge, F.; Koos, C.; Freude, W., “8.32 Tbit/s Coherent Transmission Using a Quantum-Dash Mode-Locked Laser Diode,” *Conf. on Lasers and Electro-Optics (CLEO'16), San Jose (CA), USA, June 5 – 10*, paper STh1F.1. (2016)
- [C2] **Marin-Palomo, P.**; Pfeifle, J.; Karpov, M.; Trocha, P.; Rosenberger, R.; Vijayan, K.; Wolf, S.; Kemal, J. N.; Kordts, A.; Pfeiffer, M.; Brasch, V.; Freude, W.; Kippenberg, T. J.; Koos, C., “50 Tbit/s Massively Parallel WDM Transmission in C and L Band Using Interleaved Cavity-Soliton Kerr Combs,” *Conf. on Lasers and Electro-Optics (CLEO'16), San Jose (CA), USA, June 5 – 10*, paper STu1G.1. (2016) (invited)
- [C3] **Marin-Palomo, P.**; Kemal, J. N.; Trocha, P.; Wolf, S.; Kordts, A.; Karpov, M.; Pfeiffer, M.; Brasch, V.; Freude, W.; Kippenberg, T. J.; Koos, C., “34.6 Tbit/s WDM transmission using soliton Kerr frequency combs as optical source and local oscillator,” *42nd European Conf. Opt. Commun. (ECOC'16), Düsseldorf, Germany, Sept. 18 – 22* (2016)
- [C4] **Marin-Palomo, P.**; Zepp, A.; Gladysz, S., “Characterization of the digital holographic wavefront sensor,” *SPIE 9242, Remote Sensing of Clouds and the Atmosphere XIX; and Optics in Atmospheric Propagation and Adaptive Systems XVII* **9242**, 92421T-92421T-14 (2014)

- [C5] **Marin-Palomo, P.**; Zepp, A.; Gladysz, S., “Digital holographic wavefront sensor,” *Imaging and Applied Optics 2015, Adaptive Optics: Analysis, Methods & Systems, Arlington, Virginia, USA, June 7 – 11* , paper AOT2D.1 *Optical Society of America (OSA)* (2015)
- [C6] Pfeifle, J.; Kordts, A.; **Marin-Palomo, P.**; Karpov, M.; Pfeiffer, M.; Brasch, V.; Rosenberger, R.; Kemal, J. N.; Wolf, S.; Freude, W.; Kippenberg, T. J.; Koos, C., “Full C and L-Band Transmission at 20 Tbit/s Using Cavity-Soliton Kerr Frequency Combs,” *Conf. on Lasers and Electro-Optics (CLEO'15), Postdeadline Paper Digest*, paper JTh5C.8. *Optical Society of America (OSA)* (2015)
- [C7] Kemal, J. N.; Pfeifle, J.; **Marin-Palomo, P.**; Gutierrez Pascual, M. D.; Wolf, S.; Smyth, F.; Freude, W.; Koos, C., “Parallel Multi-Wavelength Intradynne Reception Using an Optical Frequency Comb as a Local Oscillator,” *41th European Conf. Opt. Commun. (ECOC'15), Valencia, Spain, Sept. 27 – Oct. 1* , paper P.4.18. (2015)
- [C8] Hoose, T.; Billah, M. R.; **Marin-Palomo, P.**; Blaicher, M.; Dietrich, P.-I.; Hofmann, A.; Troppenz, U.; Moehrle, M.; Lindenmann, N.; Thiel, M.; Simon, P.; Hoffmann, J.; Goedecke, M. L.; Freude, W.; Koos, C., “Multi-Chip Integration by Photonic Wire Bonding: Connecting Surface and Edge Emitting Lasers to Silicon Chips,” *Optical Fiber Communication Conference (OFC'16)*, paper M2I.7 (2016)
- [C9] Ramdane, A.; Panapakkam, V.; Gaimard, Q.; Merghem, K.; Aubin, G.; Chimot, N.; Lelarge, F.; Vujicic, V.; Anthur, A.; Zhou, R.; Barry, L. P.; **Marin-Palomo, P.**; Kemal, J. N.; Pfeifle, J.; Koos, C., “Frequency combs from InAs/InP quantum dash based mode-locked lasers for multi-terabit/s data transmission,” *International Conference Laser Optics (LO'2016), St. Petersburg, Russian Federation, 27 June – 1 July* , paper R-310 (2016)

- [C10] Koos, C.; Kippenberg, T. J.; Barry, L. P.; Dalton, L. R.; Ramdane, A.; Lelarge, F.; Freude, W.; Kemal, J. N.; **Marin-Palomo, P.**; Wolf, S.; Trocha, P.; Pfeifle, J.; Weimann, C.; Laueremann, M.; Herr, T.; Brasch, V.; Watts, R. T.; Elder, D. L.; Martinez, A.; Panapakkam, V.; Chimot, N., “Multi-terabit/s transmission using chip-scale frequency comb sources,” *18th Intern. Conf. on Transparent Optical Networks (ICTON'16), Trento, Italy, July 10 – 14*, paper We.A5.1 IEEE (2016) (invited)
- [C11] Ramdane, A.; Panapakkam, V.; Gaimard, Q.; Merghem, K.; Aubin, G.; Chimot, N.; Lelarge, F.; Vujicic, V.; Anthur, A.; Zhou, R.; Barry, L. P.; **Marin-Palomo, P.**; Kemal, J. N.; Pfeifle, J.; Koos, C., “Frequency comb generation using QD-based mode locked lasers: application to multi-Terabit/s optical fiber transmission,” *International Nanophotonics Workshop iNOW-2016, 26 July – 5 August, Munich, Würzburg, Germany*
- [C12] Koos, C.; Freude, W.; Dalton, L. R.; Kippenberg, T. J.; Barry, L. P.; Ramdane, A.; Lelarge, F.; Wolf, S.; Zwickel, H.; Laueremann, M.; Weimann, C.; Hartmann, W.; Kemal, J. N.; **Marin-Palomo, P.**; Trocha, P.; Pfeifle, J.; Herr, T.; Brasch, V.; Watts, R. T.; Elder, D. L.; Martinez, A.; Panapakkam, V.; Chimot, N., “Silicon-organic hybrid (SOH) devices and their use in comb-based communication systems,” *13th International Conference on Group IV Photonics (GFP'16), Shanghai, China, August 24 – 26* (2016) (invited)
- [C13] Koos, C.; Kippenberg, T. J.; Barry, L. P.; Ramdane, A.; Lelarge, F.; Freude, W.; **Marin-Palomo, P.**; Kemal, J. N.; Weimann, C.; Wolf, S.; Trocha, P.; Pfeifle, J.; Karpov, M.; Kordts, A.; Brasch, V.; Watts, R. T.; Martinez, A.; Panapakkam, V.; Chimot, N. “Chip-scale frequency comb generators for high-speed communications and optical metrology,” *SPIE Nonlinear Frequency Generation and Conversion: Materials and Devices XVI, (LASE-SPIE'17), San Francisco (CA), USA, Jan. 28 – Feb. 2*, paper 10090-15 (2017) (invited)

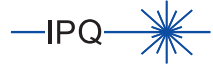
- [C14] Kemal, J. N.; **Marin-Palomo, P.**; Panapakkam, V.; Trocha, P.; Wolf, S.; Merghem, K.; Lelarge, F.; Ramdane, A.; Randel, S.; Freude, W.; Koos, C., “WDM Transmission Using Quantum-Dash Mode-Locked Laser Diodes as Multi-Wavelength Source and Local Oscillator,” *Optical Fiber Communication Conference (OFC'17), Los Angeles (CA), USA, March 19 – 23* , paper Th3F.6. (2017)
- [C15] Kemal, J. N.; **Marin-Palomo, P.**; Merghem, K.; Guy, A.; Calo, C.; Brenot, R.; Lelarge, F.; Ramdane, A.; Randel, S.; Freude, W.; Koos, C., “32QAM WDM Transmission Using a Quantum-Dash Passively Mode-Locked Laser with Resonant Feedback,” *Optical Fiber Communication Conference (OFC'17), Los Angeles (CA), USA, March 19 – 23* , paper Th5C.3. (2017) (postdeadline)
- [C16] Ganin, D.; Trocha, P.; Pfeiffer, M.; Karpov, M.; Kordts, A.; Krockenberger, J.; **Marin-Palomo, P.**; Wolf, S.; Randel, S.; Freude, W.; Kippenberg, T. J.; Koos, C., “Ultrafast Dual-Comb Distance Metrology Using Dissipative Kerr Solitons,” *Conf. on Lasers and Electro-Optics (CLEO'17), San Jose (CA), USA, May 14 – 19* , paper STh4L.6. (2017)
- [C17] Billah, M. R.; Kemal, J. N.; **Marin-Palomo, P.**; Blaicher, M.; Kutuvan-tavida, Y.; Kieninger, C.; Zwickel, H.; Dietrich, P.-I.; Wolf, S.; Hoose, T.; Xu, Y.; Troppenz, U.; Moehrle, M.; Randel, S.; Freude, W.; Koos, C., “Four-Channel 784 Gbit/s Transmitter Module Enabled by Photonic Wire Bonding and Silicon-Organic Hybrid Modulators,” *43rd European Conf. Opt. Commun. (ECOC'17), Gothenburg, Sweden, Sept. 17 – 21* , paper Th.PDP.C.1 (2017) (postdeadline)
- [C18] Koos, C.; Kippenberg, T. J.; Barry, L. P.; Ramdane, A.; Brenot, R.; Freude, W.; Randel, S.; **Marin-Palomo, P.**; Kemal, J. N.; Trocha, P.; Ganin, D.; Weimann, C.; Wolf, S.; Pfeifle, J.; Karpov, M.; Kordts, A.; Vujcic, V.; Merghem, K., “Optical frequency combs and photonic integrated circuits: Tools for high-speed communications and advanced distance metrology,” *SPIE Photonics West; Quantum Sensing and Nano Electronics and Photonics XV (OPTO-SPIE 2018), San Francisco (CA), Jan. 28 – Feb. 1* (2018) (invited)

- [C19] Koos, C.; Randel, S.; Freude, W.; Kippenberg, T. J.; **Marin-Palomo, P.**; Kemal, J. N.; Trocha, P.; Ganin, D.; Weimann, C.; Wolf, S.; Pfeifle, J.; Karpov, M.; Kordts, A.; Vujicic, V. “Optical Frequency Combs: Tools for High-Speed Communications and Optical Distance Metrology,” *10th Sino-German Joint Symposium on Opto- and Microelectronic Devices and Circuits (SODC 2018), Aachen, Germany, September 16 – 20 (2018)* (invited)
- [C20] Freude, W.; Ummethala, S.; Harter, T.; Koehnle, K.; Li, Z.; Muehlbrandt, S.; Kutuvantavida, Y.; Kemal, J. N.; **Marin-Palomo, P.**; Schaefer, J.; Tessmann, A.; Kumar Garlapati, S.; Bacher, A.; Hahn, L.; Walther, M.; Zwick, T.; Randel, S.; Koos, C., “Wireless THz-to-optical conversion with an electro-optic plasmonic modulator,” *Light: Science & Applications, Light Conference (Light Conference'19), Changchun, China, July 16 – 18 (2019)* (invited)
- [C21] Adib, M. M. H.; Mahmud, M. S.; Kemal, J. N.; **Marin-Palomo, P.**; Fuellner, C.; Ramdane, A.; Koos, C.; Freude, W.; Randel, S., “24 GBd DP-QPSK Upstream and Downstream Operation of a Colourless Coherent PON Using an MLLD-Based Frequency Comb,” *45th European Conference on Optical Communication (ECOC'19), Dublin, Ireland, September 22 – 26 , paper M.1.F.2 (2019)*

Karlsruhe Series in Photonics & Communications, Vol. 33

Edited by Profs. C. Koos, W. Freude and S. Randel

Karlsruhe Institute of Technology (KIT)
Institute of Photonics and Quantum Electronics (IPQ)
Germany



The number of devices connected to the internet and the required data transmission speeds are increasing exponentially. To keep up with this trend, data center interconnects should scale up to provide multi-Tbit/s connectivity. With typical distances from a few kilometers to 100 km, these links require the use of a high number of WDM channels. The associated transceivers should have low cost and footprint. The scalability of the number of channels, however, is still limited by the lack of adequate optical sources.

In this book, we investigate novel chip-scale frequency comb generators as multi-wavelength light sources in WDM links. With a holistic model we estimate the performance of comb-based WDM links, and we compare the transmission performance of different comb generator types, namely a quantum-dash mode-locked laser diode and a microresonator-based Kerr comb generator. We characterize their potential for massively-parallel WDM transmission with various transmission experiments. Combined with photonic integrated circuits, these comb sources offer a path towards highly scalable, compact, and energy-efficient Tbit/s transceivers.

About the Author

Pablo Marin-Palomo was born in 1990 in Tossa de Mar, Spain. In 2014, he received the Master degree in Optics and Photonics from Karlsruhe Institute of Technology (KIT), which awarded him the Dr.-Ing. (Ph.D) degree in 2021. He is now a postdoc researcher at the Vrije Universiteit Brussel (VUB), where he focuses on novel integrated light sources for THz and optical communications.

ISSN 1865-1100
ISBN 978-3-7315-1129-8

Gedruckt auf FSC-zertifiziertem Papier

